

**EMISSION SIGNATURES FROM
SUB-PARSEC BINARY SUPERMASSIVE BLACK HOLES**

A Dissertation
Presented to
The Academic Faculty

By

Khai Nguyen

In Partial Fulfillment
of the Requirements for the Degree
Doctor of Philosophy in the
School of Physics

Georgia Institute of Technology

August 2019

Copyright © Khai Nguyen 2019

**EMISSION SIGNATURES FROM
SUB-PARSEC BINARY SUPERMASSIVE BLACK HOLES**

Approved by:

Dr. Tamara Bogdanović, Advisor
School of Physics
Georgia Institute of Technology

Dr. David Ballantyne
School of Physics
Georgia Institute of Technology

Dr. Michael Eracleous
Department of Astronomy and
Astrophysics
Pennsylvania State University

Dr. Gongjie Li
School of Physics
Georgia Institute of Technology

Dr. Deidre Shoemaker
School of Physics
Georgia Institute of Technology

Date Approved: June 20, 2019

Said no more counting dollars

We'll be counting stars

Yeah, we'll be counting stars.

OneRepublic

ACKNOWLEDGEMENTS

This work is especially dedicated to my Father whose philosophy has shaped my way of thinking, and whose work ethic has shaped my character. I am grateful to everyone who has supported me throughout this educational journey - My Family, My Advisors, My Teachers and Friends. Without you, I simply could not have made it here alone.

TABLE OF CONTENTS

Acknowledgments	iv
List of Tables	x
List of Figures	xi
Summary	xv
Chapter 1: Introduction	1
1.1 Theoretical Background	1
1.2 Observational Searches for Gravitationally Bound SBHBs	4
Chapter 2: Modeling the Spectroscopic Signatures of Sub-parsec SBHB	8
2.1 Broad Emission-line Profiles from a Circular Keplerian Disk	9
2.2 Broad Emission-line Profiles from a Triple Disk System	13
2.2.1 Geometry of the triple disk system	13
2.2.2 Calculation of disk emissivities	17
2.2.3 Total flux of the composite emission-line profile	18
2.2.4 Eclipsing disks	20
2.3 Absorption of Broad Emission-line Photons by Radiatively Driven Disk Wind	22
2.3.1 Brief description of the disk wind model	23

2.3.2	Detailed implementation of the disk wind model	26
2.3.2.1	Velocity field of the disk wind	28
2.3.2.2	Velocity gradient of the wind along the line of sight, Q . .	29
2.3.2.3	Density profile of the wind	33
2.3.2.4	Optical depth of the wind	34
2.3.2.5	Relativistic Sobolev method	36
Chapter 3:	Comparison with Observations	39
3.1	Parameter Choices of the Model	39
3.2	Broad Emission-line Profiles in Absence of the Disk Wind Effect	46
3.2.1	Characteristic features of the modeled emission-line profiles	47
3.2.2	Statistical properties of emission-line profiles	51
3.2.3	Dependence of profiles on the physical parameters of the binary . .	58
3.2.4	Discussion: Modeled emission-line profiles associated with sub- parsec SBHBs.	69
3.2.4.1	Do modeled BEL profiles carry an imprint of SBHB pa- rameters?	69
3.2.4.2	Can modeled BEL profiles be compared with the ob- served profiles from SBHB candidates?	72
3.2.4.3	Simplifying assumptions and their implications	74
3.3	Improved Model for Calculation of BELs: the Effect of Accretion Disk Wind	78
3.3.1	The effect of wind optical depth on profile peaks	78
3.3.2	Characteristic features of the modeled emission-line profiles	81
3.3.3	Dependence of profiles on the physical parameters of the binary . .	87

3.3.4	Discussion: Synthetic BEL profiles in the presence of radiatively driven disk wind	92
3.4	Implications for Observational Searches	95
3.4.1	Comparison with SBHB candidates	95
3.4.2	Importance of illumination by two active black holes (AGNs)	100
3.4.3	Temporal variability of the modeled line profiles	101
3.4.4	Implications for the observed variable profiles	105
3.4.5	Quantitative comparison of modeled emission-line profiles to the observed profiles	106
Chapter 4: Properties of Binary Candidates in the Context of the SBHB Model .		111
4.1	Methods	111
4.1.1	Description of the database of modeled and observed emission-line profiles	111
4.1.2	Comparison of the modeled and observed samples using the principal component analysis	113
4.1.3	Calculation of probability distributions for inferred SBHB parameters	117
4.2	Results	120
4.2.1	Analysis of individual SBHB candidates	120
4.2.2	Properties of the entire SBHB candidate sample	125
4.3	Discussion: Predictions and Simplifications	130
4.3.1	Implications for theory and observations	130
4.3.2	Simplifications and limitations of the method	133
Chapter 5: Conclusions		136

Appendices	142
Appendix A: Selection Effects of Spectroscopic Surveys	143
A.1 Model Assumptions and Parameters	143
A.1.1 Common assumptions of spectroscopic searches for SBHBs	143
A.1.2 Key parameters of the model	146
A.2 Intrinsic Probability Density Functions	149
A.2.1 Probability of a binary residing at separation a : $\rho(a)$	149
A.2.2 Mass ratio probability distribution: $\rho(q)$	151
A.3 Extrinsic Probability Density Functions	152
A.3.1 Probability of observing a binary with a significant velocity offset: P_V	152
A.3.2 Probability of observing a binary with a significant velocity modulation: $P_{\Delta V}$	154
A.3.3 Probability of simultaneous measurement of V_{obs} and ΔV_{obs} : $P_{V,\Delta V}$	156
A.4 Discussion on the Likelihood Model	157
A.4.1 Benefits of long-term monitoring and complementary searches for SBHBs	157
A.4.2 Simplifying assumptions and their implications	159
Appendix B: Characteristic Orbital Separations	163
Appendix C: Dependence of Statistical Distribution Functions on F_c	164
Appendix D: Animation	167
Appendix E: Computation of Principal Components	168

Appendix F: Results of Analysis for 88 SBHB Candidates	173
References	197
Vita	198

LIST OF TABLES

3.1	Parameters of the Model	40
3.2	Number of peaks.	48
3.3	Physical Parameters of Profiles Shown in Figure 3.18	85
3.4	Comparison of Observed and Modeled Datasets	108
A.1	Characteristic Orbital Separations	153
F.1	Inferred Values of the Binary Parameters for the SBHB Candidates from the E12 Sample.	174

LIST OF FIGURES

2.1	Geometry of the system in which two sources can illuminate the disk around an SBH.	11
2.2	Illustration of SBHB geometry for face-on orientation of the orbit.	14
2.3	Illustration of the broad line region of a single SBH affected by the accretion disk wind, based on the model of Chiang and Murray 1996 [127]. . . .	23
2.4	Maps of the disk wind velocity gradient along the LOS, Q	32
2.5	$H\beta$ broad emission-line profiles from a circular disk calculated for different values of the disk wind optical depth.	35
2.6	$H\beta$ broad emission lines calculated for single AGN without the accretion disk wind, with the disk wind effect calculated using the classical Sobolev method, and with the disk wind effect calculated using the relativistic Sobolev method.	37
3.1	Outer radii of the primary and secondary mini-disks as a function of a and e	42
3.2	Illustration of profile shapes when absorption through accretion disk wind is negligible.	47
3.3	Profiles emitted by a single mini-disk illuminated by its central AGN only, or by the companion AGN.	49
3.4	Sequence of profiles showing temporal evolution of a composite BEL profile.	51
3.5	AIP-PS map for profiles associated with circular SBHB systems.	54
3.6	AIP-PS maps for profiles associated with eccentric SBHB systems.	55
3.7	Characteristic profile shapes occupying different regions in the AIP-PS parameter space.	56

3.8	AI-FWHM maps for emission-line profiles associated with eccentric SBHB systems.	59
3.9	Characteristic profile shapes occupying different regions in the AI-FWHM parameter space.	60
3.10	FWQM-CS maps for profiles associated with eccentric SBHB systems. . . .	62
3.11	Characteristic profile shapes in the FWQM-CS parameter space.	63
3.12	AI-KI maps for profiles associated with eccentric SBHB systems.	64
3.13	Characteristic profile shapes in the AI-KI parameter space.	65
3.14	AIP-CS maps for profiles associated with eccentric SBHB systems.	66
3.15	Characteristic profile shapes in the AIP-CS parameter space.	67
3.16	Percentage of single- and multi-peaked profiles in different models calculated for SBHBs on circular and eccentric orbits.	80
3.17	Maps of Pearson skewness coefficient vs. peak shift (AIP-PS) for profiles associated with models of SBHBs on circular and eccentric orbits, different wind configurations, and wind optical depths.	82
3.18	Appearance of individual BEL profiles in C-NW and C-3DW-100 models. .	84
3.19	AIP-PS map for profiles associated with the eccentric SBHB model E-3DW-1.	88
3.20	Maps of full width at quarter maximum vs. centroid shift (FWQM-CS) for profiles associated with eccentric SBHB systems in model E-3DW-1.	89
3.21	Maps of Pearson skewness coefficient vs. centroid shift (AIP-CS) for profiles associated with eccentric SBHB systems in model E-3DW-1.	90
3.22	AIP-PS maps for profiles associated with the observed SBHB candidates and a control sample of matching AGNs from the E12 search.	96
3.23	FWQM-CS maps for profiles associated with the observed SBHB candidates and a control sample of matching AGNs from the E12 search.	97
3.24	AIP-CS maps for profiles associated with the observed SBHB candidates and a control sample of matching AGNs from the E12 search.	97

3.25	AIP-CS maps for the emission-line profiles in the C-3DW-1 model, the scenario in which each AGN is only allowed to illuminate its own mini-disk but not that of the companion SBH, and the scenario in which only the AGN associated with the secondary SBH illuminates all three disks while the primary AGN is assigned zero luminosity.	98
3.26	FWQM-CS maps with the same legend as in Figure 3.25.	99
3.27	AIP-CS maps with the same legend as in Figure 3.25.	99
3.28	Temporal evolution of profile shapes over one orbital cycle for an SBHB with $q = 1/10$ and $q = 9/11$	102
4.1	Illustration of the reconstruction of a profile from the modeled database using principal component analysis.	112
4.2	$H\beta$ emission-line profiles from multi-epoch observations of three SBHB candidates: SDSS J93844, J95036, and J161911.	115
4.3	$H\beta$ emission-line profiles from multi-epoch observations of the SBHB candidate J153636, indicated by the time stamp.	116
4.4	2D probability density distribution in terms of $\log(a/M)$ and q for SDSS J93844, J95036, and J161911	120
4.5	2D probability density distribution in terms of θ_1 and θ_2 for SDSS J93844, J95036, and J161911	120
4.6	2D probability density distribution in terms of $\log \tau_0$ and $\log (F_2/F_1)$ for SDSS J93844, J95036, and J161911.	121
4.7	Inferred average values of binary parameters and their standard deviations for 88 SBHB candidates from the E12 survey.	124
4.8	2D probability density distributions in terms of $\log(a/M)$ and q , θ_1 and θ_2 , and $\log \tau_0$ and $\log (F_2/F_1)$ for the 88 SBHB candidates from the E12 sample. 126	
4.9	2D probability density distributions in terms of $\log(a/M)$ and q , θ_1 and θ_2 , and $\log \tau_0$ and $\log (F_2/F_1)$ for the control group of AGNs from the E12 sample.	127
4.10	Best fit for the continuous probability density function for all 88 SBHB candidates from the E12 sample in terms of the semimajor axis, and mass ratio.	129

4.11	Likelihood for detection of SBHBs given a yearly cadence of observations by the E12 spectroscopic search based on the P18 model.	131
A.1	Probability distribution function for SBHB mass ratios adopted in the Pflueger et al. [168] model.	151
A.2	Two-dimensional cuts of the multi-variate likelihood for the E12 search given by $\mathcal{L} = \rho(a) \times \rho(q) \times P_{V,\Delta V}$	158
C.1	Effect of different cutoff values F_c , representing some fiducial level of spectral noise, on a simulated line profile shape.	165
C.2	AI-KI maps for profiles associated with eccentric SBHB systems calculated for different values of F_c	166
C.3	AIP-PS maps for profiles associated with eccentric SBHB systems calculated for different values of F_c	166
D.1	Orbital evolution of the triple-disk accretion flow around SBHB (Eclipse.gif, 393K).	167
E.1	The average profile and the first eight eigenprofiles calculated for our synthetic database.	170

SUMMARY

Motivated by advances in observational searches for sub-parsec supermassive black hole binaries (SBHBs) made in the past few years, we develop a semi-analytic model to describe spectral emission-line signatures of these systems. The goal of this study is to aid the interpretation of spectroscopic searches for binaries and help test one of the leading models of binary accretion flows in the literature: SBHB in a circumbinary disk. We model SBHB accretion flows as a set of three accretion disks: two mini-disks that are gravitationally bound to the individual black holes and a circumbinary disk. In the model, we have also included treatment of radiative transfer by taking into account the effect of the radiation driven accretion disk wind on the properties of the emission-line profiles. Given a physically motivated parameter space occupied by sub-parsec SBHBs, we calculate a synthetic database of nearly 42.5 million broad optical emission-line (BEL) profiles and explore the dependence of the profile shapes on characteristic properties of SBHBs. We find that the modeled profiles show distinct statistical properties as a function of the semi-major axis, mass ratio, eccentricity of the binary, and the degree of alignment of the triple disk system. This suggests that the BEL profiles from SBHB systems can in principle be used to infer the distribution of these parameters and as such merit further investigation. The profile shapes are a more sensitive measure of the binary orbital separation and the degree of alignment of the black hole mini-disks, and are less sensitive to the SBHB mass ratio and orbital eccentricity. We also find that modeled profile shapes are more compatible with the observed sample of SBHB candidates than with our control sample

of regular AGNs. Furthermore, if the observed sample of SBHBs is made up of genuine binaries, it must include compact systems with comparable masses, and misaligned mini-disks. We also present a method for comparison of the BEL profiles of observed SBHB candidates with those calculated from our model. Using this approach, we infer the values of the binary parameters for the observed SBHB candidates and evaluate the parameter degeneracies, representative of the uncertainties intrinsic to such measurements. We find that as a population, the SBHB candidates favor the average value of the semimajor axis corresponding to $\log(a/M) \approx 4.20 \pm 0.42$ and comparable mass ratios, $q > 0.5$. If the considered SBHB candidates are true binaries, this result would strongly suggest that there is a physical process that allows initially unequal mass systems to evolve toward comparable mass ratios. Because the orbital eccentricity suffers from a large degree of degeneracy, we obtain no useful constraints on this parameter. Our method also indicates that the SBHB candidates do not favor configurations in which the mini-disks are coplanar with the binary orbital plane. If upheld for confirmed SBHBs, this finding would indicate the presence of a physical mechanism that maintains misalignment of the mini-disks (or causes them to be warped) down to sub-parsec binary separations. The probability distributions for the SBHB parameters inferred for the observed SBHB candidates and our control group of AGNs are statistically indistinguishable, implying that this method can in principle be used to interpret the observed BEL profiles once a sample of confirmed SBHBs is available, but cannot be used as a conclusive test of binarity.

CHAPTER 1

INTRODUCTION

1.1 Theoretical Background

The past ten years have marked a period of active research on supermassive black hole (SBH) pairs and binaries spearheaded by theoretical studies which have investigated how black holes grow, interact with their environment, and form pairs. Interest in them has been driven by a realization that SBHs play an important role in evolution of their host galaxies [1–3] and also, by intention to understand the parent population of merging binaries which are the prime targets for the long anticipated space-based gravitational wave (GW) observatories. We refer to dual SBHs at large separations as *pairs* and to the gravitationally bound SBHs as *binaries*, hereafter.

Theoretical studies have established that evolution of SBH pairs from kiloparsec to smaller scales is determined by gravitational interactions of individual black holes with their environment [4, 5]. These include interaction of the SBHs with their own wakes of stars and gas [a.k.a., dynamical friction; 6–9] and scattering of the SBHs by massive gas clouds and spiral arms produced by local and global dynamical instabilities during the merger [10, 11]. During these interactions the SBHs exchange orbital energy and angular momentum with the ambient medium and can in principle grow through accretion [9, 12–18]. These factors determine the SBH dynamics and whether they evolve to smaller separations to form a gravitationally bound binary. For example, [16, 19] find that SBH pairs with mass ratios $q < 0.1$ are unlikely to form binaries within a Hubble time at any redshift. On the other hand SBH pairs with initially unequal masses can evolve to be more equal-mass, through preferential accretion onto a smaller SBH. It is therefore likely that SBH pairs with $q \gtrsim 0.1$ form a parent population of bound binaries at smaller separations.

A gravitationally bound binary forms at the point when the amount of gas and stars enclosed within its orbit becomes comparable to the total mass of the two black holes. For a wide range of host properties and SBH masses this happens at orbital separations $\lesssim 10$ pc [14, 17, 20]. The subsequent rate of binary orbital evolution depends on the nature of gravitational interactions that it experiences and is still an area of active research often abbreviated as *the last parsec problem*. The name refers to a possible slow-down in the orbital evolution of the parsec-scale supermassive black hole binaries (SBHBs) caused by inefficient interactions with stars [8] and gas [12]. If present, a consequence of this effect would be that a significant fraction of SBHBs in the universe should reside at orbital separations of ~ 1 pc. Several recent theoretical studies that focus on the evolution of binaries in predominantly stellar backgrounds however report that evolution of binaries to much smaller scales continues unhindered [21–25], although the agreement about the leading physical mechanism responsible for the evolution is still not universal [26].

SBH binaries in predominantly gaseous environments have also been a topic of a number of theoretical studies [27–41]. They find that binary torques can truncate sufficiently cold circumbinary disks and create an inner low density cavity by evacuating the gas from the central portion of the disk [see 42, and references above]. SBHs in this phase can accrete by capturing gas from the inner rim of the circumbinary disk and can in this way maintain mini-disks bound to individual holes. As the binary orbit decays, the inner rim of the circumbinary disk follows it inward until the timescale for orbital decay by gravitational radiation becomes shorter than the viscous timescale¹ of the disk [27]. At that point, the rapid loss of orbital energy and angular momentum through gravitational radiation cause the binary to detach from the circumbinary disk and to accelerate towards coalescence.

Through its dependence on the viscous time scale, orbital evolution of a gravitationally bound SBHB in the circumbinary disk depends on thermodynamic properties of the disk. These are uncertain, as they are still prohibitively computationally expensive to model from

¹The time scale on which the angular momentum is transported outwards through the disk.

first principles and are unconstrained by observations. More specifically, the thermodynamics of the disk is determined by the binary dynamics and also the presence of magnetic field and radiative heating and cooling of the gas. While the role of magnetic field in circumbinary disks has been explored in some simulations [35, 36, 43–45], a fully consistent calculation of radiative processes is still beyond computational reach. Consequently, current theoretical models can be formulated as parameter studies, where difficult-to-model processes are parametrized in some fashion, but cannot uniquely predict the properties of the circumbinary regions or the emission signatures of SBHBs. The circumbinary disk model is therefore an appealing theoretical concept that must be tested through observations.

Along similar lines, observations of the orbital properties of SBHBs are key to understanding binary evolution. This is because the frequency of binaries as a function of their orbital separation is directly related to the rate at which binaries evolve towards coalescence. Theoretical models predict that the exchange of angular momentum with the ambient medium is likely to result in SBHB orbits with eccentricities $\gtrsim 0.1$, with the exact value depending on whether gravitationally bound SBHs evolve in mostly stellar or gas rich environments [46–48]. Known semi-major axis and eccentricity distributions would therefore provide a direct test for a large body of theoretical models.

Our understanding of spin magnitudes and orientations in binary SBHs also relies on theoretical considerations. Interest in this topic was triggered by the prediction of numerical relativity that coalescence of SBHs with certain spin configurations can lead to the ejection of a newly formed SBH from its host galaxy. This effect arises due to the asymmetry in emission of GWs in the final stages of an SBH merger and can lead to a GW kick of up to $\sim 5000 \text{ km s}^{-1}$ [49, 50]. Several subsequent theoretical studies found that accretion and gravitational torques can act to align the spin axes of SBHs evolving in gas rich environments and in such way minimize the GW recoil [51–55]². Mutual SBH spin alignment is not expected in gas poor environments, geometrically thick, turbulent

²See however [56] for a different view.

and magnetically dominated disks [57–59], allowing a possibility that runaway SBHs and empty nest galaxies may exist. Hence, if observations can independently provide an insight into the geometry of circumbinary disks and spin properties of SBHBs, they would be an important probe of the alignment hypothesis.

1.2 Observational Searches for Gravitationally Bound SBHBs

From an observational point of view, this study is pursued through electromagnetic searches for dual and multiple SBHs with a variety of separations, ranging from ~ 10 s kpc to sub-parsec scales. The multi-wavelength searches for SBH systems with large separations, corresponding to early stages of galactic mergers, have so far successfully identified a few dozen dual and offset active galactic nuclei (AGN; [60–65] and others).

SBHs with even smaller (parsec and sub-parsec) separations are representative of the later stages of galactic mergers in which the two SBHs are sufficiently close to form a gravitationally bound pair. Key characteristic of gravitationally bound SBHBs is that they are observationally elusive and expected to be intrinsically rare. Theorists estimate that a fraction $< 10^{-3}$ of active galactic nuclei (AGNs) at redshift $z < 0.7$ may host SBHBs [66]. This result implies that any observational search for SBHBs must involve a large sample of AGNs and that observational technique used in the search needs to distinguish signatures of binaries from those of AGNs powered by single SBHs. Observational techniques used to search for such systems have so far largely relied on direct imaging, photometry, and spectroscopic measurements [see 67, for a review]. They have recently been complemented by observations with pulsar timing arrays (PTAs). We summarize the outcomes of these different observational approaches in the next few paragraphs and note that in all cases SBHBs have been challenging to identify because of their small separation on the sky, as well as the uncertainties related to the uniqueness of their observational signatures.

Angular separation of the parsec and sub-parsec binaries is below the spatial resolution of most astronomical observations, except for radio observations using the Very Long

Baseline Interferometry (VLBI) technique. This approach has been used to identify the most convincing SBHB candidate thus far, 0402+379 [68–70], which hosts a pair of two compact radio cores at a projected separation of 7.3 pc on the sky. Recently, [71] reported that long term VLBI observations reveal relative motion of the two cores consistent with orbital motion, lending further support to the SBHB hypothesis. Apart from this serendipitously discovered system, direct imaging with VLBI did not reveal many others [72, 73], largely because this technique cannot be used in survey mode, and so it requires a prior knowledge of likely candidates.

Photometric surveys, like the Catalina Real-Time Transient Survey, the Palomar Transient Factory and others, have uncovered about 150 SBHB candidates [e.g., 74–77]. In this approach, the quasi-periodic variability in the lightcurves of monitored quasars is interpreted as a manifestation of binary orbital motion. Because of the finite temporal extent of the surveys, which must record at least several orbital cycles of a candidate binary, most photometrically identified SBHB candidates have relatively short orbital periods, of order a few years. However, irregularly sampled, stochastically variable lightcurves of “normal” quasars, powered by a single SBH, can be mistaken for periodic sources and can lead to false binary identifications in photometric surveys [78]. This possibility is supported by PTAs, which are capable of probing the gravitational wave background at nanoHertz frequencies from sources like SBHBs with orbital periods of a few years [79–81]. Specifically, the upper limit placed by PTAs largely rules out the amplitude of gravitational wave background resulting from the ~ 150 photometric binary candidates, implying that some significant fraction of them are unlikely to be SBHBs [82]. While this will lead to a downward revision in the number of photometrically identified SBHB candidates, it provides a nice example of the effectiveness of multi-messenger techniques, when they can be combined.

Spectroscopic searches for SBHBs have so far identified about a hundred candidates. They rely on the detection of a velocity shift in the broad emission-line (BEL) spectrum of an SBHB that arises as a consequence of the binary orbital motion. This approach is

similar to that for detection of single- and double-line spectroscopic binary stars, where the lines are expected to oscillate about their local rest-frame wavelength on the orbital time scale of the system. In the context of the binary model, the spectral emission lines are assumed to be associated with gaseous accretion disks that are gravitationally bound to the individual SBHs [83–85]. Given the velocity of the bound gas the BEL profiles from the SBH mini-disks are expected to be Doppler-broadened, similar to the emission lines originating in the broad line regions (BLRs) of AGNs. Moreover, several theoretical studies have shown that in unequal mass binaries accretion occurs preferentially onto the lower mass object [86–88], rendering it potentially more luminous than the primary. If so, this indicates that some fraction of SBHBs may appear as the single-line spectroscopic binaries. This realization lead to a discovery of a number of SBHB candidates based on the criterion that the culprit sources exhibit broad optical lines offset with respect to the rest frame of the host galaxy [89–96].³ Because this effect is also expected to arise in the case of a recoiling SBH receding from its host galaxy, the same approach has been used to flag candidates of that type [99–103]. The key advantage of the method is its simplicity, as the spectra that exhibit emission lines shifted relative to the galaxy rest frame are relatively straightforward to select from large archival data sets, such as the Sloan Digital Sky Survey (SDSS). Its main complication however is that the Doppler shift signature is not unique to these two physical scenarios and complementary observations are needed in order to determine the nature of the observed candidates [e.g., 67, 104–106].

To address this ambiguity a new generation of spectroscopic searches has been designed to monitor the offset of the BEL profiles over multiple epochs and target sources in which modulations in the offset are consistent with the binary orbital motion [105, 107–115]. For example, Eracleous et al. [105] searched for $z < 0.7$ SDSS quasars whose broad $H\beta$ lines are offset by $\gtrsim 1000 \text{ km s}^{-1}$ and selected 88 quasars for observational followup from the initial group of $\sim 16,000$ objects. After multiple epochs of observation 29/88 exhibit

³In an alternative approach anomalous line ratios have been used to flag SBHB candidates with perturbed BLRs [97, 98].

statistically significant epoch-to-epoch modulations in the velocity offset [105], in broad agreement with theoretical predictions for frequency of SBHBs [66].

This thesis is directly motivated by the ongoing spectroscopic searches and is organized as follows. In Chapter 2, we describe our model of SBHB systems and calculation of their BEL profiles. In Chapter 3, we describe a database of modeled BEL profiles for SBHB systems and compare its properties to those of observed SBHB candidates. In Chapter 4, we discuss physical interpretation for observed SBHB candidates obtained from a spectroscopic survey, as well as uncertainty associated with this interpretation. In the Appendix A, we describe our model used to calculate likelihood for detection of SBHBs in spectroscopic surveys, and compare its predictions with the physical interpretation obtained in the previous chapter. Finally, we conclude and discuss future prospects in Chapter 5.

CHAPTER 2

MODELING THE SPECTROSCOPIC SIGNATURES OF SUB-PARSEC SBHB

Motivated by theoretical models described in the literature and ongoing observations we consider the sub-parsec binaries with mass ratios in the range $0.1 \leq q \leq 1$, where $q = M_2/M_1$. The orbital separation and period of such binaries can be expressed in terms of the spectroscopically determined velocity offset, which is their key observable property. If the measured velocity offset can be attributed to the motion of the secondary SBH, as indicated by the accretion rate inversion found in theoretical studies of SBHBs, then the projected velocity of the secondary, u_2 , is related to its true orbital speed, $v_{\text{orb}2}$, as $u_2 = v_{\text{orb}2} \sin i |\sin \phi|$. Here i is the inclination of the orbital axis of the binary relative to the observer's line of sight (LOS; $i = 0$ is face-on) and ϕ is the orbital phase at the time of the observation ($\phi = 0$ corresponds to conjunction). Note that the expression for u_2 applies to circular orbits, an assumption which we use to obtain illustrative estimates but in our model calculations actually consider both circular and eccentric orbits. Following [105], we express the period and orbital separation in terms of the total mass $M_8 = (M_1 + M_2)/10^8 M_\odot$ and the projected velocity of the secondary, $u_{2,3} = u_2/10^3 \text{ km s}^{-1}$ as

$$a = \frac{0.11 M_8}{(1+q)^2 u_{2,3}^2} \left(\frac{\sin i |\sin \phi|}{\sin 45^\circ \sin 45^\circ} \right)^2 \text{ pc} \quad (2.1)$$

$$P = \frac{332 M_8}{(1+q)^3 u_{2,3}^3} \left(\frac{\sin i |\sin \phi|}{\sin 45^\circ \sin 45^\circ} \right)^3 \text{ yr} \quad (2.2)$$

If the measured velocity offset is instead associated with the primary SBH, the above expressions can be written in terms of the projected velocity of the primary, $u_{1,3} = q u_{2,3}$ where $u_{1,3} = u_1/10^3 \text{ km s}^{-1}$. In the expressions above we choose $i = \phi = 45^\circ$ and discuss the parameter values used in our model calculations in § 3.1.

The accretion flow is described as a set of three circular accretion disks: two mini-disks

that are gravitationally bound to the individual SBHs and a circumbinary disk. The three disks are modeled as independent BLRs, where the extent of the two mini-disks, as well as the central opening in the circumbinary disk are constrained by the size of the binary orbit and are subject to tidal truncation by the binary SBH [42, 116, 117]. In this model both accreting SBHs can shine as AGNs and illuminate their own mini-disk as well as the two other disks in the system. We assume that the bolometric luminosity of each AGN correlates with the accretion rate onto its SBH and that photoionization by the AGNs gives rise to the broad, low-ionization optical emission lines just like in “ordinary” BLRs [118, 119]. The emissivity of each disk can then be evaluated as a function of the accretion rate onto the SBHs and the disk size. We utilize the published measurements of accretion rates from simulations of SBHBs [40, 46, 86–88] in order to establish the relative bolometric luminosities of the two AGN in a binary and emissivity of each disk component. Any assumptions about the mutual orientation of the two mini-disks and circumbinary disk are relaxed and they are allowed to assume arbitrary orientations relative to the observer.

2.1 Broad Emission-line Profiles from a Circular Keplerian Disk

We describe each disk in the triple disk system as a circular Keplerian, geometrically thin accretion disk in the weak-field approximation as outlined by Chen et al. 1989 [120, 121], and Eracleous et al. 1995 [122]. Specifically, we use implementation that assumes optically thin emission from the skin of the disk (equation 19 in [120]) and neglect bending of light in gravitational field of an SBH (encoded in equation 8 of both [121, 122]). We first outline the key elements of this model (hereafter referred to as the *single disk model*) and then describe modifications we made in order to calculate BEL profiles from triple disk systems. In the single disk model the flux of the BEL profile measured in the observer’s frame can be expressed as an integral over the surface of the emitting disk defined in terms of the

properties in the disk frame:

$$F(\nu_{\text{obs}}) = \frac{M^2 \nu_0}{d^2} \int_0^{2\pi} \int_{\xi_{\text{in}}}^{\xi_{\text{out}}} I(\xi, \nu_{\text{turb}}) D_{\text{rot}}^3 \left(1 - \frac{2}{\xi}\right)^{-\frac{1}{2}} \xi d\xi d\varphi \quad (2.3)$$

where M is the mass of the central object, ν_0 is the rest frequency of the emission line, d is the distance from the center of the disk to the observer, $\xi = r/M$ is the radius in the disk in dimensionless units, ξ_{in} and ξ_{out} are the inner and outer edge of the emission region, respectively, and φ is the azimuthal angle measured in the plane of the disk (note that the symbol φ , used to denote the azimuthal angle in the single disk frame here, is different from ϕ , which is reserved for azimuthal angle in the binary black holes frame as defined later in the next § 2.2). The geometry of such a disk is illustrated in Figure 2.1.

$I(\xi, \nu_{\text{turb}})$ is the specific intensity of light emitted at radius ξ and frequency ν_{turb}

$$I(\xi, \nu_{\text{turb}}) = \frac{1}{4\pi} \frac{\epsilon(\xi)}{(2\pi)^{1/2} \sigma} \exp[-(\nu_{\text{turb}} - \nu_0)^2 / 2\sigma^2] \quad (2.4)$$

where $\epsilon(\xi)$ is the disk emissivity as a function of radius. In the single disk model $\epsilon = \epsilon_0 \cdot \xi^{-p}$ represents the emissivity of the disk illuminated by a single, central source. The emissivity constant, ϵ_0 , is proportional to the luminosity of the photoionizing source, which we assume is powered by accretion onto an SBH. For the purposes of this calculation we therefore assume that $\epsilon_0 \propto \dot{M}$. Geometric arguments, as well as photoionization calculations, indicate that $p \approx 3$ is a reasonable value for the emissivity index [118] and we adopt it in our calculations. In the next section we extend this formalism to account for illumination of the disk by two AGNs, associated with two SBHs as illustrated in Figure 2.1.

The frequency of photons emerging locally from the disk (ν_{turb}) is shifted by turbulent motion of gas and assumed to have a Gaussian distribution about the rest frequency ν_0 [121]. We adopt a characteristic velocity dispersion of the gas due to turbulent motion of $\sigma \simeq 850 \text{ km s}^{-1}$, which corresponds to a characteristic frequency shift of $\Delta\nu/\nu_0 = 850 \text{ km s}^{-1}/c \simeq 2.8 \times 10^{-3}$, where c is the speed of light. Our choice of the characteristic

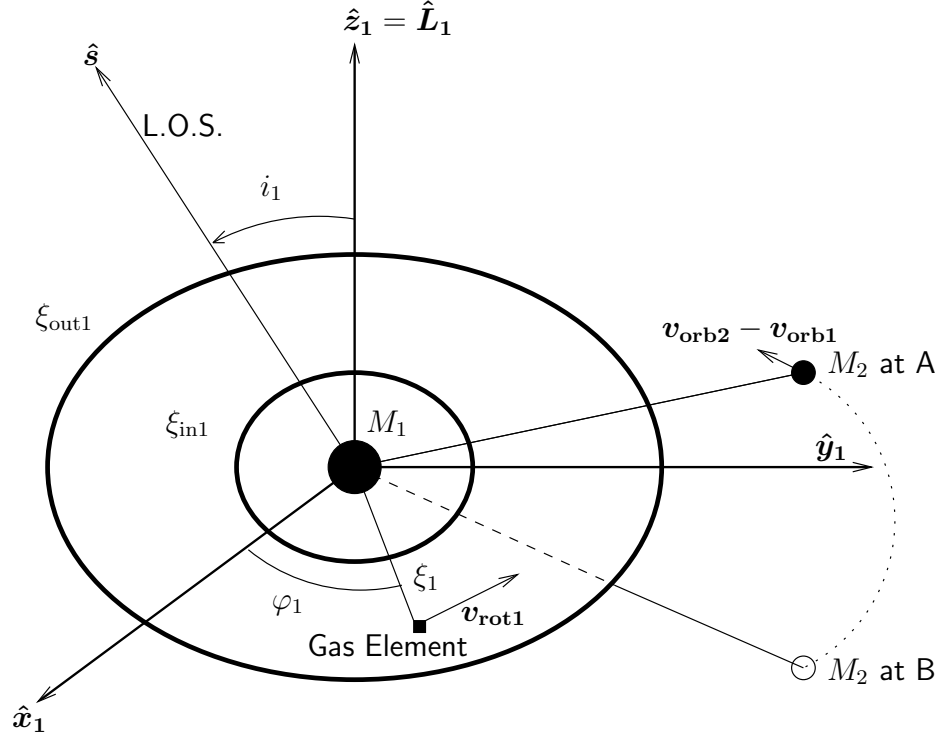


Figure 2.1: Geometry of the system in which two sources can illuminate the disk around an SBH. In this illustration the coordinate system is centered on the primary SBH defined so that the z_1 -axis is parallel to the angular momentum vector of the gas in the disk and the LOS \hat{s} belongs to the x_1z_1 plane. The illumination of the disk by the secondary AGN can be seen by a distant observer only when the secondary AGN belongs to the same half-plane with the observer (location A) and is otherwise blocked by the disk (location B).

velocity dispersion is motivated by the values inferred from radio-loud AGN with double-peaked emission lines, which have been successfully modeled with either the circular or elliptical disk models and turbulent broadening in the range of $\sim 600 - 3000 \text{ km s}^{-1}$ [123–125].

Several additional effects can impact the frequency of emitted photons, including the rotational motion of gas in the disk, relativistic Doppler boosting, and gravitational redshift. Classically, the Doppler factor associated with the motion of the gas in the disk can be expressed as

$$D_{\text{cl}} = \frac{1}{1 - \mathbf{v}_{\text{rot}} \cdot \hat{\mathbf{s}}} = (1 + \xi^{-1/2} \sin i \sin \varphi)^{-1} \quad (2.5)$$

where $\mathbf{v}_{\text{rot}} = \xi^{-1/2} \hat{\mathbf{e}}_{\phi}$ is the velocity vector of a given surface element of the disk in units of the speed of light, $\hat{\mathbf{s}}$ is the unit vector along the LOS of the observer, and i is the inclination of the disk with respect to the LOS, as illustrated in Figure 2.1. The two relativistic effects can be accounted for by adding terms for the special relativistic beaming, $D_{\text{sr}} = \sqrt{1 - v_{\text{rot}}^2}$, and general relativistic gravitational redshift, $D_{\text{gr}} = \sqrt{1 - 2/\xi}$, yielding

$$D_{\text{rot}} = \left(1 - \frac{1}{\xi}\right)^{1/2} \left(1 - \frac{2}{\xi}\right)^{1/2} D_{\text{cl}} \simeq \left(1 - \frac{3}{\xi}\right)^{1/2} D_{\text{cl}} \quad (2.6)$$

where we used the weak-field approximation (valid when $\xi \gg 1$) to obtain the final expression. For an emission element in the disk located at $\xi = 500$ the shift in the frequency of emitted light due to the relativistic effects can be estimated as $D_{\text{rot}} \simeq 0.99699 D_{\text{cl}}$. For the $H\beta$ transition this amounts to nearly 15 \AA , an offset that is in principle detectable given the spectral resolution of optical surveys and therefore should be accounted for in the model. The relativistic Doppler factor can then be expressed as

$$D_{\text{rot}} = \nu_{\text{obs}}/\nu_{\text{turb}} = (1 - 3/\xi)^{1/2} (1 + \xi^{-1/2} \sin i \sin \varphi)^{-1}. \quad (2.7)$$

where ν_{obs} marks the frequency of the photon measured by the observer. Our derivation of equation 2.3 departs from that of [121] and [122] because it does not include relativistic

bending of light and is thus applicable under two conditions. The first is that the photons are emitted by a gas element far away from the black hole ($\xi \gg 1$). The second is that emitted photons do not travel on “grazing” orbits over the black hole. Our calculation satisfies both by having the $H\beta$ photons emerge from the radii in the disk $\xi \geq 500$ and by eliminating edge-on configurations characterized by inclination angles of the disk in the range $80 - 100^\circ$.

2.2 Broad Emission-line Profiles from a Triple Disk System

In this section we describe modifications to the single disk model introduced in order to calculate the BEL profiles from the triple disk system associated with an SBHB. This is accomplished in three steps in which we: (a) define the orientation of the three disks relative to the orbital plane of the SBHB and relative to a distant observer, (b) evaluate the emissivity of each disk illuminated by the two AGNs, and (c) sum the three components of flux to calculate the composite BEL profile in the frame of the binary.

2.2.1 Geometry of the triple disk system

In order to determine the mutual orientation of the three disks and the binary orbit, as well as their relative orientation with respect to the LOS, we define three coordinate systems, each anchored to the center of its resident disk as in Figure 2.1. The coordinate system associated with the circumbinary disk coincides with that associated with the binary orbit and has the origin in the SBHB center of mass. We refer to it as the *binary* or *SBHB frame* in the rest of the text, and employ the tilde notation $\tilde{x}, \tilde{y}, \tilde{z}$ to distinguish from the coordinates of the *single* frame defined in the previous § 2.1. In addition, to distinguish among the properties calculated in these reference frames we introduce subscripts where “1” and “2” correspond to the primary and secondary mini-disks, and “3” to the circumbinary disk, respectively. Furthermore, because we carry out the calculation of flux in dimensionless, geometric units (as shown in the previous section), the subscripts also indicate that dis-

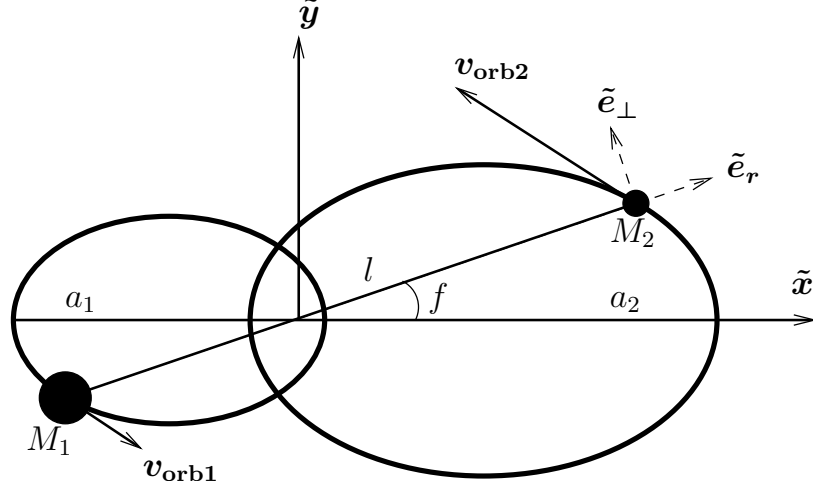


Figure 2.2: Illustration of SBHB geometry for face-on orientation of the orbit. SBHB center of mass marks the origin of the coordinate system which \tilde{z} -axis points in the direction of the orbital angular momentum of the binary (out of the page). The \tilde{x} -axis points towards the pericenter of the primary SBH orbit and is parallel to the orbital semi-major axis of the binary, $a = (a_1 + a_2)$. The orbital phase f is measured counter-clockwise from the \tilde{x} -axis to the instantaneous location of secondary SBH. The mini-disks and circumbinary disk are not shown. See text for definition of other variables.

tances are measured in units of M_1 and M_2 in the frames of the primary and secondary mini-disks, and $M = M_1 + M_2$ in the frame of the binary.

Figure 2.2 illustrates the coordinate system anchored to the binary orbital plane where the SBHB center of mass marks the origin and the \tilde{z} -axis points in the direction of the orbital angular momentum of the binary, directed out of the page (see also the animated Figure D.1 in the Appendix D for temporal evolution of the binary system). The \tilde{x} -axis points towards the pericenter of the primary SBH orbit and is parallel to the orbital semi-major axis of the binary, $a = (a_1 + a_2)$. We describe the orientation of the two SBHs in the orbital plane of the binary as a vector pointing from the primary to the secondary SBH (see Figure 2.2)

$$\mathbf{l} = l \tilde{\mathbf{e}}_r = l(\cos f \tilde{\mathbf{x}} + \sin f \tilde{\mathbf{y}}) \quad (2.8)$$

where $l = a(1 - e^2)/(1 - e \cos f)$ is the separation of the black holes, e is the orbital eccentricity, f is the orbital phase of the SBHB measured counter-clockwise from the \tilde{x} -axis to the instantaneous location of the secondary SBH, and $\tilde{\mathbf{e}}_r$ is the unit vector parallel

to l .

We define the orientation of the observer's LOS in the SBHB frame with a vector:

$$\hat{\mathbf{s}} = \sin i \cos \phi \tilde{\mathbf{x}} + \sin i \sin \phi \tilde{\mathbf{y}} + \cos i \tilde{\mathbf{z}} \quad (2.9)$$

The inclination angle, i , describes the orientation of the LOS relative to the vector of orbital angular momentum of the SBHB. For example, the inclination angle $i = 0^\circ$ represents the clockwise binary seen face-on and values $i > 90^\circ$ represent counter-clockwise binaries. The azimuthal angle ϕ is measured in the binary orbital plane, from the positive \tilde{x} -axis to the projection of the LOS, in counter-clockwise direction. For circular SBHBs varying the orbital phase f is equivalent to varying the azimuthal orientation of the observer and in this case we adopt a single nominal value of $\phi = 0^\circ$ in calculation of the BEL profiles. This is however not the case for the eccentric binaries, in which case f and ϕ take independent values.

We define the orientation of the primary mini-disk by specifying the orientation of its rotation axis (given by the unit vector of the disk angular momentum, $\hat{\mathbf{L}}_1$) in terms of the polar and azimuthal angles θ_1 and ϕ_1 measured in the SBHB frame:

$$\hat{\mathbf{L}}_1 = \sin \theta_1 \cos \phi_1 \tilde{\mathbf{x}} + \sin \theta_1 \sin \phi_1 \tilde{\mathbf{y}} + \cos \theta_1 \tilde{\mathbf{z}} . \quad (2.10)$$

Equivalently, we use θ_2, ϕ_2 to specify the orientation of the secondary disk, given by the unit vector of the disk angular momentum, $\hat{\mathbf{L}}_2$. The mini-disks are coplanar with the SBHB orbit when $\theta_1 = \theta_2 = 0^\circ$, and the gas in the mini-disks exhibits retrograde motion relative to the SBHB when $\theta_i > 90^\circ$. The azimuthal angles ϕ_1 and ϕ_2 are measured in the binary orbital plane, from the positive \tilde{x} -axis to the projections of the rotation axes of the mini-disks, in counter-clockwise direction.

With known orientations of the mini-disks and the observer in the SBHB frame we can

evaluate the inclinations of the mini-disks with respect to the LOS

$$\cos i_1 = \hat{\mathbf{L}}_1 \cdot \hat{\mathbf{s}} = \sin i \cos \phi \sin \theta_1 \cos \phi_1 + \sin i \sin \phi \sin \theta_1 \sin \phi_1 + \cos i \cos \theta_1 \quad (2.11)$$

The orientation of the secondary AGN relative to the primary mini-disk can be calculated as follows

$$\sin \theta_{M2} \cos \varphi_{M2} = \tilde{\mathbf{e}}_r \cdot \hat{\mathbf{x}}_1 = \tilde{\mathbf{e}}_r \cdot \left(\frac{\hat{\mathbf{L}}_1 \times \hat{\mathbf{s}}}{\sin i_1} \times \hat{\mathbf{L}}_1 \right) \quad (2.12)$$

$$\sin \theta_{M2} \sin \varphi_{M2} = \tilde{\mathbf{e}}_r \cdot \hat{\mathbf{y}}_1 = \tilde{\mathbf{e}}_r \cdot \frac{\hat{\mathbf{L}}_1 \times \hat{\mathbf{s}}}{\sin i_1} \quad (2.13)$$

$$\cos \theta_{M2} = \tilde{\mathbf{e}}_r \cdot \hat{\mathbf{L}}_1 = \sin \theta_1 \cos \phi_1 \cos f + \sin \theta_1 \sin \phi_1 \sin f = \sin \theta_1 \cos(\phi_1 - f) \quad (2.14)$$

where θ_{M2} and φ_{M2} are the angular coordinates describing the location of the secondary AGN in the *single* frame of the primary mini-disk. Equivalent expressions can be written for the secondary mini-disk by replacing subscript “1” with “2”

$$\cos i_2 = \hat{\mathbf{L}}_2 \cdot \hat{\mathbf{s}} \quad (2.15)$$

$$\sin \theta_{M1} \sin \varphi_{M1} = -\tilde{\mathbf{e}}_r \cdot \hat{\mathbf{y}}_2 \quad (2.16)$$

$$\cos \theta_{M1} = -\tilde{\mathbf{e}}_r \cdot \hat{\mathbf{L}}_2 \quad (2.17)$$

where the minus signs in the last two equations encode the opposition of the primary and secondary SBHs relative to the center of mass. In all configurations we assume that the circumbinary disk is co-planar with the SBHB orbit and co-rotating with it and therefore $\theta_3 \equiv 0^\circ$, $\phi_3 \equiv \phi$ and $i_3 \equiv i$ (i.e., the circumbinary disk frame is coincident with the SBHB frame). These relationships allow us to define the emissivity of surface elements in each of the three disks in the system.

2.2.2 Calculation of disk emissivities

We assign emissivities ϵ_1 , ϵ_2 and ϵ_3 to the primary, secondary and circumbinary disk, respectively. The emissivity of a gas element located at (ξ_1, φ_1) in the mini-disk of the primary SBH can be expressed as a sum of components due to the illumination by its own AGN (ϵ_{11}) and the AGN associated with the secondary SBH (ϵ_{12})

$$\epsilon_1(\xi_1, \varphi_1) = \epsilon_{11} + \epsilon_{12} = \epsilon_{10} \frac{h_1}{\xi_1^3} + \epsilon_{20} \frac{H(\cos i_1 \cos \theta_{M2}) |l_1| |\cos \theta_{M2}| - q h_2}{\left[\xi_1^2 + l_1^2 - 2\xi_1 l_1 (\hat{\xi}_1 \cdot \tilde{e}_r) \right]^{3/2}} \quad (2.18)$$

where h_1 and h_2 denote the sizes of the sources of continuum radiation associated with the two SBHs. As mentioned earlier, the subscripts indicate that h_1 and h_2 are dimensionless quantities in units of M_1 and M_2 , respectively, and l_1 is the separation of the two AGN in units of M_1 . Motivated by the X-ray studies of the broad iron line reverberation [126], we assume that the sources of continuum radiation are compact and have spatial extents of $h_1 = 10$ and $h_2 = 10$. Note that the term $q h_2$ in equation 2.18 represents conversion of h_2 into the units of M_1 , for consistency with the rest of the properties calculated in the frame of the primary mini-disk, where $q = M_2/M_1$ is the SBH mass ratio.

The second term of equation 2.18 captures the effect of the off-center illumination of the primary BLR by the secondary AGN. Figure 2.1 illustrates that this effect can be seen by a distant observer only when the side of the mini-disk illuminated by the off-center AGN is facing the observer. Alternatively, whenever the secondary AGN is blocked by the primary mini-disk (from the observer's point of view) this effect will be absent. We describe these outcomes with the Heaviside step function, $H(\cos i_1 \cos \theta_{M2})$, which takes value “1” whenever the secondary AGN belongs to the same half plane with the observer ($\cos i_1 \cos \theta_{M2} \geq 0$) and value “0” otherwise (see also the animated Figure D.1 in the Appendix D for an illustration of the off-center illumination effect).

As discussed in § 2.1, the emissivity constants ϵ_{10} and ϵ_{20} are directly proportional to the luminosity of the two AGNs, which we assume are powered by accretion onto the SBHs.

Therefore, we express the ratio of the two constants as $\dot{m} = \epsilon_{20}/\epsilon_{10} = \dot{M}_2/\dot{M}_1$. Assuming relative scaling such that $\epsilon_{10} = 1$ implies $\epsilon_{20} = \dot{m}$ and equation 2.18 becomes

$$\epsilon_1(\xi_1, \varphi_1) = \frac{10}{\xi_1^3} + \dot{m} \frac{H(\cos i_1 \cos \theta_{M2}) |l_1| \cos \theta_{M2} - 10q}{[\xi_1^2 + l_1^2 - 2\xi_1 l_1 \sin \theta_{M2} (\cos \varphi_1 \cos \varphi_{M2} + \sin \varphi_1 \sin \varphi_{M2})]^{3/2}} \quad (2.19)$$

The vertical brackets in equations 2.18 and 2.19 denote absolute values of the relevant quantities. Similarly, the emissivity of the secondary mini-disk can be expressed as:

$$\epsilon_2(\xi_2, \varphi_2) = \dot{m} \frac{10}{\xi_2^3} + \frac{H(\cos i_2 \cos \theta_{M1}) |l_2| \cos \theta_{M1} - 10/q}{[\xi_2^2 + l_2^2 + 2\xi_2 l_2 \sin \theta_{M1} (\cos \varphi_2 \cos \varphi_{M1} + \sin \varphi_2 \sin \varphi_{M1})]^{3/2}} \quad (2.20)$$

In the case of the circumbinary disk the illumination by both AGNs is off-center. We express its emissivity as that of a single accretion disk which center resides at the center of mass of the binary

$$\epsilon_3(\xi_3, \varphi_3) = \frac{10}{1+q} \frac{1}{(\xi_3^2 + l_{31}^2 + 2\xi_3 l_{31} \cos \varphi_3)^{3/2}} + \dot{m} \frac{10q}{1+q} \frac{1}{(\xi_3^2 + l_{32}^2 - 2\xi_3 l_{32} \cos \varphi_3)^{3/2}} \quad (2.21)$$

Because the coordinate system associated with the circumbinary disk coincides with the reference frame of the binary, all distances in equation 2.21 are normalized by the total mass of the binary M . Therefore, $\xi_3 = r_3/M$ is the dimensionless radial distance of the gas element to the SBHB center of mass and $l_{31} = q/(1+q)(l/M)$ and $l_{32} = 1/(1+q)(l/M)$ are the dimensionless distances from the center of mass to the primary and secondary SBHs, respectively.

2.2.3 Total flux of the composite emission-line profile

With known emissivities the flux from each disk in the SBHB system can be calculated as an integral over the surface area, according to equation 2.3. Before summing the fluxes to calculate the composite BEL profile we need to account for the Doppler shift of the photons

emitted by the primary and secondary mini-disks due to their orbital motion. Because the circumbinary disk is at rest with respect to the SBHB center of mass we apply no shift to its emission. The emitted composite profile is therefore calculated in the reference frame of the binary.

Because the orbital velocities of SBHBs considered in this work are non-relativistic, the Doppler shifts associated with the orbital motion can be evaluated in classical limit. We therefore neglect the effect of relativistic boosting in this case as well as the gravitational redshift and lensing of photons that may arise in configurations when the two SBHs are in conjunction (i.e., lined up along the observer's LOS). In classical limit, the Doppler shift associated with the orbital motion of the secondary mini-disk is $D_{\text{orb2}} = 1 / (1 - \mathbf{v}_{\text{orb2}} \cdot \hat{\mathbf{s}})$ and

$$\frac{\Delta\nu_{\text{orb2}}}{\nu_0} = \frac{\nu_{\text{obs}} - \nu_0}{\nu_0} = \frac{1}{1 - \mathbf{v}_{\text{orb2}} \cdot \hat{\mathbf{s}}} - 1 \simeq \mathbf{v}_{\text{orb2}} \cdot \hat{\mathbf{s}} \quad (2.22)$$

Here \mathbf{v}_{orb2} is the velocity vector of the secondary SBH measured in the frame of the binary in units of c and $\hat{\mathbf{s}}$ describes the orientation of the observer in the frame of the SBHB as defined earlier. Let $\mathbf{v}_{\text{orb}} = \mathbf{v}_{\text{orb2}} - \mathbf{v}_{\text{orb1}}$ be the relative velocity vector of the two SBHs, as in Figure 2.2, and

$$v_{\text{orb}}^2 = \left(\frac{2}{l} - \frac{1}{a} \right) \quad (2.23)$$

$$\mathbf{v}_{\text{orb}} = \dot{\mathbf{l}} = v_r \tilde{\mathbf{e}}_r + v_f \tilde{\mathbf{e}}_\perp = \dot{l} \tilde{\mathbf{e}}_r + l \dot{f} \tilde{\mathbf{e}}_\perp \quad (2.24)$$

$$\mathbf{v}_{\text{orb}} = \left[\frac{1}{a(1 - e^2)} \right]^{1/2} [-e \sin f \tilde{\mathbf{e}}_r + (1 - e \cos f) \tilde{\mathbf{e}}_\perp] \quad (2.25)$$

where l and a are in units of M , and as defined in previous section, $\tilde{\mathbf{e}}_r = (\cos f \tilde{\mathbf{x}} + \sin f \tilde{\mathbf{y}})$ and $\tilde{\mathbf{e}}_\perp = (-\sin f \tilde{\mathbf{x}} + \cos f \tilde{\mathbf{y}})$ are the unit vectors parallel and perpendicular to \mathbf{l} , respectively. By conservation of momentum, $\mathbf{v}_{\text{orb2}} = \mathbf{v}_{\text{orb}} / (1 + q)$, yielding the Doppler shifts for emission from the secondary and primary mini-disks

$$\Delta\nu_{\text{orb2}} = \frac{\nu_0}{1 + q} \left[\frac{1}{a(1 - e^2)} \right]^{1/2} [-\sin f \sin i \cos \phi + (\cos f - e) \sin i \sin \phi] \quad (2.26)$$

$$\Delta\nu_{\text{orb1}} = -q \Delta\nu_{\text{orb2}} \quad (2.27)$$

Because we are interested in the value of the total flux in some arbitrary normalized units (as opposed to the absolute units) the distance d from the observer to the SBHB system can be omitted because it is the same for all three disks (see equation 2.3). Given the choice of dimensionless units employed in our calculation of emissivities in equations 2.19–2.21, the components of flux associated with the primary, secondary and circumbinary disk are proportional to M_1^2 , M_2^2 and M^2 , respectively. Therefore, in the expression for the total flux the relative contributions from each disk should be scaled in terms of the SBHB mass ratio q as

$$F_{\text{tot}} = \frac{1}{(1+q)^2} F_1 + \frac{q^2}{(1+q)^2} F_2 + F_3 \quad (2.28)$$

2.2.4 Eclipsing disks

An interesting effect arises from a misaligned mini-disk is that it could block the emission of the other disks during an eclipse (see also the animated Figure D.1 in the Appendix D for an illustration of the eclipsing effect). Note that the modeled profiles presented in this thesis do not take into account the effect of eclipsing disks (specifically, the eclipse of one BLR by another). We nevertheless lay out the relevant calculation here, which will make a future implementation of this effect possible. The effect depends on location and orientation of the disks, as well as direction of the LOS. We illustrate in this section the condition for when a BEL photon originated from a position $\mathbf{P}_1(\xi_1, \varphi_1)$ on the primary disk is obscured by the secondary disk, while similar calculation can be applied to any other two disks in the triple disk system. For consistency, all related lengths in this calculation need to be scaled in terms of the same mass unit, e.g. the binary total mass M . After escaping the primary disk along the LOS, the photon intersects the secondary disk at location \mathbf{P}_2 that can be

determined by

$$(\mathbf{P}_2 - \mathbf{M}_2) \cdot \hat{\mathbf{L}}_2 = 0 \quad (2.29)$$

$$\mathbf{P}_2 = d_{12} \hat{\mathbf{s}} + \mathbf{P}_1 \quad (2.30)$$

where \mathbf{M}_2 is location of the secondary black hole,

$$\mathbf{M}_2 = \frac{l}{1+q} \tilde{\mathbf{e}}_r = \frac{l}{1+q} (\cos f \tilde{\mathbf{x}} + \sin f \tilde{\mathbf{y}}) \quad (2.31)$$

$\hat{\mathbf{L}}_2$ is direction of the secondary mini-disk angular momentum,

$$\hat{\mathbf{L}}_2 = \sin \theta_2 \cos \phi_2 \tilde{\mathbf{x}} + \sin \theta_2 \sin \phi_2 \tilde{\mathbf{y}} + \cos \theta_2 \tilde{\mathbf{z}} \quad (2.32)$$

and d_{12} is distance between the two points \mathbf{P}_1 and \mathbf{P}_2 . From 2.29 and 2.30, d_{12} can be expressed as

$$d_{12} = \frac{(\mathbf{M}_2 - \mathbf{P}_1) \cdot \hat{\mathbf{L}}_2}{\hat{\mathbf{s}} \cdot \hat{\mathbf{L}}_2} \quad (2.33)$$

In order to evaluate the previous expression, we can convert the position vector $\mathbf{P}_1(\xi_1, \varphi_1)$ from the primary mini-disk frame to the binary frame as follow

$$\mathbf{P}_1 = \xi_1 \cos \varphi_1 \hat{\mathbf{x}}_1 + \xi_1 \sin \varphi_1 \hat{\mathbf{y}}_1 = \xi_1 \cos \varphi_1 \left(\frac{\hat{\mathbf{L}}_1 \times \hat{\mathbf{s}}}{\sin i_1} \times \hat{\mathbf{L}}_1 \right) + \xi_1 \sin \varphi_1 \left(\frac{\hat{\mathbf{L}}_1 \times \hat{\mathbf{s}}}{\sin i_1} \right) \quad (2.34)$$

where the expression for $\hat{\mathbf{s}}$, $\hat{\mathbf{L}}_1$, and $\sin i_1$ in the binary frame can be found in equations 2.9, 2.10, and 2.11. Once d_{12} and \mathbf{P}_2 are evaluated from the equations 2.33 and 2.30, we can determine that the emissivity ϵ_1 at \mathbf{P}_1 is obscured by the secondary mini-disk if and

only if the following conditions are satisfied

$$\begin{cases} |\mathbf{P}_2 - \mathbf{M}_2| < \xi_{\text{out}2} \\ d_{12} > 0 \end{cases} \quad (2.35)$$

where the first condition requires that the interesection \mathbf{P}_2 is located within the secondary disk, and the second condition requires that the secondary disk blocks the emitted photon on the way out.

2.3 Absorption of Broad Emission-line Photons by Radiatively Driven Disk Wind

Notation Clarification: In this section all calculations are performed in the frame of a single disk around an individual black hole, and the binary frame defined in § 2.2 is not used. Have we followed the convention in the previous section, all coordinate axes would be subscripted by indices $i = 1$ for the primary disk around M_1 , $i = 2$ for the secondary disk around M_2 , and $i = 3$ for the circumbinary disk around the binary center of mass. To simplify the expressions and facilitate the comparisons between our results and others in the literature, we omit the index i in the rest of this section. For example, the LOS direction in the binary frame, $\hat{\mathbf{s}} = \sin i \cos \phi \tilde{\mathbf{x}} + \sin i \sin \phi \tilde{\mathbf{y}} + \cos i \tilde{\mathbf{z}}$, can be transformed to the primary and secondary mini-disk frames as

$$\hat{\mathbf{s}} = \sin i_1 \hat{\mathbf{x}}_1 + \cos i_1 \hat{\mathbf{z}}_1 = \sin i_2 \hat{\mathbf{x}}_2 + \cos i_2 \hat{\mathbf{z}}_2 \quad (2.36)$$

and will be simply expressed as $\hat{\mathbf{s}} = \sin i \hat{\mathbf{x}} + \cos i \hat{\mathbf{z}}$ in this section. All unit lengths should be scaled by the individual black hole masses for the cases of the mini-disks, or by the total mass for the case of the circumbinary disk.

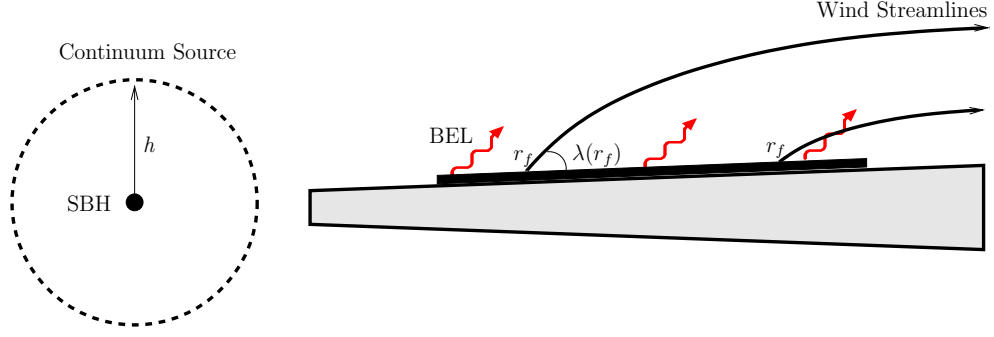


Figure 2.3: Illustration of the broad line region of a single SBH affected by the accretion disk wind, based on the model of Chiang and Murray 1996 [127]. The compact source of continuum radiation (dashed circle) photoionizes the skin of an optically thick, geometrically thin disk giving rise to the low ionization, BEL layer. Before escaping to infinity, some BEL photons are absorbed by the accretion disk wind of finite optical depth, illustrated here as a set of streamlines lifting off the disk at the foot-point with radius r_f at an angle $\lambda(r_f)$. Figure does not show the details of the inner accretion disk and is not to scale.

2.3.1 Brief description of the disk wind model

The theory that the accretion flow itself is the source of the BELs is steadily gaining support in the AGN community. Studies of the response of the line profiles to changes in the flux continuum indicate that the motion of the gas in the $H\beta$ emitting BLRs of most AGNs is consistent with the thick disk and orbits that range from elliptical, to inflowing or outflowing trajectories [128–132]. Several works have demonstrated that disk models can be used to describe emission from BLRs of most AGNs when additional radiative transfer effects of the disk atmosphere on the BEL profiles are accounted for [127, 133–137]. The origin of BELs in the upper layer of an accretion disk and the associated wind is also compelling because the same wind scenario has been invoked to explain the broad, blueshifted absorption lines seen in the rest-frame UV spectra of a subset of AGNs [138, 139] and more recently, the existence of changing look AGNs [140].

The origin of the line-driven wind in AGNs is in the inner accretion disk ($r \sim 10^{14}$ cm for $\sim 10^8 M_\odot$ black hole), where dense gas blocks the soft X-ray photons from the compact source of continuum radiation but transmits UV photons, which allows radiation pressure on resonance lines to accelerate the outflow to $\sim 0.1 c$ [133]. The wind extends to larger

radii in the disk, where it affects the structure and kinematics of the BLR gas. In this work, we explore this phenomenon in the context of the low-ionization $H\beta$ lines emerging from the BLRs surrounding SBHBs. We assume the $H\beta$ emission region to be a very thin layer on the surface of the outer accretion disk, which in AGNs extends in radial direction from $\sim 10^{15} - 10^{16}$ cm to $\sim 10^{18}$ cm in radial direction. The emissivity above the emitting layer drops abruptly because hydrogen becomes highly ionized as a result of the steep decline in the density with height. The emissivity below the emitting layer drops sharply because the flux of ionizing photons from the central source at this depth is severely attenuated (see photoionization calculation in Appendix A of [134]).

Figure 2.3 illustrates the geometry of the BLR around a single SBH in which emitted radiation is attenuated by the accretion disk wind. The radiation pressure lifts the gas from the surface of the disk and launches it along the wind streamlines, each of which is anchored to the disk at the foot-point with radius r_f , measured from the center of the disk in spherical coordinates. Each streamline makes a small angle, λ , relative to the disk which decreases as a function of radius [127],

$$\lambda(r) = \lambda(R_{\text{in}}) \frac{R_{\text{in}}}{r} \quad (2.37)$$

where R_{in} is the inner radius of each BLR (as defined in Table 3.1) and $\lambda(R_{\text{in}}) = 10^\circ$ is chosen for all three disks [134]. Before escaping to infinity, some low ionization BEL photons are absorbed by a low density accretion disk wind. The wind is highly ionized and does not contribute significantly to the emission of low-ionization lines but has a finite optical depth in these lines, thus modifying the intensity and shape of the emitted profiles.

Calculations of radiative transfer for outflows of this type are often carried out in the limit of large velocity gradient (a.k.a., Sobolev approximation, [141–144]). In this regime the photons that are not absorbed in the vicinity of the emission layer can escape to infinity, provided that the velocity of the wind projected onto the LOS is monotonically increasing. Under such circumstances the photons do not encounter multiple regions along the LOS where they can be absorbed. Since accretion disk winds are expected to accelerate radi-

ally out, e.g. and references therein [139, 145], this condition is satisfied and the Sobolev approximation allows one to uncouple the absorption layer (marked as a black strip at the bottom of the wind streamlines in Figure 2.3) from the rest of the wind. In this approximation, the characteristic thickness of the absorption layer is given by the Sobolev length, ℓ_S . The probability that the low-ionization line photons escape the wind can then be estimated as a function of the local parameters in this layer

$$\beta_e(\mathbf{r}, \hat{\mathbf{s}}) = \frac{1 - e^{-\tau(\mathbf{r}, \hat{\mathbf{s}})}}{\tau(\mathbf{r}, \hat{\mathbf{s}})}, \quad (2.38)$$

where \mathbf{r} marks the location from which the photon is emitted and the unit vector $\hat{\mathbf{s}}$ defines the direction of the LOS. The line optical depth of the absorption layer, $\tau(\mathbf{r}, \hat{\mathbf{s}})$, depends on the local mass density of neutral atoms, $\rho(\mathbf{r})$, opacity coefficient, $\varkappa(\mathbf{r})$, and turbulent velocity, $\sigma(\mathbf{r})$

$$\tau(\mathbf{r}, \hat{\mathbf{s}}) = \varkappa \rho \ell_S = \frac{\varkappa(\mathbf{r}) \rho(\mathbf{r}) \sigma(\mathbf{r})}{|\hat{\mathbf{s}} \cdot \mathbf{\Lambda}(\mathbf{r}) \cdot \hat{\mathbf{s}}|}. \quad (2.39)$$

Here, $\mathbf{\Lambda}$ is the wind velocity gradient tensor, which can be represented by its symmetric part (the rate of strain tensor) without changing the resulting inner product, $Q \equiv \hat{\mathbf{s}} \cdot \mathbf{\Lambda} \cdot \hat{\mathbf{s}}$. Defined in this way, Q is the velocity gradient of the wind along the LOS. The model assumes constant \varkappa and σ within the thin absorption layer, and the density is expressed as a power law in radius, $\rho = \rho_0 (r/M_i)^{-\eta}$, where ρ_0 is a normalization constant. Following [134], we adopt $\tau_0 = \varkappa \rho_0 \sigma$, in which case equation 2.39 can be reduced to

$$\tau = \frac{\tau_0}{|Q|} \left(\frac{r}{M_i} \right)^{-\eta}, \quad (2.40)$$

where $\tau \approx 5\tau_0$ ($7\tau_0$) represents the optical depth of the emission layer, along the direction perpendicular to the disk plane ($i = 0^\circ$), at the inner edge of the BLR with $R_{\text{in},i} = 500 M_i$ ($1000 M_i$), and assuming $\eta = 1$. Note that equation 2.39 implies that Q must have units of inverse time in order for the optical depth, τ , to be dimensionless. Keeping up with

the formulation of equations in geometric units it follows that Q and τ_0 in equation 2.40 (and hereafter) are expressed as dimensionless quantities in terms of $c^3/GM_i = M_i^{-1}$, and are properties that in this model decrease with the mass of the relevant SBH, or in the case of the circumbinary disk, binary mass. The details of this calculation, including the components of the Λ tensor and the final expression for Q , are shown in the following § 2.3.2.

An additional ingredient necessary for this calculation is the description of the poloidal component of the wind velocity along a given streamline

$$v_p(r) = v_\infty \left(1 - b \frac{r_f}{r}\right)^\gamma. \quad (2.41)$$

At the launching point on the surface of the disk (i.e., at the foot-point of the streamline), we assume that the wind velocity is comparable to the Keplerian velocity in the disk, $v_p(r_f) = (r_f/M_i)^{-1/2}$, resulting in a total speed of the wind close to the escape speed from the SBH. A choice of $b = 0.7$ and $\gamma = 1.2$, adopted here, then implies that the wind accelerates to the terminal velocity $v_\infty \approx 4.7 (r_f/M_i)^{-1/2}$, which corresponds to $v_\infty \approx 0.2c$ for the launching point at $r_f = 500 M_i$ (see § 2.3.2.1). The value of $\gamma = 1.2$ is consistent with the values inferred from observations, which range from 1.06 to 1.3, from quasars to Seyferts, respectively [138].

We assume that the disk wind driven by each AGN extends over the entire surface of its BLR. It is not clear however whether these outflows can extend from the mini-disks into the circumbinary disk, especially in configurations in which the disks are not co-planar.

2.3.2 Detailed implementation of the disk wind model

In this section we describe the new elements in the calculation of the BEL profiles, introduced as a part of the disk wind model. We refer the reader to § 2.2 for the description of geometry of a triple disk system and main steps in the calculation of the composite BEL

profiles. The same geometry and procedure are also used in this section. As before, we adopt the disk emitter model [120–122] to describe the line flux emitted by each individual disk in the system. In this context the flux of the BEL profile measured in the observer’s frame is an integral over the surface of the emitting disk defined in terms of the properties in the disk frame:

$$F_\nu(\nu_{\text{obs}}) = \frac{M^2 \nu_0}{d^2} \int_0^{2\pi} \int_{\xi_{\text{in}}}^{\xi_{\text{out}}} I_\nu(\xi, \varphi, \nu_{\text{turb}}) D_{\text{rot}}^3 \left(1 - \frac{2}{\xi}\right)^{-\frac{1}{2}} \xi d\xi d\varphi . \quad (2.42)$$

Here we assume that the emitting disk is geometrically thin and that emission arises from the $\theta \approx 90^\circ$ plane. M is the mass of the central black hole, ν_0 is the rest frequency of the emission line, d is the distance from the center of the disk to the observer, $\xi = r/M$ is the radius in the disk in dimensionless units, ξ_{in} and ξ_{out} are the inner and outer edges of the emission region, respectively, and φ is the azimuthal angle measured in the plane of the disk. D_{rot} is the relativistic Doppler factor.

$I_\nu(\xi, \varphi, \nu_{\text{turb}})$ is the specific intensity of light emitted at a polar coordinate (ξ, φ) and frequency ν_{turb} . In the disk wind model

$$I_\nu(\xi, \varphi, \nu_{\text{turb}}) = \frac{\beta_e}{4\pi} \frac{\epsilon(\xi, \varphi)}{(2\pi)^{1/2} \sigma} \exp[-(\nu_{\text{turb}} - \nu_0)^2 / 2\sigma^2] . \quad (2.43)$$

Recall that the emissivity of a BLR illuminated by a single, central AGN is axisymmetric and thus independent on φ . In our model however, every disk in the system is illuminated by two AGNs, giving rise to a non-axisymmetric emissivity pattern encoded in $\epsilon(\xi, \varphi)$, as defined in equations 2.18–2.21 (see also the animated Figure D.1 in the Appendix D for an illustration of the non-axisymmetric emissivity pattern). The broadening of the BEL profiles is assumed to be due to the turbulent velocity of the disk, σ , and is described as a Gaussian distribution around ν_0 .

The new element of the calculation is the modification of the disk emissivity by absorp-

tion of line photons in the disk wind. The absorption is characterized by a photon escape probability, $\beta_e(\mathbf{r}, \hat{\mathbf{s}})$, which represents the probability for a BEL photon, emitted from the surface of the disk at a location \mathbf{r} , to escape the wind in the direction of the LOS defined by the unit vector $\hat{\mathbf{s}}$. The escape probability is a function of the line optical depth of the wind (equation 2.38), which in turn depends on the density and velocity field of the wind. We describe how are these properties modeled in the next sub-sections.

2.3.2.1 Velocity field of the disk wind

We describe the three-dimensional velocity field of the wind in terms of the spherical velocity components v_r , v_θ and v_φ , defined with respect to the center of the disk, which is located in the xy plane and has the angular momentum vector aligned with the positive z -axis. Following the formalism developed for isotropic stellar winds we express the poloidal component of the velocity along a streamline, $\mathbf{v}_p = \mathbf{v}_r + \mathbf{v}_\theta$, as an increasing function of distance from the launching point

$$v_p(r) = v_\infty \left(1 - b \frac{r_f}{r}\right)^\gamma \quad (2.44)$$

(see [146]). The parameter $b = 1 - [v_p(r_f)/v_\infty]^{1/\gamma}$ is related to the ratio between the initial velocity of the wind at the launching point (i.e., at the foot-point of the streamline) and its terminal velocity far downstream. For the purposes of this work we choose $b = 0.7$. The parameter γ is expected to range from 1.06 for quasars to 1.3 for Seyferts [138], and we choose $\gamma = 1.2$ as a representative intermediate value. Following [127] and [134], we also adopt $v_\infty(r_f) = 4.7(GM/r_f)^{1/2}$ and the velocity components

$$v_r = v_p \cos \lambda \quad , \quad v_\theta = -v_p \sin \lambda \quad \text{and} \quad v_\varphi = \left(\frac{GM}{r}\right)^{1/2} \quad , \quad (2.45)$$

respectively. Here $\lambda = \lambda(R_{\text{in}})(R_{\text{in}}/r)$ is the wind opening angle, measured between the streamline and the disk, and $\lambda(R_{\text{in}}) = 10^\circ$, as defined in equation 2.37 and shown in

Figure 2.3. These choices imply the finite poloidal and azimuthal velocity at the foot-point of the wind, $v_p(r_f) = v_\varphi(r_f) = (GM/r_f)^{1/2}$, which combined in quadrature equal the escape velocity from the SBH. Moreover, all velocity components are characterized by non-zero velocity gradients, as required by the Sobolev method. Note also that the symmetry of a single disk system requires that $v_\theta = -v_p \sin \lambda$ when $i < 90^\circ$, and $v_\theta = v_p \sin \lambda$ when $i > 90^\circ$.

In addition, it is worth mention that our choices for b and γ are different from those previously used in the literature. For example, [127] and [134] choose $b = 1$, which leads to a simplification of the model because $v_p(r_f)$ vanishes in that case, implying that the wind starts with the zero velocity and accelerates outwards. This simplification in turn necessitates that the value of γ is exactly 1, because for any other value the gradient at the foot-point of the streamline $\partial v_p / \partial r = 0$, thus violating the requirement for high velocity gradients in the Sobolev method.

2.3.2.2 Velocity gradient of the wind along the line of sight, Q

In this section we outline the calculation of the velocity gradient of the wind along the LOS, given the velocity field of the wind defined above. As laid out in § 2.3.1, the velocity gradient can be expressed as an inner product, $Q = \hat{\mathbf{s}} \cdot \mathbf{\Lambda} \cdot \hat{\mathbf{s}}$, of the strain tensor along a given LOS. Following the coordinate systems defined in the previous section, a distant observer is located in the xz plane at an inclination angle i , relative to the z -axis (see Figure 2.2). Hence, the direction of the LOS, pointing from any point on the disk to the distant observer is given by

$$\hat{\mathbf{s}} = \cos i \hat{\mathbf{z}} + \sin i \hat{\mathbf{x}} = \sin i \cos \varphi \hat{\mathbf{r}} - \cos i \hat{\boldsymbol{\theta}} - \sin i \sin \varphi \hat{\boldsymbol{\phi}} . \quad (2.46)$$

Here we use the relationships between the unit vectors in the Cartesian and spherical-polar coordinate systems, $\hat{\mathbf{x}} = \sin \theta \cos \varphi \hat{\mathbf{r}} + \cos \theta \cos \varphi \hat{\boldsymbol{\theta}} - \sin \varphi \hat{\boldsymbol{\phi}}$ and $\hat{\mathbf{z}} = \cos \theta \hat{\mathbf{r}} - \sin \theta \hat{\boldsymbol{\theta}}$.

Setting $\theta = 90^\circ$ for any point on the surface of the disk and expanding the inner products yields

$$Q = \sin^2 i \left[\cos^2 \varphi \Lambda_{rr} - 2 \sin \varphi \cos \varphi \Lambda_{r\varphi} + \sin^2 \varphi \Lambda_{\varphi\varphi} \right] - |\cos i| \left[2 \sin i \cos \varphi \Lambda_{r\theta} - |\cos i| \Lambda_{\theta\theta} - 2 \sin i \sin \varphi \Lambda_{\theta\varphi} \right], \quad (2.47)$$

where the absolute value of $\cos i$ ensures the symmetry of solutions above and below the accretion disk, such that $Q(i) = Q(180^\circ - i)$. It is worth noting that equation 2.47 is consistent with the equation 8 in [135], who pointed out and corrected the sign error affecting the $\cos i$ terms in the expression for Q in [133], in their equation 15.

For an azimuthally symmetric disk wind ($\partial/\partial\varphi = 0$) with a small opening angle ($\cos \lambda \approx 1$), the components of the symmetric strain tensor Λ in spherical coordinates are:

$$\Lambda_{rr} = \frac{\partial v_r}{\partial r} = \frac{C_1}{\kappa M} \xi^{-3/2}, \quad (2.48)$$

$$\Lambda_{\theta\theta} = \frac{1}{r} \frac{\partial v_\theta}{\partial \theta} + \frac{v_r}{r} = \frac{\partial v_r}{\partial r} + \frac{v_r}{r} = \frac{C_1 + C_2}{\kappa M} \xi^{-3/2}, \quad (2.49)$$

$$\Lambda_{\varphi\varphi} = \frac{1}{r \sin \theta} \frac{\partial v_\varphi}{\partial \varphi} + \frac{v_r}{r} + \frac{v_\theta \cot \theta}{r} = \frac{v_r}{r} = \frac{C_2}{\kappa M} \xi^{-3/2}, \quad (2.50)$$

$$\Lambda_{\theta\varphi} = \frac{\sin \theta}{2r} \frac{\partial}{\partial \theta} \left(\frac{v_\varphi}{\sin \theta} \right) + \frac{1}{2r \sin \theta} \frac{\partial v_\theta}{\partial \varphi} = \frac{1}{2r} \frac{\partial v_\varphi}{\partial \theta} = \frac{1}{4 \sin \lambda} \frac{v_\varphi}{r} = \frac{1}{4M \sin \lambda} \xi^{-3/2}, \quad (2.51)$$

$$\Lambda_{r\varphi} = \frac{1}{2r \sin \theta} \frac{\partial v_r}{\partial \varphi} + \frac{r}{2} \frac{\partial}{\partial r} \left(\frac{v_\varphi}{r} \right) = \frac{r}{2} \frac{\partial}{\partial r} \left(\frac{v_\varphi}{r} \right) = -\frac{3}{4M} \xi^{-3/2}, \quad (2.52)$$

$$\Lambda_{r\theta} = \frac{r}{2} \frac{\partial}{\partial r} \left(\frac{v_\theta}{r} \right) + \frac{1}{2r} \frac{\partial v_r}{\partial \theta} = \frac{1}{\kappa M} \left[\frac{\sin \lambda}{2} C_2 - \left(\frac{\sin \lambda}{2} + \frac{1}{2 \sin \lambda} \right) C_1 \right] \xi^{-3/2}, \quad (2.53)$$

where $C_1 \equiv \gamma b(1-b)^{(\gamma-1)}$, $C_2 \equiv (1-b)^\gamma$ and $\kappa \equiv 1/4.7$ are constants used to simplify the expressions. We use the following relationships to calculate the components of Λ on the surface of the disk and set $r_f = r$, as different streamlines are anchored to different radii in the disk

$$v_r = v_p \cos \lambda \approx v_p \quad (2.54)$$

$$\frac{v_r}{r} = (1-b)^\gamma \frac{v_\infty}{r} = \frac{C_2}{\kappa} \xi^{-1/2} r^{-1} = \frac{C_2}{\kappa M} \xi^{-3/2} , \quad (2.55)$$

$$\frac{\partial v_r}{\partial r} = \frac{\partial v_p}{\partial r} = \gamma b(1-b)^{(\gamma-1)} \frac{v_\infty}{r} = \frac{C_1}{\kappa M} \xi^{-3/2} , \quad (2.56)$$

$$\frac{\partial}{\partial \theta} = -\frac{r}{\sin \lambda} \frac{\partial}{\partial r} , \quad (2.57)$$

where $v_\infty = \xi^{-1/2}/\kappa$, as defined above. Note that the factor of M in the denominator of equations 2.48–2.53 arises from the conversion of the disk radius into geometric units. It follows that Λ , and consequently Q , are expressed in geometric units of time, M^{-1} , as noted in § 2.3.1.

Figure 2.4 shows the maps of the velocity gradient along the LOS for different realizations of the velocity field of the wind (encoded in parameters b and γ). Each panel also shows the resulting emission line (here shown as the $H\beta$ profile) associated with a given disk wind configuration. Note that because $\tau \propto Q^{-1}$, the larger values of Q correspond to the regions of lower optical depth in the disk and vice versa. The top left panel shows a double-peaked BEL profile from a disk with no accretion disk wind, as seen by a distant observer placed on the horizontal axis extending to the right of the disk to infinity, at inclination $i = 60^\circ$. The top middle panel shows the map corresponding to the choices of b and γ adopted in this work. Note that the regions of highest optical depth are expected to coincide with the regions in the disk that give rise to the largest Doppler shifts of emitted

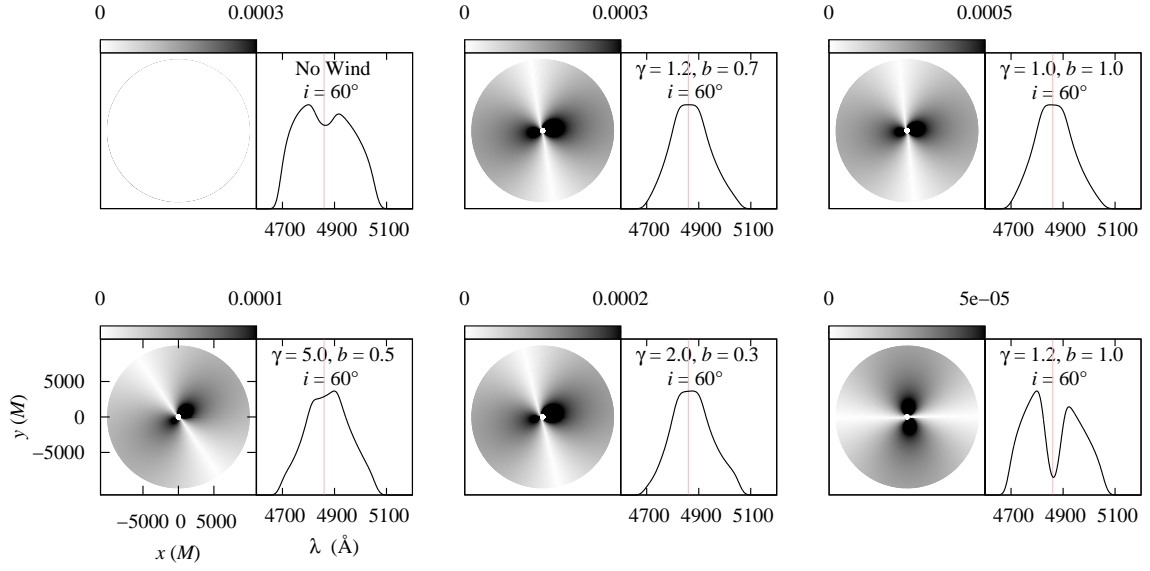


Figure 2.4: Maps of the velocity gradient along the LOS, Q , shown for different realizations of the velocity field of the wind, parametrized in terms of b and γ , and for two different orientations of the observer's LOS, i . The observer is located on the right and above the page, at an angle i relative to the normal to the page. The rotation of the disk is counter-clockwise. Each panel also shows the resulting $H\beta$ emission-line profile associated with a given disk wind configuration. Pink vertical line at 4860.09 \AA marks the rest wavelength of the $H\beta$ emission line.

photons, as seen by a distant observer. As a consequence, these photons are missing from the profile, giving rise to a narrower, single-peaked emission line.

The top right panel of Figure 2.4 shows the velocity gradient map for the choice of b and γ adopted by Chiang and Murray [127], and Flohic et al. [134], which result in the BEL profiles effectively indistinguishable from those in our model. The left and center panels in the bottom row illustrate the appearance of the velocity gradient map for the arbitrary values of b and γ , considerably different from those inferred in AGNs. Finally, the bottom right panel shows the resulting map and profile calculated for a combination of $\gamma \neq 1$ and $b = 1$ that violates the assumptions used in the Sobolev approximation (see the last paragraph of the previous section).

2.3.2.3 Density profile of the wind

We describe the density of the wind as a decreasing function of radius from the central SBH, $\rho \propto r^{-\eta}$, where $\eta > 0$ is the density index. In order to understand the range of plausible values for η we consider two different disk wind geometries in the context of the continuity equation

$$\frac{\partial \rho}{\partial t} + \nabla \cdot (\rho \mathbf{v}) = 0 . \quad (2.58)$$

For a steady state, azimuthally symmetric wind the continuity equation must satisfy conditions $\partial/\partial t = 0$ and $\partial/\partial \varphi = 0$. In spherical coordinates, this gives

$$\frac{1}{r^2} \frac{\partial (r^2 \rho v_r)}{\partial r} + \frac{1}{r \sin \theta} \frac{\partial (\rho v_\theta \sin \theta)}{\partial \theta} = 0 . \quad (2.59)$$

This equation can be further simplified if one considers a disk wind emerging from the emitting layer with $\theta = 90^\circ$

$$\frac{\partial (\rho v_r)}{\partial r} + \frac{2\rho v_r}{r} + \frac{1}{r} \frac{\partial (\rho v_\theta)}{\partial \theta} = 0 . \quad (2.60)$$

Using the definition of v_θ from equation 2.45, as well as 2.57, and assuming a small opening angle of the wind streamlines, $\sin \lambda \approx \lambda \propto 1/r$, the third term in the above equation can be approximated as

$$\frac{1}{r} \frac{\partial (\rho v_\theta)}{\partial \theta} \approx \frac{\partial (\rho v_r)}{\partial r} - \frac{\rho v_r}{r} . \quad (2.61)$$

Using this in equation 2.60 gives

$$2 \frac{\partial (\rho v_r)}{\partial r} + \frac{(\rho v_r)}{r} = 0 \quad (2.62)$$

and consequently $(\rho v_r) \propto r^{-1/2}$. Since $v_r(r = r_f) \propto v_\infty \propto r^{-1/2}$ it follows that the wind mass density must be constant as a function of radius, $\rho \propto r^0$. Therefore, a steady state, azimuthally symmetric wind, characterized by a small opening angle, is well described by the density index $\eta = 0$.

Repeating the same exercise for a steady state, spherically symmetric wind, one obtains $\eta = 1.5$. In this case the continuity equation 2.59 reduces to:

$$\frac{\partial (r^2 \rho v_r)}{\partial r} = 0 \quad (2.63)$$

which yields $(\rho v_r) \propto r^{-2}$ and hence $\rho \propto r^{-1.5}$. In this work we choose $\eta = 1$ as a representative intermediate value.

2.3.2.4 *Optical depth of the wind*

The final ingredient in the calculation of the optical depth of the disk wind is the normalization factor, $\tau_0 = \kappa \rho_0 \sigma$, used in equation 2.40. In this form τ_0 is used to define the optical depth of the surface layer at the inner edge of the BLR, in the direction perpendicular to the disk plane, so that $\tau \approx 5\tau_0$ ($7\tau_0$) at $R_{\text{in},i} = 500 M_i$ ($1000 M_i$). It is worth emphasizing that τ_0 dimensionally represents optical depth scaled by the mass of the disk's central SBH, $\propto M_i^{-1}$. Combined with the velocity gradient of the wind along the LOS, Q , which exhibits

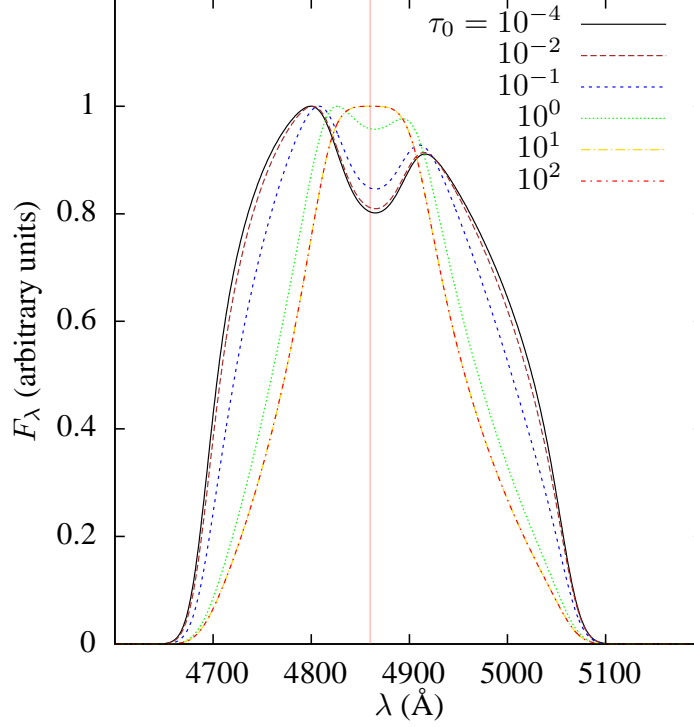


Figure 2.5: $H\beta$ broad emission-line profiles from a circular disk calculated for different values of the disk wind optical depth, τ_0 : 10^{-4} (black, solid), 10^{-2} (maroon, long-dash), 10^{-1} (blue, dashed), 1 (green, dotted), 10 (yellow, long-dash-dot) and 10^2 (red, dash-dot). Pink vertical line at 4860.09 \AA marks the rest wavelength of the $H\beta$ emission line. The parameters used in calculation of the profiles are: $\xi_{\text{in}} = 500 M$, $\xi_{\text{out}} = 10,000 M$, $i = 60^\circ$, $\sigma = 850 \text{ km s}^{-1}$, $\epsilon \propto r^{-3}$, $\gamma = 1.2$, $b = 0.7$, $\eta = 1$, and $\lambda(R_{\text{in}}) = 10^\circ$.

the same dependence, it results in the dimensionless parameter τ .

The BEL profiles in this work are calculated for a range of optical depths, given by $\tau_0 = 10^{-4}, 0.1, 1, 100$. Because the profiles calculated for $\tau_0 = 0$ and 10^{-4} are very similar, we use them interchangeably. Moreover, we verify that profile shapes do not change in shape once $\tau_0 > 100$ and do not explore the values of optical depth beyond this threshold. Such high line optical depths effectively imply a weak profile that would be difficult to discern in real spectra, due to the low contrast with respect to the continuum and the presence of noise.

Figure 2.5 illustrates the transition from the broader, double-peaked to the narrower, single-peaked BEL profiles with increasing optical depth. They are included for comparison with the previously published works, as well as an intermediate verification step for

those wishing to reproduce this calculation. The profiles are from a circular disk, illuminated by a single, central AGN and calculated for values of τ_0 and other parameters used in this work. As discussed in § 3.3.1 and § 3.3.2, a similar trend is also reflected in the composite profiles calculated from triple disk configurations of BLRs in circumbinary regions.

2.3.2.5 *Relativistic Sobolev method*

Relativistic Doppler effect is relevant in calculation of BEL profiles from the modeled BLR, i.e. a few hundred to thousand gravitational radii away from the central black hole, because the local Keplerian velocity of the gas in that region reaches a few percent the speed of light. Similar considerations are relevant for the choice classical and relativistic Sobolev method, used to calculate the disk wind optical depth, since the wind speed reaches a few times the Keplerian speed. In our model, however, the relativistic Sobolev method affects a relatively small portion of the profile database. This portion includes profiles of SBHBs with smaller BLR inner radius $R_{in} \leq 500$, small binary separations, $a \leq 10000M$, and high mini-disks inclination angles, $|i| \geq 40^\circ$. For this reason, we only employ the classical Sobolev method to calculate our profile database. We nevertheless illustrate how the application of the relativistic Sobolev method might affect some profile shapes. Figure 2.6 illustrates how a single disk wind emission profile may switch from a positive Peak Shift (the red curve's peak is on the right of the rest wavelength) and negative asymmetry (the red curve leans toward the red wing) to a negative Peak Shift and positive asymmetry (green curve) as we switch from the classical to relativistic Sobolev method. In this example, the difference between the two profiles is apparent because the outter radius of the disk is relatively small, $\xi_{out} = 2500 M$, but physical. Next, we will describe how relativistic Sobolev method might be derived for our disk wind model by generalizing the work of [147].

For a spherically symmetric wind with velocity $\beta = \beta e_r$. (speed of light $c = 1$), [147] express the line optical depth in relativistic Sobolev approximation as (see also [148] for more derivation steps),

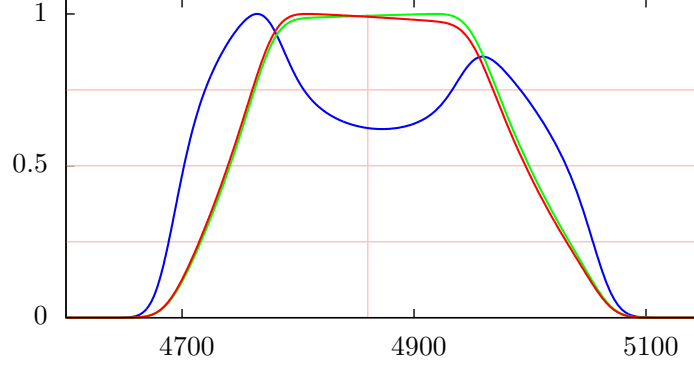


Figure 2.6: $H\beta$ broad emission lines calculated for single AGN without the accretion disk wind (blue curve), with the disk wind effect calculated using the classical Sobolev method (green), and with the disk wind effect calculated using the relativistic Sobolev method (red). The x -axis is wavelength in \AA , and the y -axis is normalized flux of the emission lines. Wind optical depth parameter, $\tau_0 = 100$. Other parameters include: $\gamma = 1.2$, $b = 0.7$, $\eta = 1$, $\lambda = 10^\circ$, $\kappa = 1/4.7$. The single AGN accretion disk parameters include: inner radius, $\xi_{\text{in}} = 500 M$; outer radius, $\xi_{\text{out}} = 2500 M$; inclination angle, $i = 60^\circ$; disk turbulent velocity, $\sigma = 850$ (km/s); and disk power law emissivity, $\epsilon \propto r^{-3}$.

$$\tau = \frac{\alpha^0}{\nu_l^0} \frac{(1 - \mu\beta)^2}{\gamma |\mu(\mu - \beta)\partial\beta/\partial r + (1 - \mu^2)(1 - \beta^2)\beta/r|} \quad (2.64)$$

where $\mu = \hat{\beta} \cdot \hat{s}$ is cosine of the angle between the wind velocity and the LOS, \hat{s} , as measured in the observer frame. $\gamma = (1 - \beta^2)^{-1/2}$. And α^0 , ν_l^0 are, respectively, the wind integrated line opacity and the emission line rest frequency as measured in the frame comoving with the wind. By following their derivation, we generalize the above expression for arbitrary velocity field β

$$\tau = \frac{\alpha^0}{\nu_l^0} \frac{(1 - \mu\beta)^2}{\gamma |(\beta(1 - \mu\beta)(\hat{s} \cdot \nabla\beta) - (1 - \beta^2)(\hat{s} \cdot \nabla\beta \cdot \hat{s})|} \quad (2.65)$$

In the classical limit, $\beta \rightarrow 0$, the above expression reduces to the classical optical depth,

$$\tau = \frac{\alpha^0}{\nu_l^0} \frac{1}{|\hat{s} \cdot \nabla\beta \cdot \hat{s}|} \quad (2.66)$$

For our model,

$$\hat{s} = \sin i \cos \varphi \hat{r} - \cos i \hat{\theta} - \sin i \sin \varphi \hat{\varphi} \quad (2.67)$$

$$\beta_r = v_r = \frac{1}{\kappa}(1-b)^\gamma \xi^{-1/2} \approx 1.11 \xi^{-1/2} \quad (2.68)$$

$$\beta_\theta = -v_r \sin \lambda(r = r_f) \approx -0.2 \xi^{-1/2} \quad (2.69)$$

$$\beta_\varphi = \xi^{-1/2} \quad (2.70)$$

Or, $\beta \approx 1.5 \xi^{-1/2}$ and it follows that

$$\hat{\mathbf{s}} \cdot \nabla \beta = -\frac{1}{2} \beta \xi^{-1} \quad (2.71)$$

$$\mu = \frac{1}{\beta} (\sin i \cos \varphi \beta_r - \cos i \beta_\theta - \sin i \sin \varphi \beta_\varphi) \quad (2.72)$$

CHAPTER 3

COMPARISON WITH OBSERVATIONS

Given a physically motivated parameter space occupied by sub-parsec SBHBs, we calculate a synthetic database of more than 42.5 million broad optical emission-line (BEL) profiles and explore the dependence of the profile shapes on characteristic properties of SBHBs. Analysis of the modeled profiles in the database shows that modeled profile shapes are more compatible with observed sample of SBHB candidates than with control sample of regular AGNs. In this chapter, we will describe the parameter choices used to generate the synthetic database in § 3.1, summarize properties of the database in §§ 3.2 and 3.3, and compare these properties with those of observed SBHB candidates in § 3.4.

3.1 Parameter Choices of the Model

Table 3.1 summarizes parameter choices for the modeled configurations of SBHB systems. The last five parameters in the table encapsulate the properties of the accretion disk wind while the other ones encode intrinsic properties of the binary, such as its orbital semi-major axis, eccentricity, alignment of the triple disks, or orientation of the orbital plane with respect to a distant observer’s LOS.

- *SBHB mass ratio, q* – Simulations of galaxy mergers that follow pairing of their massive black holes find that SBH pairs with mass ratios $q < 0.1$ are unlikely to form gravitationally bound binaries within a Hubble time at any redshift [16, 19]. They also find that SBH pairs with initially unequal masses can evolve to be more equal-mass, through preferential accretion onto a smaller SBH. Motivated by these results we choose six values of q in the range $0.1 - 1$ to represent the mass ratio of the binary.

Table 3.1. Parameters of the Model

Parameter	Value
q	1 , 9/11 , 2/3 , 3/7 , 1/3 , 1/10
a/M	5×10^3 , 10^4 , 5×10^4 , 10^5 , 10^6
e	0.0 , 0.5
f	0° , 72° , 144° , 216° , 288°
$R_{\text{in}1}/M_1$, $R_{\text{in}2}/M_2$	500 , 1000
$R_{\text{out}3}$	$3a$
i	5° , 55° , 105° , 155°
ϕ	0° , 36° , 108° , 180° , 242° , 324°
θ_1, θ_2	0° , 30° , 60° , 105° , 135° , 165°
ϕ_1, ϕ_2	0° , 25° , 60° , 185° , 210° , 235°
h_1/M_1 , h_2/M_2	10
$\sigma/\text{km s}^{-1}$	850
τ_0	$0 (10^{-4})$, 0.1 , 1 , 10^2
$\lambda(R_{\text{in}})$	10°
η	1.0
γ	1.2
b	0.7

Note. — q – SBHB mass ratio. a – Orbital semi-major axis. e – Orbital eccentricity. f – Orbital phase. $R_{\text{in},i}$, $R_{\text{out},i}$ – Inner and outer radius of the primary, secondary, or circumbinary disk. i – Inclination of the observer relative to the SBHB orbital angular momentum. ϕ – Azimuthal orientation of the observer relative to the SBHB major axis. θ_i , ϕ_i – Inclination and azimuthal orientation of the primary and secondary mini-disk relative to the SBHB orbital angular momentum. h_i – Spatial extent of the compact central source of the continuum radiation associated with each SBH. σ – Turbulent velocity of the gas. τ_0 – Normalization of the disk wind optical depth. λ – Opening angle of the disk. η – Power law index in the description of gas density. γ , b – Parameters describing the wind velocity.

- *Semi-major axis, a* – To describe orbital separations of gravitationally bound binaries we chose five values of a ranging from $5000 M$ to $10^6 M$, where we use the mass of the binary $M \equiv GM/c^2 = 1.48 \times 10^{13} \text{ cm } (M/10^8 M_\odot)$ as a measure of length in geometric units, where $G = c = 1$. For example, for the total mass of the binary of $10^8 M_\odot$ this range of semi-major axes corresponds to binary separations $\sim 0.02 - 5 \text{ pc}$.
- *Orbital eccentricity, e* – Theoretical models that follow evolution of the orbital eccentricity of SBHBs in circumbinary disks suggest that the exchange of angular momentum between them drives a steady increase in binary eccentricity which saturates in the range $0.6 - 0.8$ [27, 31, 46]. For the purposes of this calculation we choose two values of eccentricity, $e = 0.0$ and 0.5 , to model SBHBs on both circular and elliptical orbits.
- *Orbital phase, f* – Five values of the orbital phase are chosen to describe orbital evolution of SBHBs. f is measured from the positive x -axis to the instantaneous location of the secondary SBH in counter-clockwise direction, as illustrated in Figure 2.2.
- *SBHB accretion rate ratio, \dot{m}* – In the context of this model we assume that the emissivity of each BEL region is a function of the AGN luminosity and the disk size. In order to establish the relative bolometric luminosities of the two AGN we compile from the literature the values of $\dot{m} = \dot{M}_2/\dot{M}_1$ and parametrize it as a linear function of q for SBHBs on circular and eccentric orbits.

$$\dot{m} \simeq \begin{cases} 5.5 - 4.5q & e = 0.0 \\ 1.5 - 0.5q & e = 0.5 \end{cases} \quad (3.1)$$

Here \dot{M}_1 and \dot{M}_2 are the accretion rates onto the primary and secondary SBH, respectively. The two relations capture two key results observed in hydrodynamic simula-

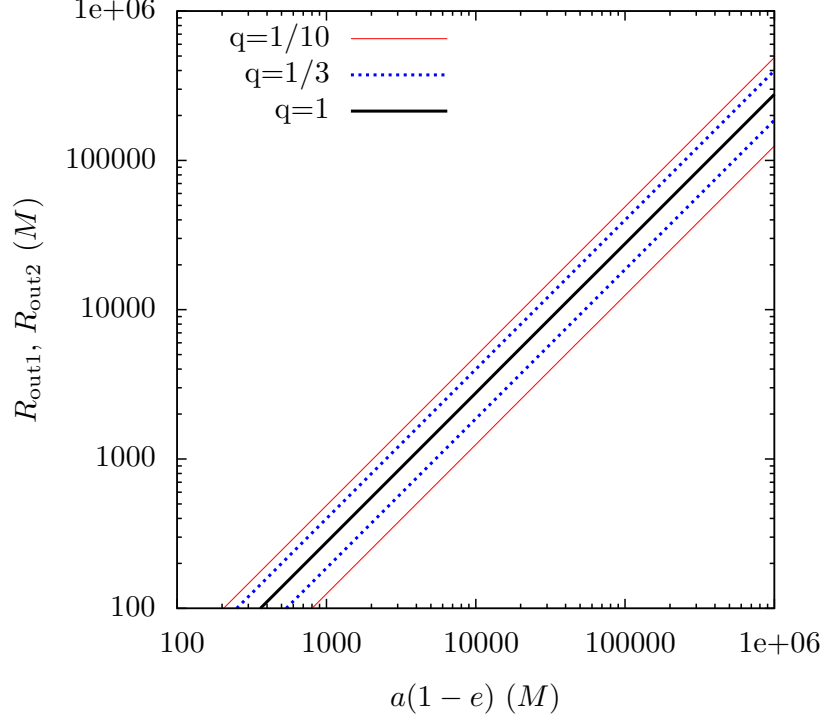


Figure 3.1: Outer radii of the primary and secondary mini-disks as a function of a and e . Lines mark SBHB mass ratios $q = 1/10$ (thin, red lines), $1/3$ (dotted, blue) and 1 (solid, black) based on the model of Paczynski [116]. For unequal mass ratios the top line marks the size of the larger (primary) mini-disk.

tions of prograde SBHBs (rotating in the same sense as the circumbinary disk; [46, 88]): (1) in unequal mass binaries accretion occurs preferentially onto the smaller of the SBHs and (2) the inversion of accretion rates is more severe for SBHBs on circular orbits. This trend has also been captured by other simulations [40, 86] and models motivated by them [149, 150].

- *Size of the broad line regions, $R_{\text{in}i}$ and $R_{\text{out}i}$* – Each disk in the triple disk system has an associated BLR defined by a pair of inner and outer radii. In the case of the mini-disks we choose two different values for the BLR inner radius $R_{\text{in}i} = 500M_i$ and $1000M_i$, where $i = 1, 2$ mark the BLR around the primary and secondary SBH, respectively. These choices are motivated by characteristic values for the inner radius of the BLRs in AGNs powered by single SBHs, which emission lines are well modeled by the emission from a Keplerian disk (for e.g., [123, 124]). The outer radii are

naturally determined by the tidal torques of the binary and do not extend beyond the Roche lobes of their SBHs. We follow the approach described by Paczynski [116] to estimate the average values of $R_{\text{out}1}$ and $R_{\text{out}2}$ based on the binary separation a , and mass ratio q (see Figure 3.1).

We define the size of the circumbinary disk BLR in terms of the SBHB semi-major axis, $R_{\text{in}3} = 2a$ and $R_{\text{out}3} = 3a$. The value of the inner radius is directly motivated by theory and simulations which show that SBHB torques create a low density hole with radius about $2a$ in the center of the circumbinary disk [27, 28, 42]. The value of the outer radius of the circumbinary disk BLR is poorly constrained and for the purposes of this calculation we adopt $R_{\text{out}3} = 3a$. Note that the BLR sizes assumed in this work are consistent with the plausible range empirically derived for low redshift AGN by Kaspi et al. [151].

- *Emissivity of the broad line regions, ϵ_i* – Each disk in the system is further characterized by the emissivity of the BLR, which arises due to the illumination by the two AGNs. For example, the emissivity of the mini-disk around the primary SBH can be expressed as $\epsilon_1 = \epsilon_{11} + \epsilon_{12}$, where ϵ_{11} and ϵ_{12} correspond to the components of emissivity due to the illumination by its own AGN and the AGN associated with the secondary SBH, respectively. The emissivity of each mini disk associated with its own AGN is described as a power law in radius, with the power law index $p = 3$, such that $\epsilon_{11} \propto \epsilon_{22} \propto R^{-p}$ [118]. The component of emissivity associated with the companion AGN (ϵ_{12} and ϵ_{21}) is calculated as a function of its distance and orientation of the mini-disk (details of the calculation can be found in § 2.2.2). The emissivity of the circumbinary disk, ϵ_3 , is calculated as a sum of emissivities due to the two off-center AGN associated with the primary and secondary SBHs.
- *Orientation of the observer relative to the binary orbit, i and ϕ* – We choose four values of the inclination angle, i , to describe the orientation of the observer's LOS

relative to the vector of orbital angular momentum of the SBHB. For example, $i = 0^\circ$ represents the clockwise binary seen face-on and values $i > 90^\circ$ represent counter-clockwise binaries. Furthermore, we select six values of the azimuthal angle ϕ measured in the binary orbital plane, from the positive x -axis to the projection of the observer's LOS, in counter-clockwise direction. For circular SBHBs varying the true anomaly f is equivalent to varying the azimuthal orientation of the observer and in this case we adopt a single nominal value of $\phi = 0^\circ$ in calculation of the BEL profiles. However, in the case of eccentric SBHBs we explore a full range of f and ϕ angles.

- *Orientation of the mini disks, θ_i and ϕ_i* – We relax assumptions about the orientation of the mini disks with respect to the binary orbit in order to study how profile shapes depend on it. We choose six values of the polar angle (θ_i) and azimuthal angle (ϕ_i) to describe the orientation of each mini disk with respect to the vector of orbital angular momentum of the binary. For example, when $\theta_1 = \theta_2 = 0^\circ$, both mini-disks are coplanar with the SBHB orbit and for $\theta_i > 90^\circ$, the gas in the mini-disks exhibits retrograde motion relative to the circumbinary disk. The azimuthal angles ϕ_i are measured in the binary orbital plane, from the positive x -axis to the projection of the rotation axis of the mini-disk, in counter-clockwise direction. The circumbinary disk is assumed to always be coplanar and in co-rotation with the binary orbit.
- *Optical depth of the disk wind, τ_0* – In this work, the BEL profiles are calculated for a range of optical depths, $\tau_0 = [10^{-4}, 10^2]$, as shown in Table 3.1. Because the profiles calculated with $\tau_0 = 0$ and 10^{-4} are very similar, we use them interchangeably. We have also verified that profile shapes remain unchanged for $\tau_0 > 100$ and we do not explore the values of optical depth beyond this threshold. We further choose one value, $\eta = 1$, to represent the radial dependance of the wind density, after verifying that the impact of this parameter on the profile shapes is relatively weak.

Note that some of the model parameters described in the above section are actually not free parameters, because they are constrained by the relevant physical processes and can be expressed in terms of the properties of the binary (this is the case with \dot{m} , $R_{\text{out}1}$, $R_{\text{out}2}$ and $R_{\text{in}3}$). The calculation of the BEL profiles requires definition of two additional parameters which have a lesser impact on their shape. Specifically, motivated by the X-ray studies of the broad iron line reverberation (see review by [126]), we assume that the central source of the continuum radiation associated with each SBH is compact and has spatial extent of $h_i = 10M_i$. Similarly, we describe the broadening of the BEL profiles due to the random (turbulent) motion of the gas in each disk as $\sigma = 850 \text{ km s}^{-1}$. We assume that the disk wind driven by each AGN extends over the entire surface of its BLR. It is not clear however whether these outflows can extend from the mini-disks into the circumbinary disk, especially in configurations in which the disks are not co-planar. In order to examine this effect we calculate profiles for three different disk wind configurations, described below.

- NW – This is the “no wind” configuration presented in § 3.2, which corresponds to a disk wind model with $\tau_0 = 0$. In this limit, the probability of escape for the line photons, defined in equation 2.38, defaults to $\beta_e = 1$. The NW database contains nearly 15 million modeled profiles – 2,545,200 realizations of SBHBs on circular orbits and 12,273,000 on eccentric orbits.
- 2DW – A disk wind develops only along the two SBH mini-disks and not in the circumbinary disk. In this setup, we calculate profiles from SBHB systems on circular orbits and with three different values of optical depth, $\tau_0 = 0.1, 1, 100$. The 2DW database contains about 7.5 million profiles – 2,545,200 realizations for every value of the optical depth.
- 3DW – A disk wind is present in all three disks. The circumbinary disk has an accretion disk wind which is radial and axisymmetric, as if driven by a single, central AGN. Here, we calculate profiles from circular SBHBs with $\tau_0 = 0.1, 1, 100$, and

from eccentric SBHBs with $\tau_0 = 1$. The 3DW database contains about 20 million profiles – 2,545,200 realizations of circular SBHBs for every value of optical depth and 12,273,000 realizations of eccentric SBHBs.

Combined together, the entire database contains about 42.5 million profiles that correspond to the same number of SBHB configurations. Note that the nominal number of simulations per disk wind configuration is determined as a product of the number of parameter choices. From these simulations we eliminate the ones in which the orientation of any disk with respect to the observer is close to edge on (between 80° and 100°). We do this to prevent the breakdown of the weak-field approximation, used in calculation of the photon Doppler shifts. This selection criterion eliminates scenarios in which the impact parameter of the line-of-sight photons flying over a SMBH becomes too small (i.e., $\lesssim 100 M_i$). Such photons experience significant gravitational redshift and gravitational bending of their trajectory. Because this happens in a small fraction of all SBHB configurations that we consider, we do not perform calculations of these effects in the strong field regime.

We describe different models by labels that encapsulate the description of the SBHB orbit, the disk wind model, and the optical depth normalization value. For example C-2DW-100 represents a set of profiles for SBHBs on circular orbits and a disk wind characterized by $\tau_0 = 100$ in both SBH mini-disks but not in the circumbinary disk. In contrast, E-3DW-1 refers to a database of profiles calculated for SBHBs on eccentric orbits, where $\tau_0 = 1$ in all three disks.

3.2 Broad Emission-line Profiles in Absence of the Disk Wind Effect

The disk wind effect is negligible when its optical depth is equal to or below $\tau_o \lesssim 10^{-4}$. In this limit, sharp peaks of the model profiles are usually preserved and the composite profiles often have multiple peaks as illustrated in Figure 3.2. In this section, we draw attention to unique features of the modeled population of profiles (§ 3.2.1) and characterize

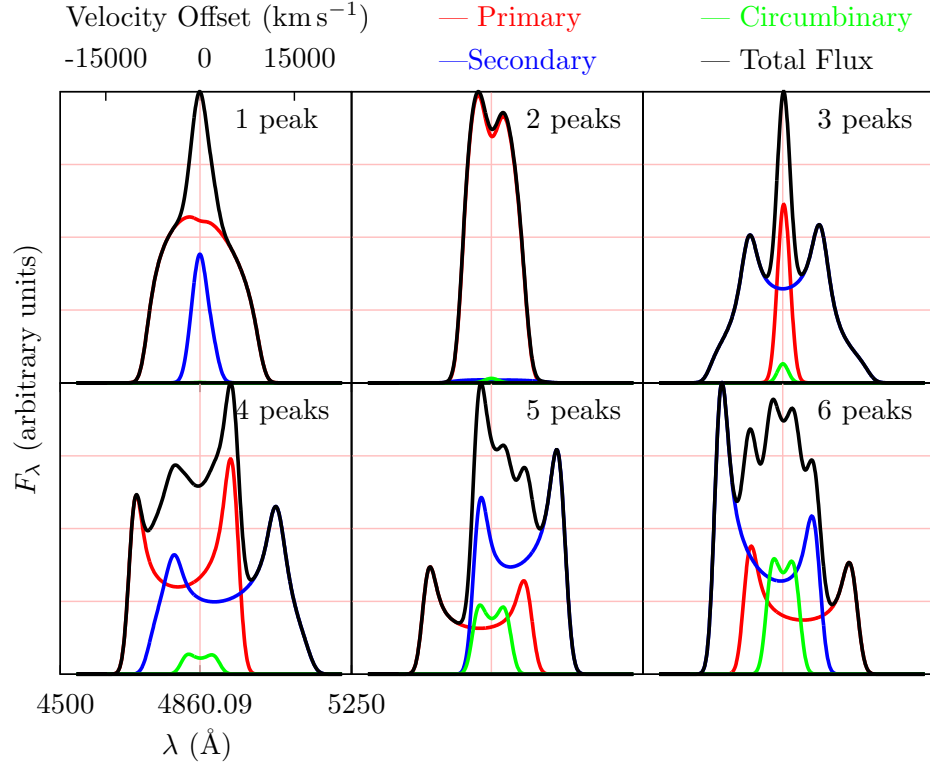


Figure 3.2: Illustration of profile shapes represented in the emission-line database when absorption through accretion disk wind is negligible. Total flux (black line) is a sum of components contributed by the primary (red), secondary (blue) and circumbinary disk (green). Flux is shown in arbitrary units against wavelength (bottom x -axis) and corresponding velocity offset relative to the binary center of mass (top x -axis). Pink vertical line at 4860.09 Å marks the rest wavelength of the $H\beta$ emission line.

their shapes in terms of commonly used statistical distribution functions (§ 3.2.2). We then investigate whether the complex, composite profile shapes preserve any dependence on the parameters of the underlying SBHB model (§ 3.2.3).

3.2.1 Characteristic features of the modeled emission-line profiles

The most striking property of the modeled BEL profiles is that they can have multiple peaks and their appearance can vary significantly over time, due to the orbital motion of the binary and the resulting variable illumination of the three disks by the two AGNs. Each disk in the triple disk system can give rise to either a single-peaked or a double-peaked profile, depending on the size of its emission region and its orientation with respect to the

Table 3.2. Number of peaks.

	a (M)	1 (%)	2 (%)	3 (%)	4 (%)	5 (%)	6 (%)
Circular	5×10^3	15.01	40.15	35.84	8.94	0.06	0.00
	10^4	28.16	54.34	17.05	0.45	0.00	0.00
	5×10^4	77.25	22.74	0.01	0.00	0.00	0.00
	10^5	87.07	12.93	0.00	0.00	0.00	0.00
	10^6	100.00	0.00	0.00	0.00	0.00	0.00
Eccentric	5×10^3	5.85	14.21	50.05	22.82	6.51	0.57
	10^4	9.03	42.36	44.05	4.39	0.17	0.00
	5×10^4	37.84	61.75	0.41	0.00	0.00	0.00
	10^5	63.97	35.98	0.05	0.00	0.00	0.00
	10^6	100.00	0.00	0.00	0.00	0.00	0.00

observer’s LOS. Generally, the larger the BLR, the more likely is the disk to produce a single-peaked profile. This is because the bulk of the emission is contributed by the outer regions on the disk characterized by lower rotational velocities. Similarly, the lower the inclination of the disk with respect to the observer, the more likely it is that the observed profile is single-peaked since the gas velocity along the LOS is low. Since in our model we account for a range of BLR sizes and inclinations, the composite BEL profiles can display anywhere from 1 to 6 peaks.

Figure 3.2 illustrates the diversity of shapes encountered in the profile database, calculated for different binary configurations. Each profile includes contribution from the primary and secondary mini-disks and the circumbinary disk. Individual profiles are broadened by rotational motion and random motion of the gas in the disk. Because the gas in the mini-disks has higher rotational velocity and is closer to the sources of continuum radiation, the BEL profiles contributed by the mini-disks often appear broader and stronger relative to the emission from the circumbinary disk.

In Table 3.2 we show the percentage of profiles characterized by a given number of peaks as a function of the orbital separation and eccentricity of the SBHB. One readily

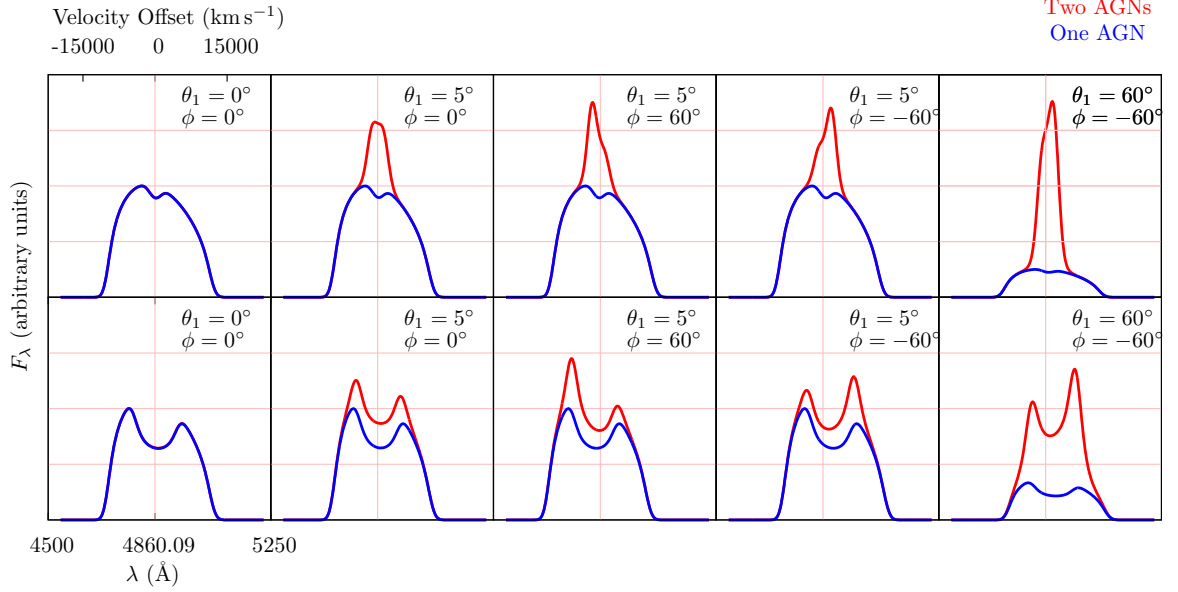


Figure 3.3: Profiles emitted by a single (primary) mini-disk illuminated by its central AGN only (blue line) and by the companion AGN (red). Contribution to the total line flux from illumination by the secondary AGN is negligible only when the mini-disk and the binary orbit are close to coplanar ($\theta_1 = 0^\circ$). Excess flux appears in the blue (red) wing of the emission line for the hotspot that moves toward (away from) the observer, as indicated by the azimuthal angle ϕ . Flux scaling is the same in all panels except for the last one, where profile flux was divided by a factor of 4 for visualization purposes. The sequence of profiles at the top and bottom are calculated for two arbitrary SBHB orbital configurations with $a = 50000 M$ and $5000 M$, respectively. Parameters shared by both systems are $q = 1$, $e = 0$, $i = 55^\circ$, $\phi_1 = 0^\circ$, $R_{\text{in}1} = 500 M_1$.

identifiable trend is that majority of profiles tend to have 1–3 peaks. The profiles with 5 and 6 peaks are relatively rare and entirely absent from SBHB systems with large orbital separations. This can be understood because SBHBs on tight orbits are characterized by compact mini-disks with high orbital velocities about the binary center of mass, both of which give rise to broad and multi-peaked lines in the wavelength space. Another trend is that SBHBs on eccentric orbits tend to have profiles with a higher number of peaks relative to the circular binaries with the same semi-major axis. This is because eccentric SBHBs sample a wider range of orbital velocities, allowing for a larger wavelength offset of individual components in the composite profile.

As mentioned in § 2.2, we assume that both accreting SBHs can shine as AGNs and illuminate all three disks in the system. In this setup, both mini-disks are illuminated

by their central AGN as well as the off-center companion AGN. The illumination of the circumbinary disk by the two AGNs is always off-center. In Figure 3.3 we show the effect of illumination of the primary mini-disk by the two AGNs (similar effect is present for the secondary mini-disk). The sequence of profiles at the top and bottom are created for two different SBHB configurations, arbitrarily chosen for illustration.

The illumination by the secondary AGN resembles an off-center hotspot on the accretion disk surface. Figure 3.3 shows that contribution to the total flux from such a hotspot sensitively depends on the alignment of the primary mini-disk with the binary orbit. Namely, when the two are coplanar ($\theta_1 = 0^\circ$), illumination due to the secondary AGN is negligible because of the small incidence angle of its photons on the mini-disk (first panel of Figure 3.3). When the mini-disk and the binary orbit are misaligned even by a small amount, the illumination by the secondary AGN can make a significant contribution to the line flux (second panel of Figure 3.3). In the case of close binaries with highly misaligned mini-disks we find that this effect can increase the line flux up to several times (last panel). Depending on whether the hotspot moves away or toward the observer (as indicated by the azimuthal angle ϕ) this extra flux may appear in the blue or the red wing of the emission line giving rise to an asymmetric profile (third and fourth panels). Therefore, the effect of illumination by a dual AGN can in principle be an indicator of the orbital alignment of the triple disk system, if it can be identified in the observed BEL profiles of candidate SBHB systems.

One more characteristic feature of the BEL profiles contributed by the triple disk system in our model is that the shape of a profile can change significantly over one orbital period of the binary. The centroids of the BEL profiles contributed by the mini-disks oscillate about the rest wavelength due to the orbital motion of the SBHs in the way similar to the spectroscopic stellar binaries. The emission from the circumbinary disk, which is anchored to the binary center of mass, is on the other hand centered on the rest wavelength of the system. As a result, a combination of the SBHB orbital motion and rotation of gas within

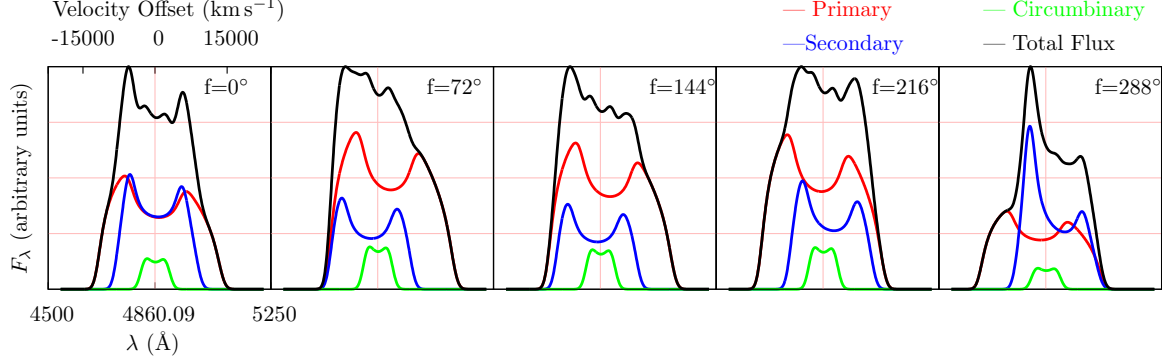


Figure 3.4: Sequence of profiles showing temporal evolution of a composite BEL profile associated with an SBHB system described by $q = 1$, $a = 5000 M$, $e = 0$, $R_{in1} = 500 M_1$, $R_{in2} = 1000 M_2$, $i = 75^\circ$, $\phi = 0^\circ$, $\theta_1 = 0^\circ$, $\theta_2 = 15^\circ$, $\phi_1 = 0^\circ$, $\phi_2 = 300^\circ$. Total flux shown in arbitrary units (black line) is a sum of components contributed by the primary (red), secondary (blue) and circumbinary disk (green). SBHB orbital phase f is marked in each panel.

each disk can produce complex and distinct features in SBHB systems relative to emission lines from stellar binaries.

Figure 3.4 shows time evolution of a profile associated with an SBHB system in which profiles from both mini-disks are double peaked and asymmetric due to relativistic Doppler boosting (i.e., exhibit a higher blue shoulder). The same effect is also noticeable in the composite profile for all orbital phases except $f = 216^\circ$, when the blue and the red shoulder of the profile become comparable. At $f = 216^\circ$ the red wings of the two mini-disk profiles line up in wavelength giving rise to a relatively strong red peak in the composite profile.

3.2.2 Statistical properties of emission-line profiles

The unique features of modeled BEL profiles associated with SBHB systems point to an intriguing possibility that, if it is possible to identify them in the observed SBHB candidates, these markers can be used to learn about the properties of the SBHBs. We analyze the trends in the modeled population of profiles by characterizing their shapes in terms of several commonly used distribution functions. These include the location of the centroid (C), asymmetry index (AI), kurtosis index (KI), full width at half and quarter maximum (FWHM and FWQM), peak shift (PS), and centroid shift (CS). We use the following defi-

nitions,

$$F = \sum_i F_{\lambda,i} \quad (3.2)$$

$$C = \frac{1}{F} \sum_i \lambda_i F_{\lambda,i} \quad (3.3)$$

$$\sigma^2 = \frac{1}{F} \sum_i (\lambda_i - C)^2 F_{\lambda,i} \quad (3.4)$$

$$\text{AI} = \frac{1}{F\sigma^3} \sum_i (\lambda_i - C)^3 F_{\lambda,i} \quad (3.5)$$

$$\text{AIP} = (C - \lambda_m)/\sigma \quad (3.6)$$

$$\text{KI} = \frac{1}{F\sigma^4} \sum_i (\lambda_i - C)^4 F_{\lambda,i} \quad (3.7)$$

$$\text{FWHM} = [\lambda_r(1/2) - \lambda_b(1/2)] \frac{c}{\lambda_0} \quad (3.8)$$

$$\text{FWQM} = [\lambda_r(1/4) - \lambda_b(1/4)] \frac{c}{\lambda_0} \quad (3.9)$$

$$\text{PS} = (\lambda_p - \lambda_0) \frac{c}{\lambda_0} \quad (3.10)$$

$$\text{CS} = (C - \lambda_0) \frac{c}{\lambda_0} \quad (3.11)$$

where $F_{\lambda,i}$ is the profile flux density at wavelength λ_i . The profile flux is normalized by the maximum flux measured at the peak wavelength, λ_p , so that $F_\lambda(\lambda_p) \equiv \max(F_{\lambda,i}) = 1$. $\lambda_b(x)$ and $\lambda_r(x)$ indicate the wavelength in the blue wing or the red wing of the profile, respectively, where the normalized flux drops to some level, x . λ_0 is the rest wavelength of the emission line and λ_m is the median wavelength that divides profile into a half, so that 50% of the flux lies to the left and to the right of it. The location of the profile centroid, C , is calculated as the flux weighted mean wavelength.

We use two measures to characterize the asymmetry of the profiles: the asymmetry index (AI) and the Pearson skewness coefficient (AIP). The positive values of AI and AIP indicate profiles skewed toward short wavelengths (i.e., blue-leaning profiles) and the negative values indicate red-leaning profiles. However, AI and AIP calculated for the same

profile sometimes have opposite signs, as they provide different measures of the profile asymmetry. Specifically, AI sensitively depends on the low intensity features in the profile wings, while AIP diagnoses the asymmetry in the bulk of the profile.

We use the kurtosis index (KI), calculated as the fourth moment of the flux distribution, to evaluate the “boxiness” of the profiles. By definition, the values of KI are always positive. Smaller values correspond to boxier profiles and larger values indicate cuspy profiles, with the top narrower than bottom. In addition, the relevant line widths, peak and centroid shifts are measured in units of velocity, as defined in equations 3.8 – 3.11.

In calculation of all these statistical properties we adopt a cutoff at $F_c = 0.01$ to mimic some fiducial level of spectral noise (but do not introduce actual fluctuations due to noise to the profiles). With “noise” subtracted from the profile, we rescale the flux above the cutoff so that the maximum flux measured at the peak wavelength has the value of 1.0. We investigate the dependance of the distribution functions characterizing the modeled profile shapes on the value of F_c in more detail in the Appendix C.

We use statistical properties defined in equations 3.5 – 3.11 to construct a multi-dimensional parameter space of the BEL profiles and investigate their distribution as a function of the underlying SBHB parameters. In the remainder of the chapter we visualize the multivariate distribution of profiles with 2-dimensional maps, which represent different projections through this parameter space. For example, in Figures 3.5 and 3.6 we plot maps of AIP and PS values for profiles calculated for circular and eccentric binary configurations, respectively. The color marks the number density of profiles and indicates which portions of the parameter space are favored by the modeled profiles.

The top left map in Figures 3.5 and 3.6 illustrates that AIP-PS distributions appear similar in the overall shape, with the eccentric sample having a wider range of the peak velocity shifts. This difference can be attributed to a wider range of orbital velocities sampled by eccentric binaries with the same semi-major axes. This topological similarity in the distribution of profiles from circular and eccentric SBHBs is present throughout the parameter

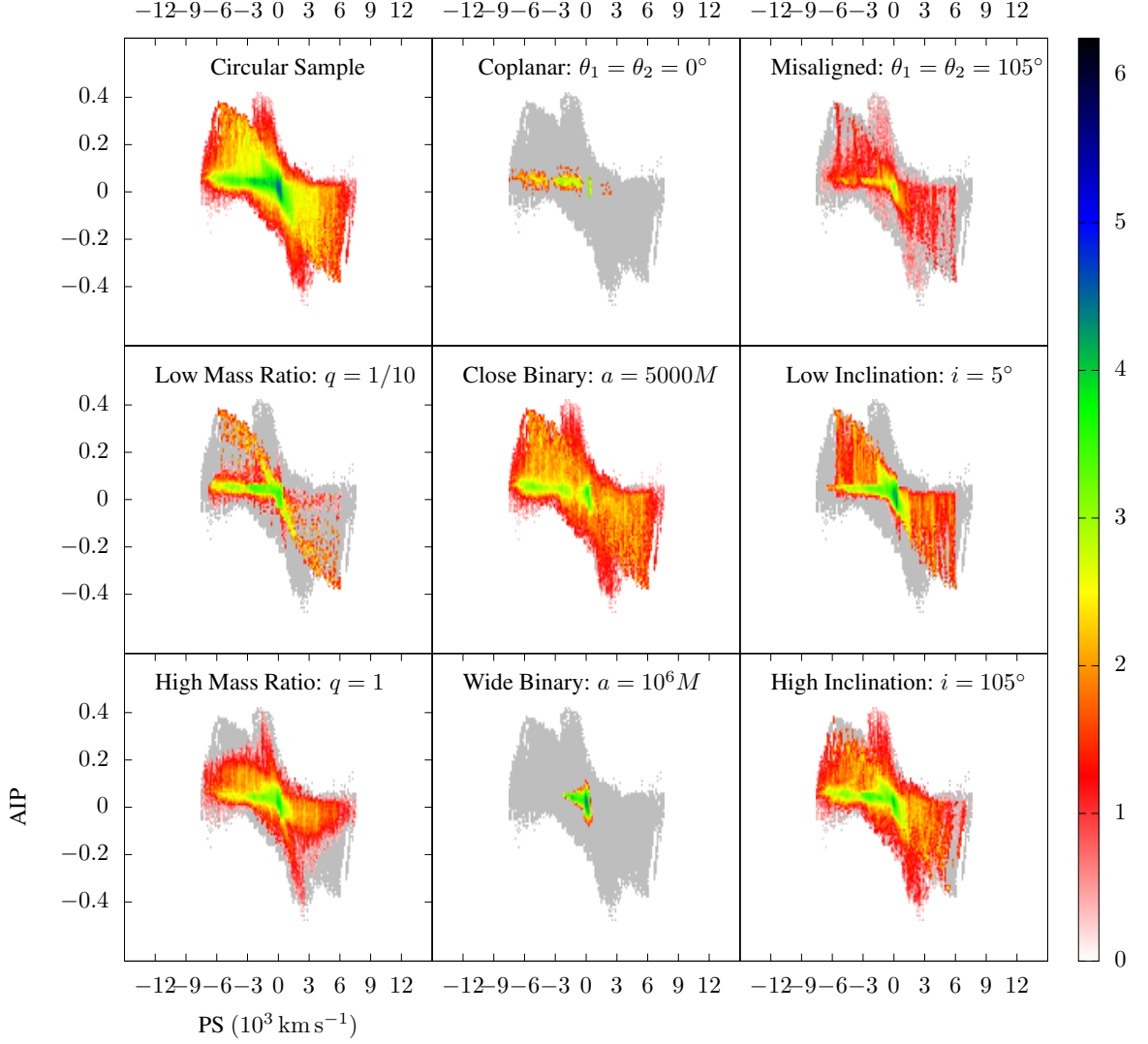


Figure 3.5: AIP-PS map for profiles associated with circular SBHB systems (top left). Remaining panels display the distribution of profiles as a function of the alignment of the triple disk system ($\theta_1 = \theta_2 = 0^\circ$ and 105°), SBHB mass ratio ($q = 1/10$ and 1), orbital separation ($a = 5000 M$ and $10^6 M$), and inclination of the observer relative to the binary orbit ($i = 5^\circ$ and 105°). Color bar indicates the density of profiles (i.e., the number of profiles in each area element) plotted on log scale. Grey color outlines the footprint of the entire distribution shown in top left.

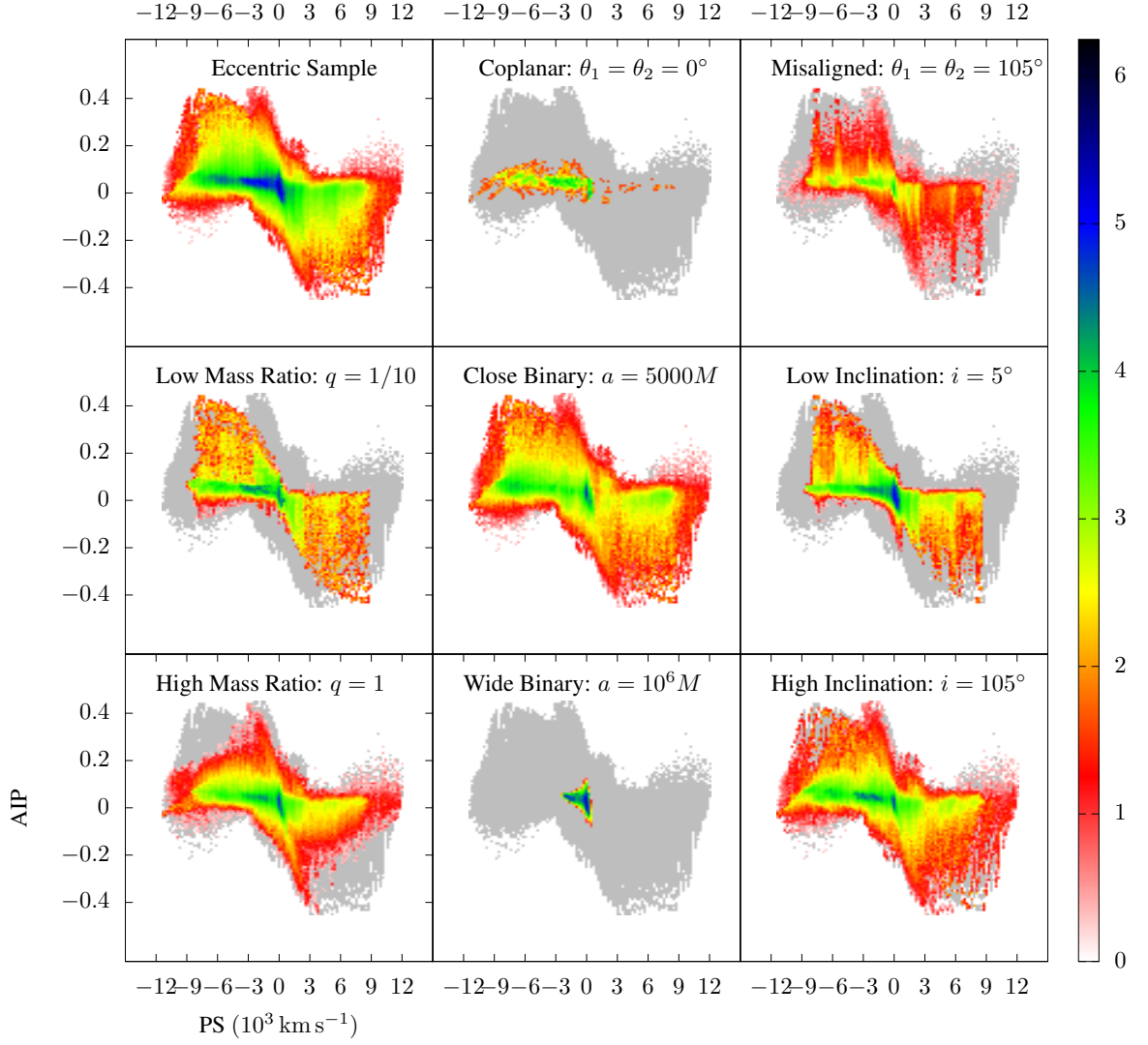


Figure 3.6: AIP-PS maps for profiles associated with eccentric SBHB systems. Map legend is the same as in Figure 3.5.

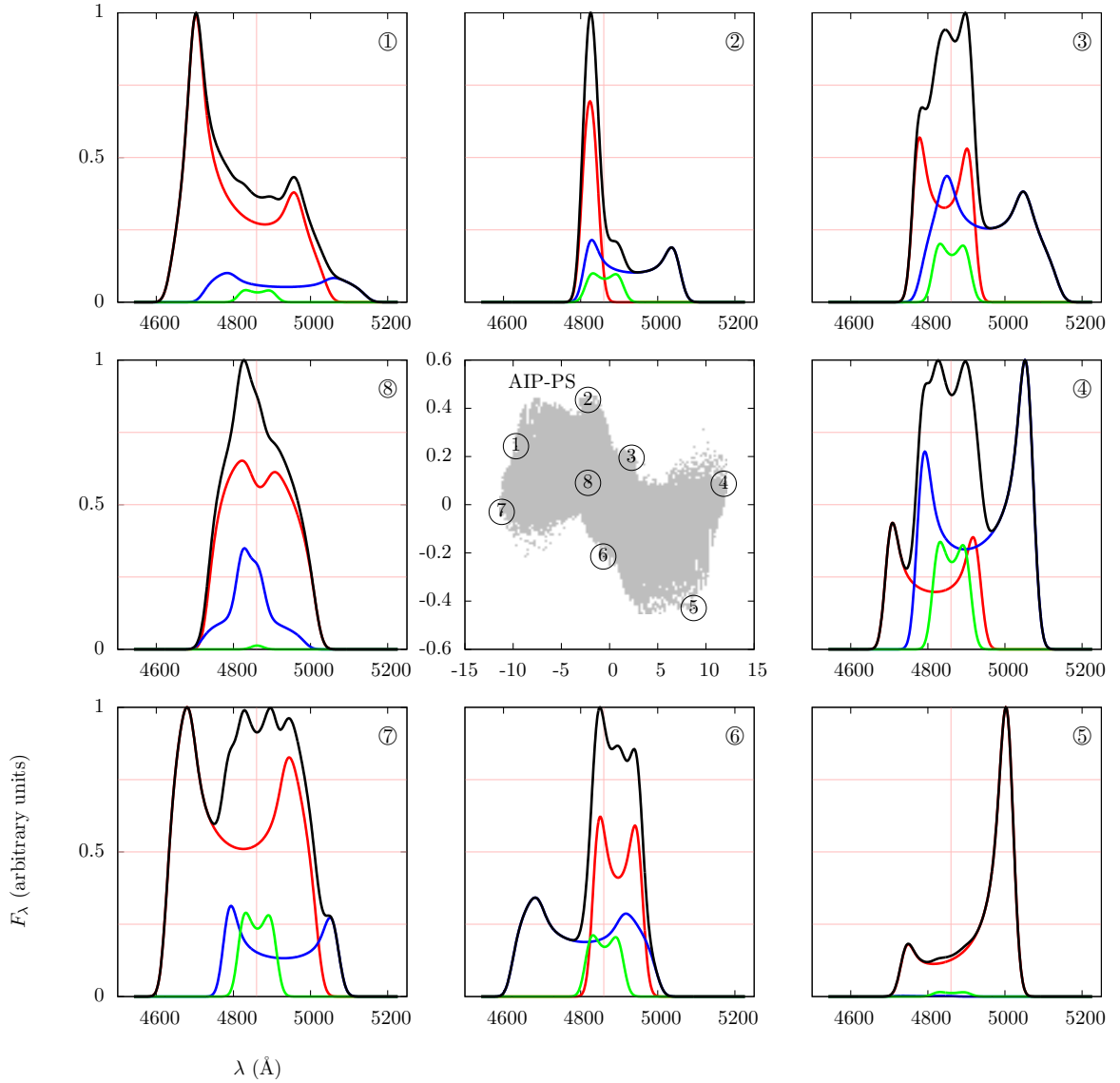


Figure 3.7: Characteristic profile shapes occupying different regions in the AIP-PS parameter space. Central panel shows footprint of the AIP-PS distribution from the top left panel of Figure 3.6 with identical scale and labeling of axes. Pink vertical line in the outer panels marks the rest wavelength of the $H\beta$ emission line.

space. Given the overlap, we plot only the distribution maps for the eccentric SBHBs in the rest of the chapter and discuss any differences between the circular and eccentric samples in the text.

Inspection of the top left panels in Figures 3.5 and 3.6 reveals that a significant fraction of profiles are fairly symmetric ($AIP \approx 0$) and likely to exhibit the maximum peak at wavelengths shorter than the rest wavelength ($PS < 0 \text{ km s}^{-1}$). The latter is a consequence of the relativistic Doppler boosting, which for each individual disk preferentially boosts the blue shoulder of its BEL profile, creating an effect which is also noticeable in the composite profile. Another feature worth noting is that in both the circular and eccentric samples, the profiles that exhibit the strongest peak at shorter wavelengths are also preferentially blue-leaning and vice versa. In the next section, we inspect the remainder of the profile parameter space for similar trends and consider their relationship with the physical properties of the SBHB.

In Figure 3.7 we show examples of line profiles from different parts of the parameter space of Figure 3.6, marked in the footprint of the map in the central panel. The shapes include profiles that exhibit symmetry (7 and 8), strong asymmetry (2 and 5), and large velocity offsets of the strongest peak (4 and 7). As discussed in § 3.2.1, the offset of the dominant peak towards longer wavelengths (evident in profiles 4 and 5) can occur in our model only under a specific circumstance: as a consequence of the illumination of a mini-disk by the companion AGN, when the hotspot is moving away from the observer. Inspection of profile 4 shows that the mini-disk with a strong hotspot is that around the secondary SBH (traced by the blue line) and around the primary SBH in profile 5 (traced by the red line). Moreover, profile 1 exemplifies the scenario where secondary illumination by the companion AGN dramatically boosts the blue wing of the profile from the primary mini-disk in configuration where the hotspot is moving towards the observer.

3.2.3 Dependence of profiles on the physical parameters of the binary

In this section, we investigate how the properties of modeled profiles vary as a function of the SBHB parameters, such as the alignment of the triple disk system, binary mass ratio, orbital separation, and inclination of the binary relative to the observer. We illustrate this dependence in the remainder of the panels in Figures 3.5 and 3.6 where we show subsets of profiles associated with the specific value of SBHB parameter. These show that profiles from SBHBs with wide orbital separations ($a = 10^6 M$) tend to be very symmetric and concentrate in the center of the AIP-PS parameter space, while close binaries ($a = 5000 M$) have a much wider footprint. By implication, this means that only profile 8 shown in Figure 3.7 can be produced by systems with large orbital separations.

Similarly, any SBHB configurations where the mini-disks are co-planar with the binary orbit (and circumbinary disk, by assumption) are characterized by symmetric profiles with $AIP \approx 0$ with dominant peak shifted towards the blue part of the spectrum. The misaligned systems on the other hand are equally likely to be blue-leaning as well as red-leaning and reside in the range $-0.4 \lesssim AIP \lesssim 0.4$. Therefore, profiles 1, 2, 3, 4, 5 and 6 cannot correspond to SBHBs with coplanar disks. As discussed in the previous paragraph, profiles 1, 4 and 5 also show strong contribution due to illumination by the companion AGNs, which is indeed expected to be most pronounced for configurations with misaligned disks. More generally, we find that the effect of illumination by the companion AGN is the main reason for difference between the AIP-PS distribution of profiles from coplanar and misaligned SBHB systems shown in Figure 3.6.

On the other hand profiles associated with SBHB systems with different mass ratios ($q = 1/10$ and 1) and different orientations of the binary orbit relative to the observer's LOS ($\theta = 5^\circ$ and 105°) show significant overlap in their distributions. Together, these plots indicate that the most important SBHB parameters that determine the degree of asymmetry and the position of the dominant peak in the BEL profile are the intrinsic alignment of the triple disk system and the orbital semi-major axis.

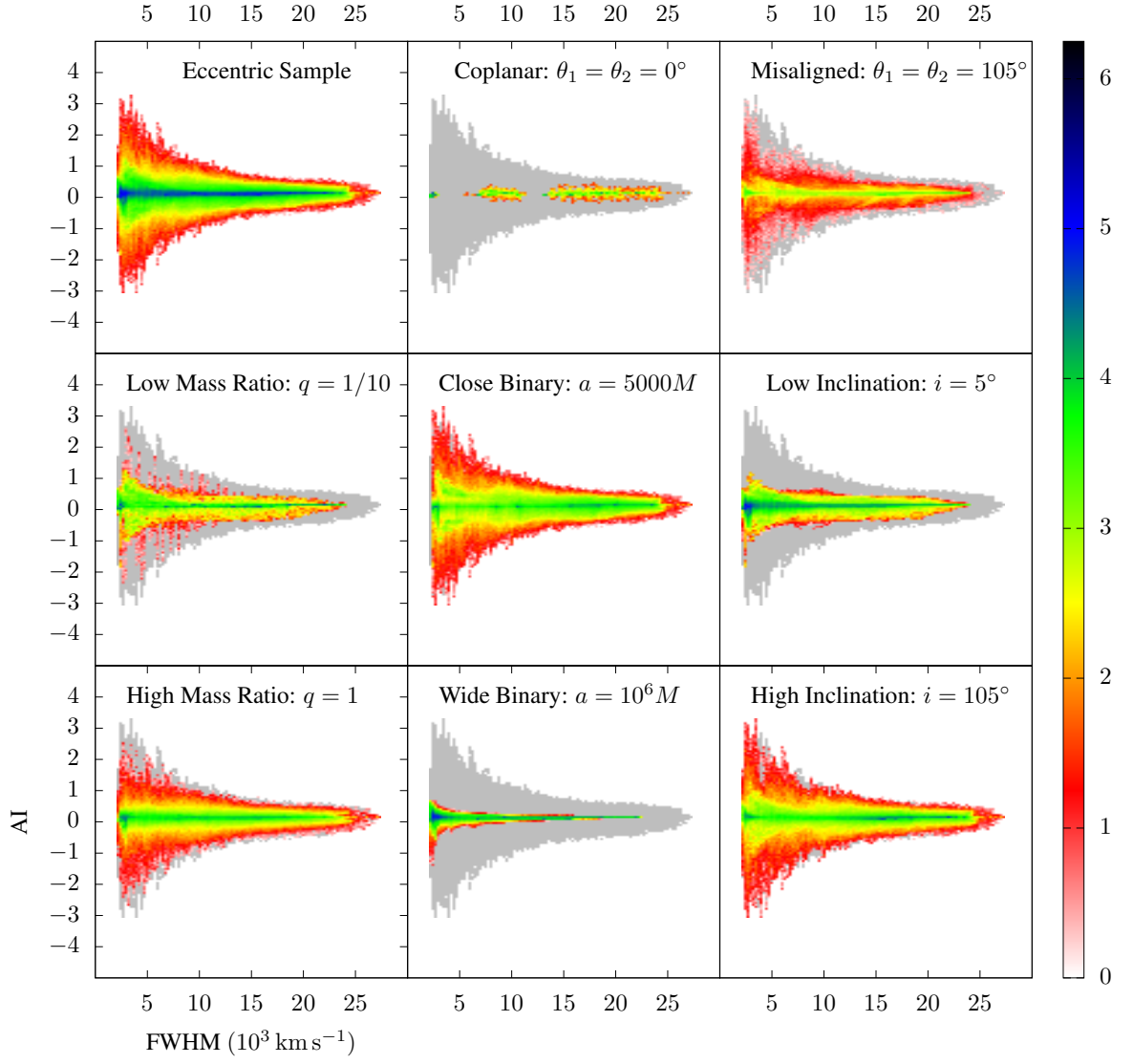


Figure 3.8: AI-FWHM maps for emission-line profiles associated with eccentric SBHB systems. Map legend is the same as in Figure 3.5.

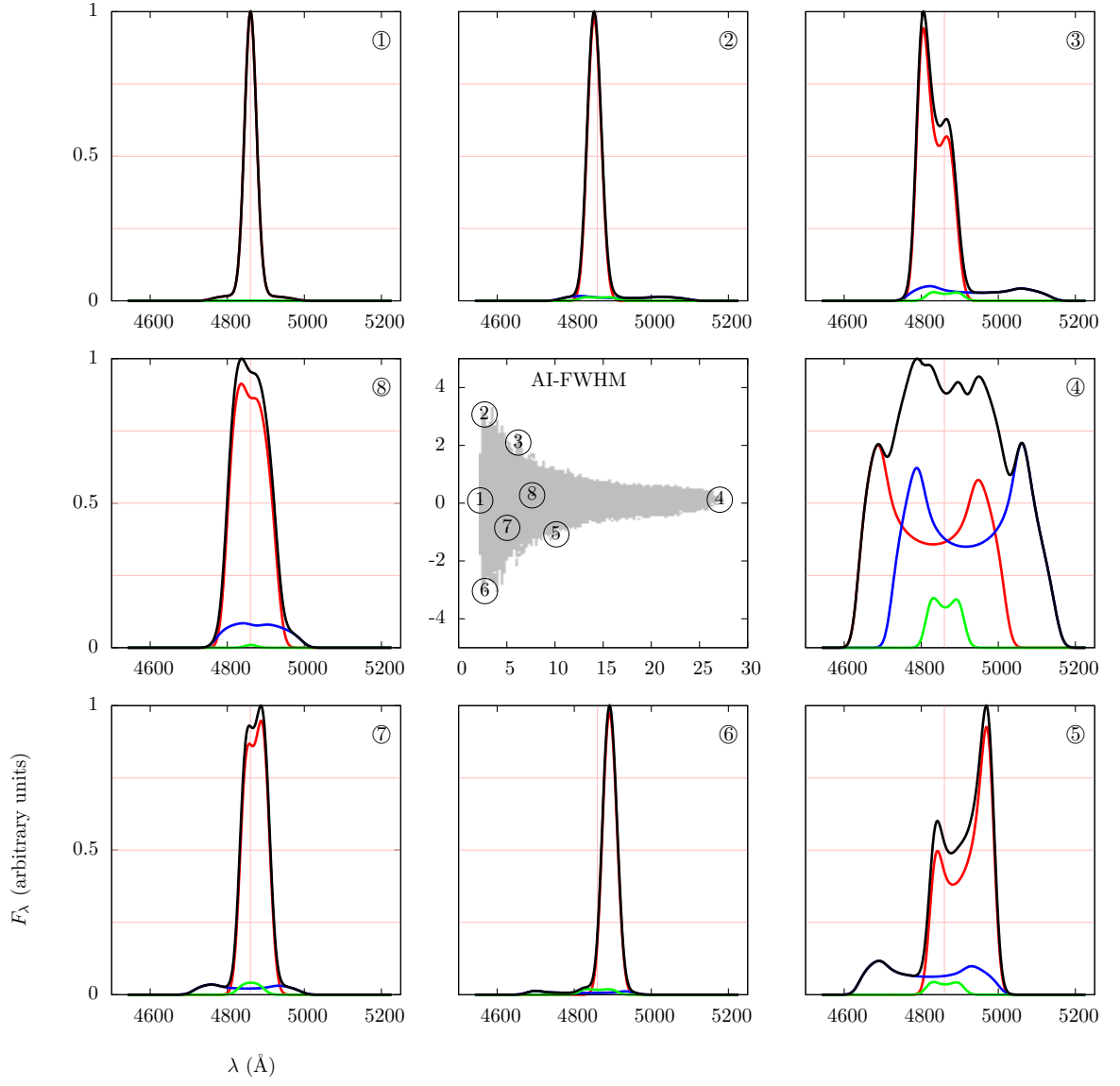


Figure 3.9: Characteristic profile shapes occupying different regions in the AI-FWHM parameter space. Central panel shows footprint of the distribution from the top left panel of Figure 3.8 with identical scale and labeling of axes.

In the remaining figures we show four more projections of the multi-dimensional parameter space of the modeled BEL profiles including AI-FWHM (Figures 3.8 and 3.9), FWQM-CS (Figures 3.10 and 3.11), AI-KI (Figures 3.12 and 3.13) and AIP-CS maps (Figures 3.14 and 3.15). While more maps (i.e., parameter combinations) can in principle be constructed for this parameter space we focus on those that show distinct statistical distributions for any given SBHB property.

Figure 3.8 shows AI-FWHM maps for the eccentric sample of binaries, where we used formulation of the asymmetry index defined in equation 3.5. The figure illustrates that profiles in the synthetic database have a wide range of FWHM values that extend to $28,000 \text{ km s}^{-1}$ for eccentric sample of SBHBs. In comparison, the circular sample of binaries (not shown) is characterized by somewhat narrower profiles and $\text{FWHM} < 23,000 \text{ km s}^{-1}$. This difference can again be attributed to a wider range of orbital velocities sampled by eccentric binaries.

Similar to Figure 3.5 this map shows that SBHB systems with coplanar disks and SBHBs on wide orbits tend to produce symmetric profiles with $\text{AI} \approx 0$, distinct from misaligned systems and close binaries. Furthermore, Figure 3.8 shows that low mass ratio systems ($q = 1/10$) and those in which SBHB orbit is close to face-on orientation relative to the observer ($\theta = 5^\circ$) also occupy a narrow range of $-1 \gtrsim \text{AI} \gtrsim 1$, relative to the footprint of the entire distribution. This means that a combination of AIP-PS and AI-FWHM maps can in principle be used to break the degeneracy between SBHBs with aligned disks or large a and SBHBs with low inclination or low values of q .

Figure 3.9 shows the characteristic profile shapes occupying the AI-FWHM parameter space. Panels 2 and 6 illustrate the ability of AI to diagnose asymmetry in the low intensity features in profile wings even when the bulk of the profile is symmetric. By the same token, profile 5 has a lower value of AI than profile 6. This makes AI an useful diagnostic whenever the spectral noise level can be accurately determined and low intensity features clearly isolated. The profiles in panels 4 and 8 of Figure 3.9 have $\text{AI} \approx 0$ showing that AI

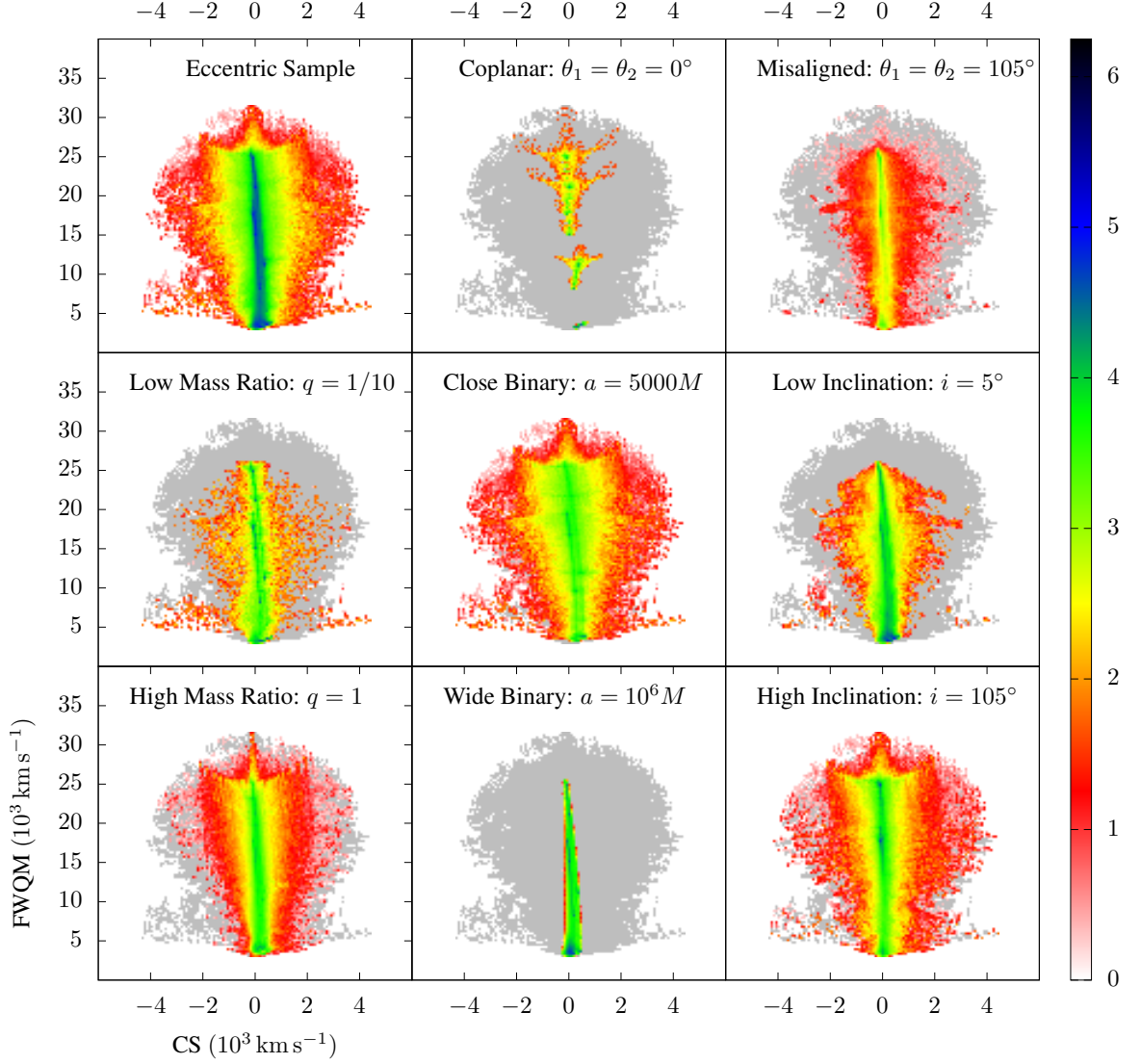


Figure 3.10: FWQM-CS maps for profiles associated with eccentric SBHB systems. Map legend is the same as in Figure 3.5.

does not diagnose the asymmetry in the bulk of the profile. This tendency is the opposite from the AIP index, which makes them complementary diagnostics. Considering this in the context of the distributions discussed in the previous paragraph indicates that the low mass ratio SBHB systems and those in which SBHB orbit is close to face-on orientation relative to the observer can produce emission lines which are asymmetric in the bulk of the profile but show no significant asymmetry in the low intensity wings.

Figure 3.11 illustrates the diversity of profile shapes encountered in FWQM-CS param-

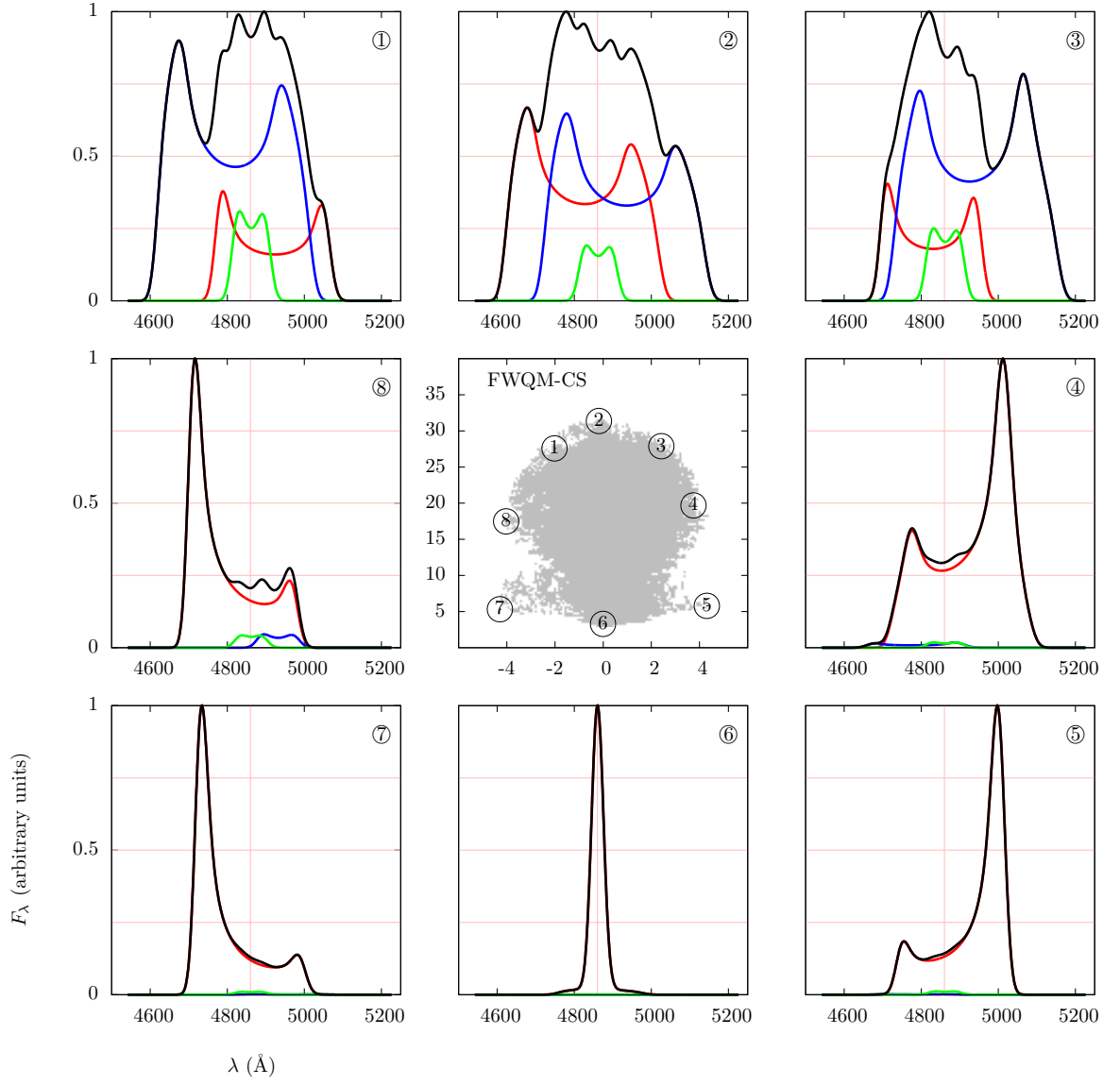


Figure 3.11: Characteristic profile shapes in the FWQM-CS parameter space. Central panel shows footprint of the distribution from the top left panel of Figure 3.10 with identical scale and labeling of axes.

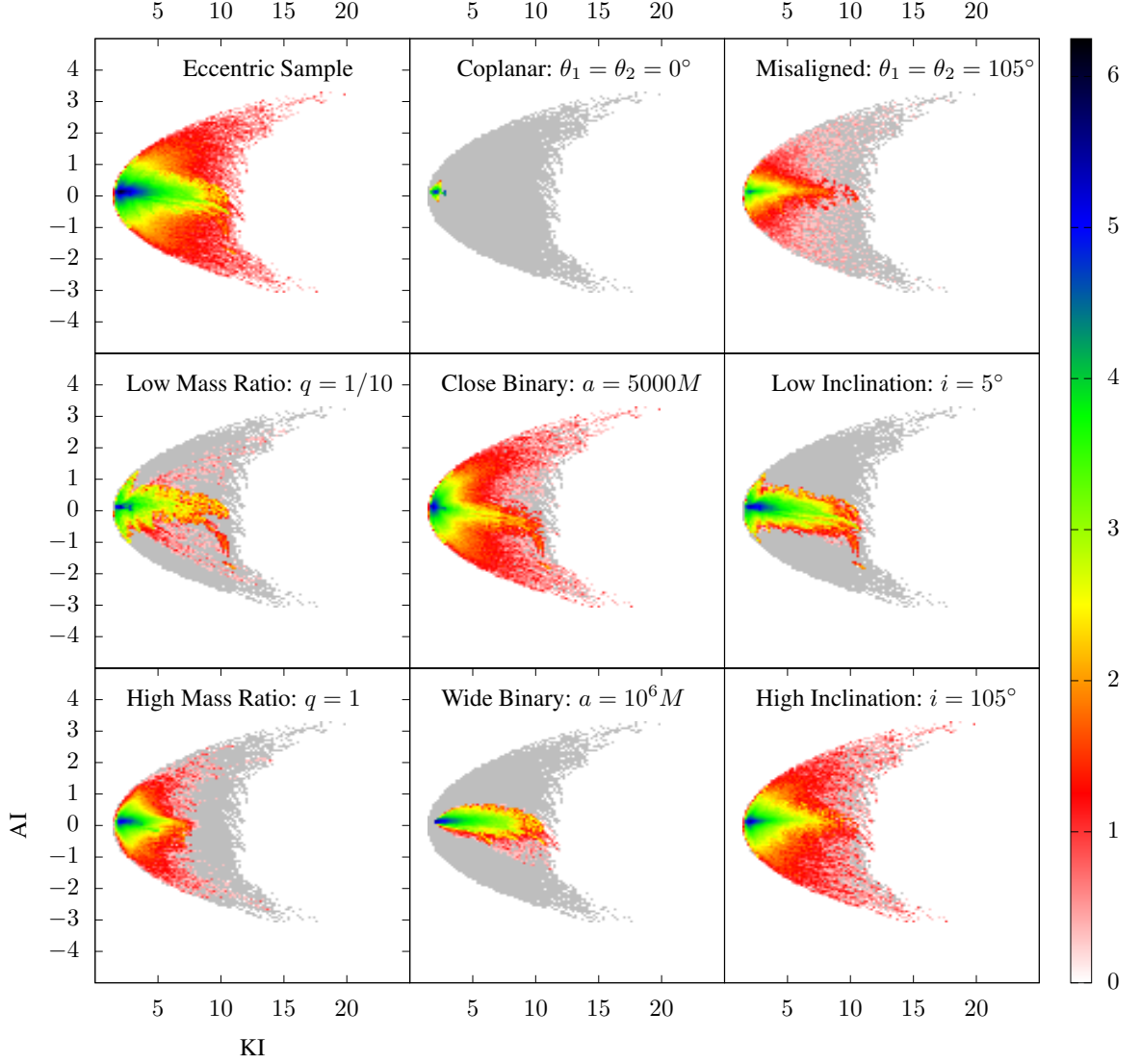


Figure 3.12: AI-KI maps for profiles associated with eccentric SBHB systems. Map legend is the same as in Figure 3.5.

eter space. Interpreted together with Figure 3.10 it shows that the profiles 1, 2 and 3 must be produced by SBHB systems which satisfy either of these conditions: $q > 1/10$, $\theta > 5^\circ$ or $a \ll 10^6 M$. Similarly, profiles 1, 3, 4, 5, 7 and 8 cannot be associated with SBHB systems in which all disks are coplanar nor with wide binaries. Furthermore, profiles 5 and 7 cannot be associated with SBHB systems with $q = 1$ and represent configurations where flux contributed by the primary mini-disk dominates over all other components.

Figures 3.12 and 3.13 show AI-KI maps and examples of the BEL profiles associated

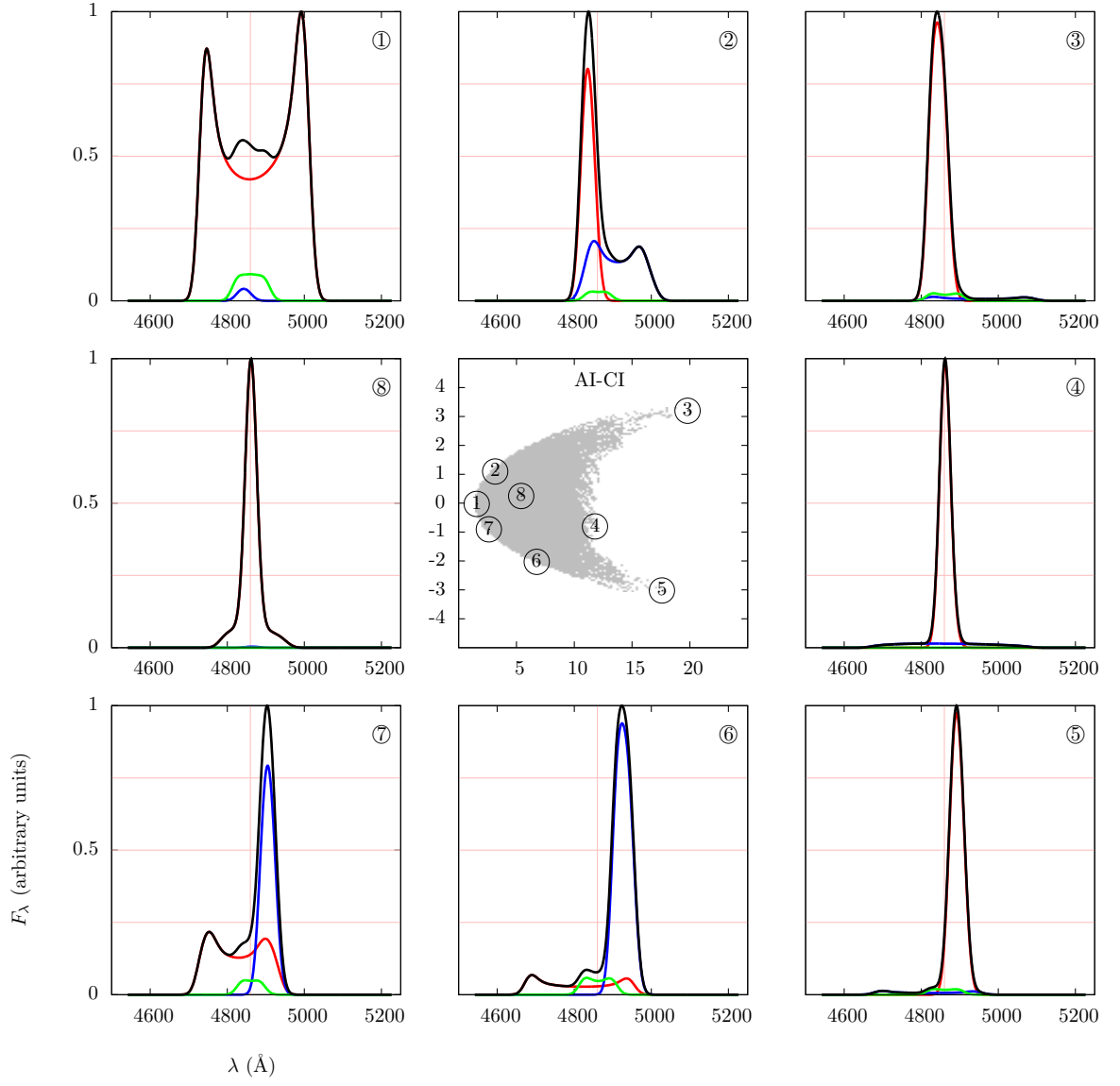


Figure 3.13: Characteristic profile shapes in the AI-KI parameter space. Central panel shows footprint of the distribution from the top left panel of Figure 3.12 with identical scale and labeling of axes.

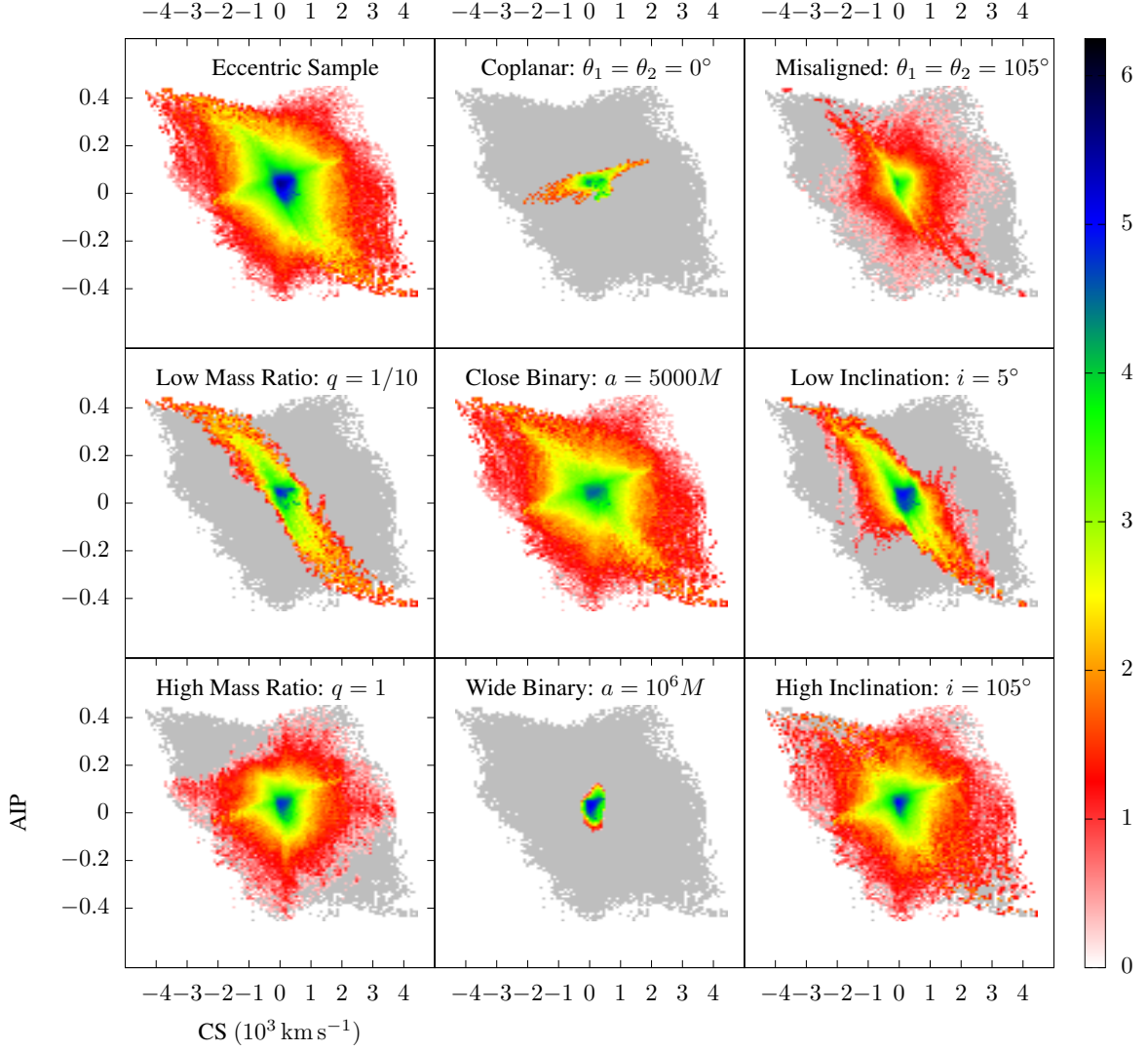


Figure 3.14: AIP-CS maps for profiles associated with eccentric SBHB systems. Map legend is the same as in Figure 3.5.

with eccentric SBHBs, respectively. A large fraction of profiles clusters around low values of AI and KI indicating a large number of symmetric and boxy shapes (see profiles 1 and 7). The AI-KI maps illustrate a strong dependence of the profile shapes on the alignment of the triple disk system, where aligned systems give rise to very boxy profiles with symmetric wings. Similarly, the asymmetry of the low intensity features in the profile wings (profiles 3 and 5) is a sensitive function of a and i but is less sensitive to q , because distributions for different values of the SBHB mass ratio overlap to a significant degree.

The pair of Figures 3.14 and 3.15 show the AIP-CS projection of the parameter space

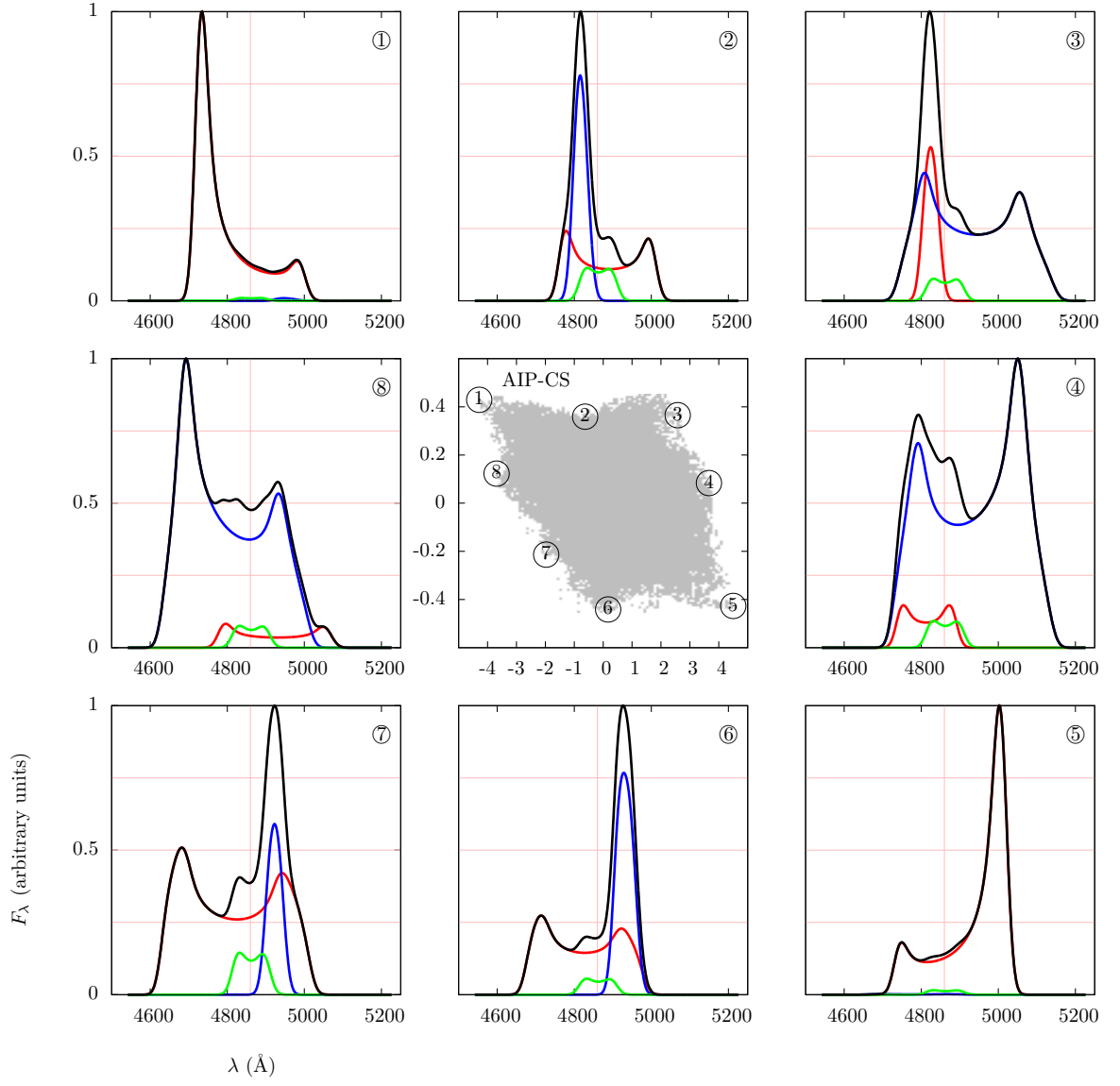


Figure 3.15: Characteristic profile shapes in the AIP-CS parameter space. Central panel shows footprint of the distribution from the top left panel of Figure 3.14 with identical scale and labeling of axes.

and the profile shapes in it, respectively. Similar to previous maps, the statistical distributions are a strong function of a , followed by the degree of triple disk alignment marked by the angles θ_1 and θ_2 . This implies that AIP-CS maps can be used as a relatively sensitive diagnostic for these properties. The statistical distributions as a function of q and i are also distinct, so AIP-CS may also be used to constrain these parameters, although with a somewhat larger degree of degeneracy.

The profile shapes shown in Figure 3.15 are drawn from the rim of the AIP-CS distribution and are representative of shapes associated with close SBHBs, those with $q \approx 1$ (with the exception of 1 and 5) and large inclination. Profiles in panels 1, 4, 5 and 8 exhibit asymmetry due to one strongly dominant peak produced by illumination of one mini-disk by the companion AGN. As discussed in § 3.2.1, this effect produces strong contribution to the flux of the composite profile in close binaries where the illuminated mini-disk is not aligned with the SBHB orbit, consistent with the binary properties shown in the AIP-CS maps. Profiles 2, 3, 6 and 7 also have a very pronounced, dominant peak which in their case arises due to incidental alignment of constituent profiles, rather than illumination by the other AGN.

In this section we analyzed the dependance of the modeled profile shapes on the key parameters describing SBHB and triple disk configurations. For convenience, we summarize the most important results below.

- The shapes of modeled BEL profiles are a sensitive function of the binary orbital separation. Compared to systems with small orbital semi-major axis, line profiles of wide SBHBs are more symmetric and occupy a relatively narrow range of values in terms of boxiness, peak and centroid shifts, and FWHM.
- Similarly, modeled profile shapes are a sensitive function of the degree of alignment in the triple disk system. Line profiles associated with SBHB systems with nearly coplanar disks tend to be symmetric, boxy, and weakly affected by the secondary illumination from the companion AGN relative to the misaligned systems.

- The synthetic BEL profiles tend to be less sensitive (or more degenerate with respect) to the SBHB mass ratio according to a majority of statistical distributions calculated in this work. The exception is the AIP-CS parameter space in which the low and high q systems trace distinct correlations.
- Besides the SBHB mass ratio, the modeled profile shapes show a comparable degree of degeneracy with respect to the binary orbital inclination relative to the observer. Compared to systems with high orbital inclination, line profiles of low inclination systems tend to be more symmetric, especially in the extended profile wings, and have somewhat lower values of FWHM. Similar to the SBHB mass ratio, the low and high inclination systems trace distinct correlations in the AIP-CS parameter space.

3.2.4 Discussion: Modeled emission-line profiles associated with sub-parsec SBHBs.

3.2.4.1 Do modeled BEL profiles carry an imprint of SBHB parameters?

The ultimate goal of this investigation is to investigate whether the BEL profiles, commonly used in spectroscopic observational searches to select SBHB candidates, can be used to decode the properties of bona fide SBHBs. In this work we make a step in this direction by first examining whether modeled BEL profile shapes convey any information about the parameters of SBHBs and their BLRs. If so, further development of this and similar models is of interest, as well as a comparison of such models with the data.

The answer to this question is not obvious a priori: while composite profiles are potentially rich in information, the properties of SBHBs may be difficult to extract because of the complex emission geometry of multiple accretion disks. In practice, this means that any model designed to represent such systems must depend on a number of parameters and so do calculated BEL profiles (listed in Table 3.1 and § 3.1 for model presented here). Because of the dependence of profiles on multiple parameters and their degeneracy, it is unlikely that a unique match between a model and an observed SBHB can be achieved by

attempting to fit the observed profile with arbitrary parameter combinations.

This argues for an approach based on statistical distributions as a more promising way to analyze profile shapes. In this approach observed profiles can be matched to the modeled database based on their values of AIP, KI, FWHM, PS and CS. Each observed profile would map into a subset of modeled profiles with similar statistical properties that represent different modeled SBHB configurations. This correspondence of one observed profile and multiple SBHB configurations is a direct manifestation of degeneracy of the SBHB parameters. As a result, one could make a statement about the likelihood that the observed profile corresponds to some given SBHB configuration. If instead of one, a temporal sequence of observed profiles from the same SBHB is available for comparison with the modeled database, this could further help to reduce degeneracy.

So far, our results in § 3.2 indicate that the modeled profiles show distinct statistical properties as a function of the semi-major axis, mass ratio, eccentricity of the binary, and the degree of alignment of the triple disk system. In our model, the SBHB systems on eccentric orbits are more likely to produce broader emission-line profiles and complex profiles with multiple peaks relative to the circular cases. Thus, an observed profile compared to the synthetic database can be assigned a finite probability in the context of this model that it originates with the circular or eccentric SBHB based on its shape (see however the discussion below).

Furthermore, mini-disks in smaller separation binaries which are misaligned with the binary orbital plane are subject to strong illumination by both AGNs in the system. As a consequence of the off-center illumination, such systems give rise to very asymmetric profiles that can exhibit significant peak or centroid velocity shifts. This is the dominant reason why all statistical distributions shown in this work are sensitive functions of parameters that control orbital separation and disk alignment. Indeed, in our model these two features of SBHB systems are most easily discernible based on profile shapes.

In comparison, the effects of the binary mass ratio and SBHB orientation relative to

a distant observer on profiles shapes are most discernible in the AIP-CS distribution (for both q and i) and AI-KI distribution (for i and to a lesser degree q). It is interesting to note that SBHBs with low q or nearly face-on orbits ($i \approx 0^\circ$) tend to show a significant degree of correlation between the Pearson's skewness coefficient and the peak or centroid velocity shifts (Figures 3.6 and 3.14), where the AIP-CS correlation is more pronounced. This implies that such SBHB systems give rise to specific asymmetric profiles. As the offset of the dominant peak increases, the profile becomes more asymmetric resulting in red leaning profiles with the strongest peak shifted towards red or the blue leaning profiles with the strongest peak shifted towards blue.

Visual inspection of such profiles indicates that their shapes tend to be strongly affected by the off-center illumination of the primary mini-disk, which dominates the flux in the composite profile. This can be understood because in our model the emission from the primary mini-disk typically dominates over that from the secondary and circumbinary disks for the smallest values of q . Even so, the composite BEL profile does not default to a fairly symmetric double peaked profile from an accretion disk about a single SBH, precisely because of the illumination by the secondary AGN.

It follows that the most characteristic features of the modeled profiles presented here are a direct consequence of the presence of multiple BLRs (giving rise to profiles with multiple peaks) and their illumination by two AGN, both of which are an inherent property of the SBHB model. The distinct statistical distributions suggest that SBHB properties are indeed imprinted in the population of modeled profiles, albeit with some degeneracy, which for any given SBHB parameter can be statistically quantified. Based on this we conclude that models of BEL profiles from SBHBs in circumbinary disks can have predictive power and as such merit further investigation.

3.2.4.2 *Can modeled BEL profiles be compared with the observed profiles from SBHB candidates?*

The next relevant question is whether the modeled BEL profiles presented here can be directly compared with those from spectroscopically selected SBHB candidates. We make several such comparisons below but note that they do not constitute a proof that the observed candidates are indeed SBH binaries.

Examination of the observed BEL profiles from SBHB candidates presented in [105], [109], [112] and [114], shows that these profiles can be asymmetric and offset but are usually quite smooth and characterized by one or two peaks, unlike some of the profiles in our database with complex structure and up to 6 peaks. Admittedly, the fraction of profiles with such high number of peaks is relatively small in our database and they are more common for eccentric binaries. On the other hand, the modeled single and double-peaked profiles are most common in SBHB configurations with semi-major axes $a \geq 5 \times 10^4 M$, which for a $10^8 M_\odot$ binary translates to ≥ 0.25 pc. Therefore, if comparison between the observed and modeled profiles is made at the face value, it would favor moderately wide bound binaries.

Note that both AIP-PS and AIP-CS correlations have been reported in spectroscopically targeted SBHB candidates and have not been found in a control sample of matching AGN [105, 113]. A qualitative comparison of the observed sample in Figure 18 of [113] with our modeled AIP-PS distributions in Figures 3.5 and 3.6 shows that they cover a similar range of AIP values but that the observed profiles tend to have peak velocity shifts in a narrow range between $-4000 \lesssim \text{PS} \lesssim 3000 \text{ km s}^{-1}$. In the context of the SBHB model this disfavors configurations of SBHBs with either the smallest or the widest orbital separations and favors moderately wide binaries and binaries with misaligned disks.

Another correlation identified in the sample of observed SBHBs by the same authors is between the third moment of the flux distribution of profiles¹, μ_3 , and FWHM. Namely,

¹Related to the properties calculated in this work as $\mu_3 = \sigma^3 \text{AI}$.

[105] report that the values of μ_3 in the observed BEL profiles tend to decrease with increasing FWHM. This correlation is not seemingly present in our modeled sample regardless of the adopted parameter cut. As noted before however, the value of AI (and that of the related parameter μ_3) sensitively depends on the noise level, which in observed profiles is very likely different from the fiducial noise level we adopt in our calculations of AI. We will take this difference into account when we carry out a more detailed comparison between the observed and modeled samples.

Along similar lines, the FWHM measured by Eracleous et al [105] in their sample of 88 candidates reaches up to $18,000 \text{ km s}^{-1}$. Our synthetic profiles are however characterized by values of FWHM as high as $23,000 \text{ km s}^{-1}$ for the circular and $28,000 \text{ km s}^{-1}$ for the eccentric sample of binaries. The modeled profiles are therefore inherently wider than those observed, regardless of the SBHB parameter cut.

The tendency of modeled profiles to exhibit richer and more diverse structure can to some degree be ascribed to their dependence on the semi-major axis, as discussed at the beginning of this section, or perhaps a larger degree of “smoothing” in real profiles due to either the presence of noise or a larger velocity dispersion of the emitting gas on average. On the other hand a mismatch in the range of measured FWHM between the two populations cannot be trivially explained. The FWHM measured in modeled profiles is a function of the orbital velocity of the gas in each disk and the orbital velocity of the binary, both of which are inherent characteristics of SBHB systems. If anything, increasing the velocity dispersion of the gas (σ) in our model, in order to produce smoother profiles, would result in even wider profiles and more tension between the observed and modeled samples.

A qualitative comparison therefore highlights some intriguing similarities and also points to differences between the two samples. The former motivate further development of models of BEL profiles from SBHB systems, given their potential to interpret profiles from observed bona fide SBHBs. The latter may arise either due to a true difference between the two samples of profiles or because physical processes giving rise to the BEL profiles

were not entirely captured by our model. It is therefore important before attempting more detailed comparisons to examine the impact of any simplifying assumptions made in the current model.

3.2.4.3 *Simplifying assumptions and their implications*

Perhaps the most important physical mechanism that can significantly modify the appearance of the spectrum and emission lines is the radiative feedback from the binary AGN, capable of driving winds and outflows from the circumbinary region. Several recent simulations of SBHBs in circumbinary disks indicate that despite strong binary torques, accretion into the central cavity continues more-less unhindered relative to the single SBH case [39, 40, 152]. This point is of particular interest because AGN feedback from an accreting binary SBH can considerably change the structure, thermodynamic and ionization properties of the circumbinary region. In this section, we assume that the emissivity of each broad line region arises due to photoionization by the two AGNs but neglect the effects of radiation pressure on the dynamics and optical depth of the emitting gas. In the next section, we will discuss properties of the profiles of low-ionization emission lines when radiative transfer effects are not neglectable by generalizing models that account for accretion disk wind [127, 133–135]. The key effect of the accretion disk wind is to modify the shape of a BEL profile. This occurs because the radiation pressure from the central AGN lifts-off the low density gas from the surface of the disk and launches it along streamlines above the disk. The photons (in this case $H\beta$) escaping from a single accretion disk encounter increased optical depth through the emission layer and as a consequence, the peaks of an initially double peaked profile move closer and eventually merge, producing a narrower single peaked profile. Comparisons of such single peaked disk-wind model profiles with emission lines from a set of SDSS quasars show that observed lines are consistent with moderately large optical depth in the disk wind and indicate that most AGNs may be subject to this type of feedback [134]. It is therefore reasonable to assume that if SBHBs in a

binary can accrete at rates comparable to the general population of AGNs, they are likely to produce similar effects. The reprocessing of the $H\beta$ photons through the accretion disk wind may indeed produce smoother and narrower profiles in better general agreement with the observed sample of SBHB candidates and AGNs in general. However, the same effect may also “wash out” some of the characteristic features encountered in our modeled profiles, thus weakening their dependence on the properties of the binary. We will assess the diagnostic power from BEL profiles affected by the accretion disk wind and associated with SBHBs in circumbinary disks in the next section.

In addition to the accretion disk wind the emissivity can also be modified by shocks, impacts of streams from the circumbinary disk onto the accretion disks around the individual SBHs [153] and by the presence of overdense lumps that may form in the inner region of the circumbinary disk [40]. These features have been predicted by some theoretical models and simulations and if indeed present in binary accretion flows, they would increase the complexity of the BEL profiles by creating hotspots and localized regions of high emissivity. The presence, persistence and exact emission properties of these features however sensitively depend on thermodynamics of the SBHB accretion flow, which remains to be understood and at the present cannot be derived from first principles. We do not account for contribution to the emissivity of the broad lines from shocks and overdensities but note that they can be added to the existing model should that be necessary.

Another approximation used in our model is that the two mini-disks, as well as the circumbinary disk are circular in shape. In this scenario, the outer edges of the mini-disks and the inner edge of the circumbinary disk are determined by SBHB tidal forces and are not free parameters of the model (see § 3.1). Simulations however show that the mini-disks and the circumbinary disk can exhibit varying degrees of eccentricity as a consequence of tidal deformation by the binary, an effect which is most pronounced for comparable-mass binaries [40]. From the stand point of our semi-analytic model this implies that additional parameters may be required in order to describe the geometry of the emission

regions around SBHBs, leading to additional degrees of freedom in profile shapes. The distinct property of an elliptical accretion disk is that it can naturally give rise to double peaked BEL profiles in which the red peak is stronger than the blue, a feature that cannot be reproduced by a circular disk [122]. In our model this type of asymmetry is present in less than 50% of the profiles and it arises in two ways: either through summation of individual profiles which results in a stronger red peak (see for example panels 6 and 7 in Figure 3.15) or due to illumination by the companion AGN (panels 4 and 5 in Figure 3.15). We therefore reproduce such an effect even though we only consider circular BLRs in our model. If our model accounted for elliptical disks the database may contain a larger fraction of profiles with the dominant red peak (reflected in the positive value of the peak velocity shift) but at the expense of a number of additional parameters.

An additional assumption used in our model is that of prograde binaries. Namely, motivated by theoretical works described in the Introduction Chapter 1 we assume that the SBHB and the circumbinary disk are coplanar and rotate in the same sense. At the same time, the mini-disks are allowed to assume arbitrary orientation (and sense of rotation) relative to the SBHB orbit. A circumbinary disk with an arbitrary orientation relative to the SBHB orbit would however still produce a single- or a double-peaked profile that is centered on the SBHB rest frame, similar to the profiles shown in this work. Since the total flux of the composite profile is dominated by the primary and secondary mini-disks, the assumption about co-planarity of the circumbinary disk should not strongly affect our results. Note however that simulations of retrograde SBHBs in circumbinary disks show a different dependence of SBH accretion rates on orbital eccentricity [154] from that assumed in Equation 3.1 of this work. This is another ingredient that can in principle be added to the model, if counter-rotating SBHB configurations are of interest.

Because we evaluate Doppler boosting and gravitational redshift in the weak field limit and neglect bending of light (see § 2.1) we can only faithfully calculate the BEL profiles that arise in configurations in which the photons are emitted far from the immediate en-

environment of black holes (i.e., at distances larger than tens of Schwarzschild radii) and in which they do not travel on grazing trajectories over the SBHs. Both of these requirements are satisfied in our model given the assumed sizes of emission regions and the fact that we do not allow for edge-on configurations characterized by the disk inclination angles in the range $80 - 100^\circ$. Along similar lines, we do not account for lensing of one mini-disk by the companion SBH when the two SBHs are in conjunction. Such configurations are expected to be rare and short lived and should not significantly affect the overall statistical distribution of the BEL profiles.

The parameter values in Table 3.1 are chosen so as to provide a relatively uniform but not necessarily dense coverage of the SBHB parameter space. This can be seen in the middle top panel of Figure 3.10, where "branches" at $\text{FWQM} \approx 22,000 \text{ km s}^{-1}$ and $27,000 \text{ km s}^{-1}$ carry an imprint of the underlying SBHB parameter choices, most likely that of the binary orbital inclination. Because of the extent of the parameter space, the number of sampled configurations quickly adds up to nearly 15 million, even with a handful of choices per parameter. While this rate of sampling may be acceptable for surveying the properties of BEL profiles, a denser coverage can be obtained for sub-regions of the parameter space.

It is worth noting that other physical processes can potentially mimic the emission signatures of SBHBs discussed here. These include but are not limited to the recoiling SBHs [155] and local and global instabilities in single SBH accretion disks that can give rise to transient bright spots and spiral arms [156, 157]. In that sense, the model described in this chapter can be used to interpret observed BEL profiles in the context of the SBHB model but cannot be used to prove that they originate with veritable SBHB systems. For example, profiles of SBHB candidates observed in multiple epochs can be compared against the synthetic database individually, in order to determine the likelihood distribution for underlying SBHB parameters for each profile independently. The entire time series of observed profiles can also be compared against the time series of matching modeled profiles as an

added consistency check for the inferred SBHB parameters.

3.3 Improved Model for Calculation of BELs: the Effect of Accretion Disk Wind

3.3.1 The effect of wind optical depth on profile peaks

In the next two sections we report properties of the BEL profiles produced in the present of disk wind effect and compare them to the ones in the previous section in which the disk wind was not accounted for. Figure 3.16 provides a comparison between the with and without disk wind effect in terms of the number of peaks that characterize their BEL profiles. In the absence of a disk wind, each BLR can give rise to a double-peaked BEL profile. Therefore, the combinations of three BLRs can produce a composite broad profile with up to six distinct peaks, depending on the relative motion of the BLRs with respect to the observer. This is indeed reported in § 3.2.1 and shown in Figure 3.16 in column “a” for each model. These columns reflect the profile demographics in the NW model, which corresponds to $\tau_0 = 0$, whereas cases “b”, “c” and “d” correspond to the increasing optical depth in the disk wind.

Figure 3.16 shows that in the absence of the accretion disk wind, the fraction of multi-peaked profiles reaches 38% for SBHBs on circular orbits and 57% for eccentric SBHBs. As reported in the previous § 3.2, SBHBs on eccentric orbits tend to have profiles with a higher number of peaks relative to the circular binaries with the same semimajor axis because the eccentric SBHBs sample a wider range of orbital velocities, allowing for a larger wavelength offset of individual components in the composite profile.

The most important trend captured by Figure 3.16 is the increase in the percentage of the single-peaked profiles with the wind optical depth in each model. For example, for SBHBs on circular orbits in the 3DW model the number of single-peaked profiles increases from 62% in the $\tau_0 = 0$ case to 98% in the $\tau_0 = 100$ case. The remaining 2% of profiles in $\tau_0 = 100$ case are double-peaked profiles, and there are no profiles with three or more peaks. A similar trend can also be found in the eccentric 3DW model, where even a moderate optical

depth ($\tau_0 = 1$) eliminates complex profiles with more than three peaks.

As mentioned in the introduction, the multi-peaked profiles produced by the NW model do not reflect the average properties of the observed sample of SBHB candidates, or the general population of AGNs, the majority of which tend to have broad but single-peaked profiles. This discrepancy provided the main motivation for further development of the model, which now includes radiative transfer through the disk wind. Figure 3.16 shows that this development results in model profiles that are consistent with observations given some appropriate value of τ_0 . For example, only about 3% of observed AGNs exhibit the double-peaked BEL profiles [125]. If sub-parsec SBHBs in circumbinary disks follow a similar trend, our models indicate that their accretion disks must have outflows with substantial optical depths ($\tau_0 > 1$).

Estimating the fraction of double-peaked profiles in the datasets obtained from the observational searches for sub-parsec SBHBs is however non-trivial. For example, the sample of candidates selected for spectroscopic monitoring by Eracleous et al. [105], and Runnoe et al. [113, 158]² includes only the sources which were in the first epoch of observations characterized by single-peaked BEL profiles. Further analysis of this sample has shown that after the subtraction from the $H\beta$ complex of the narrow $H\beta$ line and [O III] doublet, 17/88 (or about 20%) of SBHB candidates exhibit apparent double-peaked broad $H\beta$ line profiles. Because the subtraction of the narrow line components is not unique, it introduces an uncertainty that can make the resulting broad line appear double-peaked. We therefore conclude that $\lesssim 20\%$ of the SBHB candidates in the E12 sample have line profiles that are truly double-peaked. If all of these are shown to be genuine SBHBs, this would require them to have disk winds with $\tau_0 \gtrsim 0.1$.

It is interesting to note that in the 2DW model for SBHBs on circular orbits, the number of single-peaked profiles increases for optical depth $\tau_0 = 0.1$ but then levels off for $\tau_0 = 1$ and 100. In this setup, the attenuation of emitted radiation in the disk wind is only present

²We refer to it as the E12 search hereafter.

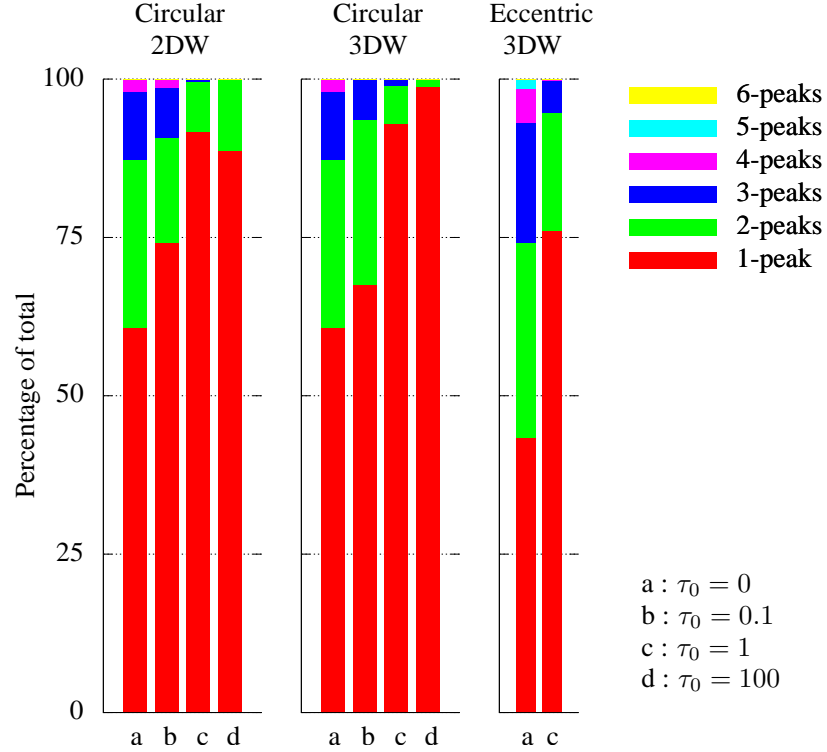


Figure 3.16: Percentage of single- and multi-peaked profiles in different models calculated for SBHBs on circular and eccentric orbits. In all models the number of single-peaked profiles increases with the optical depth in the disk wind. SBHBs on eccentric orbits tend to have profiles with a higher number of peaks relative to SBHBs on circular orbits. Each column corresponds to a different value of the optical depth, τ_0 : (a) 0, (b) 0.1, (c) 1 and (d) 100. Different colors mark profiles with one to six peaks.

in the two mini-disks but not in the circumbinary disk. Once the optical depth in the mini-disks becomes substantial, their emission is significantly attenuated relative to the circumbinary disk. This is because re-emission of the $H\beta$ line photons absorbed in the wind is unlikely, given that a hydrogen atom in $n = 4$ energy state can reach the ground state via several different radiative decay channels, can be radiatively or collisionally ionized, and collisionally excited or de-excited. While some of these processes may result in re-emission of the $H\beta$ photons, their numbers should be considerably smaller relative to the number of absorbed ones. Consequently, the circumbinary disk remains the dominant contributor to the composite BEL profile. Therefore, the number of multi-peaked profiles is in the high optical depth limit determined by the number of double-peaked profiles contributed by the circumbinary disks.

3.3.2 Characteristic features of the modeled emission-line profiles

Following the approach laid out in § 3.2.2, we analyze the trends in the modeled group of profiles by characterizing their shapes in terms of several commonly used distribution functions. These include the Pearson skewness coefficient (AIP), full width at half and quarter maximum (FWHM and FWQM), peak shift (PS), and centroid shift (CS), defined in equations 3.2–3.11. We choose these properties among other distribution functions because they provide robust measures of the dominant features in the bulk of the profile. We avoid profile shape parameters that rely on the wings on the line profiles as these are significantly affected by the noise present in the observed spectra. For more detailed analysis of the impact of the noise on spectral measurements and statistical distribution functions of profiles see our Appendix C and the Appendix in [113].

In Figure 3.17 we visualize the distribution of profiles in two-dimensional maps of AIP versus PS values calculated for all models, including SBHBs on circular and eccentric orbits, different wind configurations, and wind optical depths. The color marks the number density of profiles on a logarithmic scale and indicates which portions of the parameter

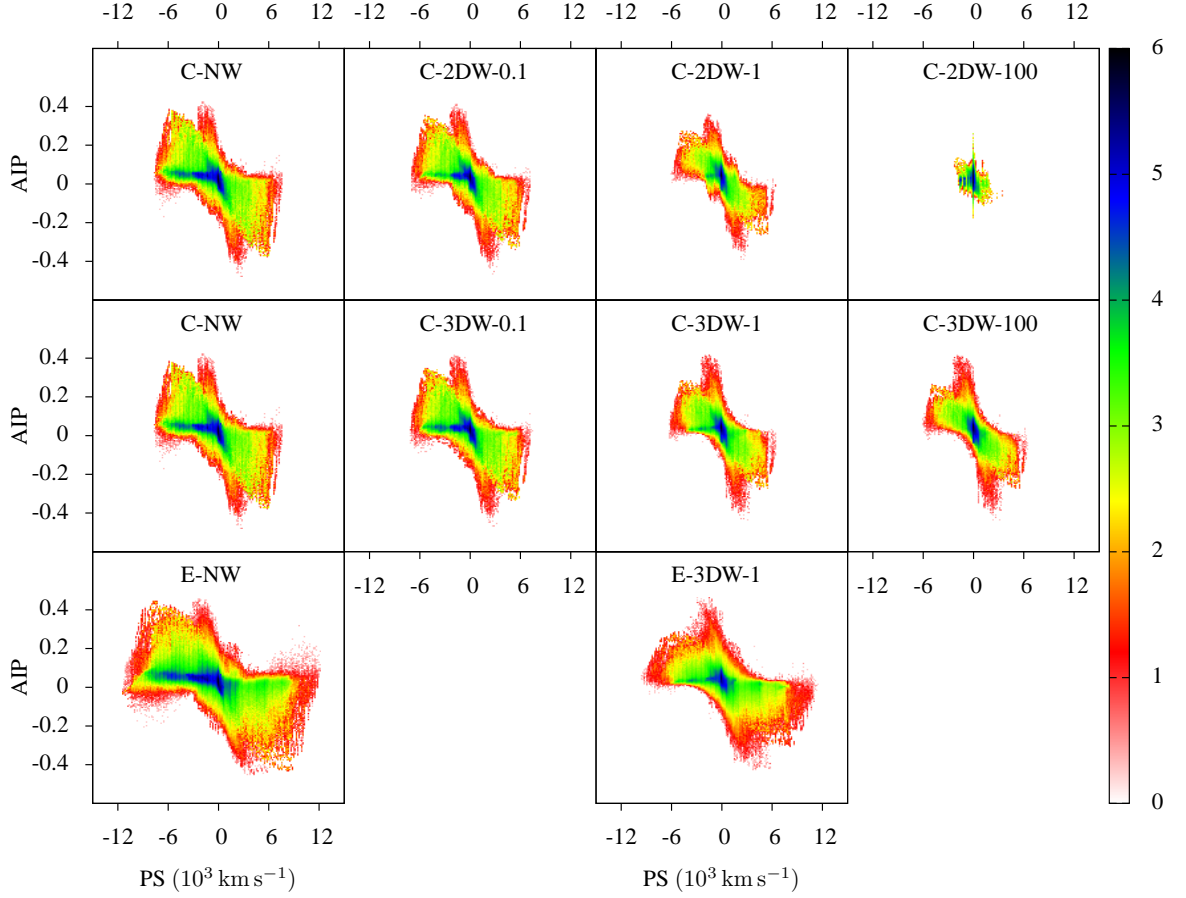


Figure 3.17: Maps of Pearson skewness coefficient vs. peak shift (AIP-PS) for profiles associated with models of SBHBs on circular and eccentric orbits, different wind configurations, and wind optical depths. The first two rows depict profile distributions in the models with SBHBs on circular orbits where there is no absorption of the BEL photons by the disk wind (NW models), the absorption occurs in the two mini-disks (2DW), or in all three disks (3DW). Third row shows the same for the models with eccentric SBHBs. In all rows the wind optical depth increases from left to right, from $\tau_0 = 0$ (NW models) to 0.1, 1, and 100 for DW models. Color bar indicates the density of profiles (i.e., the number of profiles in each area element) plotted on a log scale.

space are favored by the modeled profiles. By definition, positive values of AIP indicate profiles skewed toward short wavelengths, i.e., blue-leaning profiles, and negative values indicate red-leaning profiles. Similarly, negative values of PS indicate that the highest (or the only) peak of the profile is blueshifted with respect to the rest wavelength of the emission line and vice versa.

Inspection of the panels in Figure 3.17 reveals that in all models a significant fraction of profiles are fairly symmetric ($AIP \approx 0$) and likely to exhibit their highest peak at wavelengths shorter than the rest wavelength ($PS < 0 \text{ km s}^{-1}$). The latter is a consequence of relativistic Doppler boosting, which for each individual disk preferentially boosts the blue shoulder of its BEL profile, creating an effect that is also noticeable in the composite profile. Another feature worth noting is that in all but one sample (C-2DW-100), the profiles that exhibit the strongest peak at shorter wavelengths are also preferentially blue-leaning and vice versa. This is of interest because this trend is also present in the sample of SBHB candidates observed as a part of the E12 search [see Figure 18 in 113, and § 3.4.1 in this work for further discussion].

It is worth noting that the distribution of profiles in the model C-2DW-100 appears different with respect to the others. This is because in this model the circumbinary disk remains the dominant contributor to the composite BEL profile, while the emission from the mini-disks is suppressed by the optically thick disk wind, characterized by $\tau_0 = 100$. This model therefore includes the profiles associated with the spatially extended circumbinary disk, which are mostly single-peaked, relatively symmetric and narrow, compared to the unattenuated profiles from the mini-disks.

The most notable difference among different models is that the AIP-PS distribution of profiles becomes narrower with the increasing optical depth in the disk wind. Specifically, the measured range of peak shifts calculated in the C-3DW model for SBHBs on circular orbits is between -8000 and 8000 km s^{-1} in the scenario $\tau_0 = 0$ but is in the narrower range from -6000 to 6000 km s^{-1} in the $\tau_0 = 100$ scenario. Similarly, the AIP-PS distribution

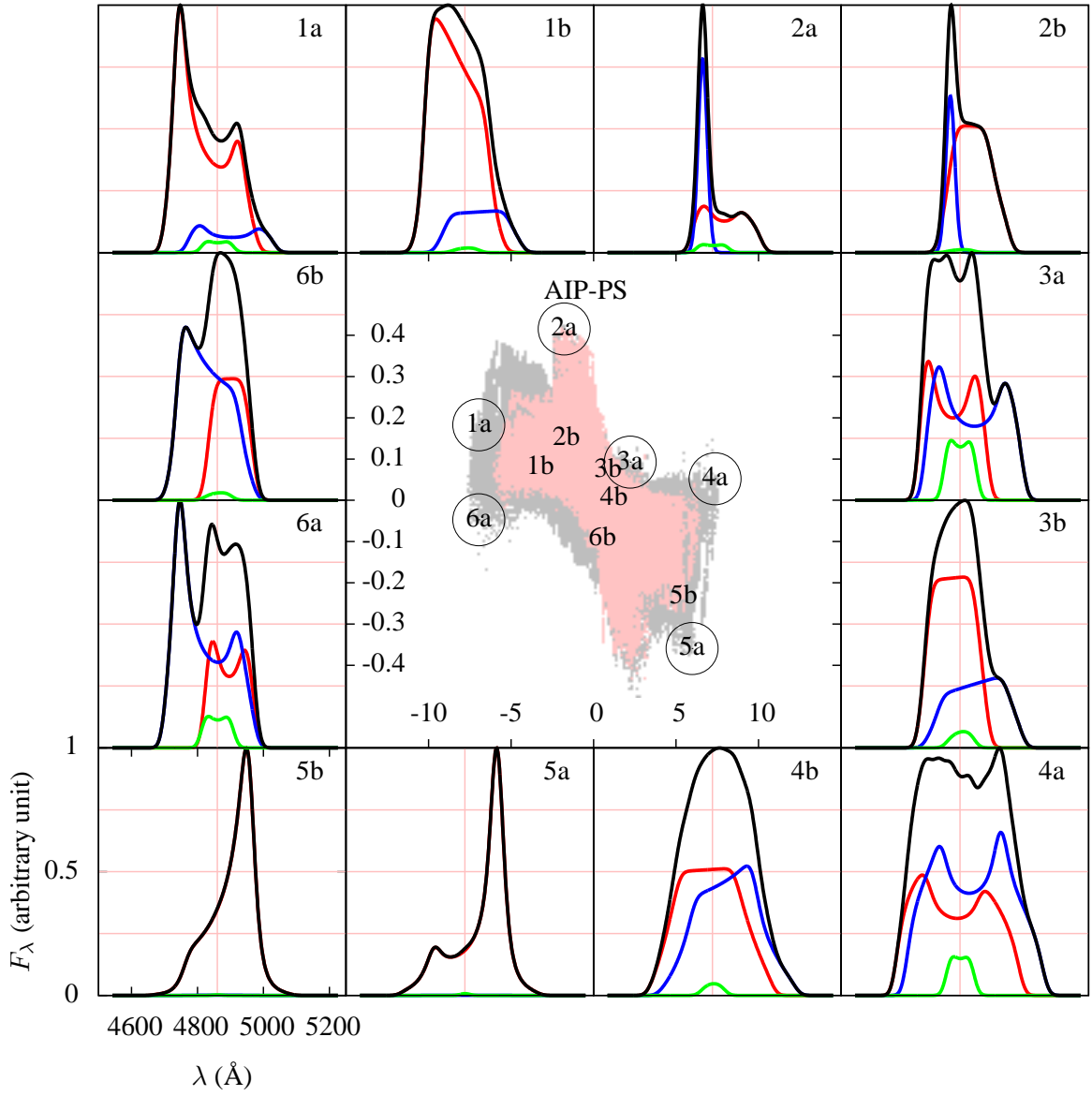


Figure 3.18: Appearance of individual BEL profiles in C-NW and C-3DW-100 models. *Central panel:* Following Fig. 3.17, gray color represents the profile distribution for $\tau_0 = 0$, while the pink overlay marks the $\tau_0 = 100$ case. Markers “a” and “b” trace the location of profiles calculated for the same SBHB configurations with zero and high optical depth, respectively. *Surrounding panels* illustrate the appearance of profiles associated with markers in the central panel. In all cases, higher optical depth in the disk wind gives rise to more symmetric profiles with a smaller number of peaks. Flux is shown in arbitrary units against wavelength marked on the bottom x -axis. Pink vertical line at 4860.09 \AA marks the rest wavelength of the $H\beta$ emission line. For all profiles, total flux (black line) is a sum of components contributed by the primary (red), secondary (blue), and circumbinary disk (green).

Table 3.3. Physical Parameters of Profiles Shown in Figure 3.18

Profile	a	q	e	R_{in1}	R_{in2}	i	ϕ	θ_1	ϕ_1	θ_2	ϕ_2	$F_{\lambda,b}^{\text{max}}/F_{\lambda,a}^{\text{max}}$
1	5000	0.818182	0.0	1000	1000	105	0	60	60	105	235	0.0011
2	5000	0.818182	0.0	500	1000	105	0	105	185	105	0	0.0013
3	5000	0.818182	0.0	1000	1000	105	0	60	0	135	235	0.0017
4	5000	0.666667	0.0	500	500	55	0	165	60	30	235	0.0029
5	5000	0.100000	0.0	500	1000	5	0	105	0	105	235	0.0014
6	5000	1.000000	0.0	1000	1000	105	0	135	0	165	60	0.0018

Note. — $F_{\lambda,b}^{\text{max}}/F_{\lambda,a}^{\text{max}}$ – the ratio between the maximum value of the flux for the attenuated profile in panel b (C-3DW-100 model), and the corresponding profile in panel a (C-NW model), before they were normalized to 1.

of profiles in the E-3DW model becomes narrower with increasing optical depth.

Figure 3.18 illustrates how individual profiles change when the optical depth in the disk wind increases. The central panel shows the footprint of the AIP-PS distributions for C-NW and C-3DW-100 models. The gray color represents the distribution in $\tau_0 = 0$ case, while the distribution overlaid in pink traces $\tau_0 = 100$ scenario. In the central panel, the markers “a” and “b” trace the location of profiles calculated for the same SBHB configurations with zero and high optical depth, respectively. In all the cases shown, the BEL profiles from the model with $\tau_0 = 100$ tend to concentrate toward the center of the AIP-PS distribution relative to the no wind scenario. It follows that higher optical depth in the disk wind gives rise to more symmetric profiles with a smaller number of peaks.

The surrounding panels in Figure 3.18 illustrate the appearance of individual profile pairs. Each composite profile (represented by the black line) is a sum of components contributed by the primary (red), secondary (blue), and circumbinary disk (green). Furthermore, Table 3.3 lists the relevant physical parameters used in the calculation of profiles in Figure 3.18. It can be seen that the increase in optical depth transforms the double-peaked profile in panel 1a to a single-peaked profile in panel 1b, mainly because the dominant component contributed by the primary mini-disk becomes single-peaked. A complex profile in panel 4a, which includes comparable contributions from the primary and secondary mini-disks, is reduced to a smoother single-peaked profile in panel 4b. Similarly, a triple-

peaked profile in panel 6a, in which the emission from the secondary mini-disk dominates, is reduced to an asymmetric, double-peaked profile in panel 6b. We also list in Table 3.3 the ratio between the maximum flux value for attenuated profiles in panels “b” ($\tau_0 = 100$) and the corresponding profiles in panels “a” ($\tau_0 = 0$), before they were normalized to 1. The ratio between the two cases is of the order of 10^{-3} , indicating strong attenuation of the absorbed profiles, relative to the NW scenario. As noted in § 3.3.1, if profile shapes of SBHBs follow a similar trend as regular AGNs (in terms of the frequency of the single- and double-peaked profiles), then their accretion disks must have outflows with optical depths $\tau_0 > 1$. Based on this, we expect that finding an AGN or an SBHB candidate characterized by a moderately high value of τ_0 should not be uncommon. For such objects however, it may be challenging to disentangle the severely attenuated BEL profile from the continuum.

As previously mentioned, each profile associated with one of the disks in the triple disk system is subject to Doppler boosting and attenuation due to absorption in the accretion disk wind. The imprints of these two phenomena include boosting of the blue shoulder of an individual profile (Doppler effect) and merging of the peaks of an initially double-peaked profile into a narrower single peak (absorption). These effects can still be recognized in the composite profiles, albeit not as easily, because a combination of three different profiles results in diverse profile shapes. As a consequence, it is not obvious which peak will dominate (or appear weakened) for a given binary configuration until the profile summation is done.

In terms of the relative contribution to the profile flux from individual disks, the mini-disk of the larger SMBH tends to dominate, because it has a larger surface area. An exception to this is scenarios illustrated by the composite profile number 6a/6b, in which the flux from the secondary mini-disk dominates even though $q = 1$. This “additional” line flux arises because of the illumination of the misaligned secondary mini-disk by both AGNs. The contribution to the profile flux from the circumbinary disk is negligible in all configurations, because it is further away from the two AGNs than the mini-disks, and because

it is co-planar with the binary orbit, and so it intercepts only a small fraction of the AGN radiation.

3.3.3 Dependence of profiles on the physical parameters of the binary

In this section we examine whether the profiles produced by the second-generation model preserve distinct statistical properties as a function of the SBHB parameters, as found for the first-generation models. This question is of importance because modification of the BEL profiles by the accretion disk wind may limit their diagnostic power by “erasing” the imprints of the underlying SBHB configurations.

As mentioned in § 3.3.2, we use statistical functions (AIP, PS, FWHM, etc.) to construct a multi-dimensional parameter space in which we place the modeled BEL profiles. Figures 3.19, 3.20, and 3.21 show the two-dimensional maps, that represent different projections through this parameter space. All maps in these three figures are computed for model E-3DW-1 and are equivalent to Figures 3.6, 3.10, and 3.14, which contain corresponding maps for the NW model. The distributions from the NW model are shown by the black dashed contours in the top left panel of Figures 3.19, 3.20, and 3.21, for comparison. The remaining panels in these figures show how the properties of modeled profiles vary as a function of the SBHB parameters, such as the alignment of the triple disk system, binary mass ratio, orbital separation, and inclination of the binary orbit relative to the observer.

Figure 3.19, for example, illustrates that profiles from SBHBs with wide orbital separations ($a = 10^6 M$) tend to be very symmetric and concentrated in the center of the AIP-PS parameter space, while close binaries ($a = 5000 M$) lead to profiles with a much wider base. Similarly, any SBHB configurations where the mini-disks are coplanar with the binary orbit (and the circumbinary disk, by assumption) are characterized by symmetric profiles with $AIP \approx 0$, majority of which have the dominant peak shifted toward the blue part of the spectrum, as a consequence of Doppler boosting. The misaligned systems are equally likely to be blue-leaning as well as red-leaning and reside in the range

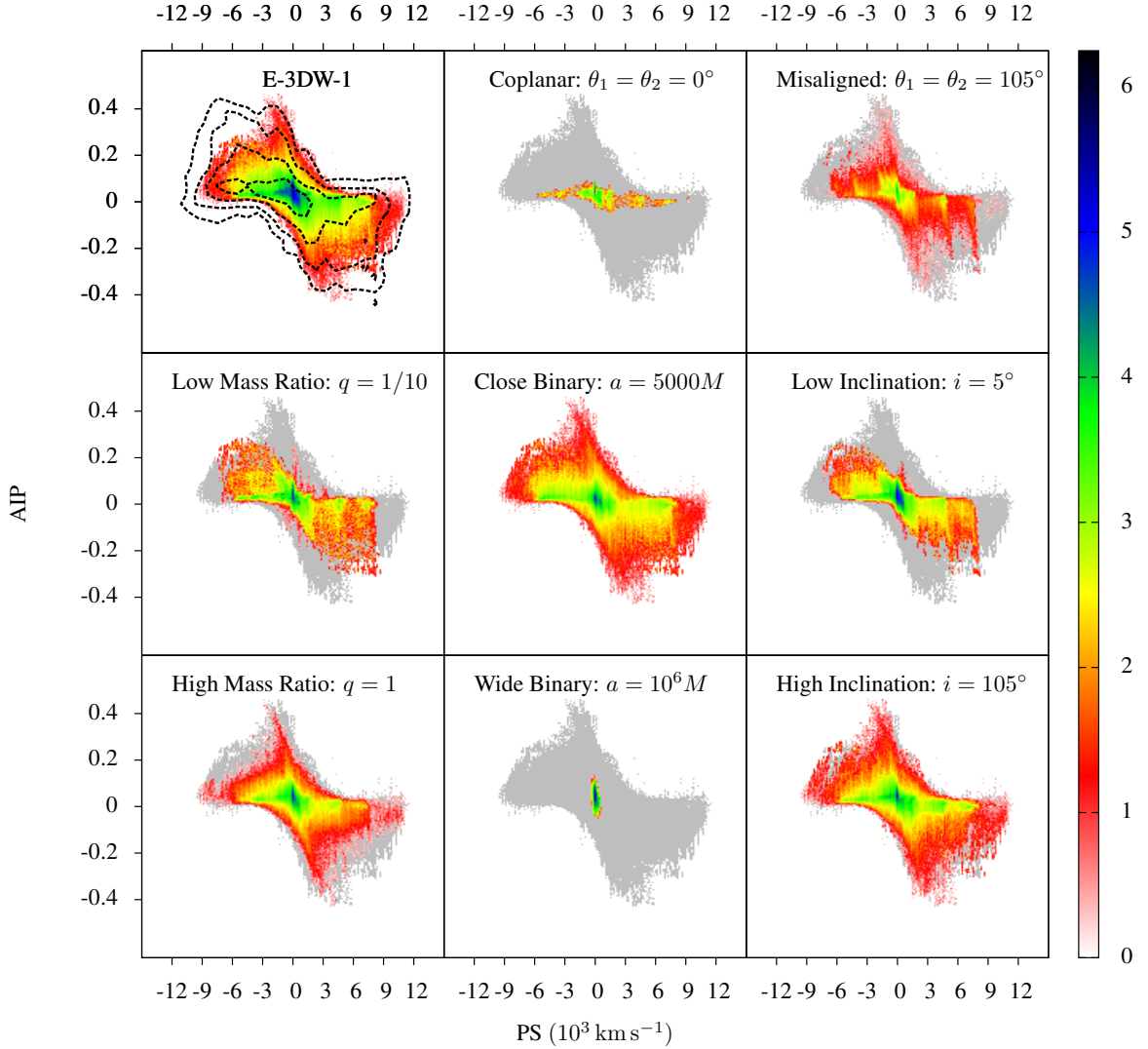


Figure 3.19: AIP-PS map for profiles associated with the eccentric SBHB model E-3DW-1 (top left). Remaining panels display the distribution of profiles as a function of the alignment of the triple disk system, SBHB mass ratio, orbital separation, and inclination of the observer relative to the binary orbit. Color bar indicates the density of profiles (i.e., the number of profiles in each area element) plotted on the log scale. Grey color outlines the footprint of the entire distribution shown in top left panel. Black dashed contours in the top left panel are drawn in increments of one, from 0.5 (outermost) to 3.5 (innermost). They correspond to the AIP-PS maps in the NW model (as shown in Figure 3.6) and are included here for easier visual comparison.

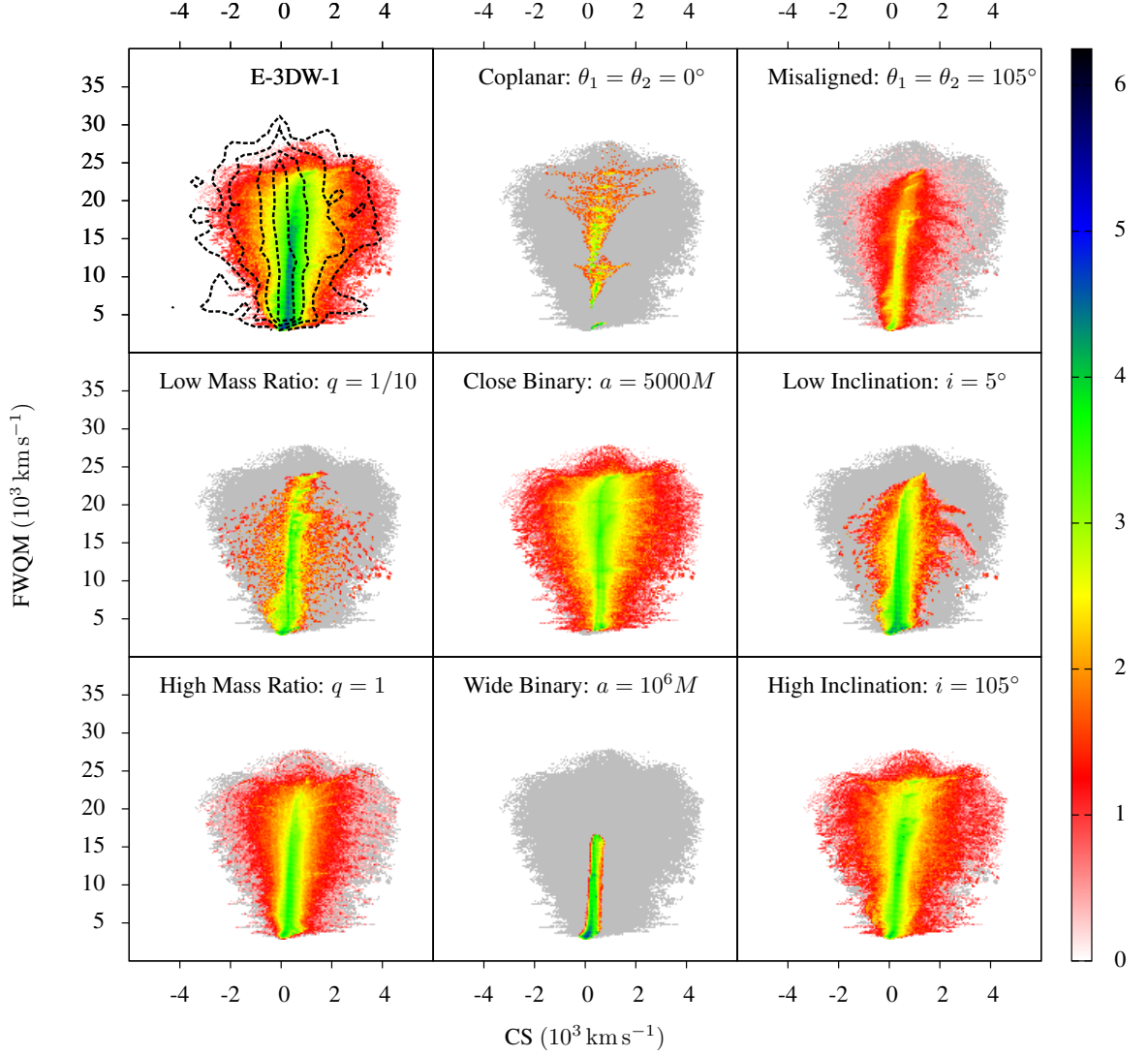


Figure 3.20: Maps of full width at quarter maximum vs. centroid shift (FWQM-CS) for profiles associated with eccentric SBHB systems in model E-3DW-1. Black dashed contours in the top left panel correspond to the FWQM-CS maps in the NW model (as shown in Figure 3.10). The map legend is the same as in Figure 3.19.

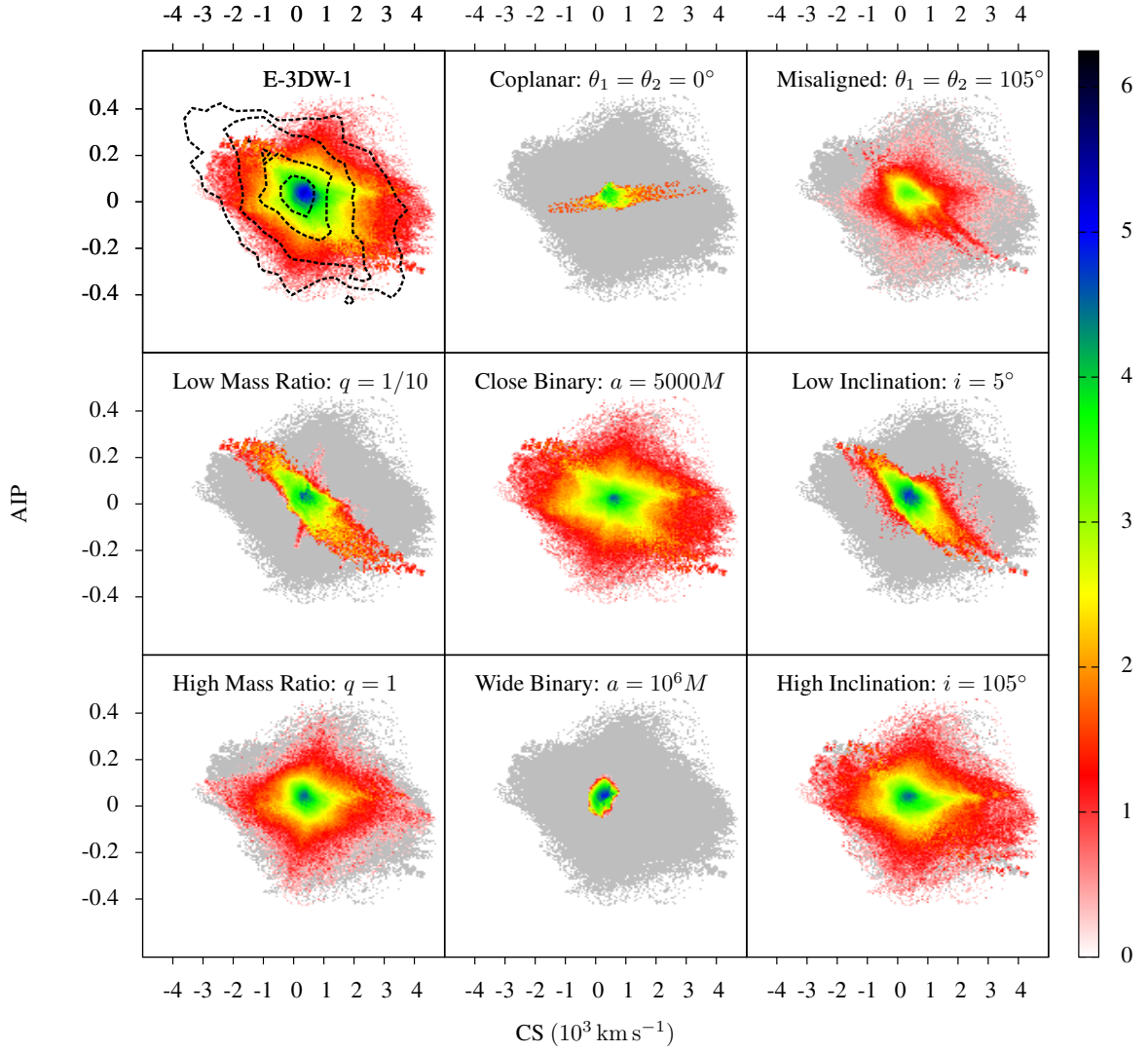


Figure 3.21: Maps of Pearson skewness coefficient vs. centroid shift (AIP-CS) for profiles associated with eccentric SBHB systems in model E-3DW-1. Black dashed contours in the top left panel correspond to the AIP-CS maps in the NW model (as shown in Figure 3.14). The map legend is the same as in Figure 3.19.

of $-0.4 \lesssim \text{AIP} \lesssim 0.4$. In contrast, profiles associated with SBHB systems with different mass ratios ($q = 1/10$ and 1) and different orientations of the binary orbit relative to the observer's LOS ($i = 5^\circ$ and 105°) show significant overlap in their distributions. Similarly to the NW model, these plots indicate that the most important SBHB parameters that determine the degree of asymmetry and the position of the dominant peak in the BEL profile are the intrinsic alignment of the triple disk system and the orbital semimajor axis. The only notable difference between the profile distributions in models E-3DW-1 and NW is that in the former, the systems with low q and i show less asymmetry ($-0.3 \lesssim \text{AIP} \lesssim 0.3$) relative to the NW model ($-0.4 \lesssim \text{AIP} \lesssim 0.4$).

Figure 3.20 shows FWQM-CS maps calculated for BEL profiles in the E-3DW-1 model. As in the NW model the profiles exhibit a wide range of centroid shifts, $|\text{CS}| < 4000 \text{ km s}^{-1}$, and can have broad bases with $\text{FWQM} < 30,000 \text{ km s}^{-1}$. In both models we find that the location of the centroid is a strong function of a in the sense that profiles from close binaries ($a = 5000 M$) can have a significantly wider range of CS values relative to the wide binaries ($a = 10^6 M$). In the E-3DW-1 model the semi-major axis also seems to be the parameter that strongly affects the profile width, since for wide separation binaries $\text{FWQM} < 17,000 \text{ km s}^{-1}$, considerably lower than for the entire sample of profiles. Indeed, we find that on average the profiles in model E-3DW-1 tend to be narrower than their counterparts in the NW model, as a consequence of modification by the disk wind of finite optical depth.

Figure 3.21 shows the AIP-CS projection of the parameter space and the profile shapes in the E-3DW-1 model. Similar to the previous maps, the statistical distributions are a strong function of a , followed by the degree of triple disk alignment marked by the angles θ_1 and θ_2 . This implies that AIP-CS maps calculated based on the second-generation model can still be used as a relatively sensitive diagnostic for these properties. The statistical distributions as a function of q and i are also distinct, so the AIP-CS combination may also be used to constrain these parameters, albeit with a somewhat larger degree of degeneracy.

The maps in the E-3DW-1 model therefore preserve the key features seen in the NW model.

In summary, we find that radiative transfer in the disk wind does affect the overall shape of BEL profiles by making them narrower on average and more symmetric in SBHB systems characterized by low q and i . Despite these differences, all correlations between profile distributions and the SBHB parameters identified in § 3.2 are preserved, indicating that their diagnostic power is not diminished. As before, we find that the shapes of modeled BEL profiles are a sensitive function of the binary orbital separation and the degree of alignment in the triple disk system. The synthetic profiles tend to be less sensitive (or more degenerate with respect) to the SBHB mass ratio and orbital inclination relative to the observer. We furthermore find a large degree of overlap between the models of SBHBs on circular and eccentric orbits and therefore do not expect that the profile shapes alone can be employed as a useful diagnostic of eccentricity. These findings can guide expectations when it comes to the analysis of the spectroscopic SBHB candidates in terms of the diagnostic value and limitations of the BEL profiles.

3.3.4 Discussion: Synthetic BEL profiles in the presence of radiatively driven disk wind

In § 3.3, we have considered the limit when radiation pressure from the two AGNs is capable of driving winds and outflows, which change the effective line optical depth of the emitting gas. As described in § 3.3.1, this results in simpler, mostly single-peaked BEL profiles, which resemble those of observed SBHB candidates and AGNs in general. However, this addition to the model inevitably makes it more complex, as it requires the introduction of new parameters to describe the properties of the accretion disk wind. The primary effect of the increase in the number of parameters is the increased degeneracy in the relationship between the properties of the BEL profiles and the underlying SBHB parameters. We show in § 3.3.3 that the correlations between profile distribution functions and the SBHB parameters identified in the first-generation model are nevertheless preserved, indicating that their diagnostic power is not diminished.

Along similar lines, the calculation of radiative transfer requires several assumptions about the properties of the accretion disk wind. The main one is that the Sobolev approximation is applicable to the accretion disk winds arising in the BLRs of SBHB systems. In this regime the photons that are not absorbed within one Sobolev length from the point of emission (or in the case of a disk, from the emission layer) can escape to infinity, provided that the velocity of the wind projected onto the LOS is monotonically increasing (see § 2.3.2.2). This condition is likely satisfied in regular AGNs, in which accretion disk winds are expected to accelerate radially out [139, 145].

In our model we also make a simplifying assumption that the two mini-disks have the same disk-wind optical depth. It is therefore worth understanding how different the physical conditions can be in the two SBH mini-disks, which tend to contribute most of the flux to the composite $H\beta$ line profile. In our model, which is motivated by hydrodynamic simulations of SBHBs in circumbinary disks, the largest contrast between the SBH mass ratios is $\dot{m} = \dot{M}_2/\dot{M}_1 \approx 5$, for circular binaries with mass ratio $q = 1/10$ (see Equation 3.1). In terms of the Eddington normalized mass ratios this implies $\dot{m}/q \approx 50$. If the emission lines from SBH mini-disks respond to the continuum radiation in the same way as in regular AGNs, the higher relative luminosity of the secondary AGN would result in a lower equivalent width of the $H\beta$ BEL profile contributed by the secondary mini-disk [correlation known as the Baldwin effect; 159]. In the context of our calculation, this implies a reduction in the contribution to the composite $H\beta$ profile from the secondary mini-disk, an effect not captured by our model. The effect is weaker for circular binaries with larger SBH mass ratios and for all eccentric SBHBs, and it disappears in all configurations when $q = 1$.

The geometry and kinematics of radiation driven outflows in SBHB systems are unknown. In the absence of any other constraints we assume that in a binary the disk wind driven by each AGN extends over the entire surface of its BLR and is not affected by the wind from the companion disk. We also assume that the properties of the disk wind (e.g.,

mass density and velocity profile) in each BLR are similar to regular AGNs. If, on the other hand, the outflows from the two mini-disks are interacting and colliding, the velocity field in the wind can become non-monotonic and the local escape probability defined in equation 2.38 would cease to be a good description of radiation transport. One would instead have a more complex distribution of the line optical depth across one or both mini-disks, which would in turn give rise to more complex profiles [142].

It is also not clear whether the outflows can extend from the mini-disks into the circumbinary disk, especially in configurations in which they are not co-planar. In this work we consider configurations in which the circumbinary disk is (a) either not affected by the disk wind (2DW models) or (b) has an accretion disk wind which is radial and axisymmetric, as if driven by a single, central AGN (3DW models). When it comes to the 2DW suite of models, a model which is clearly inconsistent with the observed sample of SBHB candidates (and appears more like regular AGNs) is C-2DW-100, in which the emission from the mini-disks is suppressed due to the high optical depth ($\tau_0 = 100$) and the emission from the circumbinary disk dominates. In the case of the 3DW models, the circumbinary disk affected by a wind makes a negligible contribution to the flux of the composite profile and hence, we do not expect the assumptions in (b) to strongly affect our results.

The dependence on the physical parameters of the SBHB makes the broad BEL profiles a promising diagnostic once a sample of genuine sub-parsec binaries is available. At this point, a comparison of the probability density distributions of modeled profiles with those from observed SBHB candidates (§ 3.3 and 4.1) suggests that, if the observed sample is made up of real binaries, it must include smaller separation SBHBs ($a \ll 10^6 M$) with misaligned disks and high mass ratios. While this is intriguing, a visual comparison of the distributions does not provide conclusive evidence that they overlap or are drawn from some larger, common distribution. We nevertheless perform a simple comparison and find that the shapes of the BEL profiles from a sample of observed SBHB candidates are more consistent with the binary model than are regular AGNs (see § 3.4.5 for more details).

A point worth reiterating is that other physical processes can potentially mimic the emission signatures of SBHBs discussed here. These include but are not limited to the recoiling SBHs [155] and local and global instabilities in single SBH accretion disks that can give rise to transient bright spots and spiral arms [156, 157]. In that sense, the model described in this work can be used to interpret observed BEL profiles in the context of the SBHB model but cannot be used to prove that they originate with genuine SBHB systems. For example, profiles of SBHB candidates observed in multiple epochs can be compared against the synthetic database individually, in order to determine the likelihood distribution for underlying SBHB parameters for each profile independently. The entire time series of observed profiles can also be compared against the time series of matching modeled profiles as an added consistency check for the inferred SBHB parameters. We defer this type of analysis to Chapter 4.

3.4 Implications for Observational Searches

3.4.1 Comparison with SBHB candidates

In this section we compare the database of modeled profiles to the emission lines observed and published as a part of the E12 search for SBHBs. The E12 campaign searched for $z < 0.7$ SDSS³ AGNs with broad $H\beta$ lines offset from the rest frame of the host galaxy by $\gtrsim 1000 \text{ km s}^{-1}$. Based on this criterion, E12 selected 88 quasars for observational followup from an initial group of about 16,000 objects. The followup observations span a temporal baseline from few weeks to 12 years in the observer’s frame. Their goal is to measure the epoch-to-epoch modulation in the velocity offset of the $H\beta$ profiles and to test the binarity hypothesis by ruling out any sources in which this modulation is not consistent with the SBHB orbital motion. After multiple epochs of followup, statistically significant changes in the velocity offset have been measured in 29/88 candidates and reported in the publications mentioned above. At present time, this approach has highlighted several promising

³Sloan Digital Sky Survey

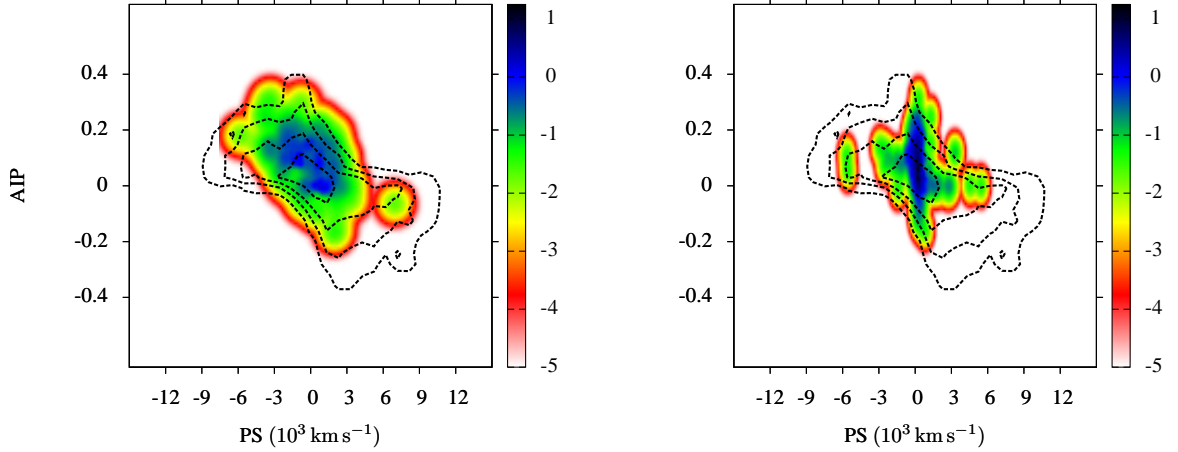


Figure 3.22: AIP-PS maps for profiles associated with the observed SBHB candidates (left) and a control sample of matching AGNs (right) from the E12 search. The maps were adaptively smoothed, normalized to the same profile number and dynamic range as in Figure 3.19, in order to facilitate direct visual comparison. Color bar indicates the normalized density of profiles plotted on the log scale. Black dashed contours correspond to the AIP-CS map in Figure 3.19 and are drawn in increments of one, from 0.5 (outermost) to 3.5 (innermost).

cases for further followup but has not yet allowed to rule out the SBHB hypothesis for any candidates.

We use a data set of broad optical emission lines (drawn from the E12 data set), which at the time of this analysis included 330 multi-epoch spectra of 88 SBHB candidates and 527 spectra for a control sample of 212 matching regular (non-binary) AGNs with similar redshifts and luminosities [see 158, for description of the candidate and control sample]. Figures 3.22, 3.23, and 3.24 show the distribution of these profiles in the AIP-PS, FWQM-CS, and AIP-CS maps respectively. Because the observed samples of SBHB candidates and regular AGNs contain only a few hundred profiles each, we perform adaptive smoothing of the maps, in order to present them in the the same form as the synthetic data (i.e., as a continuous distribution) that facilitates direct visual comparison. Specifically, the smoothing has been carried out using a two-dimensional (elliptical) Gaussian function with the width scaled linearly with the profile density from 1/10 to 1/3 of the standard deviation of the relevant parameter. These maps can be compared to the corresponding maps for modeled BEL profiles in Figures 3.19, 3.20, and 3.21. For easier visual comparison, we also

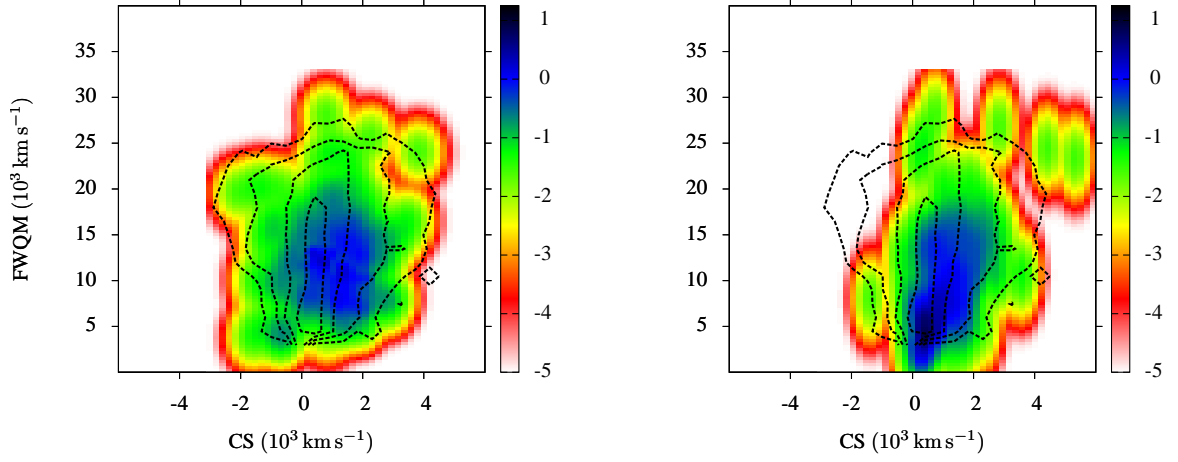


Figure 3.23: FWQM-CS maps for profiles associated with the observed SBHB candidates (left) and a control sample of matching AGNs (right) from the E12 search. Color bar indicates the normalized density of profiles plotted on the log scale. Black dashed contours correspond to the FWQM-CS map in Figure 3.20 and are drawn in increments of one, from 0.5 (outermost) to 3.5 (innermost).

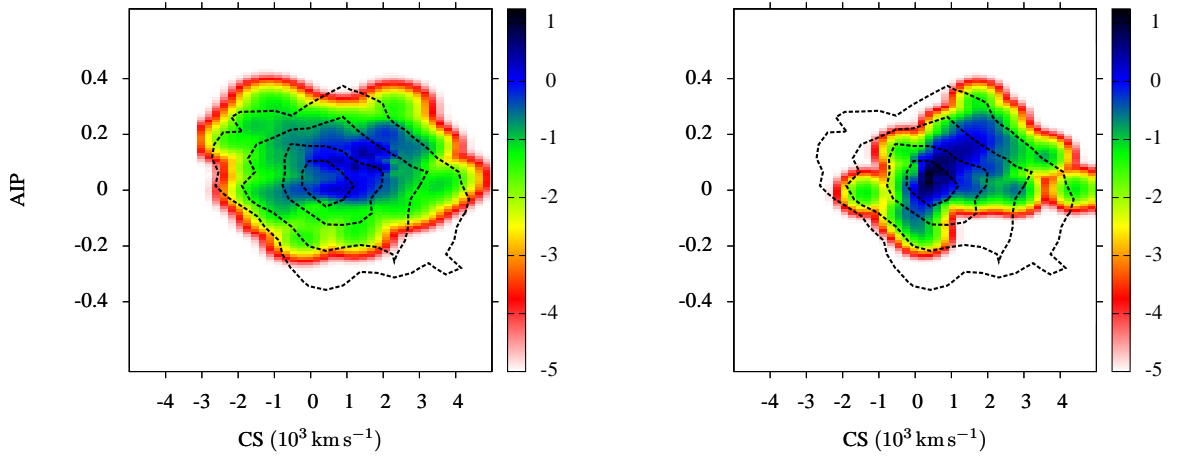


Figure 3.24: AIP-CS maps for profiles associated with the observed SBHB candidates (left) and a control sample of matching AGNs (right) from the E12 search. Color bar indicates the normalized density of profiles plotted on the log scale. Black dashed contours correspond to the AIP-CS map in Figure 3.21 and are drawn in increments of one, from 0.5 (outermost) to 3.5 (innermost).

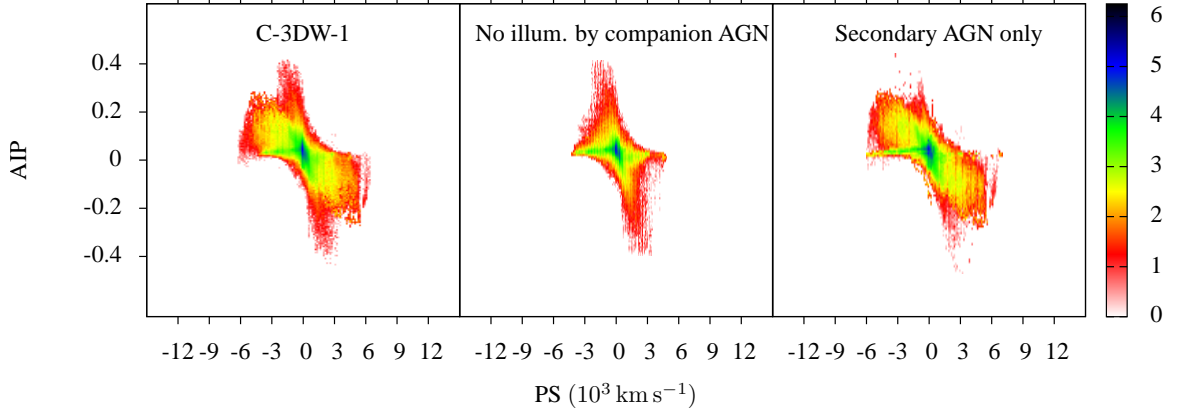


Figure 3.25: AIP-CS maps for the emission-line profiles in the C-3DW-1 model (*left*), the scenario in which each AGN is only allowed to illuminate its own mini-disk but not that of the companion SBH (*middle*), and in the scenario in which only the AGN associated with the secondary SBH illuminates all three disks, and the primary AGN is assigned zero luminosity (*right*). Color bar indicates the density of profiles plotted on a log scale.

overplot the contours representing these distributions in Figures 3.22, 3.23, and 3.24.

For example, inspection of the AIP-PS maps for the observed SBHB candidates and the sample of modeled profiles suggests that both exhibit a negative linear correlation in this projection of the parameter space (i.e., the blue leaning profiles have blueshifted peaks and vice versa). It also follows that, if the observed sample consists of genuine binaries, it must include smaller separation SBHBs ($a \ll 10^6 M$) with misaligned disks. The control sample of AGNs, shown in the right panel of Figure 3.22, on the other hand, does not show such a correlation between the profile asymmetry and peak location and is characterized by profiles with peaks that are predominantly centered on the rest frame of the host galaxy.

A comparison of the FWQM-CS maps in Figures 3.20 and 3.23 reveals that the observed SBHB candidates and the synthetic sample both contain a large fraction of profiles with a relatively broad base, characterized by $\text{FWQM} \geq 5000 \text{ km s}^{-1}$. At the same time, most of the profiles in the control sample of AGNs reside at much lower values of FWQM. Figure 3.23 also shows that a majority of the SBHB candidates and regular AGNs possess positive CS values, representing profiles with centroids redshifted relative to the frame of the host galaxy by $\sim 1000 \text{ km s}^{-1}$, on average. This prevalence of centroid redshift is

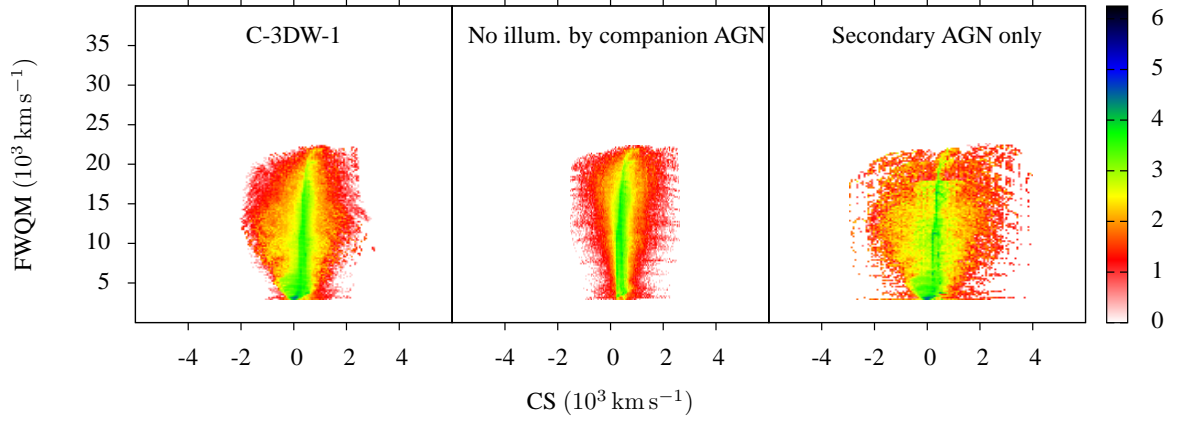


Figure 3.26: FWQM-CS maps with the same legend as in Figure 3.25.

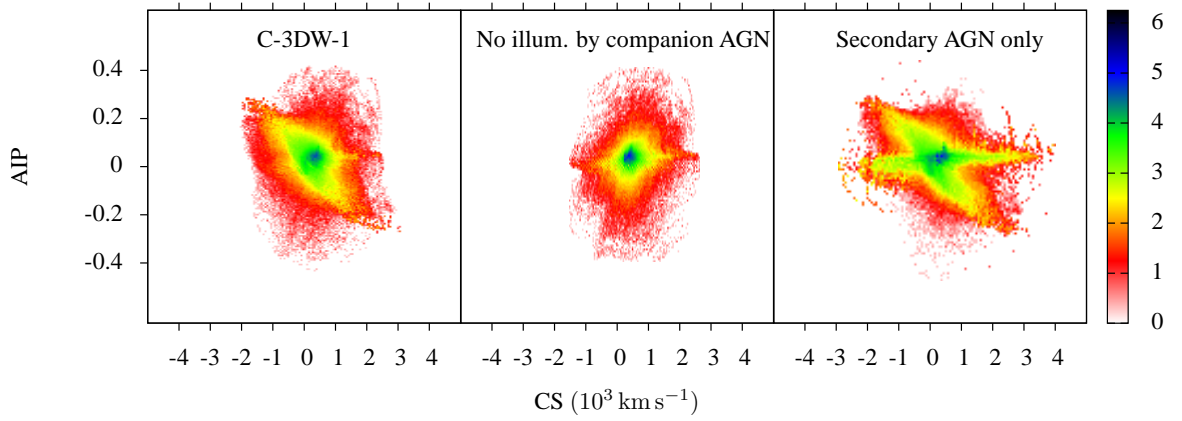


Figure 3.27: AIP-CS maps with the same legend as in Figure 3.25.

also present in the synthetic dataset but the average centroid shift is somewhat smaller for modeled profiles. Figure 3.24 shows that a majority of the SBHB candidates and regular AGNs possess emission lines with positive CS and AIP values, indicating preferentially blue leaning, asymmetric profiles with redshifted centroids. In the case of the candidate SBHBs only, the blue leaning profiles with redshifted centroids also tend to have blueshifted peaks (see Figure 3.22), and they account for about 30% of the synthetic database. In general, we find this combination of properties in profiles in which relativistic Doppler boosting plays a role. A visual comparison of the AIP-CS maps for the observed SBHB candidates and the sample of modeled profiles suggests that, if the observed sample comprises real binaries, it must include compact SBHBs ($a \ll 10^6 M$) with misaligned disks and high mass ratios, as well as the systems with high orbital inclinations relative to the observer’s LOS.

3.4.2 Importance of illumination by two active black holes (AGNs)

All BEL profiles presented in this work have been calculated assuming that both accreting SBHBs can shine as AGNs and illuminate their own mini-disk as well as the two other disks in the system (see § 2.2). The effect of illumination of one mini-disk by a companion AGN is most pronounced in binaries when their mini-disks are misaligned with the SBHB orbital plane. This geometry allows the companion AGN to effectively illuminate the mini-disk of its neighbor at relatively large incidence angles ($\gtrsim 30^\circ$). As a consequence, in some configurations, the incident flux from the companion AGN on the mini-disk can be several times higher than that of its resident AGN. As pointed out in the NW model, illumination of the triple-disk BLR by two AGNs can give rise to very asymmetric profiles, with significant peak or centroid velocity shifts. These characteristics are preserved in the improved model with accretion disk wind presented in here in this section. All statistical distributions shown in both models are sensitive functions of the SBHB orbital separation and disk alignment.

Because they require a certain degree of geometric misalignment of the mini-disks, the effects of illumination by two AGNs are less ubiquitous (i.e., they affect the shapes of a

smaller number of profiles in our database) than the effects on the BEL photons from the accretion disk wind. When present however, illumination by two AGNs tends to modify the profile shapes more dramatically than the line-driven winds. This point is illustrated in Figures 3.25, 3.26 and 3.27, which compare the AIP-PS, FWQM-CS and AIP-CS statistical distributions for three different illumination scenarios, respectively. The scenario involving illumination by two AGNs is represented by the C-3DW-1 model, shown in the first panel of all three figures. The second panel illustrates the model in which each AGN is only allowed to illuminate its own mini-disk (but not that of the companion SBH) and both AGNs illuminate the circumbinary disk. The last panel shows the distribution of profiles in the scenario in which only the AGN associated with the secondary SBH illuminates all three disks, and the primary AGN is assigned zero luminosity. The last scenario is of interest for E12 and other spectroscopic searches for binaries, which adopt in their interpretation of the data an assumption that the AGN associated with the secondary SBH is more luminous and outshines the primary.

3.4.3 Temporal variability of the modeled line profiles

In our model temporal variability of the emission lines can arise on the orbital time scale when profile modulation is associated with the orbital motion of the SBH mini-disks and/or with the changing illumination pattern by two AGNs. Alternatively, profile variability can arise on time scales different from the orbital time scale if it is associated with the change in optical depth of the wind along the LOS. While we do not explicitly model different temporal sequences for profiles with varying τ_0 , they can be created by choosing the appropriate SBHB and wind optical depth configurations from the synthetic database. The first panel of Figure 3.28 shows 20 orbital phases within one orbital cycle of an SBHB system with $q = 0.1$ and remaining parameters as shown in the caption. Red dots trace the modulation of the BEL profile associated with the orbital motion of the primary SBH and the blue dots trace the secondary. An important assumption made in the calculation

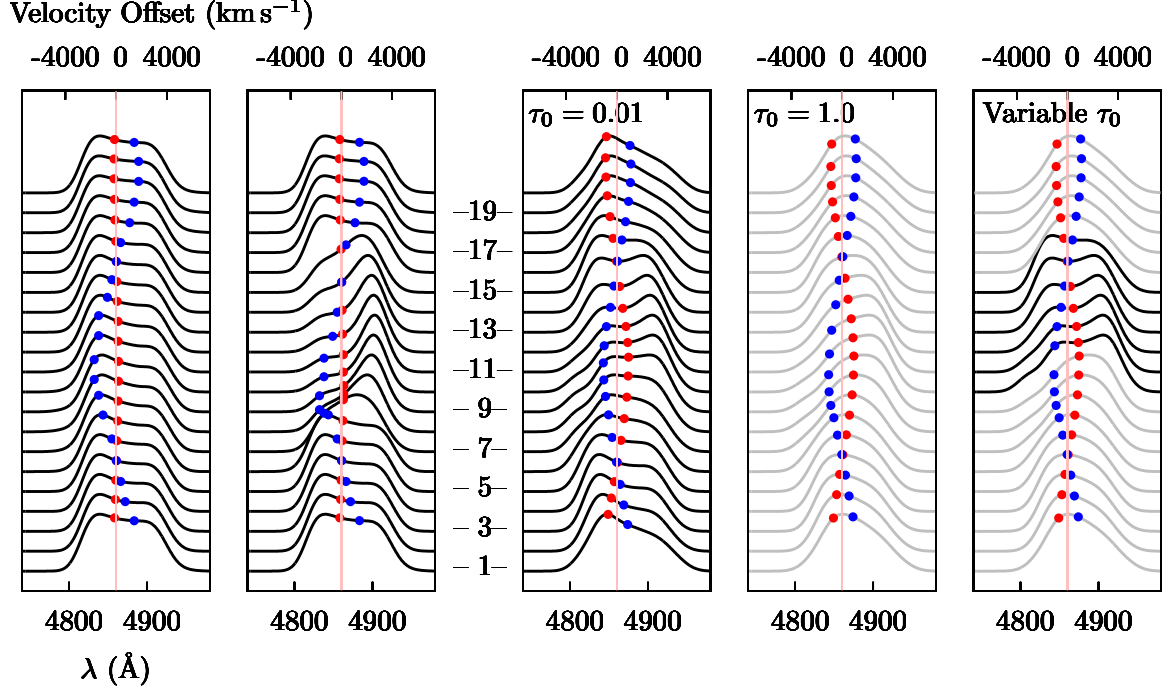


Figure 3.28: Temporal evolution of profile shapes over one orbital cycle for an SBHB with $q = 1/10$ (panels 1 and 2 from the left) and $q = 9/11$ (panels 3, 4 and 5 from the left). Red (blue) dots trace the velocity curve of the primary (secondary) SBH. *Panel 1*: Profiles calculated for $\tau_0 = 0.01$ under the assumption that each AGN can only illuminate its own mini-disk and both AGNs illuminate the circumbinary disk. *Panel 2*: Profiles calculated for $\tau_0 = 0.01$ under the (default) assumption that all three disks are illuminated by two AGNs. *Panel 3*: Profiles calculated for $\tau_0 = 0.01$. *Panel 4*: Profiles calculated for $\tau_0 = 1.0$. *Panel 5*: Profiles calculated for optical depth $\tau_0 = 0.01$ for orbital phases 10–15 and for $\tau_0 = 1.0$ in all other phases. Other parameters shared by all profiles in this figure are: $a = 2500 M$, $e = 0.0$, $R_{in1} = 500 M_1$, $R_{in2} = 500 M_2$, $i = 20^\circ$, $\phi = 50^\circ$, $\theta_1 = 15^\circ$, $\theta_2 = 160^\circ$, $\phi_1 = 0^\circ$, $\phi_2 = 180^\circ$. The phases 1–20 are equally spaced and phase 1 (20) corresponds to $f = 0^\circ$ (342°).

of these profiles is that each AGN can only illuminate its own mini-disk and both AGNs illuminate the circumbinary disk, a scenario presented in § 3.4.2. In this case, there are no significant changes to the shape or width of the composite profile and the wavelength shift is relatively small and invisible to the eye. This can be understood because at $q = 0.1$ the emission from the mini-disk of the primary SBH dominates over the mini-disk of the secondary, since the ratio of their fluxes scales as $F_2/F_1 \propto q^2$ (see Equation 2.28). Note that the primary mini-disk dominates even if one accounts for the inversion of accretion rates in unequal mass binaries, where accretion is expected to occur preferentially onto the smaller of the SBHs. Specifically, in the $q = 0.1$ configuration considered above, the accretion rate onto the secondary SBH is ~ 5 times higher than that of the primary⁴. Therefore, even though the more luminous secondary AGN in our model boosts the flux ratio by a factor of ~ 5 , this is still insufficient for the secondary BLR to outshine the primary BLR in the Balmer lines. At the same time, the contribution to the profile flux from the circumbinary disk is negligible in a majority of configurations in our model, as illustrated in Figure 3.18.

The second panel of Figure 3.28 shows BEL profiles associated with the same SBHB configuration but in this case, illumination of all three disks by both AGNs is allowed. Note that this is a default assumption used in the calculation of all profiles in our database of modeled profiles. Because this system consists of misaligned mini-disks (as indicated by the angles θ_1 and θ_2), the geometry of the system allows for illumination of the primary BLR by the secondary AGN. This effect leads to a significant change in the profile shape over the limited portion of the orbital cycle, in phases 7–15. Therefore, even though the contribution to the line flux from the secondary BLR is negligible, the illumination by the secondary AGN is not. As a result, the spectroscopic signatures of SBHBs in circumbinary disks might be unique even when their mass ratio is very low.

The remaining three panels of Figure 3.28 show different phases of the same SBHB configuration with $q = 9/11$. The effect of illumination by both AGNs is accounted for

⁴See Equation 3.1 for the description of the SBHB accretion rate ratio.

in all profiles shown in these three panels. This system is representative of SBHBs with $q \sim 1$, surrounded by mini-disks that make comparable contributions to the composite BEL profile. Because of their individual modulation in wavelength over time (indicated by the red and blue dots), the composite profile varies in both shape and width throughout the orbital cycle, but exhibits insignificant shift with respect to the rest frame of the host galaxy. To illustrate the effect of the optical depth on the profile shapes in this scenario we show the emission lines calculated for $\tau_0 = 0.01$ and 1.0 in the third and fourth panels, respectively. The primary effect of the increased optical depth in the disk wind is a transformation from a broader and occasionally double-peaked BEL profile into a smoother and narrower single-peaked profile.

To emulate a variable optical depth, in the fifth panel we show the profiles calculated for $\tau_0 = 0.01$ in phases 10–15 and the remaining profiles corresponding to the higher optical depth. Note that similar changes have been seen in the broad Balmer emission lines of some AGNs that are not SBHB candidates, which have been observed to fluctuate between a double-peaked and a single-peaked profile: NGC 5548 [160–162], Pictor A [163, 164], and Ark 120 [165, 166]. The disk-wind with changing optical depth has been suggested as a viable explanation for the appearance of these sources [134].

In summary, we find that orbital modulation in a binary with small q , in which both black holes are shining as AGN, results in smaller radial velocity offsets of the BEL profiles, determined by the velocity curve of the primary. Equal mass binaries exhibit no radial velocity offsets in binary AGN systems due to symmetry but their profiles show plenty of variation in shape on the orbital time scale. The disk wind has a weak impact on the radial velocity offsets or profile variability and its main effect is to make the profiles smoother and single-peaked. The most dramatic variations in shape are caused by illumination of one mini-disk by a companion AGN. The properties of the profile that show the biggest changes are the asymmetry (AIP) and peak shift (PS), whereas FWHM is not so strongly impacted. The effect is only noticeable over a fraction of the orbital cycle, suggesting that

if present in real SBHBs, only a fraction of binaries should be affected by it at any given time.

3.4.4 Implications for the observed variable profiles

The configuration in the fourth panel of Figure 3.28 is chosen to mimic the variability of the $H\beta$ profiles observed in NGC 5548 [see Figure 5 of 114], which has been proposed as a nearby SBHB candidate with an orbital period of 14–16 years [see also 108]. This orbital period corresponds to a $10^8 M_\odot$ SBHB with an orbital separation close to $2500 M$, similar to the example shown here. It is worth noting that this apparent similarity in profile shapes does not provide a proof of binarity for NGC 5548, because it does not rule out other non-SBHB mechanisms, which in principle may produce a similar sequence of profiles. However, should the binary hypothesis for NGC 5548 be confirmed, our model suggests that this is likely to be an SBHB with $q \sim 1$ and misaligned mini-disks, which allow for the changing illumination by the two AGNs.

The BEL profiles that exhibit significant change in their shapes from one epoch of observation to another, similar to those shown for the high mass ratio SBHB in Figure 3.28, represent a practical challenge for the spectroscopic searches for SBHBs which seek to measure the wavelength shift of the entire profile. As discussed in publications reporting on the E12 search, evolution of profile shape makes it very difficult to discern the shift of the bulk of the profile, as the former may mimic the latter. For example, Runnoe et al. [158] report reliable and statistically significant measurements of radial velocity changes in 29/88 SBHB candidates, which exhibit no variability in the shape of the broad $H\beta$ profile over the length of the monitoring campaign. In this context, E12 hypothesize that these 29 profiles correspond to the SBHB systems, where the mini-disk of the secondary SBH is the dominant contributor to the $H\beta$ line flux⁵ and as a result, the composite profile does not

⁵The SBHB interpretation adopted by E12 and other spectroscopic searches also leaves room for the primary mini-disk to be the dominant contributor to the emission line, given a binary with the mass larger by a factor q^{-3} .

change in shape or width over the observed portion of the orbital cycle.

In the context of our model the 29 candidates with relatively stable profile shapes may correspond to configurations in which the evolution of the profile shapes is slower and is not discernible on the monitoring time scale of few to ten years. This may indicate a longer period binary (with orbital period of a few hundred years) or a system where either the primary or the secondary BLR dominate the BEL flux over some fraction of the orbit. Since this behavior is consistent with a relatively diverse set of SBHB configurations in our model we cannot make more detailed inferences about the corresponding orbital separations and mass ratios.

Furthermore, 49/88 SBHB candidates in the E12 sample are characterized by variable profiles which preclude the radial velocity measurements, and the rest show no measurable radial velocity changes. By implication, the 49 candidates with variable profile shapes are consistent with $q > 0.1$ configurations modeled in this work, and with small separation binaries ($a \lesssim 10^4 M$) with misaligned disks, in which changing illumination by the two AGNs plays an important role over the observed portion of the orbit.

3.4.5 Quantitative comparison of modeled emission-line profiles to the observed profiles

This test is not straightforward to carry out due to several differences in the way the synthetic and observed samples were constructed. Firstly, in the synthetic sample we choose uniform distributions of the SBHB parameters (shown in Table 3.1) in order to obtain a uniform but not necessarily dense coverage of the SBHB parameter space. We prefer this agnostic approach to modeling because the distribution functions for various SBHB parameters are still not well constrained. Something that can be expected with a reasonable level of confidence however is that the mass ratios and orbital separations of the observed set of SBHBs are not uniformly distributed. Moreover, the fact that our database has finite size inevitably means that we are not capturing all profile shapes that an SBHBs in circumbinary disks might have. Consequently, the statistical distribution functions for simulated profiles

in Figures 3.19 – 3.21 and those for the observed sample shown in Figures 3.22 – 3.24, may share some subset of profiles but they are not drawn from the same parent distribution, and in the case of the synthetic profiles, not in a random way.

Secondly, the observed SBHB candidates have been selected based on a few more criteria, which we do not apply to the modeled profiles. Specifically, the SBHB candidates selected for further monitoring by E12 have the broad component of the BEL profile offset by $\gtrsim 1000 \text{ km s}^{-1}$, a practical requirement that makes it easier to separate the broad and narrow components of the line during the analysis. Our database however includes profiles with all values of velocity offsets, including those with $< 1000 \text{ km s}^{-1}$. Similarly, E12 only choose for followup candidates with the $\text{H}\beta$ BEL profiles which in the first epoch of observation appear single-peaked *before* subtraction of the narrow $\text{H}\beta$ and $[\text{O III}]$ lines. Since we only model the emission from the BLR, we cannot predict the appearance of the profiles with superimposed narrow-line emission. We instead compare our modeled profiles directly to the broad-line component of the observed $\text{H}\beta$ profiles [see 113, for discussion of a method for subtraction of the narrow lines.]. These differences preclude us from carrying out an apples-to-apples comparison of the modeled and observed line profiles at this point.

We can nevertheless perform a relative comparison by asking: are the modeled profiles more similar to the profiles of SBHB candidates or the control sample of regular AGN? For this test we design a following simple statistic

$$\mathcal{R}_{x-y} = \frac{\sum_i \sum_j (P_{\text{SBHB}}(x_i, y_j) - P_{\text{mod}}(x_i, y_j))^2}{\sum_i \sum_j (P_{\text{AGN}}(x_i, y_j) - P_{\text{mod}}(x_i, y_j))^2} \quad (3.12)$$

where P_{mod} , P_{SBHB} , and P_{AGN} represent the two-dimensional probability distributions of profiles drawn from the modeled, the SBHB candidate, and the regular AGN sample, respectively. Each distribution represents the probability of finding a profile in a given “pixel” of a discretized two-dimensional map, for which coordinates (x_i, y_j) mark the center of the pixel with the width Δx and Δy . For the purpose of this comparison we choose the size of each pixel to be a hundredth of the full numerical range of a distribution, i.e.

Table 3.4. Comparison of Observed and Modeled Datasets

$x - y$	\mathcal{R}_{x-y}	$x - y$	\mathcal{R}_{x-y}
AIP-PS*	0.20	KI-CS	0.55
FWHM-C	0.32	AIP-CS*	0.63
FWQM-CS*	0.34	KI- σ_2	0.79
FWHM-AI	0.40	KI-AI	0.90
FWHM-AIP	0.45	AIP- σ_2	0.94

Note. — AIP - Pearson skewness coefficient. PS - Peak shift. FWHM, FWQM - Full width at half and quarter maximum, respectively. C - Location of the centroid. CS - Centroid shift. AI - Asymmetry index. KI - Kurtosis index. σ_2 - Second moment. * Marks distributions presented in this work.

$\Delta x = (x_{\max} - x_{\min}) / 100$. We have confirmed that this choice does not affect the value of \mathcal{R}_{x-y} by comparing the smoothed distributions of the observed and modeled profiles for a variety of grid sizes, ranging from 25×25 to 1000×1000 . Defined in this way \mathcal{R}_{x-y} becomes a simple test of similarity in the overall shape of the two-dimensional distributions, without any a priory assumptions about their origin.

Table 3.4 shows \mathcal{R}_{x-y} values calculated for different profile shape parameters commonly used to analyze the BEL profiles (see § 3.2.2 for their definitions). The synthetic profiles used in calculation of \mathcal{R}_{x-y} are drawn from the model C-3DW-100. In order to mimic the selection process of the E12 search as closely as possible, before calculating P_{mod} we remove profiles with peak shifts $< 1000 \text{ km s}^{-1}$ and those that have more than one peak from the modeled sample. In this statistic, $\mathcal{R}_{x-y} = 0$ when the probability distribution of the SBHB candidates is precisely matching that of the modeled profiles. The values of $\mathcal{R}_{x-y} < 1$ correspond to a higher degree of similarity between the modeled and SBHB candidate profiles than the modeled and regular AGN profiles. Conversely, $\mathcal{R}_{x-y} > 1$ indi-

cates a higher degree of similarity between the modeled and regular AGN profiles than the modeled and candidate SBHB profiles.

As it can be seen from Table 3.4, $\mathcal{R}_{x-y} < 1$ for all statistical distribution pairs, where we mark with an asterisk the pairs presented in Figures throughout this work. It is worth noting that the distributions that we have a priori identified as more robust, because they measure the dominant features in the bulk of the profile (AIP, PS, CS similar to C, FWHM similar to FWQM), favor similarity between the observed SBHB candidate and modeled profiles. On the other hand, higher moments of the profile flux distribution, which tend to be more easily affected by the noise (σ_2 , AI, KI), on average result in higher values of \mathcal{R}_{x-y} . This simple comparison therefore seems to support the hypothesis that the shapes of the BEL profiles from a sample of observed SBHB candidates are more consistent with the binary model than are regular AGNs.

A related pertinent question is: *how large an observed SBHB sample should be for a meaningful statistical comparison between the observed and synthetic profiles?* Since 2D profile distributions, like AIP-PS shown in the top left panel of Figure 3.19, are described by their shape and dynamic range (illustrated by color), we want to find the minimum number of profiles needed to represent the shape and colors of this distribution. The AIP-PS distribution shown in the top left panel of Figure 3.19 has $N = 12$ million profiles and spans a dynamic range of 6 orders of magnitude. We use the Cochran's formula [167] to estimate a sample size large enough so that there is a finite number of profiles within the yellow (or red, or green) color region of the figure with 95% confidence.

$$n = \frac{Nn_0}{N + n_0 - 1} \quad \text{and} \quad n_0 = \frac{Z^2 P(1 - P)}{e^2} . \quad (3.13)$$

Here n and N are the sizes of the sample and the entire population, respectively. The parameter n_0 asymptotes to n in the limit when N approaches infinity. P is a proportion of the profiles with the relevant attribute (color) in the population. Since we want to draw

profiles that represent the yellow color region of the distribution, we estimate $P_{\text{yellow}} \approx 10^{2.5}/10^6 = 10^{-3.5}$, where the exponents 2.5 and 6 correspond to the values on the color bar. Z represents the number of standard deviations away from the expected proportion P_{yellow} in a normal distribution (also often referred to as “sigma”). For example, 95% confidence level corresponds to $Z = 1.96 \approx 2$. The parameter e determines the margin of error, so that the sample will have some fraction of profiles in the yellow region, within the range $[P_{\text{yellow}} \pm e]$. Since the value of P_{yellow} is small, we can choose $e = P_{\text{yellow}}$, so that the fraction of profiles in the sample drawn from the yellow region is in the range from 0 to $2P_{\text{yellow}}$.

With these values, we can estimate that the sample size of profiles, required to meaningfully reproduce the distribution of profiles in Figure 3.19, down to at least the green, yellow, red contour region, is approximately $n_{\text{green}} \sim 10^3$, $n_{\text{yellow}} \sim 10^4$ and $n_{\text{red}} \sim 10^5$, respectively. In the context of comparisons carried out in this work, these numbers can be interpreted as the minimum number of observed spectra necessary to compare the distributions of the observed and synthetic profiles. As described in paragraph 2 of § 3.4, at the time of this analysis we used 330 spectra of SBHB candidates, and 527 spectra of control sample AGNs. These numbers indicate that at present time a comparison can be made at the level of the blue and green contour regions in Figure 3.19, with a confidence level of only $Z \approx 1$ (or about 60 – 70%). Future surveys are however expected to increase the number of AGN spectra (and spectra time series) by 1 – 2 orders of magnitude, so we anticipate that our models will be useful beyond the comparison with the current data. Similar analysis applies to the remaining profile distributions. We defer a more detailed comparison of individual profiles of SBHB candidates with the synthetic database to the next Chapter 4.

CHAPTER 4

PROPERTIES OF BINARY CANDIDATES IN THE CONTEXT OF THE SBHB MODEL

In this chapter, we present a method for comparison of the modeled and observed optical BELs, based on the principal component analysis, and use it to infer the properties of 88 SBHB candidates from the E12 spectroscopic search. The new aspect of this method is that in addition to the parameter estimates it also provides a quantitative measure of the parameter degeneracy, thus allowing to establish uncertainties intrinsic to such measurements. This chapter is organized as follows. We describe the method used to infer physical parameters for the observed SBHB candidates in § 4.1 and present the results for individual SBHB candidates and the entire sample in § 4.2. In § 4.3, we discuss the implications of these results along with the limitations of our method.

4.1 Methods

4.1.1 Description of the database of modeled and observed emission-line profiles

Based on the analysis of the modeled profile database presented in the previous chapters, we have found that radiative transfer in the disk wind affects the overall shape of BEL profiles by making them narrower on average and more symmetric in SBHB systems characterized by low q and i . The shapes of modeled BEL profiles are a sensitive function of the binary orbital separation and the degree of alignment in the triple-disk system but tend to be less sensitive (or more degenerate with respect) to the SBHB mass ratio and orbital inclination relative to the observer. Because there is a large degree of overlap between the models of SBHBs on circular and eccentric orbits, we do not expect that the profile shapes alone can be employed as a useful diagnostic of eccentricity. These earlier findings guide our

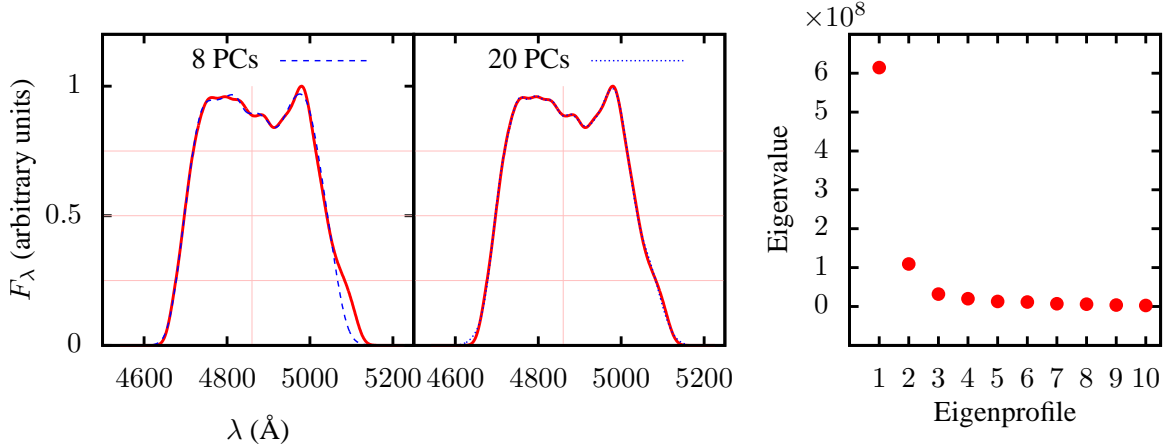


Figure 4.1: Illustration of the reconstruction of a profile from the modeled database (marked by the red solid line) using principal component analysis. The left panel shows reconstruction of the profile using the first 8 and the first 20 principal components (blue dashed and dotted lines, respectively). The right panel shows the variance of the modeled database along each principal axis, given by the eigenvalues, as a function of the order of the eigenprofile. Even though the first 8 principal components represent more than 98 percent of the total variance of the modeled database, a reliable reconstruction of more complex profiles, like the one shown, requires about 20 principal components.

expectations, in terms of the diagnostic power of the BEL profiles and degeneracy of the SBHB parameters, as we set out to quantify them in this work.

We compare the database of modeled profiles to the emission lines observed and published as a part of the E12 search for sub-parsec SBHBs. The E12 campaign searched for $z < 0.7$ Sloan Digital Sky Survey AGNs with broad $H\beta$ lines offset from the rest frame of the host galaxy by $\gtrsim 1000 \text{ km s}^{-1}$. Based on this criterion, E12 selected 88 quasars for observational follow-up from an initial group of about 15,900 objects. The follow-up observations span a temporal baseline from a few weeks to 12 yr in the observer’s frame. Their goal is to measure the epoch-to-epoch modulation in the velocity offset of the $H\beta$ profiles and to test the binarity hypothesis by ruling out any sources whose radial velocity curve is not consistent with the SBHB orbital motion.

After multiple epochs of follow-up, statistically significant changes in the velocity offset have been measured in 29/88 candidates and reported by the E12 campaign. At the present time, this approach has highlighted several promising cases for further follow-up

but has not yet allowed to rule out the SBHB hypothesis for any candidates. We use a data set of broad optical emission lines (drawn from the E12 data set), which at the time of this analysis included 330 multi-epoch spectra of 88 SBHB candidates and 527 spectra for a control sample of 212 matching regular (nonbinary) AGNs with similar redshifts and luminosities [see 113, for detailed description of the SBHB candidate sample as well as the control sample].

4.1.2 Comparison of the modeled and observed samples using the principal component analysis

The analysis carried out in previous chapters has unambiguously shown that SBHB properties are imprinted in the population of the modeled BEL profiles, albeit with some degeneracy. It has also provided a statistical statement about the collective properties of the observed SBHB candidate sample but did not provide the means to determine the parameters of individual binary candidates. We have therefore developed a method, based on the principal component analysis (PCA), which allows to infer the properties of individual SBHB candidates, as well as to quantify the uncertainties associated with those determinations.

PCA allows decomposition of a dataset into a number of linearly independent principal components, or eigenvectors. This technique is optimal for analysis of large and complex data sets, which cannot be inspected manually. For example, [91] extended the application of this technique to spectra of 9,800 SDSS quasars with the goal to identify outliers among them. The same method has been used to flag the SBHB candidates for observational followup from the spectra of $\sim 15,900$ SDSS quasars in the E12 sample. In this work, we use PCA to decompose the sample of modeled and observed BEL profiles using the same basis of eigenvectors, and to reveal the portion of the parameter space favored by the SBHB candidates, by performing a comparison of the two samples within the basis defined by the PCA eigenvectors.

In the case of a sample that consists of BEL profiles, the eigenvectors are represented by eigenprofiles. The eigenvalue that corresponds to each eigenprofile is a measure of the relative importance of that eigenvector in accounting for the variance within the sample. In this scheme, the highest weight goes to the defining features, present in the majority of the profile sample and lower weight goes to the features in which noise or a unique profile characteristic dominates. This procedure is illustrated in Figure 4.1, which shows reconstruction of one of the more complex BEL profiles selected from our database.

A large majority of BELs in our database have simpler profiles and can be successfully reconstructed with only 8 principal components. This is a reflection of the fact that the first 8 principal components represent more than 98 percent of the total variance of the modeled database. In the case of the profile shown in Figure 4.1, the first eight principal components do not fully describe the profile features, and a faithful reconstruction of this profile (and other profiles of similar complexity) requires at least about 20 principal components. Consequently, we choose the first 20 principal components to ensure that we can accurately describe all synthetic profiles in our database. The same set of eigenprofiles used for description of the synthetic database is then used to describe the profiles in the observed SBHB candidate sample and the control sample of AGNs.

Having defined a common set of basis vectors for both datasets, we use it to compare the modeled and observed profiles by calculating their Euclidean distance in the space of 20 principal components. We define a distance from a given observed profile (\mathbf{F}^o) to an arbitrary profile in the synthetic database (\mathbf{F}^s) as

$$d(\mathbf{F}^s, \mathbf{F}^o) = \left[\sum_{i=1}^{20} (T_i^s - T_i^o)^2 \right]^{1/2} \quad (4.1)$$

Here, \mathbf{F}^o and \mathbf{F}^s are vectors of size $[1 \times M]$ and $M = 600$ is the number of equal frequency bins used to describe each profile. \mathbf{T}^s and \mathbf{T}^o are the principal components associated with each profile, respectively (see Appendix E). We rank all synthetic profiles in terms of their

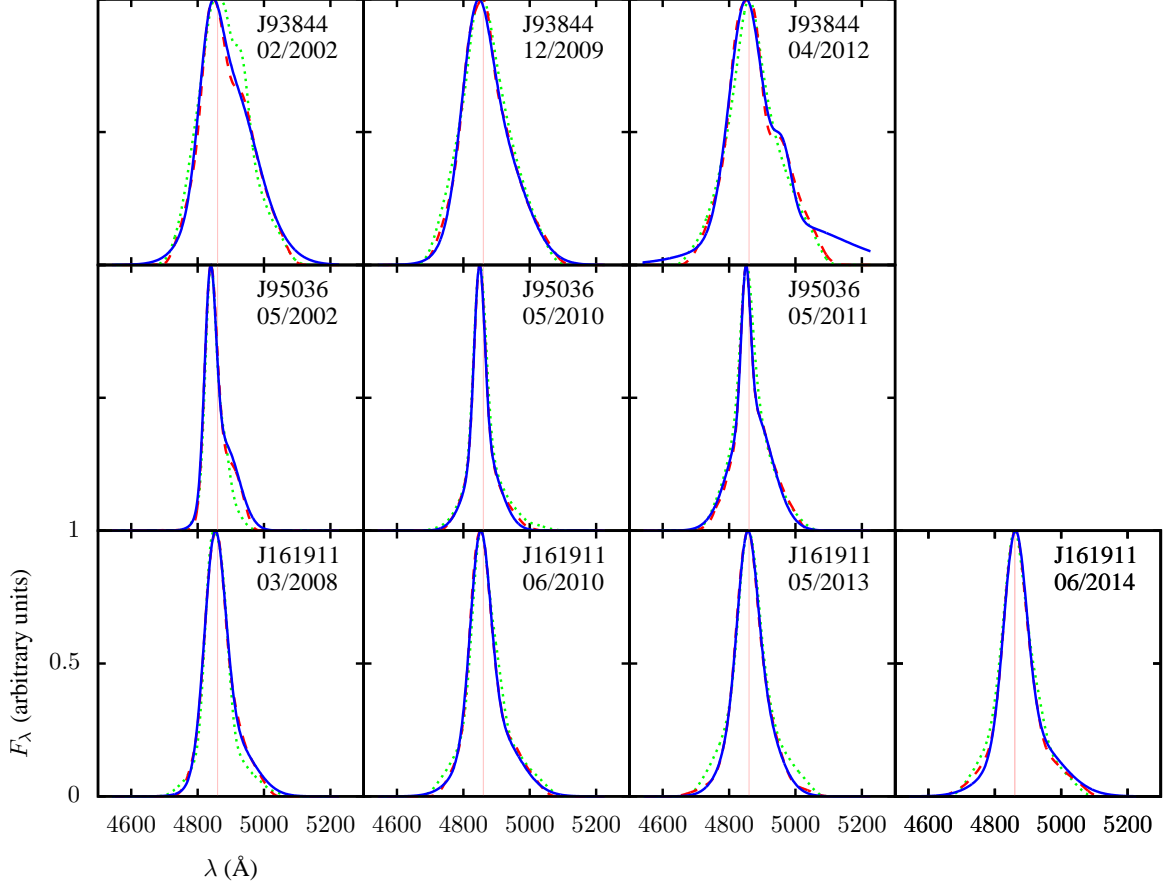


Figure 4.2: $H\beta$ emission-line profiles from multi-epoch observations of three SBHB candidates: SDSS J93844 (top row), J95036 (middle), and J161911 (bottom). For each epoch, we show the observed profile (blue solid line), the synthetic profile with the smallest (red dashed) and largest distance (green dotted) from the observed profile, contained in the nearest neighbor set.

distance from the observed profile to obtain the synthetic database sorted by distance, $\tilde{\mathbf{F}}$, such that, $d(\tilde{\mathbf{F}}^s, \mathbf{F}^o) \leq d(\tilde{\mathbf{F}}^{s+1}, \mathbf{F}^o)$.

From the ranked database we select a subset of \mathcal{N} profiles that are the nearest neighbors to the observed profile, whose value is determined as the larger of the number of profiles within some cutoff distance d_c and 6500.

$$\mathcal{N}(\mathbf{F}^o) = \max \left[k : d(\tilde{\mathbf{F}}^k, \mathbf{F}^o) < d_c(\mathbf{F}^o), 6500 \right] \quad (4.2)$$

The value of 6500 corresponds approximately to the square root of the total number of the

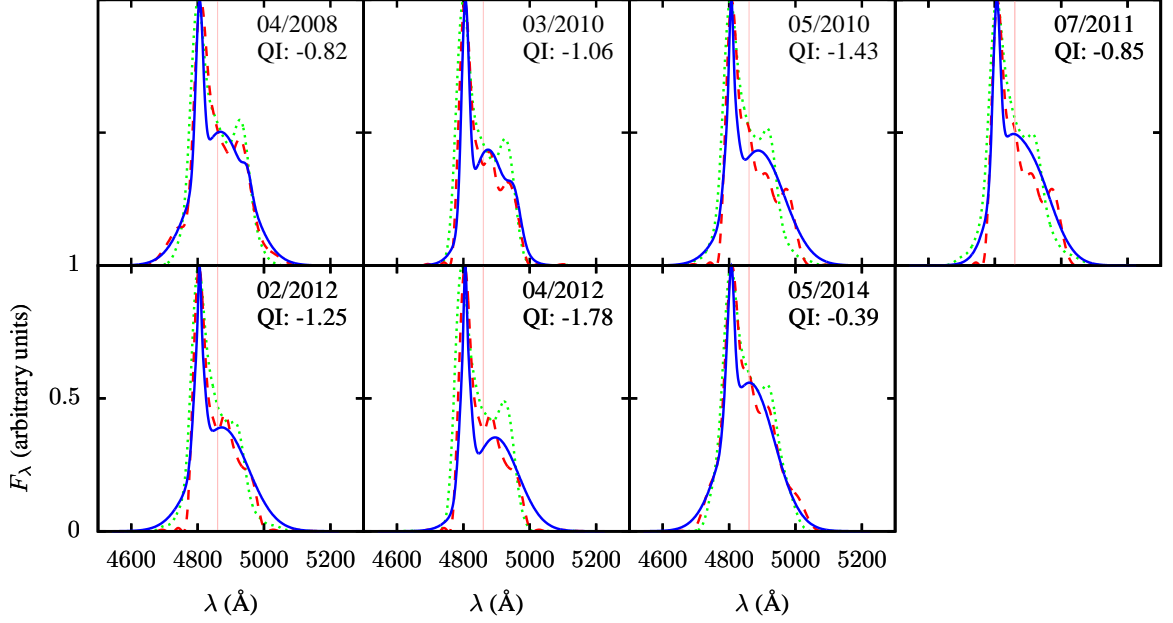


Figure 4.3: $H\beta$ emission-line profiles from multi-epoch observations of the SBHB candidate J153636, indicated by the time stamp. The observed candidate has the lowest average QI among all objects from the E12 sample of SBHB candidates, indicating that there is no close match for its profiles in the synthetic database. The meaning of different line styles and colors is the same as in Figure 4.2.

synthetic profiles in our database. The cutoff distance d_c is chosen to be 10 percent of the magnitude of the observed profile,

$$d_c(\mathbf{F}^o) = 0.1 \left[\sum_{m=1}^M (F_m^o)^2 \right]^{1/2}, \quad (4.3)$$

so that wider profiles correspond to larger cutoff distance. Here, F_m^o represents monochromatic profile flux at a given wavelength.

Therefore, each observed profile has a well-defined set of nearest neighbors in the synthetic database and a cutoff distance calculated using equation 4.3. Figure 4.2 shows a visual comparison between the multi-epoch profiles for three observed SBHB candidates (SDSS J93844, J95036, and J161911) and the profiles with the smallest (most similar) and the largest distance (least similar) belonging to their corresponding nearest neighbor sets. In a majority of cases, the nearest and furthest neighbor defined in this way are similar in

shape to the observed profiles. The exception are the cases in which the synthetic database does not contain a profile similar enough to the observed profile, as shown for the spectrum of J93844 observed in April 2012.

In order to measure the quality of the achieved match, we define the quality index (QI) as a function of the distance between the observed profile and its closest neighbor in the synthetic database

$$\text{QI} = \frac{d_c - d_{\min}}{d_c} . \quad (4.4)$$

By definition, $0 \leq \text{QI} \leq 1$ for observed profiles whose closest neighbor can be identified within its corresponding cutoff distance. In the cases when the closest neighbor cannot be found within the cutoff distance, the algorithm by default selects the closest 6500 synthetic profiles as its nearest neighbors. Such scenarios result in $\text{QI} < 0$, indicating a lower quality match, since the distance to the nearest synthetic profile $d_{\min} > d_c$. We illustrate this case in Figure 4.3, which shows a sequence of seven observed BEL profiles for the candidate J153636. QI for this object remains negative for every epoch of observation. Furthermore, its average quality index, $\text{QI} = -1.08$ (calculated as a simple average for all epochs of observation), is the lowest in the entire database, indicating that interpretation of this SBHB candidate is not reliable, simply because there is no close match for it in the synthetic database. The fraction of SBHB candidates with the negative average QI makes up about 18% of the E12 sample and we list their values in Table F.1.

4.1.3 Calculation of probability distributions for inferred SBHB parameters

The procedure described in the previous section allows us to determine a set of synthetic profiles, which are the closest neighbors to each observed profile. Since every synthetic profile corresponds to a unique set of SBHB parameters, we use the set of nearest neighbor profiles to map each observed profile into a preferred portion of the SBHB parameter space. In this approach, the average value of the SBHB parameters associated with a group of the nearest neighbor profiles represents a binary configuration favored by the observed profile,

and the variance in the value of each SBHB parameter provides a measure of its degeneracy.

The SBHB parameters favored by the observed profile are calculated as a weighted average of the values associated with its nearest neighbor profiles, in such way that the profiles closer to the observed profile contribute more to the average. The weight for each nearest neighbor profile is defined as an exponential function of its distance

$$w(\mathbf{F}^s, \mathbf{F}^o) = \begin{cases} e^{-5d/d_c}, & \{a, q, e, i\} \text{ repeat} \\ 0, & \{a, q, e, i\} \text{ do not repeat} \end{cases} \quad (4.5)$$

The first condition in equation 4.5 requires that four physical parameters of the SBHB model, namely the a , q , e , and i , are repeated in every epoch of observation of the same binary candidate. This requirement is based on a realistic expectation that the binary separation, mass ratio, eccentricity, as well as the orientation of its orbital plane are unlikely to change significantly from one epoch of observation to another, which for the E12 monitoring campaign corresponds to $\lesssim 12$ years. Other parameters of the model, such as the optical depth of the disk wind, orientation of the mini-disks, etc., are not subject to this constraint.

For example, the $H\beta$ BEL profiles associated with the SBHB candidate J95036 have been observed in three different epochs (see Figure 4.2). The three observed profiles have three sets of corresponding synthetic profiles, each containing \mathcal{N}_1 , \mathcal{N}_2 , and \mathcal{N}_3 nearest neighbor profiles, as determined by equation 4.2. If a synthetic profile from the second set has a combination of parameters $\{a, q, e, i\}$, that is repeated in some of the profiles contained in the set one and three, these profiles are assigned a non-zero weight, according to the equation 4.5. On the other hand, the synthetic profiles whose combination of parameters is not represented in all three nearest neighbor sets simultaneously are assigned zero weight. Therefore, a requirement that multi-epoch observations should map into the same portion of the $\{a, q, e, i\}$ parameter space allows us to further constrain the SBHB parameters and to reduce their degree of degeneracy.

Once the nearest neighbors of an observed profile and their weights are determined, probability distribution for a given SBHB parameter can be calculated as

$$\Pr(x = x') = \frac{\sum_{s=1}^{\mathcal{N}} w(\mathbf{F}^s, \mathbf{F}^o) : x(\mathbf{F}^s) = x'}{\sum_{s=1}^{\mathcal{N}} w(\mathbf{F}^s, \mathbf{F}^o)}, \quad (4.6)$$

where x represents an SBHB parameter of interest and \Pr is a discrete probability density function (PDF) when $x = x'$. For example, $\Pr(a = 5000M)$ is equal to the sum of the weights for all nearest neighbors of an observed profile, such that their combination of parameters includes $a = 5000M$, and is normalized by the sum of the weights. This procedure is repeated for all values of a and corresponding $\Pr(a)$ calculated for every epoch of observation in which an SBHB candidate is observed. The resulting, multi-epoch PDF is calculated as a simple average of PDFs from all epochs of observation. Finally, equipped with a PDF for every SBHB parameter, we can calculate the mean value of each parameter and its standard deviation, for every binary candidate.

In addition to the mean and standard deviation, we also calculate “entropy” and use it as a common statistical measure of degeneracy of each inferred SBHB parameter

$$\mathcal{S}_x = - \sum_{j=1}^{N_{\text{ch}}} \frac{\Pr(x = x_j) \log(\Pr(x = x_j))}{\log(N_{\text{ch}})}. \quad (4.7)$$

Here, N_{ch} denotes the number of parameter choices as shown in Table 3.1, for instance $N_{\text{ch}}(a) = 5$. According to equation 4.7, a well-defined PDF with no degeneracy corresponds to $\mathcal{S} = 0$, and a maximally degenerate, uniform PDF corresponds to $\mathcal{S} = 1$. The range of values for entropy defined in this way allows us to compare the degeneracy of different SBHB parameters on the same scale. Note that in practise, the discrete PDF defined in equation 4.6 is infact a multivariate functions where x represents a vector or a collection of all the model physical parameters, not just a single physical parameter like in the simplified example given here.

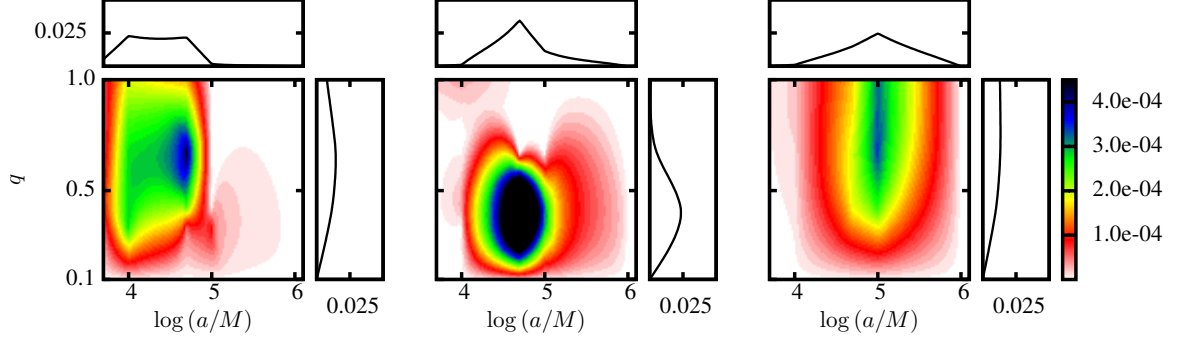


Figure 4.4: 2D probability density distribution in terms of $\log(a/M)$ and q for SDSS J93844 (left), J95036 (middle), and J161911 (right panel). The rectangular insets show the 1D projections.

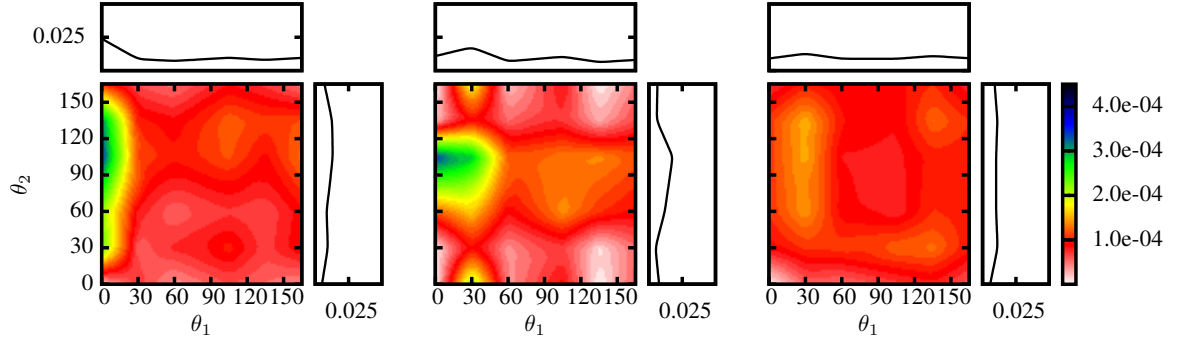


Figure 4.5: 2D probability density distribution in terms of θ_1 and θ_2 for SDSS J93844 (left), J95036 (middle), and J161911 (right panel). The rectangular insets show the 1D projections.

4.2 Results

4.2.1 Analysis of individual SBHB candidates

In this section, we present the analysis of the three SBHB candidates from the E12 sample and note that the same analysis has been carried out on the remaining group of the SBHB candidates and control AGNs. The objects SDSS J93844, J95036, and J161911 are of interest, since they have been highlighted by Runnoe et al. [158] as the most promising SBHB candidates in the sample, based on the properties of their radial velocity curves. As shown in Figure 4.2, the nearest neighbor profiles in the synthetic database provide a good description of the observed profiles for J93844, J95036, and J161911, as reflected by their average quality indices, $QI = 0.44, 0.59$ and 0.69 , respectively.

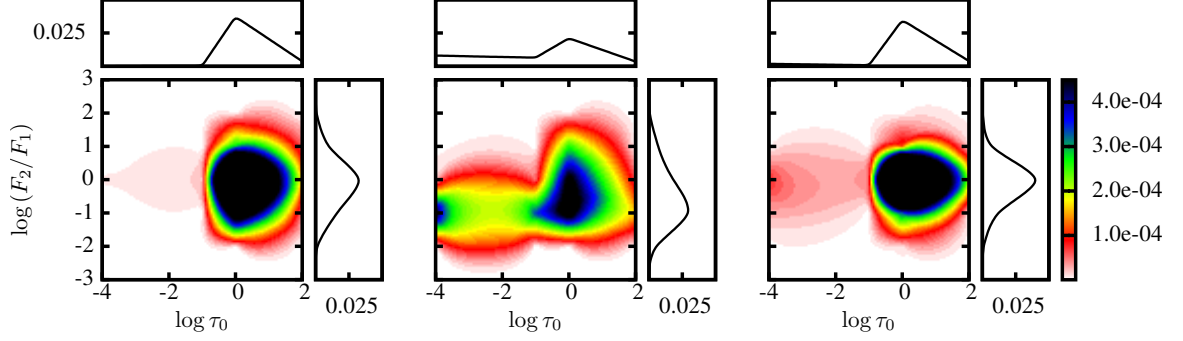


Figure 4.6: 2D probability density distribution in terms of $\log \tau_0$ and $\log (F_2/F_1)$ for SDSS J93844 (left), J95036 (middle), and J161911 (right panel). The rectangular insets show the 1D projections.

Figure 4.4 shows the PDFs for the three SBHB candidates in terms of a and q . The 2D distributions are made by dividing the parameter space into 100×100 equal bins and by interpolating the probability in each bin from the discrete PDF obtained in equation 4.6. The interpolated PDFs are then renormalized to one, resulting in values of $\sim 10^{-4}$. Visual inspection shows that the favored values of semimajor axes for all three SBHB candidates fall in the range of $\sim 10^4 - 10^5 M$. Table F.1 lists their mean values for $\log(a/M)$ and the associated standard deviations as (4.19 ± 0.34) , (4.64 ± 0.28) , and (4.81 ± 0.26) , for J93844, J95036, and J161911, respectively. Similarly, the values of q for the same three candidates are (0.65 ± 0.22) , (0.43 ± 0.17) , (0.72 ± 0.22) .

Among the three candidates, J95036 (middle) is characterized by the smallest degree of degeneracy in the inferred values of $\log(a/M)$ and q , as witnessed by their values of entropy listed in Table F.1 ($\mathcal{S}_a \approx \mathcal{S}_q = 0.44$). This is mainly because J95036 has narrower BEL profiles than the other two candidates, which place stronger constraints on the combinations of physical parameters that can produce them. In addition, the spectral features of profiles in J95036 (such as the location of the peak and profile asymmetry), show significant change from one observation to another. This epoch-to-epoch variability provides an effective way to reduce the SBHB parameter degeneracies, as it helps to eliminate parameters that are not represented in all epochs of observations (see equation 4.5).

Along similar lines, in the entire sample of the SBHB candidates, J131945 (listed as

number 56 in Table F.1) has the best constrained value of the semimajor axis. This candidate is a good example of potential gains provided by the continued spectroscopic monitoring of SBHB candidates: it has been observed 9 times between April 2002 and April 2013, whereas a majority of other objects in the sample have 3 to 4 observations and a similar baseline. This, combined with the fact that the broad base of its $H\beta$ profiles shows significant variability from one observation to another, guarantees that very few SBHB configurations can produce all of the observed profiles.

Figure 4.5 shows the PDFs for the SBHB candidates, J93844, J95036, and J161911, in terms of the angles θ_1 and θ_2 (the distributions have been calculated in the same way as those in Figure 4.4). The two angles are of interest because they describe the orientations of the two mini-disks relative to the binary orbital plane. As noted earlier, the BEL profiles presented in this work have been calculated assuming that both accreting SBHs can shine as AGNs and illuminate their own mini-disk, as well as the two other disks in the system. The effect of illumination of one mini-disk by a companion AGN is however most pronounced in binaries when their mini-disks are misaligned with the SBHB orbital plane. This nonaxisymmetric illumination pattern by the two AGNs can give rise to very asymmetric profiles whose shapes can vary on timescales shorter than the SBHB orbital period. Conversely, such profiles can in principle be a sensitive probe of their alignment.

Figure 4.5 however indicates that the three SBHB candidates under consideration have no clearly preferred values for θ_1 and θ_2 . In particular, their 1D distributions look relatively uniform. This large degree of degeneracy can in part be explained by the fact that we do not impose the requirement that the values of θ_1 and θ_2 must be repeated in every epoch of observation, as is done for the other parameters in equation 4.5. This implies that we allow for the orientations of the mini-disks to change over the course of observational campaign. Despite this degeneracy, we can still conclude that neither of the binary candidates favors the configuration in which the mini-disks are coplanar with the orbital plane. Better constraints on the mini-disk orientations can in principle be obtained, by more sophisticated

modeling of θ_1 and θ_2 as a function of the binary orbital phase.

Figure 4.6 shows the PDFs for the same three SBHB candidates in terms of the normalization of the disk wind optical depth, τ_0 , and the ratio of the $H\beta$ BEL flux contributed by the secondary and primary mini-disk, F_2/F_1 . The value of the optical depth parameter is relatively well constrained for J93844 (left panel) and J161911 (right) and it peaks at $\tau_0 \approx 1$. The same property is considerably more degenerate for J95036 (middle), which is, as noted earlier, the candidate with the narrowest BEL profiles among the three. This can be understood as the disk wind has less effect on the shapes of narrower profiles, and hence, accretion disk wind with a range of optical depths can produce profile shapes similar to the relatively narrow profiles of J95036. The degree of degeneracy in the inferred value of τ_0 can also be glimpsed from the value of entropy calculated for this parameter, which amounts to $\mathcal{S}_{\tau_0} = 0.27, 0.85$ and 0.42 for J93844, J95036, and J161911, respectively.

The property $\log(F_2/F_1)$ shown in Figure 4.6 is calculated from our model (i.e., it is not a parameter) and is of interest because it indicates which mini-disk dominates the $H\beta$ emission. In our model, the flux ratio is largely determined by two effects: (i) the accretion rates onto the primary and secondary SBH, which are assumed to power the AGN emission in the UV and X-ray band and (ii) by the surface area of the mini-disks that are emitting the BEL profiles¹. The two effects are considered competing because the ratio of mass accretion rates onto the two SBHs, \dot{M}_2/\dot{M}_1 , decreases with increasing q (see Equation 3.1), whereas the ratio of the surface areas of their mini-disks increases as $\sim q^2$. Since the latter effect dominates, we expect the two mini-disks to make comparable contributions to the BEL flux when $q \sim 1$ and to have $\log(F_2/F_1) < 0$ when $q < 1$. From the three binary candidates considered in this section, J93844 (left) and J161911 (right) have relatively high inferred mass ratios, $q \approx 0.7$, and consequently, the fluxes emitted by the two mini-disks are comparable. On the other hand, J95036 (middle) has $q \approx 0.4$ and a correspondingly lower peak value of $\log(F_2/F_1) \approx -0.5$.

¹This statement is a simplification and it does not take into account the effect of cross-illumination of the mini-disks by the companion AGN.

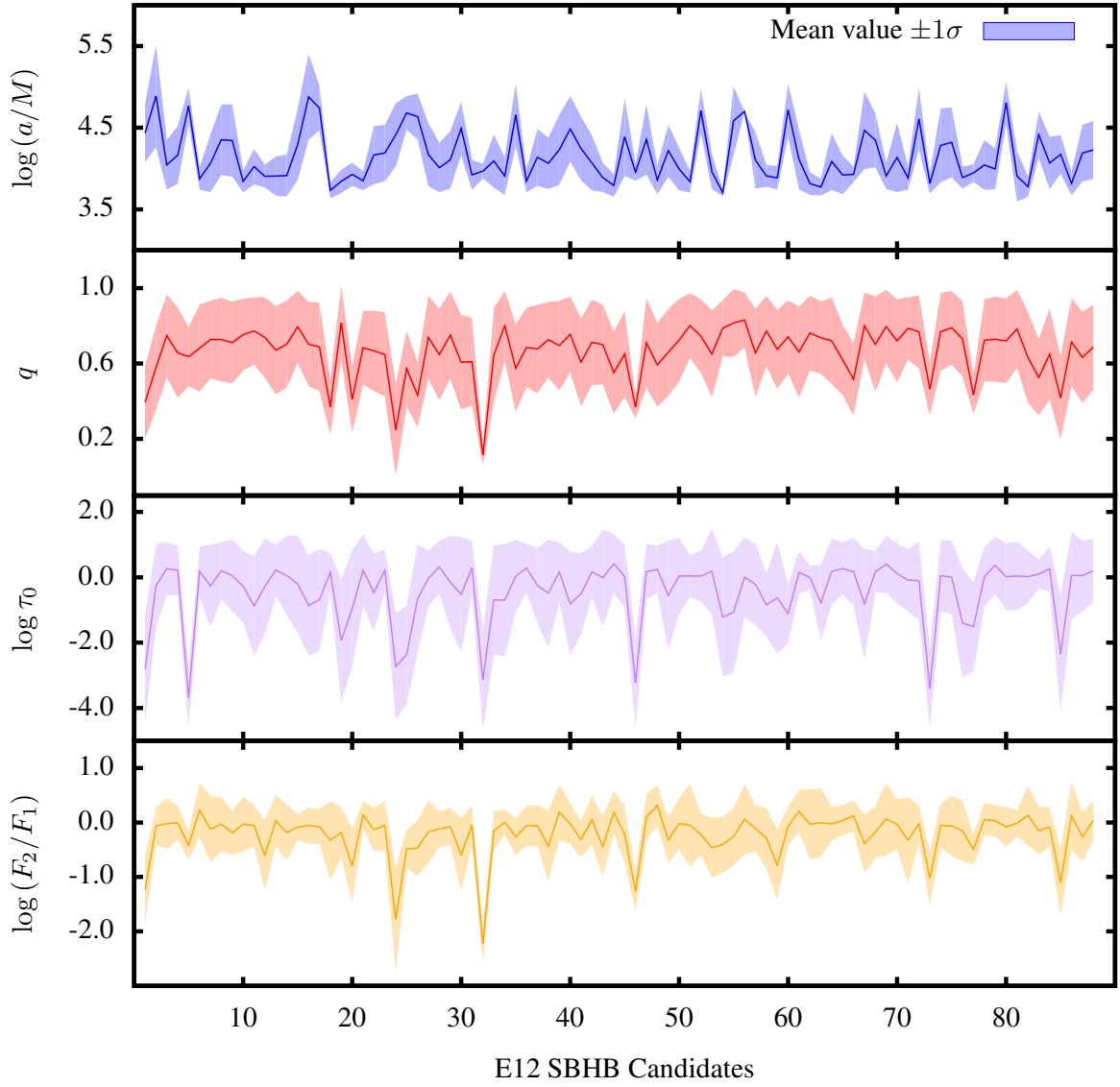


Figure 4.7: Inferred average values of binary parameters and their standard deviations for 88 SBHB candidates from the E12 survey. From top to bottom: a , q , $\log \tau_0$, and $\log(F_2/F_1)$. Data corresponding to each panel can be found in Table F.1.

Finally, we reflect on the ability of our method to infer the orbital eccentricity of an SBHB from its BEL profiles. With just two choices for this parameter in our synthetic database ($e = 0$ and $e = 0.5$), the SBHB orbital eccentricity of the observed candidates cannot be sufficiently constrained by our method. While this choice was made in order to produce a synthetic database of manageable size, it is actually not clear that expanding the database further, by adding configurations with other eccentricities, would lead to improved ability to predict eccentricity. This is because the analysis carried out in Chapter 3 already show that there is a large degree of overlap in profile properties for $e = 0$ and $e = 0.5$ cases, indicating that there is a lot of degeneracy in this parameter. We therefore conclude that distinguishing among different cases of orbital eccentricity would be difficult, even if our database contained many different values.

4.2.2 Properties of the entire SBHB candidate sample

In this section we discuss the properties of the entire sample of 88 SBHB candidates from the E12 search. The top two panels of Figure 4.7 provide a visual summary of the mean values of $\log(a/M)$ and q and their standard deviations for all 88 candidates. The preferred values of semimajor axes are similar to those of the three candidates discussed in the previous section. They range between $3.5 \lesssim \log(a/M) \lesssim 4.5$ and have standard deviations, $\sigma_a < 0.6$. In terms of the binary mass ratios, the values preferred by most candidates are in the range $0.2 \lesssim q \lesssim 0.8$ and have standard deviations in the range $0.1 \lesssim \sigma_q \lesssim 0.3$. The relative standard deviations for the inferred mass ratios, σ_q/q , tend to be about a few times larger, on average, than those calculated for the semimajor axes, indicating that there is a larger degree of degeneracy associated with the determination of q . This statement is supported by the corresponding values of entropy, which for a majority of SBHB candidates tend to be higher for q than for a .

The inferred values of the optical depth parameter cover a relatively wide range of values, $-3.4 \lesssim \log \tau_0 \lesssim 0.4$, seem to be moderately degenerate and characterized by the

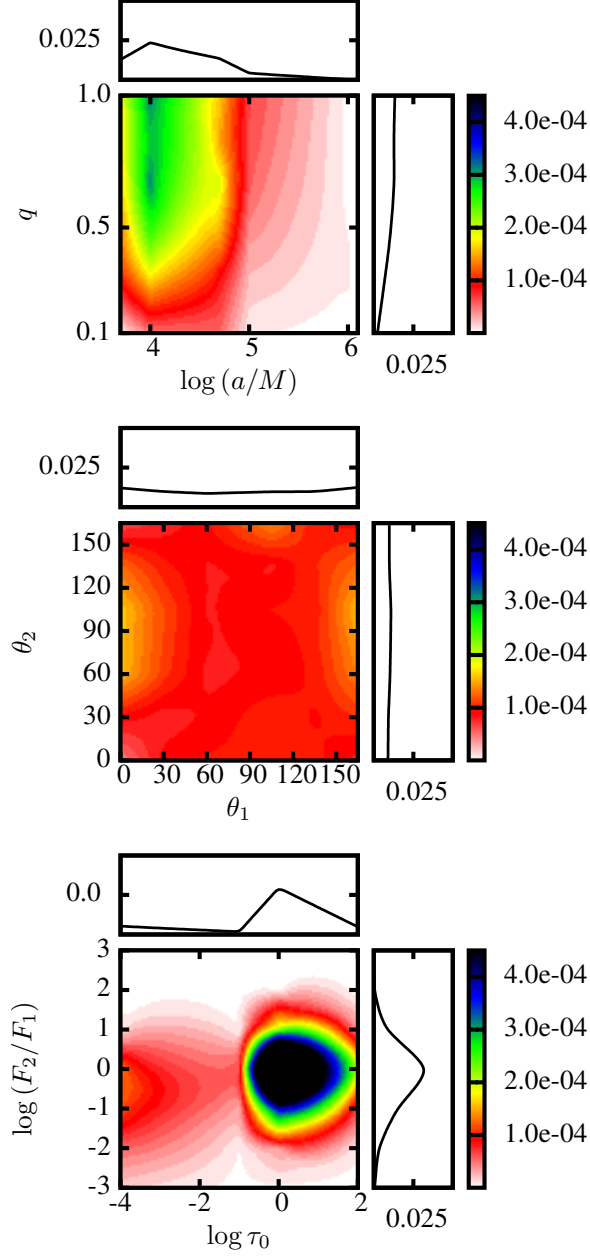


Figure 4.8: 2D probability density distributions in terms of $\log(a/M)$ and q (top), θ_1 and θ_2 (middle), and $\log \tau_0$ and $\log(F_2/F_1)$ (bottom) for the 88 SBHB candidates from the E12 sample. The rectangular insets show the 1D projections.

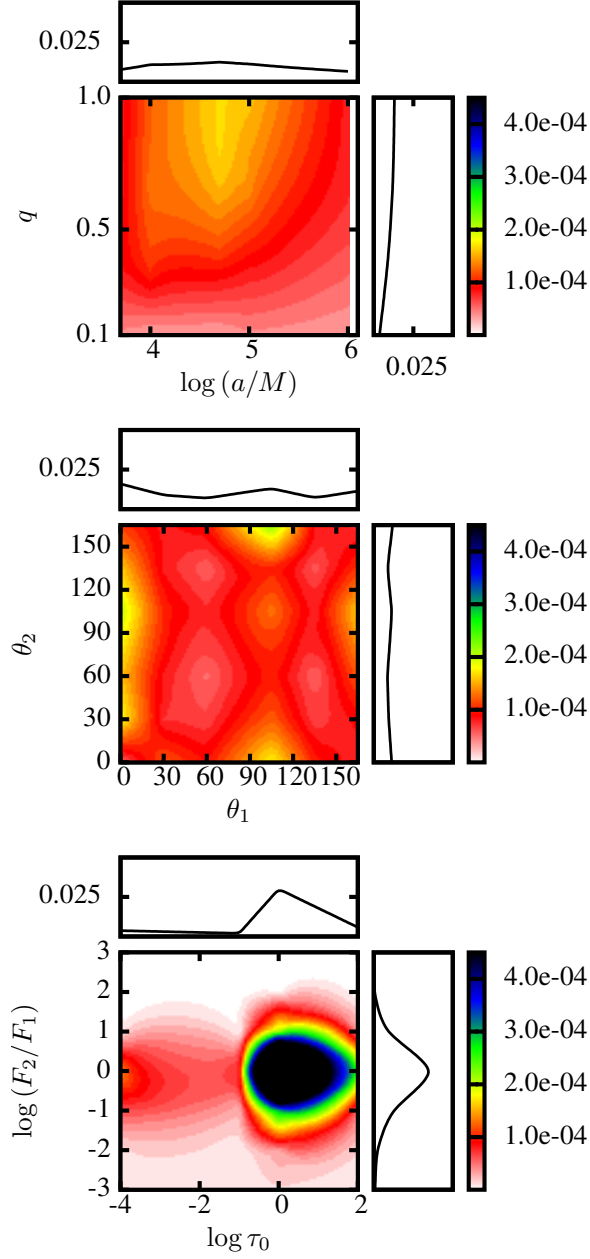


Figure 4.9: 2D probability density distributions in terms of $\log(a/M)$ and q (top), θ_1 and θ_2 (middle), and $\log \tau_0$ and $\log(F_2/F_1)$ (bottom) for the control group of AGNs from the E12 sample. The rectangular insets show the 1D projections.

average value of entropy $\mathcal{S}_{\tau_0} \approx 0.5$. It is interesting to note that our database includes the value of optical depth parameter as high as $\tau_0 = 100$ but no SBHB candidate favors the average value higher than a few. Visual inspection of Figure 4.7 shows that the systems with the lowest value of τ_0 also tend to favor the lowest values of q . Inspection of the BEL profiles for these systems shows that they tend to be double-peaked and relatively smooth. Such profiles are well described by synthetic profiles in our database produced by systems in which the primary AGN is the dominant contributor to the BEL flux and the optical depth of its disk wind is low, so that the double-peaked nature of the profile is preserved.

Similarly, the inferred values of the flux ratio for majority of the SBHB candidates correspond to comparable contributions to the line flux by the primary and secondary mini-disks. An exception to this are a few candidates with the flux ratio as low as $\log(F_2/F_1) \approx -2$, which also correspond to the systems with the lowest inferred values of mass ratio. This correlation is expected, based on the scaling of the mini-disk areas with the binary mass ratio, as explained in the previous section. The entropy for this parameter spans a wide range of values from one SBHB candidate to another, $0.06 \lesssim \mathcal{S}_{F_2/F_1} \lesssim 0.7$, indicating that the predictive power for the flux ratio varies a lot for different systems.

Figure 4.8 shows the PDFs for the entire sample of 88 SBHB candidates from the E12 search. The distributions are calculated as the simple averages of distributions for individual candidates, equivalent to those shown in Figures 4.4 to 4.6. The top panel shows that as a population, the SBHB binary candidates favor the value of semimajor axis corresponding to $\log(a/M) \approx 4.20 \pm 0.42$ and comparable mass ratios, $q > 0.5$. There is no strong preference for a particular value of the angles θ_1 and θ_2 and therefore, they are unconstrained. The most interesting aspect of this statement is the implication that binary candidates do not seem to favor the configuration in which the mini-disks are coplanar with the orbital plane. The bottom panel of Figure 4.8 captures the probability distributions very similar to those shown in the left and right panel of Figure 4.6, with $\tau_0 \approx 1$ and $F_2/F_1 \approx 1$.

We perform the analysis on the spectra of the control group of AGNs in the same

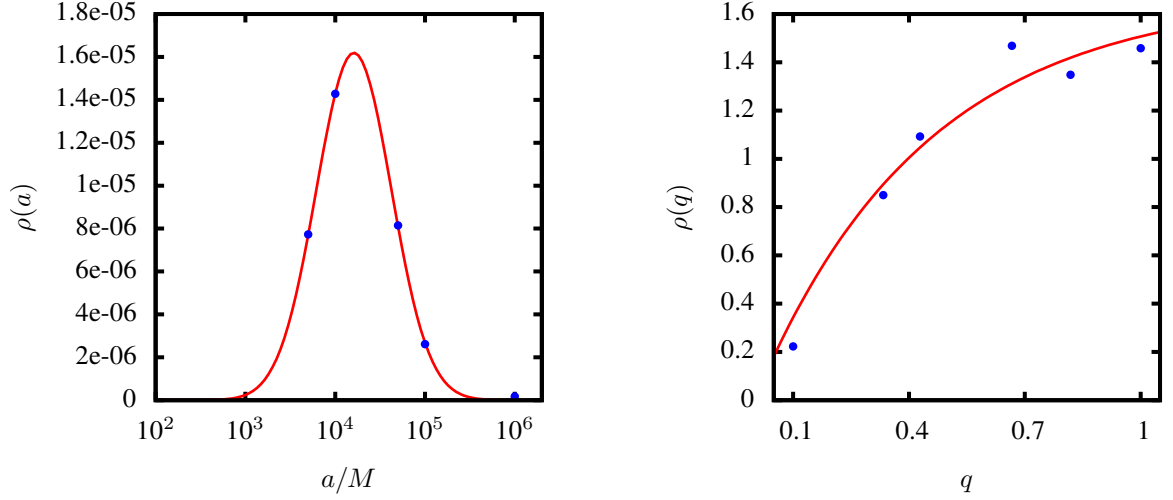


Figure 4.10: Best fit for the continuous probability density function for all 88 SBHB candidates from the E12 sample in terms of the semimajor axis (left panel) and mass ratio (right). The blue dots mark the probability density determined by the comparison of the observed BEL profiles from the SBHB candidates and synthetic profiles using our method.

way and show their resulting PDFs in Figure 4.9. While the control group of AGNs favors somewhat larger average value of the semimajor axis and a larger standard deviation, $\log(a/M) \approx 4.60 \pm 0.72$, the probability distributions for the two groups of objects are statistically indistinguishable. Specifically, neither shows preference in terms of θ_1 and θ_2 , while the favored values for τ_0 and F_2/F_1 are the same for both groups. This similarity indicates that the approach presented here can be used to infer the parameters once an SBHB candidate is confirmed as a real binary, but cannot be used as a conclusive test of binarity.

For practical purposes we also provide the analytic fits to the 1D distribution functions for the semi-major axis and the mass ratio for all 88 SBHB candidates. The continuous PDF for $\log(a/M)$ can be described by a normal distribution shown in the left panel of Figure 4.10 and expressed as

$$\rho(a) \propto \exp \left[-\frac{[\log(a/M) - 4.2]^2}{2 \times 0.42^2} \right], \quad 3.7 \leq \log(a/M) \leq 6. \quad (4.8)$$

Equivalently, the continuous PDF for q can be described with an exponential distribution

shown in the right panel of Figure 4.10 and expressed as

$$\rho(q) \propto 1 - \exp \left[-\frac{q}{0.44} \right], \quad 0.1 \leq q \leq 1 \quad (4.9)$$

4.3 Discussion: Predictions and Simplifications

4.3.1 Implications for theory and observations

If the E12 sample of SBHB binary candidates were true binaries, their inferred PDFs would be a combination of the intrinsic properties of the binary (orbital separation, mass ratio, etc.) as well as the selection effects inherent to the spectroscopic search. The E12 and other spectroscopic searches are in principle sensitive to SBHBs with orbital separations in the range $\sim 10^3 - 10^4 M$ [168, P18 hereafter]. The low and high end cutoffs for this range are set by two effects: (a) the binaries at smaller separations tend to evolve at a higher rate, making their detection less probable and (b) those at larger separations have radial velocity variations (determined from their BELs) too low to be detected by spectroscopic surveys on the timescales of years. Taking these considerations into account we use the model developed by P18 (we also briefly describe the model in the appendix A) to calculate the likelihood for detection of subparsec SBHBs given the parameters and selection effects of the E12 search. It is worth emphasizing that this likelihood and our interpretation of the SBHB candidates presented in § 4.2 are obtained independently, and therefore, their comparison provides a consistency check for the results obtained by our method.

The panels of Figure 4.11 show the likelihood for detection of SBHBs given a yearly cadence of observations by the E12 spectroscopic search based on the P18 model of $10^7 M_\odot$ binaries with the accretion rate through the circumbinary disk corresponding to $\dot{M} = 0.1\dot{M}_E$. Here, $\dot{M}_E = L_E/\eta c^2$ is the Eddington accretion rate, η is the radiative efficiency, $L_E = 4\pi GMm_p c/\sigma_T$ is the Eddington luminosity, σ_T is the Thomson cross section, and other constants have their usual meaning. The left and right panel illustrate the likelihood map for the SBHBs in which the primary or the secondary mini-disk make the

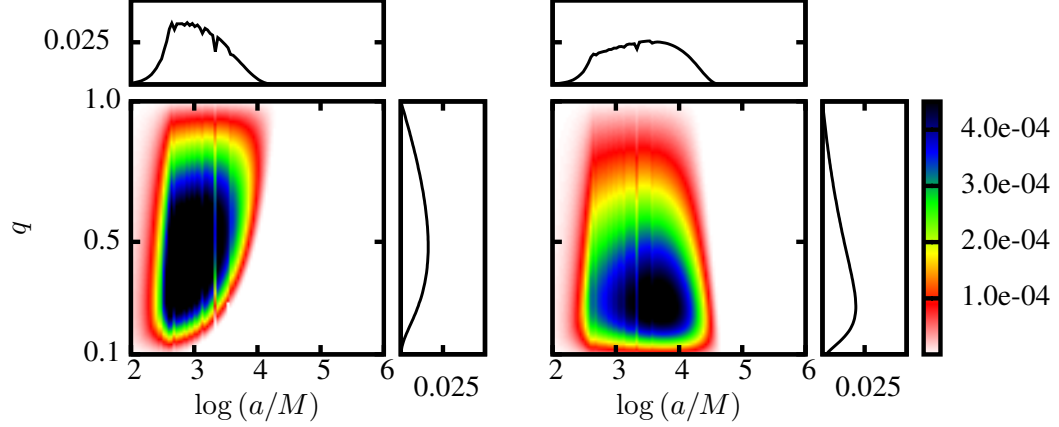


Figure 4.11: Likelihood for detection of SBHBs given a yearly cadence of observations by the E12 spectroscopic search based on the P18 model of $10^7 M_\odot$ binaries with the accretion rate through the circumbinary disk corresponding to $\dot{M} = 0.1\dot{M}_E$. The left (right) panel illustrates the likelihood map for the SBHBs in which the primary (secondary) mini-disk make the dominant contribution to the flux of the $H\beta$ emission line. The color bar marks the normalization of the likelihood, which is arbitrary and chosen to match Figures 4.8 and 4.9.

dominant contribution to the flux of the $H\beta$ emission line, respectively.

In the case when the emission from the primary mini-disk dominates, there is a positive correlation between the mass ratio q and the maximum semimajor axis that a detected SBHB can have. This is because as q increases, the radial velocity due to the reflex motion of the primary SBH also increases. It follows that the binaries with larger mass ratios are favored in this case because they can be detected at larger orbital separations. Conversely, in the case when the emission from the secondary mini-disk dominates, the reflex motion of the secondary SBH is maximized for smallest values of q . As a consequence, this scenario favors lower mass ratio binaries. Another difference worth pointing out is that the scenario when the primary mini-disk dominates places a stronger constraint on the binary semimajor axis, since in this case $a < 10^4 M$, whereas $a < \text{few} \times 10^4 M$ when the secondary dominates, for parameters used in calculation of Figure 4.11.

The analysis presented in § 4.2 indicates that a majority of SBHB candidates in the E12 sample favor values of the mass ratio $q > 0.5$ and the flux ratios $F_2/F_1 \approx 1$. They are therefore consistent with the scenario in which the emission from the primary mini-disk

makes the dominant contribution to the flux of the $H\beta$ emission line. This is of interest for two reasons. Firstly, it is contrary to the assumption commonly made by the spectroscopic surveys in the interpretation of their results. This assumption is directly motivated by a number of theoretical studies of SBHBs in circumbinary disks which show that in unequal-mass binaries accretion occurs preferentially onto the smaller of the two SBHs, which orbits closer to the inner edge of the circumbinary disk [40, 46, 86, 88, 169]. Taken at face value, this suggests that the AGN associated with the secondary SBH may be more luminous than the primary. However, as noted earlier, the flux of the BELs is not only determined by the bolometric luminosity of the AGN but also by the size of its BLR, which in our model given by the surface areas of the two mini-disks (the flux contribution by the circumbinary disk is small and can be neglected in all physically motivated configurations investigated by our model). Therefore, an important implication of our results for observational searches is that they should consider the case in which the measured radial velocity curves are associated with the primary SBH, and which would consequently point to more compact systems of SBHBs.

Secondly, the preference for the higher values of q among the observed SBHB candidates also suggests that, if these are real binaries, there is a physical process that allows initially unequal mass systems to evolve toward comparable mass ratios. As noted in the paragraph above, that prediction already seems to be borne out by the local simulations of SBHBs in circumbinary disks, which show that accretion occurs preferentially onto the smaller of the SBHs. This presents an interesting challenge for cosmological models of binary evolution, which predict that sub-parsec SBHBs with lower mass ratios should be more abundant than those with comparable mass ratios [e.g., 170, see also P18 and references therein]. If true SBHBs indeed favor comparable mass ratios, this would strongly suggest that the accretion rate inversion reported by the local simulations of SBHBs in circumbinary disks is an important ingredient that must be included in the cosmological models.

Another result worth reflecting on is that the observed SBHB candidates in our sample seem to favor configurations in which the mini-disks are misaligned (or warped) relative to the binary orbital plane. This is of interest because gravitational torques between the SBHs and the triple disk system can cause precession of the mini-disks, while diffusive processes can align the SBH spins and the mini-disk axes with the orbital axis [55, 171]. If so, the alignment of the SBHB-spin-disk system is expected to evolve with binary separation, and the orientation of the mini-disks inferred from observations may be an important indicator of whether the mechanism leading to coplanar alignment is efficient.

Finally, it is worth noting that the E12 spectroscopic campaign has measured statistically significant epoch-to-epoch velocity modulations for 29/88 SBHB candidates (marked with “1” in Table F.1). They have not obtained measurements of the velocity modulation for the remainder of the candidates whose profiles change in shape significantly from one epoch of observation to another. This is because significant changes in a BEL profile shape can either mimic or hide the change caused by the radial velocity modulation due to binary orbital motion, thus precluding a reliable measurement of the profile offset along the wavelength axis [see Appendix A in 158, for analysis of this effect]. The method presented here is however particularly effective for SBHBs whose profile shapes change in time, because in these systems we obtain stronger constraints on the binary parameters, as discussed in § 4.2. The two analyses therefore provide independent constraints complimentary to one another, because they infer SBHB properties from two different aspects of BEL profiles: their offset and their shape.

4.3.2 Simplifications and limitations of the method

Because the method presented here is built upon our SBHB model and databases presented in chapters 2 and 3, the assumptions used there are also shared with this method. We direct the reader to the previous chapters for detailed discussion of the implications of these simplifying assumptions and only address the new aspects, relevant to the comparison of

modeled profiles with observations.

As noted in the previous section, the approach presented here is based on the analysis of the shapes of BELs and it does not explicitly incorporate the radial velocity curve modeling for candidates with a sequence of observed profiles. This is because our synthetic database presently contains profiles for only five equidistant orbital phases per SBHB configuration, whereas the spectroscopic searches with cadence of months to years correspond to a higher frequency of sampling of the SBHB radial velocity curves on average.

The sparse sampling adopted in our synthetic database is a practical compromise motivated by considerations about its size. Because of the extent of the parameter space, the number of sampled configurations quickly adds up to about 42.5 million, even with a handful of choices per parameter. Note however that for promising SBHB candidates a denser coverage can be obtained for the sub-regions of the parameter space occupied by the binary configurations of interest. This includes a higher rate of sampling in the orbital phase, so to attempt to match the orbital phase of the observed SBHB candidates. This would provide a more stringent consistency check for the SBHB model by requiring that all observed profiles associated with a given SBHB candidate map into the consistent values of a , q , e , i (a requirement already used in this work), *and* that the time-domain evolution of the profile shapes is consistent with the expected evolution of the orbital phase.

Another point worth noting is related to the inferred orbital separation of the candidate SBHBs. According to Figure 4.8, our method suggests that some portion of the candidates may be described by the semimajor axes as small as $5000 M$. Depending on the exact mass ratio and orbital eccentricity, these separations correspond to SBHBs with mini-disks gravitationally truncated to a size of $\sim 10^3 M$ (see Figure 3.1), or about $\sim 10^{-3} - 10^{-2}$ pc for a binary with the mass of $10^7 - 10^8 M_{\odot}$, respectively. By the time the mini-disks reach such compact sizes, their optical BLRs may be substantially truncated, resulting in the dimming of the broad optical emission lines considered in this work. A consequence of the BEL dimming would be a non-detection of some fraction of such compact SBHBs.

Conversely, the same effect would be reflected in a more precipitous decrease of the PDFs of SBHB candidates with semimajor axes below $a \sim 10^4 M$. The physics of binary BLRs is however not sufficiently understood in order to place firm constraints on their sizes (or photoionization properties for that matter). For this reason, we make no assumptions about the sizes of optical BLRs in binary mini-disks and attempt to circumvent the complexity by adopting the simplest of assumptions: if optical BLRs still exist in the most compact of SBHBs considered in our model, then their emission properties are set by the properties of the SBHB and the size of its mini-disks.

This work lays out an approach that can be used to quantify the SBHB parameters and their uncertainties once a sample of genuine sub-parsec binaries is available. A point worth reiterating however is that other physical processes can potentially mimic the emission signatures of SBHBs included in our database. These include but are not limited to the recoiling SBHs [155] and local and global instabilities in single SBH accretion disks that can give rise to transient bright spots and spiral arms [156, 157]. In that sense, the model described in this work can be used to interpret observed BEL profiles in the context of the SBHB model but cannot be used to prove that they originate with genuine SBHB systems.

CHAPTER 5

CONCLUSIONS

This thesis is motivated by advances in observational searches for SBHBs made in the past few years which are represented by better designed, multi-wavelength and multi-year observational campaigns. Observational challenges notwithstanding, spectroscopic searches for SBHBs seem capable of delivering statistically significant sample of binary candidates and their first results are broadly consistent with theoretical predictions. While selection of a well-defined sample of SBHBs remains a principal goal in this research field, an equally important and timely consideration is what can be learned once such sample is available. In this context we develop a model to calculate the BEL profiles from SBHBs in circumbinary disks guided by a wealth of theoretical results in the literature, and a method to compare the modeled BELs to those of the observed binary candidates. The most important results of the thesis are as follows

- The BEL profiles presented in this work have been calculated assuming that each accreting SBH can shine as an AGN and illuminate its own mini-disk as well as the two other disks in the system. The illumination by two AGNs gives rise to the characteristic BEL profiles, with shapes distinct from those produced by a single BLR illuminated by the central AGN. Moreover, as a consequence of the evolving illumination pattern from the two AGNs, the BEL profiles associated with the SBHBs in circumbinary disks can exhibit significant variability on the orbital time scale of the system. We identify this as a key spectroscopic signature of the SBHB systems but cannot rule out a possibility that these features are mimicked by transient bright spots and spiral arms in single SBH accretion disks (Nguyen and Bogdanovic 2016) [172].

- We analyze the modeled BEL profiles in terms of the commonly used statistical distribution functions in order to determine their dependence on the underlying binary parameters, and find that in the model where the disk wind effects are neglected, and in models where absorption of BEL photon through the radiatively driven disk wind is included, the modeled profiles show distinct properties as a function of the binary semi-major axis, eccentricity, mass ratio, alignment of the triple disk system and orientation relative to the observer. The most characteristic features of modeled profiles are a direct consequence of the presence of multiple BLRs and their illumination by two accretion powered SBHs, both of which are a unique property of the SBHB model. Thus, models of BEL profiles from SBHBs in circumbinary disks have predictive power and can in principle be used to infer distribution of these parameters in real binaries (Nguyen and Bogdanovic 2016 [172]; Nguyen et al. 2019 [173]).
- Under the influence of accretion disk winds the BEL profiles appear narrower, more symmetric, and predominantly single-peaked. All correlations between the profile shape parameters and SBHB parameters identified in the NW model are nevertheless preserved, indicating that their diagnostic power is not diminished. Analysis of 42.5 million modeled BEL profiles reveals that their shapes are a better indicator of the binary orbital separation and the degree of misalignment in the triple disk system, and are less sensitive to the SBHB mass ratio and orbital eccentricity. These findings can guide expectations related to the diagnostic value and limitations of the BEL profiles in spectroscopic searches for SBHBs (Nguyen et al. 2019) [173].
- We perform a comparison of the modeled BEL profiles with those for the observed SBHB candidates and a control sample of (non-binary) AGNs from the E12 sample. We find that the profile shapes from a sample of SBHB candidates are more consistent with the binary model than are regular AGNs. Furthermore, the comparison of the modeled profiles with the SBHB candidates indicates that, if the observed

sample comprises genuine binaries, it must include systems with smaller separations ($a \ll 10^6 M$), comparable masses, and misaligned (or possibly warped) mini-disks. Similarly, if all candidates are shown to be genuine SBHBs, this would require their BLRs to be enshrouded in disk winds with optical depth $\gtrsim 0.1$ (Nguyen et al. 2019) [173].

- We presented an analytic model that can be used to determine the likelihood for detection of sub-parsec SBHBs in current and future spectroscopic searches. The model uses a simple theoretical prescription for orbital evolution of SBHBs in circumbinary disks, from an instance when they form a gravitationally bound pair to the point of coalescence. Combined with the selection effects of spectroscopic surveys, it returns a multivariate likelihood for SBHB detection as a function of M , q , a and \dot{M} . We find that most SBHBs, which are in principle detectable by spectroscopic surveys with yearly cadence of observations, are expected to reside at orbital separations $\lesssim \text{few} \times 10^4 M$, where they spend $\leq 0.5\%$ of their life as gravitationally bound binaries. This expectation is consistent with the inferred semi-major axes of the observed SBHB candidates (Model presented in Pflueger et al. 2018) [168].
- We present a method for comparison of the modeled and observed optical BELs, based on the principal component analysis, and use it to infer the properties of 88 SBHB candidates from the E12 spectroscopic survey. The new aspect of this method is that in addition to the parameter estimates it also provides a quantitative measure of the parameter degeneracy, thus allowing to establish the uncertainty intrinsic to such measurements (Nguyen et al. 2019b, in prep).
- We find that as a population, the observed SBHB candidates favor the average value of the semimajor axis corresponding to $\log(a/M) \approx 4.20 \pm 0.42$, in agreement with expectations based on orbital evolution of SBHBs in circumbinary disks and the selection effects of spectroscopic surveys. They also favor configurations with com-

comparable mass ratios, $q > 0.5$, although this parameter suffers from a larger degree of degeneracy than a . We provide the analytic fits to the 1D distribution functions of these parameters in the text. If the SBHB candidates analyzed here are shown to be true binaries, this result would strongly suggest that there is a physical process that allows initially unequal mass systems to evolve toward comparable mass ratios (e.g., accretion that occurs preferentially onto the smaller of the SBHs). Our method does not provide useful constraints on the orbital eccentricity, because this parameter suffers from a large degree of degeneracy (Nguyen et al. 2019b, in prep).

- The angles that describe the orientation of the primary and secondary SBH mini-disks relative to the orbital plane cannot be well constrained. The SBHB candidates however do not favor configurations in which the mini-disks are coplanar with the binary orbital plane. If this finding is preserved for confirmed SBHBs, it would point to the presence of a physical mechanism which maintains the misalignment of the mini-disks (or causes them to be warped) down to sub-parsec binary separations. If so, the alignment of the mini-disks (and SBH spins if they are related to the mini-disk orientation) should evolve with binary separation. In this case, the orientation of the mini-disks inferred from observations would be an important indicator of whether the mechanism leading to the coplanar alignment is efficient, as predicted by some theoretical models (Nguyen et al. 2019b, in prep).
- The inferred values of the normalization for the optical depth of the accretion disk wind in the two mini-disks cover a relatively wide range of values, $-3.4 \lesssim \log \tau_0 \lesssim 0.4$, and are moderately degenerate. Similarly, a majority of SBHB candidates in the E12 sample favor the values of $F_2/F_1 \approx 1$, and are consistent with the scenario in which the emission from the primary mini-disk either makes a dominant or a comparable contribution to the flux of the $H\beta$ emission line. An important implication of this result for spectroscopic searches for SBHBs is that they should consider the

case in which a measured radial velocity curve is associated with the primary SBH, in addition to the commonly made assumption that they are associated with the secondary. The main difference between the two is that, all other things being the same, the former interpretation corresponds to more compact (and thus more strongly constrained) systems of SBHBs compared to the latter case (Nguyen et al. 2019b, in prep).

- We find that epoch-to-epoch variability of the observed BELs provides an effective way to reduce the SBHB parameter degeneracies, as it helps to eliminate parameters that are not represented in all epochs of observations. Some of the strongest parameter constraints obtained with our method are achieved for individual SBHB candidates with many available observations (e.g., nine), thus providing an example of potential gains provided by the continued spectroscopic monitoring (Nguyen et al. 2019b, in prep).
- In addition to the observed SBHB candidates, we perform the analysis of the spectra of a control group of AGNs and compare the two. The control AGNs favor somewhat larger average value of the semimajor axis (albeit statistically indistinguishable from the SBHB candidate value) and exhibit a larger degree of degeneracy in this parameter. The probability distributions for the remainder of the SBHB parameters look nearly the same for the two groups of objects. This similarity confirms that the approach presented here can be used to infer the parameters once a group of confirmed SBHBs is available, but cannot be used as a conclusive test of binarity (Nguyen et al. 2019b, in prep).

Further improvements to the presented method are possible by explicitly incorporating the modeling of the time-domain evolution of profile shapes into the model, at the expense of creating a larger database of modeled profiles, with a higher sampling of the relevant SBHB parameters as a function of time. This would provide a more stringent consis-

tency check by requiring that all observed profiles associated with a given SBHB candidate map into the consistent values of the binary parameters (a requirement already used in this work) *and* that the time-domain evolution of the profile shapes is consistent with the SBHB model. We defer this type of analysis to future work. Finally, we emphasize that the model described in this work cannot be used to prove that the observed SBHB candidates are real binaries, but it can be used to interpret the observed BEL profiles once a sample of confirmed SBHBs is available.

Appendices

APPENDIX A

SELECTION EFFECTS OF SPECTROSCOPIC SURVEYS

The binary separation a is one of the best constrained parameters in the model since the synthetic BEL profiles are highly sensitive to it. Physical interpretation of all candidates in the E12 survey shows that the total distribution has a peak around $a = 10^4 M$ which can be best explained through selection effects of the spectroscopic methods applied in the survey. In general, binaries with separation that are too small, tend to evolve quickly to even smaller separation and hence have a lower intrinsic probability to be existed; while binaries with separation that are too wide, tend to have lower orbital velocity along the LOS (velocity offset) and hence are highly disregarded by spectroscopic surveys which usually set a lower limit on the observed velocity offset, i.e. $\geq 1000 \text{ km s}^{-1}$ was chosen in E12, in order to eliminate profiles from systems of regular AGNs. Taking into account both the intrinsic and extrinsic probabilities, the E12 survey are more likely to detect binaries with "medium" separation of around $[10^3 M, 10^4 M]$ [168]. In this chapter we will aim to quantify these spectroscopic selection effects. Most of the work in this chapter has been published in [168] and we will consider the E12 campaign as an illustrative example while similar considerations can be applied to other spectroscopic surveys in general.

A.1 Model Assumptions and Parameters

A.1.1 Common assumptions of spectroscopic searches for SBHBs

The principal assumption made by all spectroscopic searches is that some fraction of SBHBs at sub-parsec orbital separations are contained in a region comparable to or larger in size than the BLRs of regular AGNs that do not host SBHBs. If the emission properties of BLRs that host SBHBs remain qualitatively similar to the single AGN case, it follows that

their dynamical perturbation by SBHBs can in principle be reflected in the low-ionization broad emission-line (BEL) profiles [e.g., 29, 83, 84, 97, 98]. The BELs of particular interest are $H\alpha$ $\lambda 6563$, $H\beta$ $\lambda 4861$ and $Mg\ II$ $\lambda 2798$, because they are prominent in AGN spectra and are commonly used as tracers of dense, low-ionization gas in BLRs at low ($H\alpha$ at $z < 0.4$) and high redshift ($Mg\ II$ at $z < 2.5$).

Spectroscopic searches rely on the detection of the Doppler-shift in the BEL spectrum of an SBHB candidate that arise as a consequence of the binary orbital motion. This approach is reminiscent of a well established technique for detection of the single- and double-line spectroscopic binary stars. In both classes of spectroscopic binaries, the lines are expected to oscillate about their local rest frame wavelength on the orbital time scale of a system. In the context of the binary model, the spectral emission lines are assumed to be associated with the gas accretion disks that are gravitationally bound to the individual SBHs [29, 83, 84]. Given the velocity of the bound gas the BEL profiles from the SBH mini-disks are expected to be Doppler-broadened, similar to the emission lines originating in the broad line regions (BLRs) of AGNs. Moreover, several theoretical studies have shown that in unequal mass binaries accretion occurs preferentially onto the lower mass object [86–88], rendering it potentially more luminous than the primary. If so, this indicates that some fraction of SBHBs may appear as the single-line spectroscopic binaries.

This realization lead to a discovery of a number of SBHB candidates based on the criterion that the culprit sources exhibit broad optical lines offset with respect to the rest frame of the host galaxy [89–96].¹ Because this effect is also expected to arise in the case of a recoiling SBH receding from its host galaxy, the same approach has been used to flag candidates of that type [99–103]. The key advantage of the method is its simplicity, as the spectra that exhibit emission lines shifted relative to the galaxy rest frame are relatively straightforward to select from large archival data sets, such as the Sloan Digital Sky Survey (SDSS). Its main complication however is that the Doppler shift signature is not unique

¹In an alternative approach anomalous line ratios have been used to flag SBHB candidates with perturbed BLRs [97, 98].

to these two physical scenarios and complementary observations are needed in order to determine the nature of the observed candidates [e.g., 67, 104]. To address this ambiguity a new generation of spectroscopic searches has been designed to monitor the offset of the BEL profiles over multiple epochs and target sources in which modulations in the offset are consistent with the binary orbital motion [105, 107, 109–112, 114].

The E12 survey searched for $z < 0.7$ SDSS quasars whose broad $H\beta$ lines are offset by $\gtrsim 1000 \text{ km s}^{-1}$ and selected 88 quasars for observational followup from the initial group of $\sim 16,000$ objects. The followup observations span a temporal base line from few weeks to 12 years in the observer’s frame. Their goal is to measure the epoch-to-epoch modulation in the velocity offset of the $H\beta$ profiles and to test the binarity hypothesis. The relative velocity of the broad $H\beta$ profiles between different epochs has been measured with an uncertainty of $\lesssim 40 \text{ km s}^{-1}$ for 80% of the sample and $\lesssim 55 \text{ km s}^{-1}$ for the entire sample. After multiple epochs of followup, statistically significant changes in the velocity offset have been measured in 29/88 candidates and reported in their publications.

To describe the selection effects of the E12 survey, we therefore adopt two criteria, $V_{\text{lim}} = 1000 \text{ km s}^{-1}$ for the initial velocity offset and $\Delta V_{\text{lim}} = 40 \text{ km s}^{-1}$ for velocity modulations. It is worth noting that some spectroscopic campaigns do not impose a cut in the initial velocity offset and consider as SBHB candidates all AGN for which ΔV_{lim} is not zero and is consistent with the binary orbital motion [110–112, 115]. The advantage of the latter approach is that it starts with a larger statistical sample of AGN which are searched for apparent radial velocity variations. But the more stringent selection criteria in the former approach reduce the chance of confusion with regular AGN, the majority of which are characterized by $V_{\text{lim}} < 1000 \text{ km s}^{-1}$. In this case however it may take longer to detect radial velocity variations, since for circular orbits the SBHBs spend most of their time at the highest velocity offsets, where the projected acceleration is the lowest.

The assumption that the flux in the BEL is dominated by the portion of the gas flow bound to the secondary SBH is motivated by a number of theoretical studies of SBHBs

in circumbinary disks [e.g., 27, 28]. These studies show that binary torques can truncate a sufficiently cold circumbinary accretion flow and create an inner, low density cavity by evacuating the gas from the central portion of the circumbinary disk [42]. SBHs in this phase accrete by capturing the gas from the inner rim of the circumbinary disk and in this way can maintain mini-disks bound to individual holes. Hydrodynamic simulations of prograde binaries (rotating in the same sense as the circumbinary disk) indicate that in unequal mass binaries accretion occurs preferentially onto the smaller of the two objects, which orbits closer to the inner edge of the circumbinary disk [40, 46, 88, 169, 174]. Taken at face value, this suggests that the AGN associated with the secondary SBH may be more luminous than the primary, making the system analogous to single-line spectroscopic binary stars. This assumption does not change the observational results of the spectroscopic surveyes, only their inference about which of the SBHs is active. However, our model indicates that contribution to the optical broad emission lines by the BLR bound to the primary SBH is not negligible and can be dominant in the majority of SBHB configurations. This is because the surface area of the mini-disks Hence, we will consider separately the two assumptions and discuss their different inferences.

A.1.2 Key parameters of the model

We describe each SBHB configuration in terms of four intrinsic parameters: the total mass of the binary ($M = M_1 + M_2$), its mass ratio ($q = M_2/M_1 \leq 1$), the orbital separation (a), and the effective accretion rate through the disk ($\dot{M} = \dot{M}_1 + \dot{M}_2$). We only consider SBHBs on circular orbits for simplicity and provide constraints and considerations relevant for each parameter below.

We consider binaries with a mass between $10^7 M_\odot$ and $10^9 M_\odot$ and a range of values for q that is motivated by simulations of galaxy mergers that follow pairing of their SBHs. These show that SBH pairs with mass ratios $q < 0.1$ are less likely to form gravitationally bound binaries within a Hubble time at any redshift, primarily due to the inefficiency of

dynamical friction on the lower mass SBH [16, 19]. They also find that SBH pairs with initially unequal masses tend to evolve towards equal masses, through preferential accretion onto a smaller SBH. This trend is also consistent with that found by [170], based on the more recent Illustris simulation. We therefore adopt $0.1 \leq q \leq 1$ in this model, leading to a range of masses for the secondary SBHs, of $10^6 M_\odot \lesssim M_2 \leq 10^9 M_\odot$. This range is consistent with the masses of SBHs powering the regular AGN, not hosting SBHBs, commonly observed by SDSS and similar ground based, spectroscopic surveys.

We further consider a range of orbital separations that characterize gravitationally bound SBHBs. Qualitatively, a gravitationally bound SBHB forms when the amount of gas and stars enclosed within its orbit becomes comparable to M . This orbital separation is comparable to the radius of gravitational influence of a single SBH, where the circular velocity around the black hole equals the stellar velocity dispersion, $r_{\text{inf}} = GM/\sigma_*^2$. Combining this with the $M - \sigma_*$ relationship reported in [175] we obtain

$$r_{\text{inf}} \approx 14 M_8^{0.645} \text{ pc} = 2.9 \times 10^6 M M_8^{-0.355}. \quad (\text{A.1})$$

where $M_8 \equiv M/10^8 M_\odot$. We therefore assume that gravitationally bound binaries form when $a_{\text{max}} \sim 10^6 M$ for a wide range of SBHB masses. In this work we follow their evolution from a_{max} to $a_{\text{min}} = 10^2 M$, below which the tidal truncation is likely to render the BLR of the secondary SBH too compact to emit prominent broad optical emission lines.

For each SBHB configuration we parametrize the rate of orbital evolution of the binary using the effective accretion rate, $0.01\dot{M}_E \leq \dot{M} \leq \dot{M}_E$. Here $\dot{M}_E = L_E/\eta c^2$ is the Eddington accretion rate, η is the radiative efficiency, $L_E = 4\pi GMm_p c/\sigma_T$ is the Eddington luminosity, σ_T is the Thomson cross section and other constants have their usual meaning. For an SBHB embedded in the circumbinary disk, \dot{M} corresponds to the accretion rate through the geometrically thin and optically thick gas disk described by the Shakura-Sunyaev α -disk model [176].

It is worth noting that the Shakura-Sunyaev solution for an accretion disk around a single SBH implies that for each M and \dot{M} there is a critical radius beyond which the disk is gravitationally unstable to fragmentation and star formation. This truncation radius in general arises somewhere between $10^2 - 10^6 M$, depending on the properties of the disk and the mass of the SBH [see equations 15 and 16 in 32, for example]. This is commonly considered as the outer edge of the accretion disk beyond which the transport of angular momentum transitions from accretion torques to some other mechanism, either stellar or gaseous. Given that the structure and stability of circumbinary accretion disks is an area of active research, the existence and location of such outer truncation radius are still open questions. In light of this fundamental uncertainty we adopt \dot{M} as a proxy for the rate of angular momentum transport by any physical mechanism and do not require the presence of a stable circumbinary disk on all scales. Specifically, we use it to describe the rate of angular momentum transport that would correspond to that of a disk with an accretion rate \dot{M} around a single SBH with the mass M , equal to that of the SBHB.

In summary, we use the following parameters to describe the properties of the SBHB and selection effects of the E12 spectroscopic survey:

$$\begin{aligned}
10^7 M_\odot &\leq M \leq 10^9 M_\odot \\
0.1 &\leq q \leq 1 \\
10^2 M &\leq a \leq 10^6 M \\
0.01 \dot{M}_E &\leq \dot{M} \leq \dot{M}_E \\
V_{\text{lim}} = 1,000 \text{ km s}^{-1} &\quad \text{and} \quad \Delta V_{\text{lim}} = 40 \text{ km s}^{-1}
\end{aligned}$$

A.2 Intrinsic Probability Density Functions

A.2.1 Probability of a binary residing at separation a : $\rho(a)$

For each configuration we evaluate the rate of orbital evolution of the binary and a probability that it resides at some orbital separation, a . The total probability of finding the SBHB anywhere between the formation radius and coalescence can be defined as

$$\int_{a_{\max}}^0 \rho(a) da = \int_{10^6 M}^0 \frac{da}{\dot{a}} \frac{1}{t_{\text{tot}}} \equiv 1, \quad (\text{A.2})$$

where $\rho(a)$ is the probability density and t_{tot} is the total time it takes the SBHB to evolve from a_{\max} to coalescence. Because the rate of orbital evolution, \dot{a} , is a function of M , q and \dot{M} it follows that $\rho(a) \equiv \rho(a|M, \dot{M}, q)$. Hereafter, we adopt a simplifying assumption that the values of M , \dot{M} , and q are constant throughout the evolution of an SBHB, and discuss the implications in § A.4.2.

If the orbital evolution of the binary is driven by a circumbinary disk, the rate of shrinking of the SBHB orbit can be described in terms of the viscous inflow rate at the disk inner edge as

$$\dot{a}_{\text{visc}} = -\frac{3}{2}\alpha \left(\frac{h}{r}\right)^2 V_{\text{Kep}} \quad (\text{A.3})$$

where $\alpha = 0.1$ is the viscosity parameter, h/r is the aspect ratio of the disk, and $V_{\text{Kep}} = (2a/M)^{-1/2}$ is the circular orbital speed of the circumbinary disk with an inner edge at the radius $r = 2a$ [28]. Using the expression for h/r by [176], we obtain the infall rate for the gas pressure (outer) and radiation pressure dominated (inner) portion of the disk:

$$\dot{a}_{\text{gas}} = -4.24 \times 10^{-6} c \alpha^{4/5} \dot{m}^{2/5} \tilde{a}^{-2/5} M_8^{-1/5}, \quad (\text{A.4})$$

$$\dot{a}_{\text{rad}} = -1.21 \times 10^2 c \alpha \dot{m}^2 \tilde{a}^{-5/2}. \quad (\text{A.5})$$

where we introduce dimensionless parameters $\dot{m} = \dot{M}/\dot{M}_E$ and $\tilde{a} = a/M$, so that \dot{a} is

expressed in terms of the speed of light. SBHBs whose orbital evolution is driven by the emission of gravitational waves (GWs) shrink at the rate given by the expression from [177] for circular orbits

$$\dot{a}_{\text{gw}} = -12.8c \frac{q}{(1+q)^2} \tilde{a}^{-3} . \quad (\text{A.6})$$

We use the above expressions for the rate of orbital shrinking to calculate the time that a gravitationally bound SBHB spends evolving through each regime

$$t_x = \int_{a_{x,i}}^{a_{x,f}} \frac{da}{\dot{a}_x} , \quad (\text{A.7})$$

where “x” stands for “gas”, “rad” or “gw”, and a_i and a_f are the initial and final orbital separations which determine the boundaries of a particular regime, as defined in Appendix B. After evaluating the integral in equation A.7 for constant M , q and \dot{M} we obtain

$$t_{\text{gas}} = 8.3 \times 10^7 \text{ s } \alpha^{-4/5} \dot{m}^{-2/5} M_8^{6/5} \left[\tilde{a}_{\text{gas},i}^{7/5} - \tilde{a}_{\text{gas},f}^{7/5} \right] , \quad (\text{A.8})$$

$$t_{\text{rad}} = 1.2 \text{ s } \alpha^{-1} \dot{m}^{-2} M_8 \left[\tilde{a}_{\text{rad},i}^{7/2} - \tilde{a}_{\text{rad},f}^{7/2} \right] , \text{ and} \quad (\text{A.9})$$

$$t_{\text{gw}} = 9.6 \text{ s } \frac{(1+q)^2}{q} M_8 \left[\tilde{a}_{\text{gw},i}^4 - \tilde{a}_{\text{gw},f}^4 \right] . \quad (\text{A.10})$$

The total time to coalescence is given by

$$t_{\text{tot}} = t_{\text{gas}} + t_{\text{rad}} + t_{\text{gw}} . \quad (\text{A.11})$$

Note that the rate of evolution through the circumbinary disk can, in principle, be a function of q , when the mass of the circumbinary disk is smaller than the mass of the secondary SBH and the circumbinary disk is the sole driver of orbital evolution (a.k.a., the secondary-dominated regime), as discussed in [32] and [178] and adopted in the study by [111]. Here we make a different assumption, that even if the size of the circumbinary disk is finite, some other mechanism takes over angular momentum transport beyond the outer

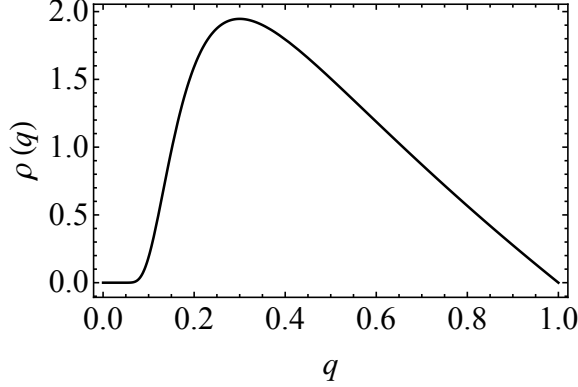


Figure A.1: Probability distribution function for SBHB mass ratios adopted in the Pflueger et al. [168] model. This is motivated by the results of cosmological simulations, as discussed in § A.2.2.

truncation radius, resulting in the steady orbital evolution of the SBHB described by some characteristic \dot{M} , regardless of the binary mass ratio. We discuss the implications of this assumption in § A.4.2.

A.2.2 Mass ratio probability distribution: $\rho(q)$

Even though the orbital evolution of bound SBHBs in this model only weakly depends on q , it is still expected that the mass ratio of the SBH pairs that successfully form bound binaries are characterized by some initial distribution. This distribution results from the cosmological evolution of SBHs through galactic mergers and accretion in stages preceding the formation of a gravitationally bound binary. In order to account for this property we adopt an analytic expression for probability density loosely motivated by cosmological simulations that follow mergers of galaxies [16, 19, 170] and dark matter halos [179, 180]

$$\rho(q) = \gamma q^{-0.3} (1 - q) e^{-\beta/q^2} \quad (\text{A.12})$$

where $\gamma = 2.79$ and $\beta = 3.28 \times 10^{-2}$ are the dimensionless parameters obtained from normalization of this distribution. Figure A.1 illustrates the shape of the resulting distribution function, which peaks at $q \approx 1/3$. In reality the mass ratio distribution of SBHBs

is a function of the total binary mass, redshift, and other parameters. We neglect these dependences for simplicity and note that because of the modularity of the model the above analytic expression can be readily replaced with a different prescription for $\rho(q)$. We discuss implications of these assumptions in § A.4.2.

A.3 Extrinsic Probability Density Functions

A.3.1 Probability of observing a binary with a significant velocity offset: P_V

The previous two sections describe the *intrinsic* probability that an SBHB exists at a certain orbital separation given the properties of the binary and some characteristic rate at which it evolves. In this section we discuss the ability of the spectroscopic searches to detect such binaries when they impose a selection criterion that the BEL profiles must be offset from the rest frame of the galaxy by some specified $V_{\text{lim}} \neq 0$.

According to the assumptions adopted by E12 and similar surveys this velocity offset can be attributed to the orbital motion of the secondary SBH, with orbital speed relative to the center of mass of the binary, $V_2 = c/(1+q) \tilde{a}^{1/2}$. Projected along the observer's line of sight this orbital speed corresponds to an observed velocity offset of

$$V_{\text{obs}} = \frac{1}{1+q} \frac{c}{\tilde{a}^{1/2}} \sin \phi \cos \theta \quad (\text{A.13})$$

where we define the angles in the coordinate system centered on the SBHB center of mass, so that the observer is located along the x -axis at infinity, ϕ defines the orbital phase of the secondary measured from the positive x -axis toward the positive y -axis, and θ is the angle between the orbital plane and the observer's line of sight.

The SBHB associated with this line-of-sight velocity can have a maximum orbital separation of

$$a_V^{\text{max}} = \frac{9 \times 10^4 M}{(1+q)^2} \left(\frac{V_{\text{obs}}}{10^3 \text{ km s}^{-1}} \right)^{-2}, \quad (\text{A.14})$$

Table A.1: Characteristic Orbital Separations

q	M (M_{\odot})	a_V^{\max} ($10^3 M$)	$a_{\Delta V}^{\min}$ ($10^2 M$)	$a_{\Delta V}^{\max}$ ($10^3 M$)
0.1	10^7	74	22	66
0.1	10^8	74	4.7	21
0.1	10^9	74	1.0	6.6
0.3	10^7	53	22	61
0.3	10^8	53	4.7	19
0.3	10^9	53	1.0	6.1
1	10^7	23	22	49
1	10^8	23	4.7	16
1	10^9	23	1.0	4.9

Note. — a_V^{\max} and $a_{\Delta V}^{\max}$ – largest detectable values of SBHB orbital separation set by the selection effects of the E12 survey. $a_{\Delta V}^{\min}$ – minimum orbital separation below which the model assumption $\Omega\Delta t \ll 1$ breaks down.

where we set V_{obs} equal to $V_{\text{lim}} = 1000 \text{ km s}^{-1}$. Table A.1 illustrates the values of a_V^{\max} set by this cutoff for several different SBHB configurations. It is worth noting that, if the spectroscopic surveys instead of the secondary provide a measurement of the radial velocity of the primary SBH, the value of a_V^{\max} would be smaller by a factor of q^2 .

We infer the probability for detection of an SBHB by placing the observer on a sphere, centered on the SBHB, and by considering all SBHB configurations where the angles θ and ϕ are such that $V_{\text{obs}} \geq V_{\text{lim}}$ and the velocity offset from the binary motion is detected. The probability of detection is then given by the ratio of the surface area where this condition is satisfied and the total area of the sphere. The surface area where the condition is satisfied is contiguous and confined within the range of θ and ϕ , which can be obtained from equation A.13 as

$$\begin{aligned}
 \theta &= [0, A] = \left[0, \arccos \left(\frac{\zeta}{\sin \phi} \right) \right] \text{ and} \\
 \phi &= [C, \frac{\pi}{2}] = \left[\arcsin \zeta, \frac{\pi}{2} \right],
 \end{aligned} \tag{A.15}$$

where A and C are the parameters corresponding to the expressions defined in the second square bracket, used as integration limits in equation A.16, and $\zeta \equiv (1 + q) \tilde{a}^{1/2} V_{\text{lim}}/c$ is a dimensionless parameter. The probability for detection of the velocity offset is then:

$$P_V = \frac{2}{\pi} \int_C^{\pi/2} d\phi \int_0^A \sin \theta d\theta . \quad (\text{A.16})$$

We express $\theta = \theta(\phi)$, since this form simplifies the integral considerably and use symmetry to integrate over one octant and multiply the result by 8. The analytic solution of this integral is

$$P_V = 1 - \frac{2}{\pi} \left[\arcsin \zeta + \zeta \ln \left(\frac{1 + \cos(\arcsin \zeta)}{\zeta} \right) \right] . \quad (\text{A.17})$$

A.3.2 Probability of observing a binary with a significant velocity modulation: $P_{\Delta V}$

The criterion used by *all* spectroscopic searches to select viable SBHB candidates, regardless of their assumptions about V_{lim} , is that the epoch-to-epoch modulation in the observed line of sight velocity must be different from zero and consistent with the SBHB orbital motion. In practice, this implies $\Delta V_{\text{obs}} \geq \Delta V_{\text{lim}}$ in order for the SBHB to be detected, where

$$\begin{aligned} \Delta V_{\text{obs}} &= V_2' \sin(\phi + \Omega \Delta t) \cos \theta - V_2 \sin \phi \cos \theta \\ &\approx \frac{1}{1 + q} \frac{c}{\tilde{a}^{1/2}} \cos \phi \cos \theta \sin(\Omega \Delta t) . \end{aligned} \quad (\text{A.18})$$

Here V_2 and V_2' are the orbital velocities of the secondary SBH in the earlier and later epoch of observation, respectively, and $\Omega = c^3/(GM\tilde{a}^{3/2})$ is the angular velocity of the SBHB on a circular orbit. Δt is the time elapsed between the two measurements of the velocity offset, defined in the frame of the SBHB, which for the E12 search corresponds to time scales from weeks to years. We adopt $\Delta t = 1$ yr hereafter as a representative value.

Since most SBHBs targeted by the E12 search are expected to have longer orbital periods than the observational baseline, we assume that they traverse only a small portion

of their orbit on this time scale. Consequently, $V_2 \approx V_2'$ and $\Omega\Delta t \ll 1$, leading to the approximation in equation A.18 [see also 111, for a similar approach]. This assumption in our model breaks down when $\Omega\Delta t \sim 1$ and the time between subsequent observations becomes comparable to the orbital period of the SBHB. We calculate the orbital separations at which this happens for different configurations of SBHBs and list them in Table A.1 as $a_{\Delta V}^{\min}$. Note that this is merely a limitation of the model presented here, which does not preclude the use of velocity modulation of the broad lines as a criterion for selection of SBHBs with $a < a_{\Delta V}^{\min}$ in observations.

From equation A.18 we find the maximum orbital separation of the SBHB associated with the measured ΔV_{obs} as

$$a_{\Delta V}^{\max} = \frac{2.2 \times 10^4 M}{\sqrt{(1+q)}} \left(\frac{\Delta V_{\text{obs}}}{40 \text{ km s}^{-1}} \right)^{-1/2} \left(\frac{\Delta t}{1 \text{ yr}} \right)^{1/2} M_8^{-1/2}, \quad (\text{A.19})$$

where we have taken $\sin(\Omega\Delta t) \approx \Omega\Delta t$, which is justified in the previous paragraph. Note also that for the purposes of deriving equation A.19 we have adopted the fiducial value $\Delta V_{\text{obs}} = \Delta V_{\text{lim}} = 40 \text{ km s}^{-1}$. It follows that all SBHB candidates selected by this survey have orbital semi-major axes smaller than $a_{\Delta V}^{\max}$. For illustration we list the values of $a_{\Delta V}^{\max}$ corresponding to different SBHB configurations in Table A.1. If the spectroscopic surveys provide measurements of the radial velocity of the primary SBH instead of the secondary, the value of $a_{\Delta V}^{\max}$ would be smaller by a factor of $q^{1/2}$.

The spectroscopic searches that impose the selection cutoff in terms of both V_{lim} and ΔV_{lim} have two upper limits on the maximum value of the SBHB orbital separation, corresponding to a_V^{\max} and $a_{\Delta V}^{\max}$. In this case, the true detection limit is given by the smaller of the two values. Based on this limit, our model implies that assuming a cadence of observations comparable to $\Delta t = 1 \text{ yr}$, and the selection criteria adopted in this model, SBHBs with orbital separations $< \text{few} \times 10^4 M$ are in principle detectable by spectroscopic searches. If we integrate the probability density $\rho(a)$, given in equation A.2, from $a_{\min} = 10^2 M$

to this cutoff, we find that the SBHBs of interest only reside in this range of separations for $\leq 0.5\%$ of their lifetime. It follows that for every one detected there should be > 200 undetected gravitationally bound SBHBs with similar properties at larger separations, once the effects of the SBHB orbital orientation are taken into account in addition to their rate of evolution.

Solving for the limits on θ and ϕ , for which the criterion $\Delta V_{\text{obs}} \geq \Delta V_{\text{lim}}$ is satisfied, we obtain

$$\begin{aligned}\theta &= [0, B] = \left[0, \arccos \left(\frac{\xi}{\cos \phi} \right) \right] \\ \phi &= [0, D] = [0, \arccos \xi]\end{aligned}\tag{A.20}$$

where again we define θ as $\theta(\phi)$, which allows for exact analytic integration of $P_{\Delta V}$. The parameters B and D set the integration limits for $P_{\Delta V}$ and ξ is the dimensionless parameter defined as

$$\xi \equiv \frac{(1+q) \tilde{a}^{1/2}}{\sin(\Omega \Delta t)} \frac{\Delta V_{\text{lim}}}{c}\tag{A.21}$$

The resulting probability of detection of an SBHB with a given velocity modulation can be defined in the same way as in equation A.16. The analytic solution of this integral is

$$P_{\Delta V} = \frac{2}{\pi} \left[\arccos \xi - \xi \ln \left(\frac{1 + \sin(\arccos \xi)}{\xi} \right) \right].\tag{A.22}$$

Note that $P_{\Delta V}$ is derived in an approximate way in [111] and that the two solutions differ.

A.3.3 Probability of simultaneous measurement of V_{obs} and ΔV_{obs} : $P_{V, \Delta V}$

The spectroscopic searches that only consider the criterion $\Delta V_{\text{obs}} \geq \Delta V_{\text{lim}}$ for selection of SBHB candidates should use $P_{\Delta V}$ as the relevant probability distribution. The spectroscopic searches that additionally impose $V_{\text{obs}} \geq V_{\text{lim}}$ are looking for SBHB candidates satisfying both criteria *simultaneously*. In practice this means that, for every plausible

SBHB configuration we must find the range of angles of θ and ϕ on the sky for which both criteria are satisfied. The overlap can be determined by examining the integration limits for P_V and $P_{\Delta V}$ given in equations A.15 and A.20 for the first octant. The lower limits on θ are in both cases zero therefore, the lower limit of the θ integral of $P_{V,\Delta V}$ is zero. The upper limits on θ for P_V and $P_{\Delta V}$ differ, implying that the overlap is limited by the smaller of A and B , or $\min(A, B)$. Examining the limits of ϕ shows that the integration lower limit must be $\min(C, D)$ and its upper limit, $\min(D, \pi/2)$.

$$P_{V,\Delta V} = \frac{2}{\pi} \int_{\min(C,D)}^{\min(D,\pi/2)} d\phi \int_0^{\min(A,B)} \sin \theta d\theta \quad (\text{A.23})$$

This results in a probability

$$P_{V,\Delta V} = \frac{2}{\pi} \int_{\min(C,D)}^{\min(D,\pi/2)} \nu(A, B) d\phi \quad (\text{A.24})$$

where we have integrated over θ and provided a simplified expression in terms of ϕ that can be integrated numerically. The function ν is defined as

$$\nu(A, B) \equiv \left[1 - \frac{\cos A}{2} - \frac{\cos B}{2} - \left| \frac{\cos B}{2} - \frac{\cos A}{2} \right| \right]. \quad (\text{A.25})$$

Note that if $D < C$ the ϕ the integral returns a zero probability (i.e., no overlap), since all angles are considered in the first octant and must be $\leq \pi/2$.

A.4 Discussion on the Likelihood Model

A.4.1 Benefits of long-term monitoring and complementary searches for SBHBs

The likelihood distribution presented in the previous section can, in principle, be calculated for every single SBHB candidate, given a minimum of two spectroscopic measurements of velocity offset, necessary to establish V_{obs} and ΔV_{obs} . The true power of SBHB monitoring however comes from repeated measurements, which define the velocity curve of the SBHB

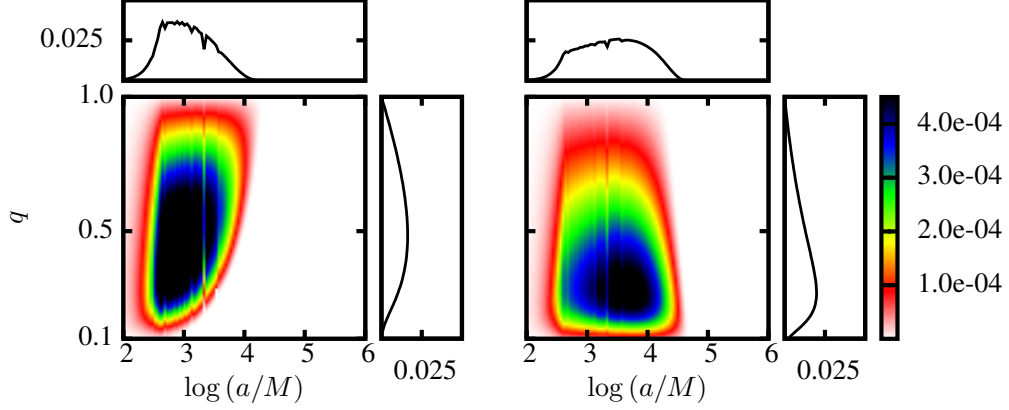


Figure A.2: Two-dimensional cuts of the multi-variate likelihood for the E12 search given by $\mathcal{L} = \rho(a) \times \rho(q) \times P_{V,\Delta V}$. The likelihood is calculated by assuming the BLR bound to the primary black hole (left panel), or the secondary black hole (right panel). Likelihood is calculated for SBHB with $M = 10^7 M_\odot$ and $\dot{M} = 0.1 \dot{M}_E$. Color marks the value of the likelihood, \mathcal{L} . An open source python script for calculation and plotting of the likelihood is available online at https://github.com/bbhpsu/Pflueger_et_al18.

with increasing confidence. More specifically, repeated measurements provide constraints on $V_2 \cos \theta$, the amplitude of the velocity curve and the orbital period P . Because $V_2 \cos \theta = V_{\text{obs}} / \sin \phi \geq V_{\text{obs}}$, the amplitude provides a stronger constraint on the orbital separation than just two measurements of the velocity offset.

$$\tilde{a} < (1 + q)^{-2} \left(\frac{V_2 \cos \theta}{c} \right)^{-2}. \quad (\text{A.26})$$

Note that the spectroscopic measurements alone cannot uniquely confirm the identity of an SBHB, because for the majority of configurations considered in this model the binary orbital period is longer than the temporal baseline of observations. This precludes measurement of multiple orbital cycles, which has traditionally been used as a criterion for binarity in stellar systems. Therefore, in the case of SBHB candidates the spectroscopic observations need to be supplemented by additional, independent observational evidence that can help to further elucidate their nature.

Some of the more promising complementary approaches include the direct VLBI imaging at millimeter and radio wavelengths of nearby SBHB candidates ($z \lesssim 0.1$) with sep-

arations $a \gtrsim 0.01$ pc [181]. The two approaches are complementary since VLBI is not a surveying technique and it depends on other approaches to define the candidate sample. The emission properties of SBHB candidates at these wavelengths are however largely unknown and difficult to uniquely predict from theory, making such observations risky but potentially highly rewarding, should any SBHBs be detected.

It is worth noting that SBHBs that are in principle accessible to spectroscopic surveys also overlap with a population targeted by the ongoing photometric surveys and PTAs. These are the SBHBs with orbital periods of a few years

$$P = 3.1 \text{ yr} \left(\frac{a}{10^3 M} \right)^{3/2} M_8 \quad (\text{A.27})$$

corresponding to the more compact systems ($a \lesssim 0.01$ pc) considered in this model. The possibility of detection of SBHB candidates with more than one technique is exciting as it may provide additional means to test their nature.

Note that candidates with velocity curves which are inconsistent with the SBHB model can be ruled out based on spectroscopic observations, even if they have been monitored for less than a full orbital cycle. Hence, the spectroscopic followup alone can be effective in narrowing down the sample of SBHB candidates by rejecting those inconsistent with the binarity hypothesis. This approach is adopted and laid out in [158].

A.4.2 Simplifying assumptions and their implications

One important assumption made in this work is that M , q , and \dot{M} are constant throughout the SBHB evolution and that the binary orbit remains circular. While the evolution in time of any of these parameters is fairly uncertain, there is general understanding of how they may affect the binary orbit. For example, the SBHB may increase its mass through accretion of gas, which is assumed to happen for at least a fraction of SBHB evolutionary time, when the SBHB is detectable through emission of broad lines.

Similarly, simulations of SBHBs in circumbinary disks find that the secondary SBH tends to accrete at a higher rate than the primary [40, 46, 86, 88]. If so, the early evolution of the SBH pairs towards more equal-mass ratios, discussed in § A.1.2, is expected to continue after the gravitationally bound SBHB has formed. This is, for example, indicated by the Illustris simulation in which $q \approx 1$ pairs dominate over all other mass ratios at SBH separations of ~ 1 kpc [see Figure 2 in 170]. If this mode of growth is favored, it is plausible that by the time they reach orbital separations accessible to the spectroscopic searches ($a \lesssim \text{few} \times 10^4 M$) the SBHB may already be quite close to $q \approx 1$. The increase in M and q can lead to the shrinking of the SBHB orbit as a consequence of conservation of orbital angular momentum, and so can evolution from an initially eccentric to a circular orbit. It is however expected that these processes are secondary to the circumbinary disk torques in driving the orbital evolution [see 41, for a comprehensive review of this issue], which is in our model encoded in \dot{M} .

It is worth emphasizing that in this model \dot{M} is used as a free parameter that describes an effective rate of orbital evolution that can arise due to the circumbinary disk *combined* with additional mechanisms unrelated to accretion torques. As such, \dot{M} sets the upper limit on but does not imply the mass accretion rate onto the two SBHs throughout their orbital evolution². The SBHBs can also be transported to sub-parsec scales through (scattering) interactions with stars [21–23, 25]. Those SBHBs that reside in clumpy disks may undergo multiple scatterings resulting in stochastic orbital evolution [10, 11]. These processes are not explicitly captured in this analytic model, which assumes that \dot{M} does not change in time or as a function of the orbital separation of a binary. It is, nevertheless, expected that once a circumbinary disk is in place, the evolution of the SBHB due to its interaction with this disk should proceed efficiently, on a time scale shorter than that for evolution by gravitational scattering. This can be ascribed to the “conveyor belt” nature of the disk which transports the SBHB angular momentum to large distances, where it takes only a

²For this reason we refrain from making predictions about the luminosity or the growth in mass of the SBHs based on \dot{M} .

small amount of mass to absorb it.

It is worth noting that the rate of binary evolution is expected to decrease in the *secondary-dominated regime*: the stage in which the mass of the secondary SBH dominates over the local circumbinary disk, and the circumbinary disk is the sole driver of orbital evolution [32, 178]. In this scenario, the disk cannot effectively “absorb” the SBHB’s orbital angular momentum leading to longer residence times of the binary. We do not account for this effect and as a consequence possibly overestimate the rate of evolution of SBHBs in this regime. For example, SBHBs with $M > 10^7 M_\odot$ and $q > 0.1$ transition into the secondary-dominated regime when they are within the detection window of spectroscopic searches, at separations $\lesssim \text{few} \times 10^4 M$ [see Figures 3 and 4 in 32]. The longer residence-time of SBHBs in this range would lead to an increased likelihood of their detection, relative to predictions reported in this work.

In this work we only consider SBHBs on circular orbits for simplicity. Allowing for eccentric orbits would primarily result in larger maximum orbital separations given by a_V^{\max} and $a_{\Delta V}^{\max}$, because eccentric binaries sweep over a wider range of speeds and accelerations over the course of one orbit, relative to their circular counterparts. Therefore, eccentric SBHBs that reach the detection window of spectroscopic searches would be characterized by a wider range of orbital separations. Their probability and likelihood distributions would nevertheless remain qualitatively similar to those reported in this work. Taking into consideration that addition of one more free parameter (eccentricity) would result in a considerably more complicated model, we choose a simpler (circular) model without much loss of generality.

An implicit assumption made in our model is that the optical BLR of the secondary SBH is present and its signatures detectable over a range of relevant SBHB separations that span from $10^2 M$ to $\text{few} \times 10^4 M$. In reality, the extent and emission properties of the BLRs surrounding SBHs in a binary are largely unknown. Even without tangible proof, their existence seems plausible in at least a fraction of SBHBs, because they are so ubiqui-

tous in regular AGN. This question can be directly tested by a combination of observational techniques described in § A.4.1 once a robust sample of SBHBs is established. For example, if the spectroscopic surveys show a lack of SBHBs, relative to the numbers detected by the photometric surveys or inferred from the PTA measurements, this would point to phenomenology different from BLRs of regular AGN.

Finally, in this model we make no assumptions about the underlying SBHB mass function (instead, M is treated as a free parameter) and luminosity distribution function, because they are highly uncertain. Should these properties be better constrained in the future, they can be added to the model a posteriori.

APPENDIX B

CHARACTERISTIC ORBITAL SEPARATIONS

Here we describe the calculation of characteristic binary orbital separations which determine the boundaries between the regimes that an SBHB evolves through. These orbital separations represent the limits of the integral in equation A.7, used to evaluate the time that SBHB spends in each evolutionary regime. Namely, after the gravitationally bound binary forms at $a_{\max} \approx 10^6 M$, it can evolve through the gas pressure dominated, radiation pressure dominated region of the circumbinary disk, and finally, GW regime to coalescence. We find that while some SBHBs can pass through all three regimes, other binaries may transition into the GW phase directly from the gas pressure dominated regime. Which scenario plays out depends on the properties of the binary and the circumbinary disk.

We therefore evaluate the characteristic orbital separations for all relevant transitions by equating the infall rates given in equations A.4–A.6 as follows

$$\dot{a}_{\text{gas}} = \dot{a}_{\text{rad}}, \quad a_{\text{ch1}} = 3550 M \alpha^{2/21} \dot{m}^{16/21} M_8^{2/21}, \quad (\text{B.1})$$

$$\dot{a}_{\text{rad}} = \dot{a}_{\text{gw}}, \quad a_{\text{ch2}} = 1.13 \times 10^{-2} M \alpha^{-2} \frac{q^2}{(1+q)^4} \dot{m}^{-4}, \quad (\text{B.2})$$

$$\dot{a}_{\text{gas}} = \dot{a}_{\text{gw}}, \quad a_{\text{ch3}} = 311 M \alpha^{-8/26} \frac{q^{10/26}}{(1+q)^{10/13}} \dot{m}^{-2/13} M_8^{1/13}. \quad (\text{B.3})$$

APPENDIX C

DEPENDENCE OF STATISTICAL DISTRIBUTION FUNCTIONS ON F_c

In this section we investigate the dependence of the distribution functions, characterizing the modeled profile shapes, on the value of F_c , a cutoff used to mimic some fiducial level of spectral noise. As noted in § 3.2.2 we adopt $F_c = 0.01$ in calculation of statistical properties presented in this work but do not introduce actual fluctuations due to noise to the profiles. Figure C.1 illustrates how different noise levels impact the line profile shapes, where in addition to $F_c = 0.01$ we examine the values of 0.1 and 0.2. With “noise” subtracted from the profile, we rescale the flux above this cutoff so that the maximum flux measured at the peak wavelength always has the value of 1.0.

One apparent consequence of the higher level of noise is that it can mask low intensity features present in the profile wings and hence, affect its statistical properties. The middle and right panel of Figure C.1 show that when the noise conceals the low intensity feature between 4900 and 5200 Å the profile centroid (marked by the green vertical line) changes from $C = 4842$ Å to 4830 Å to 4828 Å for $F_c = 0.01$, 0.1 and 0.2, respectively. The sensitivity to the level of noise is particularly pronounced for higher order distribution functions that depend on the term $(\lambda_i - C)^n$, where index n represents the order (see § 3.2.2). For example, the value of AI, which is proportional to the third moment, indicates that the profile changes from asymmetric (AI = 2.21 at $F_c = 0.01$) to relatively symmetric (AI = 0.35 at $F_c = 0.1$) with increasing F_c . Similarly, the value of KI, which is proportional to the fourth moment, indicates a transition from a cuspy (KI = 9.75 at $F_c = 0.01$) to a more boxy profile (KI = 2.02 at $F_c = 0.1$).

This behavior of higher order distribution functions is illustrated in Figure C.2 which shows the AI-KI maps associated with eccentric SBHB systems and calculated for different values of F_c . They show that the overall footprint of the 2-dimensional distribution

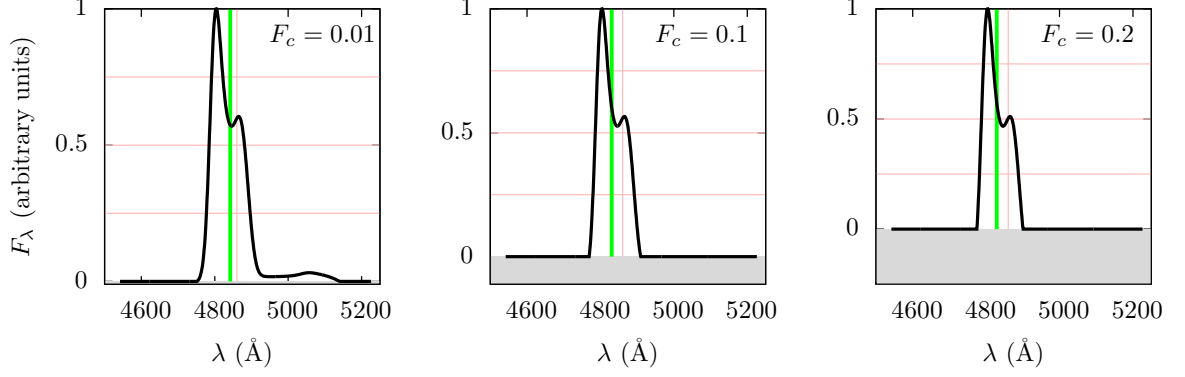


Figure C.1: Effect of different cutoff values F_c , representing some fiducial level of spectral noise, on a simulated line profile shape. For each profile the location of the centroid and the rest wavelength are marked by the green and pink vertical lines, respectively. The flux above the “noise” level is rescaled so that the maximum flux measured at the peak wavelength has the value of 1.0.

increases for the higher levels of noise while at the same time the average profile (traced by the blue and green colors) becomes more boxy.

The value of the Pearson skewness coefficient, AIP, on the other hand exhibits a weak dependance on F_c . For the profile in Figure C.1 for example, $AIP = 0.21$ at $F_c = 0.01$ and $AIP = 0.19$ at $F_c = 0.1$. As discussed earlier, the AI and AIP provide different measures of the profile asymmetry. This is because the AI sensitively depends on the low intensity features in the profile wings and AIP diagnoses the asymmetry in the bulk of the profile. This property of AIP is captured in Figure C.3, which shows the AIP-PS maps associated with eccentric SBHB systems. The map footprint and distribution of values in different panels show little change as both AIP and PS are weak functions of F_c .

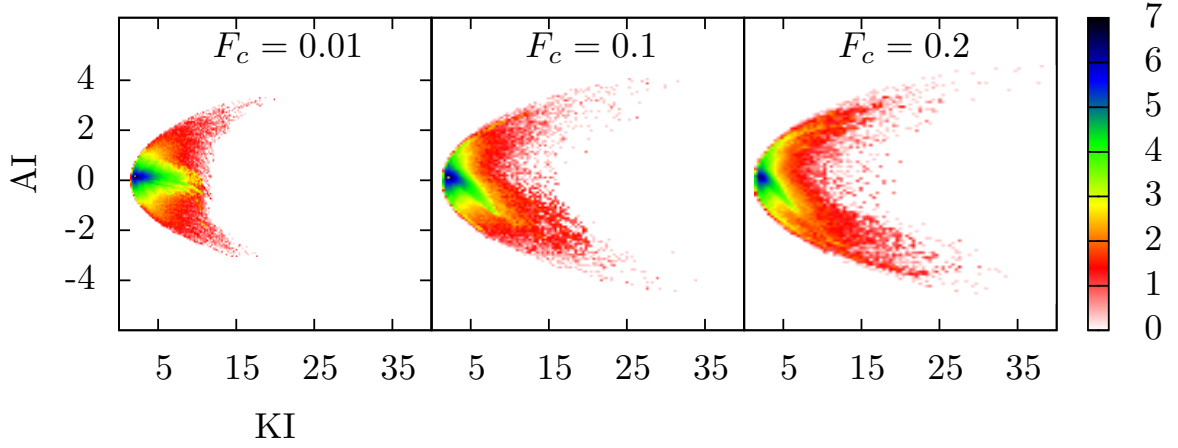


Figure C.2: AI-KI maps for profiles associated with eccentric SBHB systems calculated for different values of F_c . Map footprint and distribution of values vary for different adopted levels of noise indicating that AI and KI are sensitive functions of F_c .

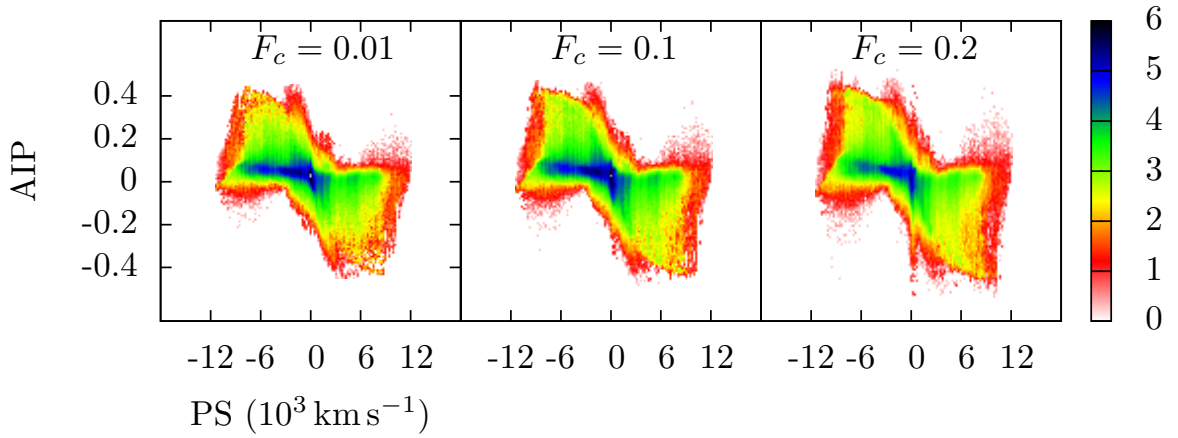


Figure C.3: AIP-PS maps for profiles associated with eccentric SBHB systems calculated for different values of F_c . Map footprint and distribution of values in different panels show little change as both AIP and PS are weak functions of F_c .

APPENDIX D

ANIMATION

Figure D.1: Orbital evolution of the triple-disk accretion flow around SBHB. The embedded animation can be viewed in Adobe Reader version ≥ 7 (no longer supported on Linux). Alternatively, click [\[here\]](#) to open the supplemental file (Eclipse.gif, 393K).

APPENDIX E

COMPUTATION OF PRINCIPAL COMPONENTS

In this section we briefly outline the approach used to calculate principal components and eigenprofiles for the profiles in our synthetic database. Each profile in the database is defined within the frequency range $(0.93, 1.07) \nu_0$ and is discretized using 600 equal frequency bins, where ν_0 represents the rest frame frequency of the $H\beta$ emission line. We carry out the analysis in frequency space and only convert to wavelength space for visualization purposes (i.e., in figures). Moreover, all profiles are normalized in such a way that their maximum flux values are unity.

The database of all modeled profiles can then be described as a matrix \mathbf{F} of size $[N \times M]$, where $N \approx 4.25 \times 10^7$ rows represent the number of profiles and $M = 600$ columns represent the number of frequency bins. The average profile of the database can be calculated as a vector $\bar{\mathbf{F}}$ of size $[1 \times M]$ with elements

$$\bar{F}_m = \frac{1}{N} \sum_{n=1}^N F_m^n . \quad (\text{E.1})$$

The average profile of the synthetic database, shown in the top left panel of Figure E.1, is single peaked and fairly symmetric. All profiles in the synthetic database can be derived as a linear combination of the average profile and a finite number of eigenprofiles calculated for the synthetic database

$$F_m^n \approx \bar{F}_m + \sum_{i=1}^I T_i^n P_m^i , \quad (\text{E.2})$$

where “ \approx ” indicates that the profile reconstruction calculated in this way is an approximation of the actual profile due to truncation of the linear series in equation E.2. Here, \mathbf{T} is a matrix of size $[N \times I]$ containing the principal components corresponding to each eigenprofile. In this work we choose $I = 20$ principal components, which is sufficient to precisely

reconstruct all synthetic profiles in our database, and note that the choice $I = M = 600$ (the maximum possible value) does not improve the accuracy of reconstruction. The matrix \mathbf{P} of size $[M \times I]$ describes the set of eigenprofiles used to decompose the profiles in the modeled database and each column of this matrix represents one eigenprofile. Furthermore, the matrix \mathbf{P}' with the size $[I \times M]$ is the transpose of \mathbf{P} .

The first-order eigenprofile, \mathbf{P}_1 , is a unit vector pointing in the direction with the largest projected variance of the profile database. Similarly, the k^{th} -order eigenprofile, \mathbf{P}_k , is a unit vector pointing in the direction with the largest projected variance and is perpendicular to the $k - 1$ lower-order eigenprofiles. For example,

$$\mathbf{P}_1 = \arg \max_{\mathbf{V}: \mathbf{V}'\mathbf{V}=1} (\mathbf{V}'\mathbf{X}'\mathbf{X}\mathbf{V}) \quad (\text{E.3})$$

$$\mathbf{P}_2 = \arg \max_{\mathbf{V}: \mathbf{V}'\mathbf{V}=1, \mathbf{V}'\mathbf{P}_1=0} (\mathbf{V}'\mathbf{X}'\mathbf{X}\mathbf{V}) \quad \dots \quad (\text{E.4})$$

Here, \mathbf{V} is a unit vector pointing in some arbitrary direction and \mathbf{X} is a matrix with elements $X_m^n = F_m^n - \overline{F}_m$. $\mathbf{X}'\mathbf{X}$ therefore represents the variance of the database and is proportional to its covariance matrix. $\mathbf{V}'\mathbf{X}'\mathbf{X}\mathbf{V}$ represents the projection of the variance along the direction \mathbf{V} . The first-order principal axis, \mathbf{P}_1 , is selected to be the unit vector \mathbf{V} that maximizes the quantity $\mathbf{V}'\mathbf{X}'\mathbf{X}\mathbf{V}$. The second-order principal axis, \mathbf{P}_2 , points in a different direction \mathbf{V} that maximizes $\mathbf{V}'\mathbf{X}'\mathbf{X}\mathbf{V}$ and is perpendicular to \mathbf{P}_1 . Note that here, the principal axes are the eigenvectors of the matrix $\mathbf{X}'\mathbf{X}$, and the projected variances, $\mathbf{V}'\mathbf{X}'\mathbf{X}\mathbf{V}$, are the eigenvalues.

Since $\mathbf{X}'\mathbf{X}$ is positive semi-definite, its eigenvectors can be found by using the process of singular value decomposition. We use the following notation to describe this procedure

$$\mathbf{P} = \text{svd}(\mathbf{X}'\mathbf{X}) . \quad (\text{E.5})$$

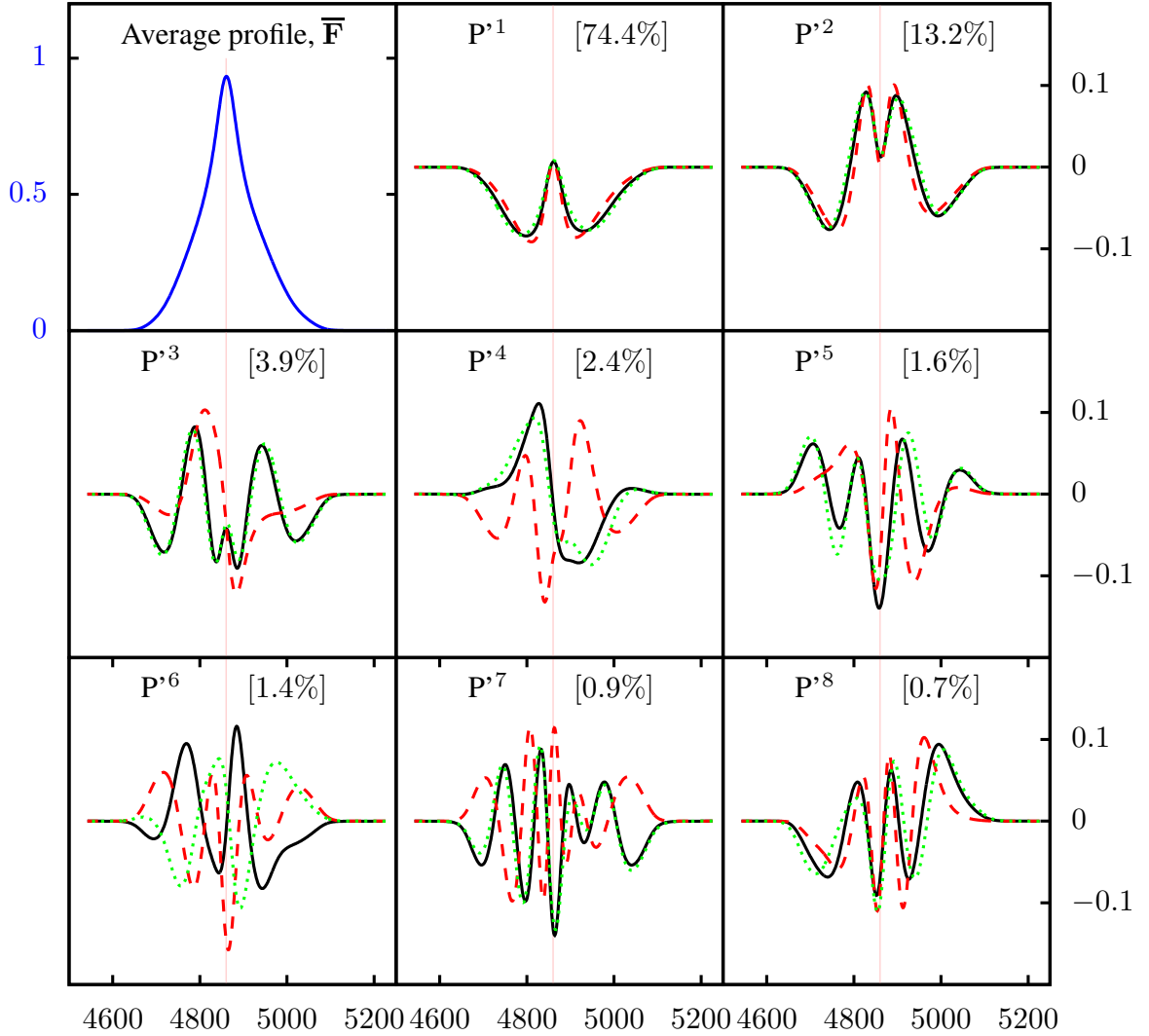


Figure E.1: The average profile (top left panel) and the first eight eigenprofiles (solid black lines) calculated for our synthetic database. The number in brackets marks the percentage of the database variance that corresponds to each eigenprofile. The red dashed (green dotted) line marks the eigenprofiles calculated for the portion of the modeled profiles from circular (eccentric) SBHBs.

The shapes of the first eight eigenprofiles, formally expressed as vectors \mathbf{P}'^i with size $[1 \times M]$, are shown in Figure E.1 as black curves. For example, the top middle panel of Figure E.1 shows that \mathbf{P}'^1 is an almost symmetric profile that accounts for 74.4% of the variance of the database profiles, \mathbf{P}'^2 accounts for 13.2%, and so on.

In our calculation, we divide the synthetic database into two portions, consisting of profiles calculated for the SBHBs on circular orbits (denoted by ${}^c\mathbf{X}$) and for the SBHBs on eccentric orbits (${}^e\mathbf{X}$). We compute the covariance for each of the subsets, ${}^c\mathbf{X}$ and ${}^e\mathbf{X}$, before obtaining the total covariance by applying the partition relation

$$(\mathbf{X}'\mathbf{X})_b^a = ({}^c\mathbf{X}'{}^c\mathbf{X})_b^a + ({}^e\mathbf{X}'{}^e\mathbf{X})_b^a + \frac{{}^cN {}^eN}{({}^cN + {}^eN)} ({}^c\bar{F}_a - {}^e\bar{F}_a) ({}^c\bar{F}_b - {}^e\bar{F}_b) . \quad (\text{E.6})$$

Equation E.6 is numerically convenient because it allows parallel computing of $\mathbf{X}'\mathbf{X}$. While we only divide the data into circular and eccentric SBHB cases (in order to compare them), one can in principle repeat this procedure for an arbitrary number of data subsets, making the analysis of large datasets more efficient. The parallelization can then be achieved by calculating the average profiles, ${}^c\bar{\mathbf{F}}$ and ${}^e\bar{\mathbf{F}}$, as in equation E.1, and by taking advantage of the property of the covariance matrix

$$(\mathbf{X}'\mathbf{X})_b^a = \sum_{n=1}^N (F_a^n - \bar{F}_a) (F_b^n - \bar{F}_b) = \sum_{n=1}^N F_a^n F_b^n - \frac{1}{N} \sum_{n=1}^N F_a^n \sum_{n=1}^N F_b^n . \quad (\text{E.7})$$

Figure E.1 shows that within the first 2 orders, the eigenprofiles for circular and eccentric cases are quite similar. The first significant difference between the two appears in the third order, where ${}^e\mathbf{P}'^3$ has a much more complex shape than ${}^c\mathbf{P}'^3$. This is in agreement with the finding reported in Chapter 3 that eccentric SBHBs can in principle produce more complex profiles due to a wider range of orbital velocities sampled by the orbiting binary. The eigenprofiles calculated for the entire database (including both circular and eccentric SBHBs) are more similar to those of the eccentric than circular SBHBs. This because our database contains a comparable number of eccentric cases (${}^eN = 24,546,000$) and circular

cases (${}^cN = 17,816,400$).

APPENDIX F
RESULTS OF ANALYSIS FOR 88 SBHB CANDIDATES

Table F.1: Inferred values of the binary parameters for the SBHB candidates from the E12 sample. SDSS – Name of the SBHB candidate. $\log(a/M)$ – average value of $\log(a/M)$ with one standard deviation. \mathcal{S}_a – entropy associated with the value of $\log(a/M)$. q – average value of the mass ratio with one standard deviation. \mathcal{S}_q – entropy associated with the value of q . $\log \tau_0$ – average value of $\log \tau_0$ with one standard deviation. \mathcal{S}_{τ_0} – entropy associated with the value of $\log \tau_0$. $\log(F_2/F_1)$ – average value of $\log(F_2/F_1)$ with one standard deviation. $\mathcal{S}_{F_2/1}$ – entropy associated with the value of $\log(F_2/F_1)$. QI – Quality index. E12 – 0 (1) corresponds to the SBHB candidates for which a statistically significant radial velocity modulation has not (has) been measured from observations.

	SDSS	$\log(a/M)$	\mathcal{S}_a	q	\mathcal{S}_q	$\log \tau_0$	\mathcal{S}_{τ_0}	$\log(F_2/F_1)$	$\mathcal{S}_{F_2/1}$	QI	E12
1	1224	4.44 ± 0.35	0.38	0.39 ± 0.19	0.80	-2.81 ± 1.64	0.43	-1.24 ± 0.63	0.58	-0.09	1
2	2444	4.89 ± 0.63	0.86	0.58 ± 0.22	0.84	-0.26 ± 1.27	0.78	-0.07 ± 0.34	0.29	0.46	0
3	15530	4.05 ± 0.30	0.55	0.75 ± 0.22	0.83	0.27 ± 0.81	0.41	-0.02 ± 0.46	0.42	0.44	1
4	20011	4.17 ± 0.35	0.62	0.66 ± 0.24	0.89	0.21 ± 0.75	0.36	-0.01 ± 0.31	0.14	0.38	0
5	21259	4.77 ± 0.22	0.49	0.64 ± 0.16	0.71	-3.68 ± 0.94	0.28	-0.42 ± 0.26	0.36	-0.08	0
6	22014	3.88 ± 0.14	0.42	0.68 ± 0.23	0.89	0.18 ± 0.76	0.33	0.23 ± 0.50	0.49	0.52	0
7	31715	4.07 ± 0.35	0.61	0.73 ± 0.21	0.85	-0.26 ± 1.26	0.41	-0.12 ± 0.60	0.57	0.07	1
8	74007	4.35 ± 0.43	0.77	0.73 ± 0.22	0.85	0.20 ± 0.86	0.35	-0.03 ± 0.50	0.27	0.34	1
9	74157	4.34 ± 0.44	0.79	0.71 ± 0.22	0.83	0.05 ± 1.11	0.53	-0.19 ± 0.40	0.15	0.21	0
10	75403	3.84 ± 0.14	0.42	0.75 ± 0.19	0.76	-0.28 ± 1.09	0.38	-0.03 ± 0.50	0.56	0.35	0
11	80327	4.02 ± 0.22	0.40	0.77 ± 0.18	0.86	-0.88 ± 1.52	0.75	-0.06 ± 0.38	0.32	0.45	0
12	81329	3.91 ± 0.14	0.39	0.74 ± 0.21	0.84	-0.28 ± 1.46	0.67	-0.60 ± 0.64	0.48	0.46	0

Table F.1: continued

	SDSS	$\log(a/M)$	\mathcal{S}_a	q	\mathcal{S}_q	$\log \tau_0$	\mathcal{S}_{τ_0}	$\log(F_2/F_1)$	$\mathcal{S}_{F_2/1}$	QI	E12
13	82150	3.91 ± 0.24	0.50	0.67 ± 0.23	0.88	0.22 ± 0.78	0.42	0.03 ± 0.47	0.56	0.05	1
14	82930	3.91 ± 0.26	0.53	0.70 ± 0.23	0.89	0.05 ± 1.21	0.51	-0.18 ± 0.51	0.53	0.22	0
15	83223	4.29 ± 0.44	0.77	0.79 ± 0.19	0.78	-0.20 ± 1.49	0.66	-0.09 ± 0.24	0.09	0.66	0
16	84313	4.88 ± 0.53	0.77	0.70 ± 0.22	0.89	-0.86 ± 1.54	0.72	-0.06 ± 0.34	0.34	0.46	0
17	85431	4.74 ± 0.27	0.55	0.69 ± 0.23	0.88	-0.69 ± 1.56	0.49	-0.08 ± 0.32	0.25	0.59	0
18	91833	3.73 ± 0.09	0.20	0.37 ± 0.15	0.64	0.16 ± 0.59	0.14	-0.33 ± 0.72	0.29	-0.55	0
19	91928	3.84 ± 0.14	0.41	0.81 ± 0.20	0.76	-1.94 ± 1.88	0.74	-0.18 ± 0.47	0.40	0.26	1
20	92712	3.93 ± 0.14	0.39	0.41 ± 0.18	0.77	-0.96 ± 1.77	0.91	-0.80 ± 0.68	0.70	0.17	1
21	93100	3.85 ± 0.12	0.32	0.68 ± 0.19	0.80	0.21 ± 1.10	0.62	0.14 ± 0.26	0.14	0.43	0
22	93653	4.17 ± 0.35	0.68	0.67 ± 0.21	0.87	-0.46 ± 1.17	0.36	-0.13 ± 0.40	0.39	0.11	0
23	93844	4.19 ± 0.34	0.67	0.65 ± 0.22	0.88	0.21 ± 0.65	0.27	-0.05 ± 0.45	0.47	0.44	1
24	94603	4.41 ± 0.39	0.66	0.25 ± 0.24	0.41	-2.73 ± 1.62	0.47	-1.78 ± 0.95	0.57	-0.71	1
25	94620	4.68 ± 0.21	0.40	0.57 ± 0.20	0.89	-2.36 ± 1.51	0.72	-0.49 ± 0.36	0.34	0.35	1
26	95036	4.64 ± 0.28	0.44	0.43 ± 0.17	0.44	-0.66 ± 1.65	0.85	-0.47 ± 0.51	0.46	0.59	1
27	95539	4.17 ± 0.38	0.59	0.74 ± 0.22	0.83	-0.03 ± 0.85	0.33	-0.17 ± 0.58	0.55	0.16	1

Table F.1: continued

	SDSS	$\log(a/M)$	S_a	q	S_q	$\log \tau_0$	S_{τ_0}	$\log(F_2/F_1)$	$S_{F_2/1}$	QI	E12
28	101438	4.01 ± 0.30	0.56	0.65 ± 0.24	0.91	0.31 ± 0.80	0.40	-0.12 ± 0.33	0.22	0.43	0
29	102106	4.11 ± 0.35	0.62	0.75 ± 0.23	0.85	-0.15 ± 1.42	0.61	-0.07 ± 0.34	0.24	0.14	0
30	102839	4.49 ± 0.33	0.61	0.61 ± 0.25	0.95	-0.52 ± 1.76	0.82	-0.59 ± 0.66	0.54	0.59	0
31	104132	3.92 ± 0.18	0.49	0.61 ± 0.23	0.92	0.29 ± 0.81	0.43	-0.05 ± 0.36	0.29	0.56	0
32	105041	3.97 ± 0.09	0.16	0.11 ± 0.06	0.17	-3.13 ± 1.53	0.52	-2.22 ± 0.36	0.40	-0.76	1
33	105203	4.09 ± 0.33	0.62	0.64 ± 0.25	0.90	-0.69 ± 1.66	0.83	-0.15 ± 0.36	0.36	0.22	0
34	110051	3.91 ± 0.23	0.53	0.80 ± 0.19	0.76	-0.70 ± 1.72	0.75	0.00 ± 0.23	0.09	-0.09	0
35	110556	4.66 ± 0.38	0.70	0.58 ± 0.23	0.91	0.03 ± 1.11	0.54	-0.26 ± 0.34	0.28	0.72	1
36	110742	3.85 ± 0.14	0.42	0.69 ± 0.21	0.82	0.29 ± 0.73	0.36	-0.06 ± 0.37	0.40	0.55	0
37	111329	4.14 ± 0.35	0.66	0.68 ± 0.23	0.87	-0.25 ± 1.16	0.37	-0.06 ± 0.38	0.36	0.59	0
38	111537	4.06 ± 0.31	0.64	0.73 ± 0.20	0.85	-0.49 ± 1.64	0.58	-0.43 ± 0.65	0.52	-0.35	1
39	111916	4.23 ± 0.43	0.79	0.69 ± 0.24	0.89	0.16 ± 0.91	0.39	0.19 ± 0.51	0.52	0.22	0
40	112751	4.49 ± 0.40	0.66	0.75 ± 0.20	0.76	-0.81 ± 1.59	0.64	-0.02 ± 0.37	0.36	0.40	0
41	113330	4.25 ± 0.39	0.63	0.61 ± 0.23	0.85	-0.50 ± 1.24	0.57	-0.31 ± 0.33	0.39	0.44	1
42	113651	4.07 ± 0.34	0.63	0.71 ± 0.23	0.87	0.17 ± 0.78	0.30	0.05 ± 0.46	0.33	0.31	0

Table F.1: continued

	SDSS	$\log(a/M)$	\mathcal{S}_a	q	\mathcal{S}_q	$\log \tau_0$	\mathcal{S}_{τ_0}	$\log(F_2/F_1)$	$\mathcal{S}_{F_2/1}$	QI	E12
43	113706	3.89 ± 0.18	0.50	0.70 ± 0.21	0.83	-0.02 ± 1.48	0.81	-0.44 ± 0.56	0.52	0.57	0
44	113904	3.79 ± 0.14	0.36	0.55 ± 0.22	0.84	0.41 ± 0.90	0.40	0.19 ± 0.39	0.43	0.02	1
45	115158	4.39 ± 0.48	0.64	0.65 ± 0.23	0.90	0.02 ± 0.96	0.60	-0.21 ± 0.52	0.58	0.06	1
46	115449	3.96 ± 0.11	0.25	0.37 ± 0.06	0.44	-3.23 ± 1.39	0.54	-1.27 ± 0.35	0.30	-0.11	0
47	115644	4.36 ± 0.43	0.73	0.71 ± 0.24	0.88	0.17 ± 0.85	0.41	0.10 ± 0.43	0.37	0.44	0
48	120924	3.86 ± 0.17	0.49	0.59 ± 0.22	0.88	0.24 ± 0.72	0.44	0.31 ± 0.37	0.44	0.36	1
49	121113	4.22 ± 0.32	0.64	0.66 ± 0.23	0.89	-0.55 ± 1.67	0.83	-0.32 ± 0.42	0.36	0.48	0
50	122811	4.00 ± 0.26	0.56	0.72 ± 0.22	0.86	0.04 ± 1.17	0.44	-0.02 ± 0.47	0.45	0.20	0
51	123001	3.84 ± 0.13	0.42	0.80 ± 0.17	0.71	0.04 ± 0.66	0.30	-0.05 ± 0.76	0.59	0.35	0
52	124551	4.71 ± 0.27	0.54	0.75 ± 0.20	0.78	0.04 ± 0.77	0.27	-0.22 ± 0.38	0.26	0.55	0
53	125142	3.96 ± 0.21	0.48	0.65 ± 0.23	0.88	0.19 ± 1.31	0.77	-0.46 ± 0.55	0.53	0.47	1
54	125809	3.71 ± 0.04	0.04	0.79 ± 0.15	0.63	-1.22 ± 1.82	0.47	-0.40 ± 0.52	0.06	-0.20	0
55	130534	4.59 ± 0.42	0.76	0.81 ± 0.18	0.73	-1.07 ± 1.86	0.65	-0.26 ± 0.53	0.49	-0.01	0
56	131945	4.70 ± 0.00	0.00	0.83 ± 0.15	0.34	0.00 ± 1.21	0.55	0.06 ± 0.65	0.57	0.24	1
57	132704	4.10 ± 0.35	0.60	0.66 ± 0.23	0.88	-0.22 ± 1.25	0.48	-0.11 ± 0.42	0.15	-0.27	0

Table F.1: continued

	SDSS	$\log(a/M)$	S_a	q	S_q	$\log \tau_0$	S_{τ_0}	$\log(F_2/F_1)$	$S_{F_2/1}$	QI	E12
58	133432	3.91 ± 0.13	0.39	0.77 ± 0.19	0.76	-0.84 ± 0.96	0.67	-0.29 ± 0.56	0.56	0.51	0
59	134617	3.89 ± 0.14	0.42	0.68 ± 0.21	0.89	-0.63 ± 1.71	0.76	-0.78 ± 0.65	0.51	0.49	0
60	140007	4.72 ± 0.32	0.64	0.74 ± 0.19	0.83	-1.11 ± 0.90	0.42	-0.07 ± 0.36	0.33	0.37	0
61	140251	4.11 ± 0.37	0.68	0.66 ± 0.24	0.91	0.15 ± 0.65	0.27	0.21 ± 0.39	0.34	0.26	1
62	140700	3.82 ± 0.14	0.42	0.76 ± 0.20	0.83	-0.01 ± 0.37	0.08	-0.03 ± 0.64	0.61	0.33	0
63	141213	3.77 ± 0.10	0.41	0.74 ± 0.19	0.78	-0.78 ± 1.16	0.26	-0.00 ± 0.63	0.44	0.16	0
64	141300	4.09 ± 0.35	0.66	0.72 ± 0.23	0.87	0.18 ± 1.01	0.42	-0.03 ± 0.31	0.20	0.40	0
65	143123	3.92 ± 0.24	0.61	0.62 ± 0.19	0.83	0.27 ± 0.79	0.34	0.04 ± 0.28	0.29	0.42	0
66	143455	3.93 ± 0.09	0.15	0.52 ± 0.19	0.88	0.17 ± 1.03	0.33	0.12 ± 0.29	0.43	0.44	0
67	151132	4.47 ± 0.47	0.82	0.80 ± 0.18	0.74	-0.81 ± 1.68	0.66	-0.39 ± 0.53	0.51	0.24	1
68	151443	4.35 ± 0.33	0.62	0.70 ± 0.25	0.93	0.16 ± 0.64	0.10	-0.17 ± 0.48	0.40	0.65	0
69	152316	3.91 ± 0.16	0.40	0.80 ± 0.19	0.77	0.41 ± 0.87	0.43	0.06 ± 0.67	0.53	0.46	0
70	152939	4.14 ± 0.42	0.65	0.72 ± 0.22	0.82	0.11 ± 0.92	0.47	-0.03 ± 0.45	0.45	0.22	0
71	152942	3.88 ± 0.14	0.40	0.79 ± 0.16	0.73	-0.09 ± 0.95	0.31	-0.33 ± 0.79	0.62	0.32	0
72	153434	4.61 ± 0.38	0.74	0.77 ± 0.19	0.80	-0.10 ± 1.21	0.51	-0.03 ± 0.35	0.26	0.38	0

Table F.1: continued

	SDSS	$\log(a/M)$	S_a	q	S_q	$\log \tau_0$	S_{τ_0}	$\log(F_2/F_1)$	$S_{F_2/1}$	QI	E12
73	153636	3.82 ± 0.12	0.27	0.46 ± 0.14	0.65	-3.40 ± 1.21	0.76	-1.02 ± 0.50	0.45	-1.08	1
74	153644	4.28 ± 0.45	0.85	0.77 ± 0.21	0.81	0.04 ± 1.09	0.49	-0.05 ± 0.40	0.37	-0.12	1
75	154340	4.32 ± 0.43	0.76	0.79 ± 0.20	0.79	0.00 ± 1.12	0.45	-0.06 ± 0.55	0.50	0.34	0
76	154637	3.89 ± 0.14	0.42	0.73 ± 0.20	0.86	-1.40 ± 1.67	0.73	-0.15 ± 0.55	0.49	0.15	1
77	155654	3.95 ± 0.11	0.12	0.43 ± 0.10	0.57	-1.51 ± 1.36	0.67	-0.49 ± 0.28	0.38	0.15	1
78	160243	4.04 ± 0.31	0.71	0.72 ± 0.22	0.84	0.02 ± 0.91	0.46	0.06 ± 0.31	0.17	0.25	0
79	160536	3.99 ± 0.25	0.51	0.73 ± 0.23	0.86	0.37 ± 0.88	0.41	0.03 ± 0.29	0.21	0.41	0
80	161911	4.81 ± 0.26	0.50	0.72 ± 0.22	0.89	0.02 ± 1.02	0.42	-0.08 ± 0.36	0.32	0.69	1
81	162914	3.91 ± 0.31	0.60	0.78 ± 0.21	0.80	0.04 ± 1.04	0.43	-0.01 ± 0.24	0.08	0.11	1
82	163020	3.78 ± 0.12	0.42	0.63 ± 0.24	0.90	0.02 ± 0.80	0.37	0.13 ± 0.55	0.62	-0.19	0
83	165118	4.41 ± 0.28	0.65	0.53 ± 0.20	0.82	0.09 ± 0.44	0.14	-0.15 ± 0.43	0.41	0.51	0
84	165255	4.07 ± 0.32	0.58	0.65 ± 0.24	0.90	0.26 ± 0.70	0.32	-0.08 ± 0.36	0.32	0.66	0
85	170341	4.17 ± 0.24	0.44	0.42 ± 0.22	0.73	-2.34 ± 1.78	0.29	-1.10 ± 0.61	0.53	0.07	0
86	171448	3.82 ± 0.15	0.42	0.71 ± 0.23	0.88	0.06 ± 1.33	0.64	0.12 ± 0.63	0.54	-0.45	0
87	172711	4.19 ± 0.35	0.61	0.63 ± 0.24	0.89	0.05 ± 1.07	0.44	-0.27 ± 0.45	0.43	0.68	0

Table F.1: continued

	SDSS	$\log(a/M)$	S_a	q	S_q	$\log \tau_0$	S_{τ_0}	$\log(F_2/F_1)$	$S_{F_2/1}$	QI	E12
88	180545	4.23 ± 0.35	0.64	0.69 ± 0.23	0.89	0.20 ± 0.98	0.42	0.04 ± 0.36	0.26	0.25	0

REFERENCES

- [1] L. Ferrarese and D. Merritt, “A Fundamental Relation between Supermassive Black Holes and Their Host Galaxies,” *ApJ*, vol. 539, pp. L9–L12, Aug. 2000.
- [2] K. Gebhardt, R. Bender, G. Bower, A. Dressler, S. M. Faber, A. V. Filippenko, R. Green, C. Grillmair, L. C. Ho, J. Kormendy, T. R. Lauer, J. Magorrian, J. Pinkney, D. Richstone, and S. Tremaine, “A Relationship between Nuclear Black Hole Mass and Galaxy Velocity Dispersion,” *ApJ*, vol. 539, pp. L13–L16, Aug. 2000.
- [3] S. Tremaine, K. Gebhardt, R. Bender, G. Bower, A. Dressler, S. M. Faber, A. V. Filippenko, R. Green, C. Grillmair, L. C. Ho, J. Kormendy, T. R. Lauer, J. Magorrian, J. Pinkney, and D. Richstone, “The Slope of the Black Hole Mass versus Velocity Dispersion Correlation,” *ApJ*, vol. 574, pp. 740–753, Aug. 2002.
- [4] M. C. Begelman, R. D. Blandford, and M. J. Rees, “Massive black hole binaries in active galactic nuclei,” *Nature*, vol. 287, pp. 307–309, Sep. 1980.
- [5] L. Mayer, “Massive black hole binaries in gas-rich galaxy mergers; multiple regimes of orbital decay and interplay with gas inflows,” *Classical and Quantum Gravity*, vol. 30, no. 24, p. 244 008, Dec. 2013.
- [6] S. Chandrasekhar, “Dynamical Friction. I. General Considerations: the Coefficient of Dynamical Friction.,” *ApJ*, vol. 97, p. 255, Mar. 1943.
- [7] E. C. Ostriker, “Dynamical Friction in a Gaseous Medium,” *ApJ*, vol. 513, pp. 252–258, Mar. 1999.
- [8] M. Milosavljević and D. Merritt, “Formation of Galactic Nuclei,” *ApJ*, vol. 563, pp. 34–62, Dec. 2001.
- [9] A. Escala, R. B. Larson, P. S. Coppi, and D. Mardones, “The Role of Gas in the Merging of Massive Black Holes in Galactic Nuclei. I. Black Hole Merging in a Spherical Gas Cloud,” *ApJ*, vol. 607, pp. 765–777, Jun. 2004.
- [10] D. Fiacconi, L. Mayer, R. Roškar, and M. Colpi, “Massive Black Hole Pairs in Clumpy, Self-gravitating Circumnuclear Disks: Stochastic Orbital Decay,” *ApJ*, vol. 777, p. L14, Nov. 2013.
- [11] R. Roškar, D. Fiacconi, L. Mayer, S. Kazantzidis, T. R. Quinn, and J. Wadsley, “Orbital decay of supermassive black hole binaries in clumpy multiphase merger remnants,” *MNRAS*, vol. 449, pp. 494–505, May 2015.

- [12] A. Escala, R. B. Larson, P. S. Coppi, and D. Mardones, “The Role of Gas in the Merging of Massive Black Holes in Galactic Nuclei. II. Black Hole Merging in a Nuclear Gas Disk,” *ApJ*, vol. 630, pp. 152–166, Sep. 2005.
- [13] M. Dotti, M. Colpi, and F. Haardt, “Laser Interferometer Space Antenna double black holes: dynamics in gaseous nuclear discs,” *MNRAS*, vol. 367, pp. 103–112, Mar. 2006.
- [14] M. Dotti, M. Colpi, F. Haardt, and L. Mayer, “Supermassive black hole binaries in gaseous and stellar circumnuclear discs: orbital dynamics and gas accretion,” *MNRAS*, vol. 379, pp. 956–962, Aug. 2007.
- [15] M. Dotti, M. Ruszkowski, L. Paredi, M. Colpi, M. Volonteri, and F. Haardt, “Dual black holes in merger remnants - I. Linking accretion to dynamics,” *MNRAS*, vol. 396, pp. 1640–1646, Jul. 2009.
- [16] S. Callegari, S. Kazantzidis, L. Mayer, M. Colpi, J. M. Bellovary, T. Quinn, and J. Wadsley, “Growing Massive Black Hole Pairs in Minor Mergers of Disk Galaxies,” *ApJ*, vol. 729, p. 85, Mar. 2011.
- [17] F. M. Khan, I. Berentzen, P. Berczik, A. Just, L. Mayer, K. Nitadori, and S. Callegari, “Formation and Hardening of Supermassive Black Hole Binaries in Minor Mergers of Disk Galaxies,” *ApJ*, vol. 756, p. 30, Sep. 2012.
- [18] D. Chapon, L. Mayer, and R. Teyssier, “Hydrodynamics of galaxy mergers with supermassive black holes: is there a last parsec problem?” *MNRAS*, vol. 429, pp. 3114–3122, Mar. 2013.
- [19] S. Callegari, L. Mayer, S. Kazantzidis, M. Colpi, F. Governato, T. Quinn, and J. Wadsley, “Pairing of Supermassive Black Holes in Unequal-Mass Galaxy Mergers,” *ApJ*, vol. 696, pp. L89–L92, May 2009.
- [20] L. Mayer, S. Kazantzidis, P. Madau, M. Colpi, T. Quinn, and J. Wadsley, “Rapid Formation of Supermassive Black Hole Binaries in Galaxy Mergers with Gas,” *Science*, vol. 316, pp. 1874–, Jun. 2007.
- [21] P. Berczik, D. Merritt, R. Spurzem, and H.-P. Bischof, “Efficient Merger of Binary Supermassive Black Holes in Nonaxisymmetric Galaxies,” *ApJ*, vol. 642, pp. L21–L24, May 2006.
- [22] M. Preto, I. Berentzen, P. Berczik, and R. Spurzem, “Fast Coalescence of Massive Black Hole Binaries from Mergers of Galactic Nuclei: Implications for Low-frequency Gravitational-wave Astrophysics,” *ApJ*, vol. 732, p. L26, May 2011.

- [23] F. M. Khan, A. Just, and D. Merritt, “Efficient Merger of Binary Supermassive Black Holes in Merging Galaxies,” *ApJ*, vol. 732, p. 89, May 2011.
- [24] F. M. Khan, M. Preto, P. Berczik, I. Berentzen, A. Just, and R. Spurzem, “Mergers of Unequal-mass Galaxies: Supermassive Black Hole Binary Evolution and Structure of Merger Remnants,” *ApJ*, vol. 749, p. 147, Apr. 2012.
- [25] F. M. Khan, K. Holley-Bockelmann, P. Berczik, and A. Just, “Supermassive Black Hole Binary Evolution in Axisymmetric Galaxies: The Final Parsec Problem is Not a Problem,” *ApJ*, vol. 773, p. 100, Aug. 2013.
- [26] E. Vasiliev, F. Antonini, and D. Merritt, “The Final-parsec Problem in Nonspherical Galaxies Revisited,” *ApJ*, vol. 785, p. 163, Apr. 2014.
- [27] P. J. Armitage and P. Natarajan, “Eccentricity of Supermassive Black Hole Binaries Coalescing from Gas-rich Mergers,” *ApJ*, vol. 634, pp. 921–927, Dec. 2005.
- [28] A. I. MacFadyen and M. Milosavljević, “An Eccentric Circumbinary Accretion Disk and the Detection of Binary Massive Black Holes,” *ApJ*, vol. 672, pp. 83–93, Jan. 2008.
- [29] T. Bogdanović, B. D. Smith, S. Sigurdsson, and M. Eracleous, “Modeling of Emission Signatures of Massive Black Hole Binaries. I. Methods,” *ApJS*, vol. 174, pp. 455–480, Feb. 2008.
- [30] T. Bogdanović, T. Bode, R. Haas, P. Laguna, and D. Shoemaker, “Properties of accretion flows around coalescing supermassive black holes,” *Classical and Quantum Gravity*, vol. 28, no. 9, p. 094 020, May 2011.
- [31] J. Cuadra, P. J. Armitage, R. D. Alexander, and M. C. Begelman, “Massive black hole binary mergers within subparsec scale gas discs,” *MNRAS*, vol. 393, pp. 1423–1432, Mar. 2009.
- [32] Z. Haiman, B. Kocsis, and K. Menou, “The Population of Viscosity- and Gravitational Wave-driven Supermassive Black Hole Binaries Among Luminous Active Galactic Nuclei,” *ApJ*, vol. 700, pp. 1952–1969, Aug. 2009.
- [33] K. Hayasaki, “A New Mechanism for Massive Binary Black-Hole Evolution,” *PASJ*, vol. 61, pp. 65–, Feb. 2009.
- [34] C. Roedig, A. Sesana, M. Dotti, J. Cuadra, P. Amaro-Seoane, and F. Haardt, “Evolution of binary black holes in self gravitating discs. Dissecting the torques,” *A&A*, vol. 545, A127, Sep. 2012.

- [35] J.-M. Shi, J. H. Krolik, S. H. Lubow, and J. F. Hawley, “Three-dimensional Magnetohydrodynamic Simulations of Circumbinary Accretion Disks: Disk Structures and Angular Momentum Transport,” *ApJ*, vol. 749, p. 118, Apr. 2012.
- [36] S. C. Noble, B. C. Mundim, H. Nakano, J. H. Krolik, M. Campanelli, Y. Zlochower, and N. Yunes, “Circumbinary Magnetohydrodynamic Accretion into Inspiring Binary Black Holes,” *ApJ*, vol. 755, p. 51, Aug. 2012.
- [37] B. Kocsis, Z. Haiman, and A. Loeb, “Gas pile-up, gap overflow and Type 1.5 migration in circumbinary discs: application to supermassive black hole binaries,” *MNRAS*, vol. 427, pp. 2680–2700, Dec. 2012.
- [38] —, “Gas pile-up, gap overflow and Type 1.5 migration in circumbinary discs: general theory,” *MNRAS*, vol. 427, pp. 2660–2679, Dec. 2012.
- [39] D. J. D’Orazio, Z. Haiman, and A. MacFadyen, “Accretion into the central cavity of a circumbinary disc,” *MNRAS*, vol. 436, pp. 2997–3020, Dec. 2013.
- [40] B. D. Farris, P. Duffell, A. I. MacFadyen, and Z. Haiman, “Binary Black Hole Accretion from a Circumbinary Disk: Gas Dynamics inside the Central Cavity,” *ApJ*, vol. 783, p. 134, Mar. 2014.
- [41] R. R. Rafikov, “Accretion and Orbital Inspiral in Gas-assisted Supermassive Black Hole Binary Mergers,” *ApJ*, vol. 827, no. 2, p. 111, 2016.
- [42] D. N. C. Lin and J. Papaloizou, “Tidal torques on accretion discs in binary systems with extreme mass ratios,” *MNRAS*, vol. 186, pp. 799–812, Mar. 1979.
- [43] B. Giacomazzo, J. G. Baker, M. C. Miller, C. S. Reynolds, and J. R. van Meter, “General Relativistic Simulations of Magnetized Plasmas around Merging Supermassive Black Holes,” *ApJ*, vol. 752, p. L15, Jun. 2012.
- [44] B. D. Farris, R. Gold, V. Paschalidis, Z. B. Etienne, and S. L. Shapiro, “Binary Black-Hole Mergers in Magnetized Disks: Simulations in Full General Relativity,” *Physical Review Letters*, vol. 109, no. 22, p. 221 102, Nov. 2012.
- [45] R. Gold, V. Paschalidis, Z. B. Etienne, S. L. Shapiro, and H. P. Pfeiffer, “Accretion disks around binary black holes of unequal mass: General relativistic magnetohydrodynamic simulations near decoupling,” *Phys. Rev. D*, vol. 89, no. 6, p. 064 060, Mar. 2014.
- [46] C. Roedig, M. Dotti, A. Sesana, J. Cuadra, and M. Colpi, “Limiting eccentricity of subparsec massive black hole binaries surrounded by self-gravitating gas discs,” *MNRAS*, vol. 415, pp. 3033–3041, Aug. 2011.

- [47] A. Sesana, A. Gualandris, and M. Dotti, “Massive black hole binary eccentricity in rotating stellar systems,” *MNRAS*, vol. 415, pp. L35–L39, Jul. 2011.
- [48] K. Holley-Bockelmann and F. M. Khan, “Galaxy Rotation and Rapid Supermassive Binary Coalescence,” *ApJ*, vol. 810, p. 139, Sep. 2015.
- [49] M. Campanelli, C. O. Lousto, Y. Zlochower, and D. Merritt, “Maximum Gravitational Recoil,” *Physical Review Letters*, vol. 98, no. 23, p. 231 102, Jun. 2007.
- [50] C. O. Lousto and Y. Zlochower, “Hangup Kicks: Still Larger Recoils by Partial Spin-Orbit Alignment of Black-Hole Binaries,” *Physical Review Letters*, vol. 107, no. 23, p. 231 102, Dec. 2011.
- [51] T. Bogdanović, C. S. Reynolds, and M. C. Miller, “Alignment of the Spins of Supermassive Black Holes Prior to Coalescence,” *ApJ*, vol. 661, pp. L147–L150, Jun. 2007.
- [52] M. Dotti, M. Volonteri, A. Perego, M. Colpi, M. Ruszkowski, and F. Haardt, “Dual black holes in merger remnants - II. Spin evolution and gravitational recoil,” *MNRAS*, vol. 402, pp. 682–690, Feb. 2010.
- [53] M. Dotti, M. Colpi, S. Pallini, A. Perego, and M. Volonteri, “On the Orientation and Magnitude of the Black Hole Spin in Galactic Nuclei,” *ApJ*, vol. 762, p. 68, Jan. 2013.
- [54] K. A. Sorathia, J. H. Krolik, and J. F. Hawley, “Magnetohydrodynamic Simulation of a Disk Subjected to Lense-Thirring Precession,” *ApJ*, vol. 777, p. 21, Nov. 2013.
- [55] M. C. Miller and J. H. Krolik, “Alignment of Supermassive Black Hole Binary Orbits and Spins,” *ApJ*, vol. 774, p. 43, Sep. 2013.
- [56] G. Lodato and D. Gerosa, “Black hole mergers: do gas discs lead to spin alignment?” *MNRAS*, vol. 429, pp. L30–L34, Feb. 2013.
- [57] P. C. Fragile and P. Anninos, “Hydrodynamic Simulations of Tilted Thick-Disk Accretion onto a Kerr Black Hole,” *ApJ*, vol. 623, pp. 347–361, Apr. 2005.
- [58] P. C. Fragile, O. M. Blaes, P. Anninos, and J. D. Salmonson, “Global General Relativistic Magnetohydrodynamic Simulation of a Tilted Black Hole Accretion Disk,” *ApJ*, vol. 668, pp. 417–429, Oct. 2007.
- [59] J. C. McKinney, A. Tchekhovskoy, and R. D. Blandford, “Alignment of Magnetized Accretion Disks and Relativistic Jets with Spinning Black Holes,” *Science*, vol. 339, pp. 49–, Jan. 2013.

- [60] S. Komossa, V. Burwitz, G. Hasinger, P. Predehl, J. S. Kaastra, and Y. Ikebe, “Discovery of a Binary Active Galactic Nucleus in the Ultraluminous Infrared Galaxy NGC 6240 Using Chandra,” *ApJ*, vol. 582, pp. L15–L19, Jan. 2003.
- [61] M. Koss, R. Mushotzky, E. Treister, S. Veilleux, R. Vasudevan, N. Miller, D. B. Sanders, K. Schawinski, and M. Trippe, “Chandra Discovery of a Binary Active Galactic Nucleus in Mrk 739,” *ApJ*, vol. 735, p. L42, Jul. 2011.
- [62] M. J. Koss, A. Glidden, M. Baloković, D. Stern, I. Lamperti, R. Assef, F. Bauer, D. Ballantyne, S. E. Boggs, W. W. Craig, D. Farrah, F. Fürst, P. Gandhi, N. Gehrels, C. J. Hailey, F. A. Harrison, C. Markwardt, A. Masini, C. Ricci, E. Treister, D. J. Walton, and W. W. Zhang, “NuSTAR Resolves the First Dual AGN above 10 keV in SWIFT J2028.5+2543,” *ApJ*, vol. 824, p. L4, Jun. 2016.
- [63] X. Liu, F. Civano, Y. Shen, P. Green, J. E. Greene, and M. A. Strauss, “Chandra X-Ray and Hubble Space Telescope Imaging of Optically Selected Kiloparsec-scale Binary Active Galactic Nuclei. I. Nature of the Nuclear Ionizing Sources,” *ApJ*, vol. 762, p. 110, Jan. 2013.
- [64] J. M. Comerford, D. Pooley, R. S. Barrows, J. E. Greene, N. L. Zakamska, G. M. Madejski, and M. C. Cooper, “Merger-driven Fueling of Active Galactic Nuclei: Six Dual and Offset AGNs Discovered with Chandra and Hubble Space Telescope Observations,” *ApJ*, vol. 806, p. 219, Jun. 2015.
- [65] R. S. Barrows, J. M. Comerford, J. E. Greene, and D. Pooley, “Spatially Offset Active Galactic Nuclei. I. Selection and Spectroscopic Properties,” *ApJ*, vol. 829, p. 37, Sep. 2016.
- [66] M. Volonteri, J. M. Miller, and M. Dotti, “Sub-Parsec Supermassive Binary Quasars: Expectations at $z \gtrsim 1$,” *ApJ*, vol. 703, pp. L86–L89, Sep. 2009.
- [67] T. Bogdanović, “Supermassive Black Hole Binaries: The Search Continues,” in *Gravitational Wave Astrophysics*, C. F. Sopuerta, Ed., ser. Astrophysics and Space Science Proceedings, vol. 40, 2015, p. 103.
- [68] C. Rodriguez, G. B. Taylor, R. T. Zavala, A. B. Peck, L. K. Pollack, and R. W. Romani, “A Compact Supermassive Binary Black Hole System,” *ApJ*, vol. 646, pp. 49–60, Jul. 2006.
- [69] C. Rodriguez, G. B. Taylor, R. T. Zavala, Y. M. Pihlström, and A. B. Peck, “H I Observations of the Supermassive Binary Black Hole System in 0402+379,” *ApJ*, vol. 697, pp. 37–44, May 2009.

- [70] R. Morganti, B. Emons, and T. Oosterloo, “Broad H I absorption in the candidate binary black hole 4C37.11 (B2 0402+379),” *A&A*, vol. 496, pp. L9–L12, Mar. 2009.
- [71] K. Bansal, G. B. Taylor, A. B. Peck, R. T. Zavala, and R. W. Romani, “Constraining the Orbit of the Supermassive Black Hole Binary 0402+379,” *ApJ*, vol. 843, p. 14, Jul. 2017.
- [72] S. Burke-Spolaor, “A radio Census of binary supermassive black holes,” *MNRAS*, vol. 410, pp. 2113–2122, Feb. 2011.
- [73] J. Condon, J. Darling, Y. Y. Kovalev, and L. Petrov, “VLBA observations of a complete sample of 2MASS galaxies,” *ArXiv e-prints*, Oct. 2011.
- [74] M. J. Valtonen, H. J. Lehto, K. Nilsson, J. Heidt, L. O. Takalo, A. Sillanpää, C. Villforth, M. Kidger, G. Poyner, T. Pursimo, S. Zola, J.-H. Wu, X. Zhou, K. Sadakane, M. Drozd, D. Koziel, D. Marchev, W. Ogloza, C. Porowski, M. Siwak, G. Stachowski, M. Winiarski, V.-P. Hentunen, M. Nissinen, A. Liakos, and S. Dogru, “A massive binary black-hole system in OJ287 and a test of general relativity,” *Nature*, vol. 452, pp. 851–853, Apr. 2008.
- [75] M. J. Graham, S. G. Djorgovski, D. Stern, A. J. Drake, A. A. Mahabal, C. Donalek, E. Glikman, S. Larson, and E. Christensen, “A systematic search for close supermassive black hole binaries in the Catalina Real-time Transient Survey,” *MNRAS*, vol. 453, pp. 1562–1576, Oct. 2015.
- [76] M. Charisi, I. Bartos, Z. Haiman, A. M. Price-Whelan, M. J. Graham, E. C. Bellm, R. R. Laher, and S. Márka, “A population of short-period variable quasars from PTF as supermassive black hole binary candidates,” *MNRAS*, vol. 463, pp. 2145–2171, Dec. 2016.
- [77] T. Liu, S. Gezari, W. Burgett, K. Chambers, P. Draper, K. Hodapp, M. Huber, R.-P. Kudritzki, E. Magnier, N. Metcalfe, J. Tonry, R. Wainscoat, and C. Waters, “A Systematic Search for Periodically Varying Quasars in Pan-STARRS1: An Extended Baseline Test in Medium Deep Survey Field MD09,” *ApJ*, vol. 833, p. 6, Dec. 2016.
- [78] S. Vaughan, P. Uttley, A. G. Markowitz, D. Huppenkothen, M. J. Middleton, W. N. Alston, J. D. Scargle, and W. M. Farr, “False periodicities in quasar time-domain surveys,” *MNRAS*, vol. 461, pp. 3145–3152, Sep. 2016.
- [79] L. Lentati, S. R. Taylor, C. M. F. Mingarelli, A. Sesana, S. A. Sanidas, A. Vecchio, R. N. Caballero, K. J. Lee, R. van Haasteren, S. Babak, C. G. Bassa, P. Brem, M. Burgay, D. J. Champion, I. Cognard, G. Desvignes, J. R. Gair, L. Guillemot, J. W. T. Hessels, G. H. Janssen, R. Karuppusamy, M. Kramer, A. Lassus, P. Lazarus, K. Liu, S. Osłowski, D. Perrodin, A. Petiteau, A. Possenti, M. B. Purver, P. A. Rosado, R.

- Smits, B. Stappers, G. Theureau, C. Tiburzi, and J. P. W. Verbiest, “European Pulsar Timing Array limits on an isotropic stochastic gravitational-wave background,” *MNRAS*, vol. 453, pp. 2576–2598, Nov. 2015.
- [80] R. M. Shannon, V. Ravi, L. T. Lentati, P. D. Lasky, G. Hobbs, M. Kerr, R. N. Manchester, W. A. Coles, Y. Levin, M. Bailes, N. D. R. Bhat, S. Burke-Spolaor, S. Dai, M. J. Keith, S. Osłowski, D. J. Reardon, W. van Straten, L. Toomey, J.-B. Wang, L. Wen, J. S. B. Wyithe, and X.-J. Zhu, “Gravitational waves from binary supermassive black holes missing in pulsar observations,” *Science*, vol. 349, pp. 1522–1525, Sep. 2015.
- [81] Z. Arzoumanian, A. Brazier, S. Burke-Spolaor, S. J. Chamberlin, S. Chatterjee, B. Christy, J. M. Cordes, N. J. Cornish, K. Crowter, P. B. Demorest, X. Deng, T. Dolch, J. A. Ellis, R. D. Ferdman, E. Fonseca, N. Garver-Daniels, M. E. Gonzalez, F. Jenet, G. Jones, M. L. Jones, V. M. Kaspi, M. Koop, M. T. Lam, T. J. W. Lazio, L. Levin, A. N. Lommen, D. R. Lorimer, J. Luo, R. S. Lynch, D. R. Madison, M. A. McLaughlin, S. T. McWilliams, C. M. F. Mingarelli, D. J. Nice, N. Palliyaguru, T. T. Pennucci, S. M. Ransom, L. Sampson, S. A. Sanidas, A. Sesana, X. Siemens, J. Simon, I. H. Stairs, D. R. Stinebring, K. Stovall, J. Swiggum, S. R. Taylor, M. Vallisneri, R. van Haasteren, Y. Wang, W. W. Zhu, and NANOGrav Collaboration, “The NANOGrav Nine-year Data Set: Limits on the Isotropic Stochastic Gravitational Wave Background,” *ApJ*, vol. 821, p. 13, Apr. 2016.
- [82] A. Sesana, Z. Haiman, B. Kocsis, and L. Z. Kelley, “Testing the Binary Hypothesis: Pulsar Timing Constraints on Supermassive Black Hole Binary Candidates,” *ApJ*, vol. 856, no. 1, p. 42, 2018.
- [83] C. M. Gaskell, “Quasars as supermassive binaries,” in *Liege International Astrophysical Colloquia*, J.-P. Swings, Ed., ser. Liege International Astrophysical Colloquia, vol. 24, Jun. 1983, pp. 473–477.
- [84] ———, “Evidence for Binary Orbital Motion of a Quasar Broad-Line Region,” *ApJ*, vol. 464, p. L107, Jun. 1996.
- [85] T. Bogdanović, M. Eracleous, and S. Sigurdsson, “Emission lines as a tool in search for supermassive black hole binaries and recoiling black holes,” *New Astronomy reviews*, vol. 53, pp. 113–120, Jul. 2009.
- [86] P. Artymowicz and S. H. Lubow, “Mass Flow through Gaps in Circumbinary Disks,” *ApJ*, vol. 467, p. L77, Aug. 1996.
- [87] A. Gould and H.-W. Rix, “Binary Black Hole Mergers from Planet-like Migrations,” *ApJ*, vol. 532, pp. L29–L32, Mar. 2000.

- [88] K. Hayasaki, S. Mineshige, and H. Sudou, “Binary Black Hole Accretion Flows in Merged Galactic Nuclei,” *PASJ*, vol. 59, pp. 427–441, Apr. 2007.
- [89] T. Bogdanović, M. Eracleous, and S. Sigurdsson, “SDSS J092712.65+294344.0: Recoiling Black Hole or a Subparsec Binary Candidate?” *ApJ*, vol. 697, pp. 288–292, May 2009.
- [90] M. Dotti, C. Montuori, R. Decarli, M. Volonteri, M. Colpi, and F. Haardt, “SDSSJ092712.65+294344.0: a candidate massive black hole binary,” *MNRAS*, vol. 398, pp. L73–L77, Sep. 2009.
- [91] T. A. Boroson and T. R. Lauer, “A candidate sub-parsec supermassive binary black hole system,” *Nature*, vol. 458, pp. 53–55, Mar. 2009.
- [92] S. Tang and J. Grindlay, “The Quasar SDSS J153636.22+044127.0: A Double-Peaked Emitter in a Candidate Binary Black Hole System,” *ApJ*, vol. 704, pp. 1189–1194, Oct. 2009.
- [93] R. Decarli, M. Dotti, C. Montuori, T. Liimets, and A. Ederoclite, “The Peculiar Optical Spectrum of 4C+22.25: Imprint of a Massive Black Hole Binary?” *ApJ*, vol. 720, pp. L93–L96, Sep. 2010.
- [94] R. S. Barrows, C. H. S. Lacy, D. Kennefick, J. Kennefick, and M. S. Seigar, “Unusual double-peaked emission in the SDSS quasar J093201.60 + 031858.7,” *New Astronomy*, vol. 16, pp. 122–127, Feb. 2011.
- [95] P. Tsalmantza, R. Decarli, M. Dotti, and D. W. Hogg, “A Systematic Search for Massive Black Hole Binaries in the Sloan Digital Sky Survey Spectroscopic Sample,” *ApJ*, vol. 738, p. 20, Sep. 2011.
- [96] C.-W. Tsai, T. H. Jarrett, D. Stern, B. Emonts, R. S. Barrows, R. J. Assef, R. P. Norris, P. R. M. Eisenhardt, C. Lonsdale, A. W. Blain, D. J. Benford, J. Wu, B. Stalder, C. W. Stubbs, F. W. High, K. L. Li, and A. K. H. Kong, “WISE J233237.05-505643.5: A Double-peaked, Broad-lined Active Galactic Nucleus with a Spiral-shaped Radio Morphology,” *ApJ*, vol. 779, p. 41, Dec. 2013.
- [97] C. Montuori, M. Dotti, M. Colpi, R. Decarli, and F. Haardt, “Search for sub-parsec massive binary black holes through line diagnosis,” *MNRAS*, vol. 412, pp. 26–32, Mar. 2011.
- [98] C. Montuori, M. Dotti, F. Haardt, M. Colpi, and R. Decarli, “Search for sub-parsec massive binary black holes through line diagnosis - II,” *MNRAS*, vol. 425, pp. 1633–1639, Sep. 2012.

- [99] S. Komossa, H. Zhou, and H. Lu, “A Recoiling Supermassive Black Hole in the Quasar SDSS J092712.65+294344.0?” *ApJ*, vol. 678, pp. L81–L84, May 2008.
- [100] G. A. Shields, D. J. Rosario, K. L. Smith, E. W. Bonning, S. Salviander, J. S. Kalirai, R. Strickler, E. Ramirez-Ruiz, A. A. Dutton, T. Treu, and P. J. Marshall, “The Quasar SDSS J105041.35+345631.3: Black Hole Recoil or Extreme Double-Peaked Emitter?” *ApJ*, vol. 707, pp. 936–941, Dec. 2009.
- [101] F. Civano, M. Elvis, G. Lanzuisi, K. Jahnke, G. Zamorani, L. Blecha, A. Bongiorno, M. Brusa, A. Comastri, H. Hao, A. Leauthaud, A. Loeb, V. Mainieri, E. Piconcelli, M. Salvato, N. Scoville, J. Trump, C. Vignali, T. Aldcroft, M. Bolzonella, E. Bressert, A. Finoguenov, A. Fruscione, A. M. Koekemoer, N. Cappelluti, F. Fiore, S. Giodini, R. Gilli, C. D. Impey, S. J. Lilly, E. Lusso, S. Puccetti, J. D. Silverman, H. Aussel, P. Capak, D. Frayer, E. Le Floch, H. J. McCracken, D. B. Sanders, D. Schiminovich, and Y. Taniguchi, “A Runaway Black Hole in COSMOS: Gravitational Wave or Slingshot Recoil?” *ApJ*, vol. 717, pp. 209–222, Jul. 2010.
- [102] A. Robinson, S. Young, D. J. Axon, P. Kharb, and J. E. Smith, “Spectropolarimetric Evidence for a Kicked Supermassive Black Hole in the Quasar E1821+643,” *ApJ*, vol. 717, pp. L122–L126, Jul. 2010.
- [103] E. Lusso, R. Decarli, M. Dotti, C. Montuori, D. W. Hogg, P. Tsalmanza, M. Fumagalli, and J. X. Prochaska, “The nature of massive black hole binary candidates - II. Spectral energy distribution atlas,” *MNRAS*, vol. 441, pp. 316–332, Jun. 2014.
- [104] L. Č. Popović, “Super-massive binary black holes and emission lines in active galactic nuclei,” *New Astronomy Reviews*, vol. 56, pp. 74–91, Feb. 2012.
- [105] M. Eracleous, T. A. Boroson, J. P. Halpern, and J. Liu, “A Large Systematic Search for Close Supermassive Binary and Rapidly Recoiling Black Holes,” *ApJS*, vol. 201, p. 23, Aug. 2012.
- [106] A. J. Barth, V. N. Bennert, G. Canalizo, A. V. Filippenko, E. L. Gates, J. E. Greene, W. Li, M. A. Malkan, A. Pancoast, D. J. Sand, D. Stern, T. Treu, J.-H. Woo, R. J. Assef, H.-J. Bae, B. J. Brewer, S. B. Cenko, K. I. Clubb, M. C. Cooper, A. M. Diamond-Stanic, K. D. Hiner, S. F. Hönig, E. Hsiao, M. T. Kandrashoff, M. S. Lazarova, A. M. Nierenberg, J. Rex, J. M. Silverman, E. J. Tollerud, and J. L. Walsh, “The Lick AGN Monitoring Project 2011: Spectroscopic Campaign and Emission-line Light Curves,” *ApJS*, vol. 217, p. 26, Apr. 2015.
- [107] E. Bon, P. Jovanović, P. Marziani, A. I. Shapovalova, N. Bon, V. Borka Jovanović, D. Borka, J. Sulentic, and L. Č. Popović, “The First Spectroscopically Resolved Sub-parsec Orbit of a Supermassive Binary Black Hole,” *ApJ*, vol. 759, p. 118, Nov. 2012.

- [108] E. Bon, S. Zucker, H. Netzer, P. Marziani, N. Bon, P. Jovanović, A. I. Shapovalova, S. Komossa, C. M. Gaskell, L. Č. Popović, S. Britzen, V. H. Chavushyan, A. N. Burenkov, S. Sergeev, G. La Mura, J. R. Valdés, and M. Stalevski, “Evidence for Periodicity in 43 year-long Monitoring of NGC 5548,” *ApJS*, vol. 225, p. 29, Aug. 2016.
- [109] R. Decarli, M. Dotti, M. Fumagalli, P. Tsalmantza, C. Montuori, E. Lusso, D. W. Hogg, and J. X. Prochaska, “The nature of massive black hole binary candidates - I. Spectral properties and evolution,” *MNRAS*, vol. 433, pp. 1492–1504, Aug. 2013.
- [110] Y. Shen, X. Liu, A. Loeb, and S. Tremaine, “Constraining Sub-parsec Binary Supermassive Black Holes in Quasars with Multi-epoch Spectroscopy. I. The General Quasar Population,” *ApJ*, vol. 775, p. 49, Sep. 2013.
- [111] W. Ju, J. E. Greene, R. R. Rafikov, S. J. Bickerton, and C. Badenes, “Search for Supermassive Black Hole Binaries in the Sloan Digital Sky Survey Spectroscopic Sample,” *ApJ*, vol. 777, p. 44, Nov. 2013.
- [112] X. Liu, Y. Shen, F. Bian, A. Loeb, and S. Tremaine, “Constraining Sub-parsec Binary Supermassive Black Holes in Quasars with Multi-epoch Spectroscopy. II. The Population with Kinematically Offset Broad Balmer Emission Lines,” *ApJ*, vol. 789, p. 140, Jul. 2014.
- [113] J. C. Runnoe, M. Eracleous, G. Mathes, A. Pennell, T. Boroson, S. Sigurðsson, T. Bogdanović, J. P. Halpern, and J. Liu, “A Large Systematic Search for Close Supermassive Binary and Rapidly Recoiling Black Holes. II. Continued Spectroscopic Monitoring and Optical Flux Variability,” *ApJS*, vol. 221, p. 7, Nov. 2015.
- [114] Y.-R. Li, J.-M. Wang, L. C. Ho, K.-X. Lu, J. Qiu, P. Du, C. Hu, Y.-K. Huang, Z.-X. Zhang, K. Wang, and J.-M. Bai, “Spectroscopic Indication of a Centi-parsec Supermassive Black Hole Binary in the Galactic Center of NGC 5548,” *ApJ*, vol. 822, p. 4, May 2016.
- [115] L. Wang, J. E. Greene, W. Ju, R. R. Rafikov, J. J. Ruan, and D. P. Schneider, “Searching for Binary Supermassive Black Holes via Variable Broad Emission Line Shifts: Low Binary Fraction,” *ApJ*, vol. 834, p. 129, Jan. 2017.
- [116] B. Paczynski, “A model of accretion disks in close binaries,” *ApJ*, vol. 216, pp. 822–826, Sep. 1977.
- [117] J. F. Sepinsky, B. Willems, and V. Kalogera, “Equipotential Surfaces and Lagrangian Points in Nonsynchronous, Eccentric Binary and Planetary Systems,” *ApJ*, vol. 660, pp. 1624–1635, May 2007.

- [118] S. Collin-Souffrin and A. M. Dumont, “Emission spectra of weakly photoionized media in active nuclei of galaxies,” *A&A*, vol. 213, pp. 29–48, Apr. 1989.
- [119] —, “Line and continuum emission from the outer regions of accretion discs in active galactic nuclei. II - Radial structure of the disc,” *A&A*, vol. 229, pp. 292–328, Mar. 1990.
- [120] K. Chen, J. P. Halpern, and A. V. Filippenko, “Kinematic evidence for a relativistic Keplerian disk - ARP 102B,” *ApJ*, vol. 339, pp. 742–751, Apr. 1989.
- [121] K. Chen and J. P. Halpern, “Structure of line-emitting accretion disks in active galactic nuclei - ARP 102B,” *ApJ*, vol. 344, pp. 115–124, Sep. 1989.
- [122] M. Eracleous, M. Livio, J. P. Halpern, and T. Storchi-Bergmann, “Elliptical accretion disks in active galactic nuclei,” *ApJ*, vol. 438, pp. 610–622, Jan. 1995.
- [123] M. Eracleous and J. P. Halpern, “Doubled-peaked emission lines in active galactic nuclei,” *ApJS*, vol. 90, pp. 1–30, Jan. 1994.
- [124] —, “Completion of a Survey and Detailed Study of Double-peaked Emission Lines in Radio-loud Active Galactic Nuclei,” *ApJ*, vol. 599, pp. 886–908, Dec. 2003.
- [125] I. V. Strateva, M. A. Strauss, L. Hao, D. J. Schlegel, P. B. Hall, J. E. Gunn, L.-X. Li, Ž. Ivezić, G. T. Richards, N. L. Zakamska, W. Voges, S. F. Anderson, R. H. Lupton, D. P. Schneider, J. Brinkmann, and R. C. Nichol, “Double-peaked Low-Ionization Emission Lines in Active Galactic Nuclei,” *AJ*, vol. 126, pp. 1720–1749, Oct. 2003.
- [126] P. Uttley, E. M. Cackett, A. C. Fabian, E. Kara, and D. R. Wilkins, “X-ray reverberation around accreting black holes,” *A&A Rev.*, vol. 22, p. 72, Aug. 2014.
- [127] J. Chiang and N. Murray, “Reverberation Mapping and the Disk-Wind Model of the Broad-Line Region,” *ApJ*, vol. 466, p. 704, Aug. 1996.
- [128] B. J. Wills and I. W. A. Browne, “Relativistic beaming and quasar emission lines,” *ApJ*, vol. 302, pp. 56–63, Mar. 1986.
- [129] M. C. Bentz, J. L. Walsh, A. J. Barth, N. Baliber, V. N. Bennert, G. Canalizo, A. V. Filippenko, M. Ganeshalingam, E. L. Gates, J. E. Greene, M. G. Hidas, K. D. Hiner, N. Lee, W. Li, M. A. Malkan, T. Minezaki, Y. Sakata, F. J. D. Serduke, J. M. Silverman, T. N. Steele, D. Stern, R. A. Street, C. E. Thornton, T. Treu, X. Wang, J.-H. Woo, and Y. Yoshii, “The Lick AGN Monitoring Project: Broad-line Region Radii and Black Hole Masses from Reverberation Mapping of $H\beta$,” *ApJ*, vol. 705, pp. 199–217, Nov. 2009.

- [130] K. D. Denney, B. M. Peterson, R. W. Pogge, A. Adair, D. W. Atlee, K. Au-Yong, M. C. Bentz, J. C. Bird, D. J. Brokofsky, E. Chisholm, M. L. Comins, M. Dietrich, V. T. Doroshenko, J. D. Eastman, Y. S. Efimov, S. Ewald, S. Ferbey, C. M. Gaskell, C. H. Hedrick, K. Jackson, S. A. Klimanov, E. S. Klimek, A. K. Kruse, A. Laderoute, J. B. Lamb, K. Leighly, T. Minezaki, S. V. Nazarov, C. A. Onken, E. A. Petersen, P. Peterson, S. Poindexter, Y. Sakata, K. J. Schlesinger, S. G. Sergeev, N. Skolski, L. Stieglitz, J. J. Tobin, C. Unterborn, M. Vestergaard, A. E. Watkins, L. C. Watson, and Y. Yoshii, “Reverberation Mapping Measurements of Black Hole Masses in Six Local Seyfert Galaxies,” *ApJ*, vol. 721, pp. 715–737, Sep. 2010.
- [131] C. J. Grier, A. Pancoast, A. J. Barth, M. M. Fausnaugh, B. J. Brewer, T. Treu, and B. M. Peterson, “The Structure of the Broad-line Region in Active Galactic Nuclei. II. Dynamical Modeling of Data From the AGN10 Reverberation Mapping Campaign,” *ApJ*, vol. 849, p. 146, Nov. 2017.
- [132] P. R. Williams, A. Pancoast, T. Treu, B. J. Brewer, A. J. Barth, V. N. Bennert, T. Buehler, G. Canalizo, S. B. Cenko, K. I. Clubb, M. C. Cooper, A. V. Filippenko, E. Gates, S. F. Hoenig, M. D. Joner, M. T. Kandrashoff, C. D. Laney, M. S. Lazarova, W. Li, M. A. Malkan, J. Rex, J. M. Silverman, E. Tollerud, J. L. Walsh, and J.-H. Woo, “The Lick AGN Monitoring Project 2011: Dynamical Modeling of the Broad-line Region,” *ApJ*, vol. 866, p. 75, Oct. 2018.
- [133] N. Murray and J. Chiang, “Disk Winds and Disk Emission Lines,” *ApJ*, vol. 474, pp. 91–103, Jan. 1997.
- [134] H. M. L. G. Flohic, M. Eracleous, and T. Bogdanović, “Effects of an Accretion Disk Wind on the Profile of the Balmer Emission Lines from Active Galactic Nuclei,” *ApJ*, vol. 753, p. 133, Jul. 2012.
- [135] L. S. Chajet and P. B. Hall, “Magnetohydrodynamic disc winds and linewidth distributions,” *MNRAS*, vol. 429, pp. 3214–3229, Mar. 2013.
- [136] —, “Magnetohydrodynamic disc winds and line width distributions - II,” *MNRAS*, vol. 465, pp. 1741–1756, Feb. 2017.
- [137] T. Waters, A. Kashi, D. Proga, M. Eracleous, A. J. Barth, and J. Greene, “Reverberation Mapping of the Broad Line Region: Application to a Hydrodynamical Line-driven Disk Wind Solution,” *ApJ*, vol. 827, p. 53, Aug. 2016.
- [138] N. Murray, J. Chiang, S. A. Grossman, and G. M. Voit, “Accretion Disk Winds from Active Galactic Nuclei,” *ApJ*, vol. 451, p. 498, Oct. 1995.
- [139] D. Proga and T. R. Kallman, “Dynamics of Line-driven Disk Winds in Active Galactic Nuclei. II. Effects of Disk Radiation,” *ApJ*, vol. 616, pp. 688–695, Dec. 2004.

- [140] C. L. MacLeod, P. J. Green, S. F. Anderson, A. Bruce, M. Eracleous, M. Graham, D. Homan, A. Lawrence, A. LeBleu, N. P. Ross, J. J. Ruan, J. Runnoe, D. Stern, W. Burgett, K. C. Chambers, N. Kaiser, E. Magnier, and N. Metcalfe, “Changing-look Quasar Candidates: First Results from Follow-up Spectroscopy of Highly Optically Variable Quasars,” *ApJ*, vol. 874, no. 1, p. 8, 2019.
- [141] J. I. Castor, “Spectral line formation in Wolf-Rayet envelopes.,” *MNRAS*, vol. 149, pp. 111–127, 1970.
- [142] G. B. Rybicki and D. G. Hummer, “A generalization of the Sobolev method for flows with nonlocal radiative coupling,” *ApJ*, vol. 219, pp. 654–675, Jan. 1978.
- [143] F. E. Irons, “Clarification of Sobolev’s derivation of the escape-probability method of radiative transfer,” *J. Quant. Spec. Radiat. Transf.*, vol. 44, pp. 361–371, Sep. 1990.
- [144] F. Hamann, K. T. Korista, and S. L. Morris, “On the Geometry, Covering Factor, and Scattering-Emission Properties of QSO Broad Absorption-Line Regions,” *ApJ*, vol. 415, p. 541, Oct. 1993.
- [145] D. Proga, J. M. Stone, and T. R. Kallman, “Dynamics of Line-driven Disk Winds in Active Galactic Nuclei,” *ApJ*, vol. 543, pp. 686–696, Nov. 2000.
- [146] R.-P. Kudritzki and J. Puls, “Winds from Hot Stars,” *ARA&A*, vol. 38, pp. 613–666, 2000.
- [147] D. Hutsemekers and J. Surdej, “Formation of P Cygni line profiles in relativistically expanding atmospheres,” *ApJ*, vol. 361, pp. 367–380, Oct. 1990.
- [148] D. J. Jeffery, “The Sobolev Optical Depth for Time-dependent Relativistic Systems,” *ApJ*, vol. 440, p. 810, Feb. 1995.
- [149] D. Gerosa, B. Veronesi, G. Lodato, and G. Rosotti, “Spin alignment and differential accretion in merging black hole binaries,” *MNRAS*, vol. 451, pp. 3941–3954, Aug. 2015.
- [150] M. D. Young and C. J. Clarke, “Binary accretion rates: dependence on temperature and mass ratio,” *MNRAS*, vol. 452, pp. 3085–3091, Sep. 2015.
- [151] S. Kaspi, D. Maoz, H. Netzer, B. M. Peterson, M. Vestergaard, and B. T. Januzzi, “The Relationship between Luminosity and Broad-Line Region Size in Active Galactic Nuclei,” *ApJ*, vol. 629, pp. 61–71, Aug. 2005.
- [152] J.-M. Shi and J. H. Krolik, “Three-dimensional MHD Simulation of Circumbinary Accretion Disks. II. Net Accretion Rate,” *ApJ*, vol. 807, p. 131, Jul. 2015.

- [153] C. Roedig, J. H. Krolik, and M. C. Miller, “Observational Signatures of Binary Supermassive Black Holes,” *ApJ*, vol. 785, p. 115, Apr. 2014.
- [154] C. Roedig and A. Sesana, “Migration of massive black hole binaries in self-gravitating discs: retrograde versus prograde,” *MNRAS*, vol. 439, pp. 3476–3489, Apr. 2014.
- [155] L. Blecha, D. Sijacki, L. Z. Kelley, P. Torrey, M. Vogelsberger, D. Nelson, V. Springel, G. Snyder, and L. Hernquist, “Recoiling black holes: prospects for detection and implications of spin alignment,” *MNRAS*, vol. 456, pp. 961–989, Feb. 2016.
- [156] H. M. L. G. Flohic and M. Eracleous, “Interpreting the Variability of Double-Peaked Emission Lines in Active Galactic Nuclei with Stochastically Perturbed Accretion Disk Models,” *ApJ*, vol. 686, pp. 138–147, Oct. 2008.
- [157] K. T. Lewis, M. Eracleous, and T. Storchi-Bergmann, “Long-term Profile Variability in Active Galactic Nucleus with Double-peaked Balmer Emission Lines,” *ApJS*, vol. 187, pp. 416–446, Apr. 2010.
- [158] J. C. Runnoe, M. Eracleous, A. Pennell, G. Mathes, T. Boroson, S. Sigurðsson, T. Bogdanović, J. P. Halpern, J. Liu, and S. Brown, “A large systematic search for close supermassive binary and rapidly recoiling black holes - III. Radial velocity variations,” *MNRAS*, vol. 468, pp. 1683–1702, Jun. 2017.
- [159] J. A. Baldwin, “Luminosity Indicators in the Spectra of Quasi-Stellar Objects,” *ApJ*, vol. 214, pp. 679–684, Jun. 1977.
- [160] B. M. Peterson, A. J. Barth, P. Berlind, R. Bertram, K. Bischoff, N. G. Bochkarev, A. N. Burenkov, F.-Z. Cheng, M. Dietrich, A. V. Filippenko, E. Giannuzzo, L. C. Ho, J. P. Huchra, J. Hunley, S. Kaspi, W. Kollatschny, D. C. Leonard, Y. F. Malkov, T. Matheson, M. Mignoli, B. Nelson, P. Papaderos, J. Peters, R. W. Pogge, V. I. Pronik, S. G. Sergeev, E. A. Sergeeva, A. I. Shapovalova, G. M. Stirpe, S. Tokarz, R. M. Wagner, I. Wanders, J.-Y. Wei, B. J. Wilkes, H. Wu, S.-J. Xue, and Z.-L. Zou, “Steps toward Determination of the Size and Structure of the Broad-Line Region in Active Galactic Nuclei. XV. Long-Term Optical Monitoring of NGC 5548,” *ApJ*, vol. 510, pp. 659–668, Jan. 1999.
- [161] A. I. Shapovalova, V. T. Doroshenko, N. G. Bochkarev, A. N. Burenkov, L. Carasco, V. H. Chavushyan, S. Collin, J. R. Valdés, N. Borisov, A.-M. Dumont, V. V. Vlasuyk, I. Chilingarian, I. S. Fioktistova, and O. M. Martinez, “Profile variability of the $H\alpha$ and $H\beta$ broad emission lines in NGC 5548,” *A&A*, vol. 422, pp. 925–940, Aug. 2004.

- [162] S. G. Sergeev, V. T. Doroshenko, S. A. Dzyuba, B. M. Peterson, R. W. Pogge, and V. I. Pronik, “Thirty Years of Continuum and Emission-Line Variability in NGC 5548,” *ApJ*, vol. 668, pp. 708–720, Oct. 2007.
- [163] J. P. Halpern and M. Eracleous, “Emergence of double-peaked emission lines in the broad-line radio galaxy Pictor A,” *ApJ*, vol. 433, pp. L17–L20, Sep. 1994.
- [164] J. W. Sulentic, P. Marziani, T. Zwitter, and M. Calvani, “Pictor A: A new double-peaked emission-line quasar,” *ApJ*, vol. 438, pp. L1–L4, Jan. 1995.
- [165] D. Alloin, C. Boisson, and D. Pelat, “Evidence for an accretion disc in AKN 120,” *A&A*, vol. 200, pp. 17–20, Jul. 1988.
- [166] P. Marziani, M. Calvani, and J. W. Sulentic, “Twin peaks - IC 4329A and Arakelian 120,” *ApJ*, vol. 393, pp. 658–665, Jul. 1992.
- [167] W. Cochran, *Sampling Techniques*, Third. Wiley, 1977.
- [168] B. J. Pflueger, K. Nguyen, T. Bogdanović, M. Eracleous, J. C. Runnoe, S. Sigurdsson, and T. Boroson, “Likelihood for Detection of Subparsec Supermassive Black Hole Binaries in Spectroscopic Surveys,” *ApJ*, vol. 861, p. 59, Jul. 2018.
- [169] R. Günther and W. Kley, “Circumbinary disk evolution,” *A&A*, vol. 387, pp. 550–559, May 2002.
- [170] L. Z. Kelley, L. Blecha, and L. Hernquist, “Massive black hole binary mergers in dynamical galactic environments,” *MNRAS*, vol. 464, pp. 3131–3157, Jan. 2017.
- [171] J. F. Hawley and J. H. Krolik, “Sound Speed Dependence of Alignment in Accretion Disks Subjected to Lense-Thirring Torques,” *ApJ*, vol. 866, p. 5, Oct. 2018.
- [172] K. Nguyen and T. Bogdanović, “Emission Signatures from Sub-parsec Binary Supermassive Black Holes. I. Diagnostic Power of Broad Emission Lines,” *ApJ*, vol. 828, 68 (Paper I), Sep. 2016.
- [173] K. Nguyen, T. Bogdanović, J. C. Runnoe, M. Eracleous, S. Sigurdsson, and T. Boroson, “Emission Signatures from Sub-parsec Binary Supermassive Black Holes. II. Effect of Accretion Disk Wind on Broad Emission Lines,” *ApJ*, vol. 870, 16 (Paper II), Jan. 2019.
- [174] P. Artymowicz and S. H. Lubow, “Dynamics of binary-disk interaction. 1: Resonances and disk gap sizes,” *ApJ*, vol. 421, pp. 651–667, Feb. 1994.
- [175] N. J. McConnell and C.-P. Ma, “Revisiting the Scaling Relations of Black Hole Masses and Host Galaxy Properties,” *ApJ*, vol. 764, p. 184, Feb. 2013.

- [176] N. I. Shakura and R. A. Sunyaev, “Black holes in binary systems. Observational appearance.,” *A&A*, vol. 24, pp. 337–355, 1973.
- [177] P. C. Peters, “Gravitational Radiation and the Motion of Two Point Masses,” *Physical Review*, vol. 136, pp. 1224–1232, Nov. 1964.
- [178] R. R. Rafikov, “Structure and Evolution of Circumbinary Disks around Supermassive Black Hole Binaries,” *ApJ*, vol. 774, p. 144, Sep. 2013.
- [179] K. R. Stewart, J. S. Bullock, E. J. Barton, and R. H. Wechsler, “Galaxy Mergers and Dark Matter Halo Mergers in Λ CDM: Mass, Redshift, and Mass-Ratio Dependence,” *ApJ*, vol. 702, pp. 1005–1015, Sep. 2009.
- [180] P. F. Hopkins, K. Bundy, D. Croton, L. Hernquist, D. Keres, S. Khochfar, K. Stewart, A. Wetzel, and J. D. Younger, “Mergers and Bulge Formation in Λ CDM: Which Mergers Matter?” *ApJ*, vol. 715, pp. 202–229, May 2010.
- [181] D. J. D’Orazio and A. Loeb, “Repeated Imaging of Massive Black Hole Binary Orbits with Millimeter Interferometry: Measuring Black Hole Masses and the Hubble Constant,” *ApJ*, vol. 863, no. 2, p. 185, 2018.

VITA

Khai H. Nguyen

CONTACT 837 State Street NW, Room C101 404-981-1343
INFORMATION Atlanta, GA 30332 khainguyen@gatech.edu

RESEARCH Active galactic nuclei, supermassive black hole binaries, semi-
INTERESTS analytic modeling of emission signatures, statistical analysis of
large synthetic and observed data sets, parallel and high performance
computing.

EDUCATION **Georgia Institute of Technology**, Atlanta, GA

Ph.D., Physics, *Expected*: Summer 2019

- Thesis Topic: *Emission Signatures from Sub-parsec Binary Supermassive Black Holes*
- Advisor: Dr. Tamara Bogdanović
- Ph.D. Minor: Planetary Science, School of Earth and Atmospheric Sciences

California State University of Fullerton, Fullerton, CA

M.S., Physics, May 2012

- Topic: *Generalized Bose-Einstein and Fermi-Dirac Statistics*
- Advisor: Dr. Ionel Tifrea

Saginaw Valley State University, Saginaw, MI

B.S., Mathematics and Physics (Double Major), December 2009